

# Small-Scale Object Sensing with Terahertz Synthetic Aperture Radar

Von der Fakultät für Ingenieurwissenschaften,  
Abteilung Elektrotechnik und Informationstechnik  
der Universität Duisburg-Essen

zur Erlangung des akademischen Grades

Doktor der Ingenieurwissenschaften (Dr.-Ing.)

genehmigte Dissertation

von

**Aman Batra**

aus

Sonipat, Indien

Gutachter:

Prof. Dr.-Ing. Thomas Kaiser  
Prof. Dr.-Ing. Diana Göhringer

Tag der mündlichen Prüfung: 13.10.2021



# Acknowledgments

First and foremost, I would like to express my sincere gratitude to my supervisor Prof. Dr.-Ing. Thomas Kaiser, who provided me the opportunity of doctoral studies (a dream being carried from high school) at the esteemed Institute of Digital Signal Processing (DSV), the University of Duisburg-Essen. It is an honor for me to work under his supervision. His constant support and motivation, and the ideology of “Think-Complete” were guiding forces that helped me throughout my doctoral tenure. Without his guidance, it would be difficult for me to reach where I am right now. I learned a lot from him and will keep this treasure for my entire life.

I would also like to express my deep gratitude to Prof. Dr.-Ing. Diana Göhringer, Professor at the Chair of Adaptive Dynamic Systems, the Technische Universität Dresden, for her valuable guidance, constructive discussions, sincere support and being my co-supervisor.

Special thanks to Dipl.-Ing. Michael Wiemeler, my group leader at DSV. His contribution and insights throughout my doctoral tenure have been invaluable. There were times when I was stuck with research problems, and he was always there to guide me and collaboratively look for solutions. His guidance and endless discussions has been excellent support for me and helped me achieve my goals in a suitable time frame.

I would also like to thank and acknowledge the contribution of Dipl.-Ing. Theo Kreul in my journey at DSV. His ideas, knowledge, and experience have been helpful in achieving my goal with great results. His suggestions provided a sense of reliability, and his constant support in measurement campaigns was indispensable. From endless conferencing calls to telephonic conversations and e-mails, he was always there to help.

I would also like to thank Prof. Dr.-Ing. Klaus Solbach from DSV for his guidance in the domain of radar and high-frequencies.

I am also thankful for the support in my measurement campaigns provided by Dipl.-Ing. Heinz Schreiber at DSV. He helped me with the smooth functioning of the devices to ease my work.

My sincere thanks to Ms. Sabine Jankowski, Dr. Munisch Wadwa and Ms. Petra Stawicki for helping me throughout my doctoral tenure at DSV with all the administrative and organizational work. I am very thankful for their kindness and support in improving my German language skills.

The support provided at DSV by Dr. Feng Zheng and Dipl.-Ing. Marc Hoffmann in the domain of RFID was really appreciating.

I am also thankful to Prof. Dr. Mats I. Pettersson for hosting me as a visiting scholar for two-weeks at the Department of Mathematics and Natural Sciences, the Blekinge Institute of Technology, Sweden. The overall support from him and his department's colleagues helped me to gain more insights into my research work.

I would also like to thank Dr. Mohammed El-Absi from DSV for nice collaboration in the sector of THz SLAM.

Many thanks to all the former and current DSV colleagues who are part of my journey, directly or indirectly. I would like to mention that I am very thankful for the excellent collaborations, and for providing me with a friendly and supportive environment at work. All the coffee breaks and team meetings on the terrace were indeed fun together.

I would also like to acknowledge the MARIE consortium for all the support and great collaborations.

I am also very thankful to the German Research Foundation (Deutsche Forschungsgemeinschaft, DFG) for providing funding for the Ph.D. tenure.

Additionally, I am also thankful to the Faculty of Physics, the University of Duisburg-Essen, for providing access to their GPU server ("PhysLab").

Last but not the least, I want to express my sincere gratitude to my family. Many thanks to my cousin Dr. Tushar Batra, who introduced me to the fascinating world of science and motivated me to pursue engineering and doctoral studies. I owe everything to my parents, who supported me in following my dreams. I am thankful to my sister for assisting me in the world of engineering. I would like to credit my wife for my achievements. I am very grateful to her for being my backbone and keeping me motivated. Her perpetual support, patience, and kindness made it possible to pursue this dream.

*I dedicate this dissertation to my parents for everything they have done to make this possible.*

**Aman Batra**

Duisburg, Germany  
December, 2021

# Abstract

Synthetic Aperture Radar (SAR) is a remote sensing technique widely used in the microwave spectrum below 30 GHz, which provides a long exploration range but lacks spatial resolution in the range of sub-m. Presently, higher frequency regions are explored. The Terahertz (THz) spectrum seems promising in this regard, as it offers sub-mm resolution due to the available large bandwidth and smaller wavelength in this frequency region. Although the visible and infrared spectrums offer much higher resolution, they lack penetration depth.

The THz spectra broaden the SAR applications to high-resolution imaging and localization, non-destructive testing, and material characterization. However, this spectrum has its own set of challenges, mainly in the form of high atmospheric attenuation and free space path loss, limiting the sensing range. Despite the limitations, the THz spectrum has a great potential in enabling short-range applications, especially in an indoor environment. One potential application case could be a high-resolution indoor environment map to assist in emergency situations. This dissertation focuses on indoor THz SAR and its applications. One significant difference in comparison to well-established space/air-borne SAR operating at microwave spectrum is the mapping object's dimension associated with the spatial resolution, which is much smaller at the THz. Therefore, small-scale objects are in the foreground in this work.

A fundamental building block to investigate the THz SAR is the requirement of a simulation framework. Therefore, a simulation framework is designed based on electromagnetic field calculations in 3D space, including actual material properties, shape and dimensions. The framework is developed to virtualize a testbed and generates comparable results to the measurements. It is further extended to investigate the impact of motion errors. SAR technique relies on the transceiver's accurate positioning information provided by the inertial measurement unit and global positioning system (GPS). This approach cannot be considered for the indoor THz SAR due to the lack of GPS coverage and the requirement of sub-mm positioning accuracy. High positioning accuracy is required because a minimal trajectory deviation is in the range of carrier wavelength. Compensation of the impact of these errors, popularly known as motion compensation (MOCO), is one of the significant challenges at the THz spectrum and addressed in this work. The impact of sub-mm motion errors is analyzed, and a method is presented for MOCO using a passive

tags-based indoor localization system. Besides, an indoor unmanned aerial vehicle based THz simultaneous localization and mapping system is presented.

Further, the dissertation presents 2D imaging configurations based on specular and diffuse reflections, which provide specific valuable information about the measured object. Based on an optimized configuration, 2D imaging of indoor objects in free space and concealed/hidden environments are presented to evaluate the high-resolution imaging and penetration capabilities. Imaging environments with single and multi-object are considered in addition to a long reference range of  $\geq 1$  m. The THz spectrum is always concerned with the sensing range, and most state-of-the-art demonstrations with bandwidth  $\geq 100$  GHz are limited by a reference range of  $\leq 1$  m. This dissertation also presents the method of estimating the maximum sensing range and validating it with measurements. In addition, the dissertation addresses 3D imaging and provides a comparative analysis of image enhancement for the frequency spectrum ranging from 5 GHz to 1.5 THz. The generated high-resolution SAR images in the dissertation are further analyzed for geometric parameter extraction, roughness analysis, and autonomous object detection and classification using machine learning.

Machine learning has gained popularity in recent years, and one of the significant applications of this technology is object detection and classification at the visible spectrum. In establishing this application, the visible spectrum plays an essential role by offering very high-resolution in the range of  $\mu m$ , and the availability of millions/billions of training data sets. A primary constraint on using this technology in the sector of microwave radar imaging is the limited resolution. However, the THz spectrum opens a new paradigm by providing image quality comparable to optical systems. In this work, a training data set of the THz SAR images of indoor objects is generated, and a method is proposed for object detection and classification.

Another primary objective is to address real-time THz SAR imaging. The computational power or time requirement for SAR image processing increases drastically at the THz spectrum, due to the many pixels or voxels to be processed. The pixel/voxel dimensions are in the range of sub-mm, and the number of pixels/voxels can vary from millions to billions for a given image. Image reconstruction algorithms such as backprojection lack data dependencies and inherit a high degree of parallelism, which could be used to reduce the computation time. Three possible prominent signal processing architectures are central processing unit, graphical processing unit, and field-programmable gate arrays. Therefore, in this thesis, SAR 2D and 3D image reconstruction are investigated with all three architectures. Based on the findings, an optimized processing scheme is presented and demonstrated in consideration of the parallel processing technique. Besides, the THz SAR advancement sector of non-line of sight sensing is also addressed in this work.

To summarize, this dissertation presents a complete outlook on small-scale THz SAR ranging from simulation framework design to real-time demonstrations.

# Zusammenfassung

Synthetic Aperture Radar (SAR) ist eine Fernerkundungstechnik, die im Mikrowellenspektrum unterhalb von 30 GHz breite Anwendung findet und eine große Erkundungsreichweite bietet, der es aber an räumlicher Auflösung im Bereich von sub-m mangelt. Derzeit werden höhere Frequenzbereiche erforscht. Das Terahertz (THz) Spektrum scheint dahingehend vielversprechend, da es durch der verfügbaren großen Bandbreite und kleineren Wellenlänge in diesem Frequenzbereich eine Auflösung im Bereich von sub-mm bietet. Das sichtbare und das infrarote Spektrum bieten zwar eine viel höhere Auflösung, aber es fehlt diesen Spektren an Eindringtiefe in Materialien.

Die THz-Spektren erweitern die SAR-Anwendungen um hochauflösende Bildgebung und Lokalisierung, zerstörungsfreie Prüfung und Materialcharakterisierung. Dieses Spektrum hat jedoch seine eigenen Herausforderungen, hauptsächlich in Form von hoher atmosphärischer Dämpfung und Pfadverlusten im freien Raum, die den Erfassungsbereich einschränken. Trotz dieser Einschränkungen hat das THz-Spektrum ein großes Potenzial für Anwendungen im Nahbereich, insbesondere in Innenräumen. Ein möglicher Anwendungsfall könnte eine hochauflösende Karte der Innenraumumgebung zur Unterstützung in Notfallsituationen sein. Diese Dissertation konzentriert sich auf THz SAR Techniken in Innenräumen und deren Anwendungen. Ein signifikanter Unterschied im Vergleich zum etablierten weltraum-/luftgestützten SAR, das im Mikrowellenspektrum arbeitet, ist die Dimension des Kartierungsobjekts in Verbindung mit der räumlichen Auflösung, die im THz Bereich viel kleiner ist. Daher stehen in dieser Arbeit kleinräumige Objekte im Vordergrund.

Ein grundlegender Baustein zur Untersuchung der THz SAR ist die Notwendigkeit eines Simulationsrahmens. Die vorliegende Dissertation entwirft einen solchen Simulationsrahmen, der auf elektromagnetischen Feldberechnungen im 3D-Raum basiert und tatsächliche Materialeigenschaften, Form und Abmessungen von Objekten einbezieht. Weiterhin wird ein Framework entwickelt, um in einem virtuellen Testbed Simulationsergebnisse anhand von realen Messungen zu validieren. Das Framework wird weiter ausgebaut, um den Einfluss von Bewegungsfehlern zu untersuchen. Die klassische SAR Technik unterhalb 30 GHz verlässt sich auf genaue Positionierungsinformationen des Transceivers, die von einem Inertialsystem und dem globalen Positionierungssystem (GPS) bereitgestellt werden. Dieser Ansatz kommt für THz SAR in Innenräumen nicht in

Frage, da keine GPS Abdeckung in Innenräumen vorhanden bzw. eine Positionierungsgenauigkeit im sub-mm Bereich erforderlich ist. Eine hohe Positionierungsgenauigkeit ist erforderlich, da minimalste Abweichungen von einer Trajektorie in der Größenordnung der Trägerwellenlänge die bildverarbeitenden Algorithmen scheitern lassen. Die Kompensation der Auswirkungen dieser Fehler, allgemein bekannt als Bewegungskompensation (MOCO), ist eine der wesentlichen Herausforderungen im THz Spektrum und wird in dieser Arbeit aufgegriffen. Die Auswirkungen von sub-mm Bewegungsfehlern werden analysiert und eine Methode der MOCO unter Verwendung eines auf passiven Tags basierenden Indoor-Lokalisierungssystems vorgestellt. Außerdem wird ein auf einem unbemannten Luftfahrzeug basierendes THz Lokalisierungs- und Kartierungssystem für Innenräume vorgestellt.

Weiterhin werden in der Dissertation 2D-Abbildungskonfigurationen auf Basis von spiegelnden und diffusen Reflexionen vorgestellt, die spezifische und wertvolle Informationen über das gemessene Objekt liefern. Basierend auf einer optimierten Konfiguration werden 2D-Abbildungen von Innenraumobjekten im freien Raum und in verdeckten/versteckten Umgebungen vorgestellt, um die hochauflösenden Abbildungs- und Durchdringungsfähigkeiten zu bewerten. Neben einem großen Entfernungsmessbereich von  $\geq 1$  m werden Abbildungsumgebungen mit Einzel- und Multi-Objekten betrachtet. Im THz-Spektrum steht immer der Erfassungsbereich im Interesse der Untersuchungen, jedoch sind die meisten Demonstrationen nach dem Stand der Technik mit einer Bandbreite von  $\geq 100$  GHz durch einen Erfassungsbereich von  $\leq 1$  m begrenzt. In dieser Dissertation wird auch eine Methode zur Abschätzung des maximalen Erfassungsbereichs vorgestellt und mit Messungen validiert. Darüber hinaus befasst sich die Dissertation mit der 3D-Bildgebung und liefert eine vergleichende Analyse zur Bildverbesserung für das Frequenzspektrum von 5 GHz bis 1,5 THz. Die in der Dissertation erzeugten hochauflösenden SAR-Bilder werden weiter zur Extraktion geometrischer Parameter, zur Rauigkeitsanalyse und zur autonomen Objekterkennung und -klassifizierung mittels maschinellem Lernen analysiert.

Maschinelles Lernen hat in den letzten Jahren an Popularität gewonnen, und eine der wichtigsten Anwendungen dieser Technologie ist die Objekterkennung und -klassifizierung im sichtbaren Spektrum. Bei der Etablierung dieser Anwendung spielt das sichtbare Spektrum eine wesentliche Rolle, da es eine sehr hohe Auflösung im Bereich von  $\mu m$  und die Verfügbarkeit von Millionen/Milliarden von Trainingsdatensätzen bietet. Ein Haupthindernis für den Einsatz von Maschinellern im Bereich der Mikrowellen-Radarabbildung ist die begrenzte Auflösung. Das THz-Spektrum eröffnet jedoch ein neues Paradigma, indem es eine mit optischen Systemen vergleichbare Bildqualität bietet. In dieser Dissertation wird daher ein Trainingsdatensatz der THz SAR Bilder von Objekten in Innenräumen erzeugt und eine Methode zur Objekterkennung und -klassifizierung vorgeschlagen.

Ein weiteres primäres Ziel ist es, die THz SAR Bildgebung in Echtzeit anzugehen. Die Rechenleistung bzw. der Zeitbedarf für die SAR-Bildverarbeitung steigt im THz-Spektrum aufgrund der vielen zu verarbeitenden Pixel bzw. Voxel drastisch an. Die

Pixel-/Voxelabmessungen liegen im sub-mm-Bereich, die Anzahl der Pixel/Voxel kann von Millionen bis zu Milliarden für ein bestimmtes Bild variieren. Bildrekonstruktionsalgorithmen wie die Rückprojektion haben keine Datenabhängigkeiten und besitzen einen hohen Grad an Parallelisierbarkeit, was zur Reduzierung der Rechenzeit genutzt werden kann. Mögliche und prominente Signalverarbeitungsarchitekturen für THz SAR Algorithmen sind neben der Zentrale Verarbeitungseinheit die grafischen Verarbeitungseinheiten und feldprogrammierbare-gate-arrays. Daher wird in dieser Arbeit die SAR 2D- und 3D-Bildrekonstruktion mit allen drei Architekturen untersucht. Basierend auf den Ergebnissen wird ein optimiertes Verarbeitungsschema unter Berücksichtigung der Parallelverarbeitungstechnik vorgestellt und demonstriert. Zusätzlich wird in dieser Arbeit auch der THz SAR Fortschrittssektor der Sensorik mit verdeckten Sichtlinien behandelt.

Zusammenfassend stellt diese Arbeit einen vollständigen Ausblick auf THz-SAR im kleinen Maßstab dar, der vom Entwurf des Simulationsrahmens bis zu Echtzeit-Demonstrationen reicht.



# Contents

<b>1</b>	<b>Introduction</b>	<b>1</b>
1.1	Synthetic Aperture Radar . . . . .	2
1.2	Motivation . . . . .	3
1.3	Research Project: SFB/TRR 196 MARIE . . . . .	4
1.4	Outline and Contributions . . . . .	5
<b>2</b>	<b>Theoretical Framework</b>	<b>11</b>
2.1	Signal Processing and System Model . . . . .	11
2.2	Indoor SAR Geometry and System Parameters . . . . .	13
2.3	Raw Data Generation with 3D Electromagnetic Field Calculations . . . . .	15
2.3.1	Target Design . . . . .	15
2.3.2	Excitation Waveform and Probe . . . . .	16
2.3.3	Raw Data and Power Flow . . . . .	18
2.4	Image Reconstruction . . . . .	20
2.4.1	Backprojection . . . . .	21
2.4.2	Resulting SAR Images . . . . .	21
2.5	Conclusive Remark . . . . .	23
<b>3</b>	<b>Impact of Motion Errors and Compensation</b>	<b>25</b>
3.1	System Model . . . . .	27
3.1.1	SAR Motion Error Geometry . . . . .	27
3.1.2	Localization System . . . . .	28
3.2	Simultaneous Localization and Mapping . . . . .	29
3.3	Translational Trajectory Deviations Effects . . . . .	31
3.3.1	Simulation Analysis . . . . .	32
3.3.2	Analysis of Different Localization Cut-off Requirement in 3D Space . . . . .	36
3.3.3	Experimental Analysis . . . . .	39
3.4	Motion Compensation with Passive Localization System . . . . .	41
3.5	Conclusive Remark . . . . .	45

<b>4</b>	<b>2D Imaging and Analysis</b>	<b>47</b>
4.1	Planar Aperture 2D Imaging Configurations . . . . .	48
4.1.1	Simulation Analysis of Imaging Plane with SDR and DR . . . . .	50
4.1.2	Measurement Analysis of Imaging Plane with SDR and DR . . . . .	52
4.2	Imaging of Indoor Objects . . . . .	57
4.3	Analysis . . . . .	59
4.3.1	Geometric Parameters Extraction . . . . .	60
4.3.2	Comparison of Small and Large Bandwidth Imaging . . . . .	61
4.3.3	Impact of Surface Roughness . . . . .	63
4.4	Concealed and Hidden Object Imaging . . . . .	64
4.4.1	Metallic Structure in Cardboard Box . . . . .	65
4.4.2	Small Components covered with Foam in Plastic Box . . . . .	66
4.4.3	Electrical Cables in Plastic Mount . . . . .	66
4.4.4	Plastic Mount in Cardboard Box and Post behind the Box . . . . .	68
4.5	Maximum Sensing Range . . . . .	68
4.5.1	Methodology . . . . .	69
4.5.2	Validation . . . . .	70
4.6	Conclusive Remark . . . . .	73
<b>5</b>	<b>3D Imaging and Object Detection-Classification</b>	<b>75</b>
5.1	System Model . . . . .	76
5.2	Analysis of Imaging up to 1.5 THz . . . . .	77
5.2.1	Testbed . . . . .	77
5.2.2	Imaging . . . . .	79
5.3	Multi-Object Environment Mapping . . . . .	86
5.4	Object Detection . . . . .	88
5.5	Object Classification . . . . .	92
5.6	Conclusive Remark . . . . .	94
<b>6</b>	<b>Hardware-Software Accelerated Imaging</b>	<b>97</b>
6.1	Processing Paradigm . . . . .	99
6.2	Signal Processing Architecture . . . . .	100
6.3	Design Methodology . . . . .	102
6.4	CPU-based . . . . .	103
6.4.1	Single-core Processing . . . . .	104
6.4.2	Multi-core Processing . . . . .	107
6.5	FPGA-based . . . . .	109
6.6	CPU-GPU-based . . . . .	110
6.7	Hybrid Multi-Processing-Threading CPU-GPU-based . . . . .	112
6.8	Conclusive Remark . . . . .	114

<b>7 Conclusion and Outlook</b>	<b>117</b>
7.1 Conclusion . . . . .	117
7.2 Outlook . . . . .	120
7.2.1 THz Non-Line of Sight Sensing . . . . .	121
<b>List of Publications</b>	<b>123</b>
<b>Bibliography</b>	<b>125</b>



# List of acronyms

<b>2D</b>	Two-dimensional
<b>3D</b>	Three-dimensional
<b>API</b>	Application-Specific Interface
<b>Band 1</b>	5-10 GHz
<b>Band 2</b>	75-110 GHz
<b>Band 3</b>	220-330 GHz
<b>Band 4</b>	325-500 GHz
<b>Band 5</b>	850-1100 GHz
<b>Band 6</b>	1100-1500 GHz
<b>BPA</b>	Backprojection Algorithm
<b>BoVW</b>	Bag of Visual Words
<b>CDF</b>	Cumulative Distribution Function
<b>CPU</b>	Central Processing unit
<b>CR</b>	Corner Reflector
<b>CUDA</b>	Compute Unified Device Architecture
<b>DBSCAN</b>	Density-Based Spatial Clustering of Applications with Noise
<b>DPU</b>	Decentralized Processing Unit
<b>DR</b>	Diffuse Reflections
<b>DSV</b>	Institute of Digital Signal Processing
<b>EM</b>	Electromagnetic
<b>FLOPS</b>	Floating Point Operations per Second
<b>FPGA</b>	Field-Programmable Gate Array
<b>FSPL</b>	Free Space Path Loss
<b>F-B</b>	Forward-Backward
<b>G-B</b>	Glass Bottle
<b>GPS</b>	Global Positioning System
<b>GPU</b>	Graphics Processing Unit
<b>HDL</b>	Hardware Description Language
<b>HPC</b>	High-Performance Computing
<b>IF</b>	Intermediate Frequency

<b>i-FFT</b>	Inverse-Fast Fourier Transform
<b>IMU</b>	Inertial Measurement Unit
<b>INS</b>	Inertial Navigation System
<b>iREC</b>	Image Reconstruction
<b>LiDAR</b>	Light Detection and Ranging
<b>LoS</b>	Line of Sight
<b>L-R</b>	Left-Right
<b>MARIE</b>	Mobile Material Characterization and Localization by Electromagnetic Sensing
<b>M-C</b>	Metallic Compass
<b>MIMO</b>	Multiple-Input-Multiple-Output
<b>mmWave</b>	Millimeter Wave
<b>MOCO</b>	Motion Compensation
<b>M-P</b>	Metallic Post
<b>MPI</b>	Message Passing Interface
<b>M-S</b>	Metallic Sphere
<b>NDT</b>	Non-Destructive Testing
<b>N-LoS</b>	Non-Line of Sight
<b>OpenMP</b>	Open-Multi Processing
<b>P-B</b>	Plastic Bottle
<b>PE</b>	Processing Element
<b>PEC</b>	Perfect Electric Conductor
<b>P-EWM</b>	Plastic Electrical Wire Mount
<b>Radar</b>	Radio Detection and Ranging
<b>RCS</b>	Radar Cross-Section
<b>RDA</b>	Range Doppler Algorithm
<b>RFID</b>	Radio-Frequency Identification
<b>RS</b>	Roughest
<b>RS-FM</b>	Roughest Face Mannequin
<b>RS-ST</b>	Rough-Smooth
<b>RTL</b>	Register Transfer Level
<b>RTof</b>	Round-Trip Time-of-Flight
<b>SAR</b>	Synthetic Aperture Radar
<b>SLAM</b>	Simultaneous Localization and Mapping
<b>SPP</b>	Signal Processing Platform
<b>ST</b>	Smoothest
<b>SURF</b>	Speeded-Up Robust Features
<b>SVM</b>	Support Vector Machine
<b>THz</b>	Terahertz
<b>UAV</b>	Unmanned Aerial Vehicle
<b>U-D</b>	Upward-Downward
<b>VNA</b>	Vector Network Analyzer
<b>W-B</b>	Wooden-Box

# Notation

## Symbols with Latin letters

$x$	Vector
$\mathbf{X}$	Matrix
$\mathbf{X}^*$	Complex Conjugate of $\mathbf{X}$
$dim(\mathbf{X})$	Dimension of $\mathbf{X}$
$row_i \mathbf{X}$	Row $i$ of $\mathbf{X}$
$col_i \mathbf{X}$	Column $i$ of $\mathbf{X}$
$\mathbf{X}_{2D}$	2D-Matrix
$\mathbf{X}_{3D}$	3D-Matrix
$ x $	Magnitude of vector $x$
$max(x)$	Maximum of vector $x$
$A$	Antenna Area for Localization
$A_k$	Amplitude of Reflectivity from $k^{\text{th}}$ Scatterer
$B_w$	Bandwidth
$c$	Speed of Light in Vacuum
$c_n$	Phase Velocity
$f_c$	Center or Carrier Frequency
$f_D$	Doppler Bandwidth
$h$	Standard Deviation of Surface Irregularities
$K$	Number of Scatterers
$L_r$	Antenna Length or Diameter
$L_s$	Synthetic Aperture Length
$L_s, y$	Synthetic Aperture Length along $y$ -axis
$L_s, z$	Synthetic Aperture Length along $z$ -axis
$n$	index of aperture position
$n$	Refractive Index
$N$	Total Number of Aperture Positions
$N_f$	Number of Frequency Points
$N_i$	Number of Rows in a Matrix

$N_j$	Number of Columns in a Matrix
$N_k$	Number of 2D layers in a 3D Matrix
$N_p$	Number of Pixels or Voxels to be Processed
$N_{p,2D}$	Number of Pixels to be Processed
$N_{p,3D}$	Number of Voxels to be Processed
$N_{\text{tag}}$	Number of Tags
$N_y$	Number of Aperture Positions along $y$ -axis
$N_z$	Number of Aperture Positions along $z$ -axis
$\mathbf{P}$	Position in 3D space
$p(t)$	Time-Domain Transmit Signal
$P_t$	Transmit Power
$P_T$	VNA Transmit Base Power
$P_r$	Received Power
$P(w)$	Frequency-Domain Transmit Signal
$r_x$	Resolution along x-axis
$r_y$	Resolution along y-axis
$r_z$	Resolution along z-axis
$r_{\text{gr}}$	Resolution along Ground or Ground-Range Resolution
$R$	Range or Slant Range
$R_i$	Ideal Range
$R_m$	Modified Range
$R_{\text{ref}}$	Reference Range
$s_{\text{cm}}(t)$	Time-Domain Range Compressed Signal
$s(t)$	Time-Domain Received Signal or Echoes
$s_k(t)$	Received Signal from $k^{\text{th}}$ Scatterer
$s_z(t)$	Time-Domain Zero-padded Recieved Signal
$S$	Reflection Coefficient
$S_{11}$	One-Port VNA Reflection Coefficient
$S_M$	Measured Reflection Coefficient
$S_P$	Predicted Reflection Coefficient
$t$	Time-domain
$t_d$	Time of Flight
$T_c$	Computation Time
$T_D$	Signal Duration
$T_{\text{ser}}$	Serial or Sequential Processing Execution Time
$T_{\text{par}}$	Parallel Processing Execution Time
$u$	Vector of Azimuth Sampling Positions
$U$	Number of Azimuth Positions
$v$	Vector of Elevation Sampling Positions
$V$	Number of Elevation Positions
$v_{\text{az}}$	Extracted Azimuth Vector
$v_r$	Extracted Range Vector

$V_r$	Velocity
$w_a(u)$	Square of Received Signal Strength in Respect to Zero-Doppler Plane
$w_r(t)$	Time-Domian Signal Envelope
$X_c$	Beam Footprint Swath Center
$(x, y, z)$	Cartesian Coordinates
$(x^m, y^m, z^m)$	Cartesian Coordinates in Reference to $(x, y, z)$
$(x_e, y_e, z_e)$	Erros along $x$ -, $y$ - and $z$ -axis
$(X_E, Y_E, Z_E)$	Estimated Positions along $x$ -, $y$ - and $z$ -axis
$(X_0, Z_0)$	Distance (Range) along $x$ - and $z$ -axis

## Symbols with Greek letter

$\lambda$	Wavelength
$\lambda_c$	Center or Carrier Wavelength
$\epsilon_r$	Relative Permittivity
$\eta$	Time Associated with Azimuth Position
$\sigma$	RCS
$\alpha$	Noise Figure for Localization
$\kappa_r$	Chirp-Rate
$\theta_{-3 \text{ dB}}$	$-3$ dB Antenna Beamwidth
$\theta_i$	Incidence Angle
$\theta_l$	Look Angle
$\theta_r$	Reflection Angle
$\theta_{r,c}$	Squint Angle
$\phi_y$	Yaw-Rotational Angle along $y$ -axis
$\omega$	Frequency-Domain
$\Delta u$	Step Size
$\Delta u_y$	Step Size along $y$ -axis
$\Delta u_z$	Step Size along $z$ -axis



# Introduction

Radio Detection and Ranging, abbreviated as Radar, uses electromagnetic (EM) waves for sensing. The radar history is linked with the pioneer contribution in radio technology by Scottish scientist James Clerk Maxwell and German physicist Heinrich Hertz in the late 19th century [1]. Maxwell proposed the presence of EM waves in free space, and Hertz's experiments validated it in 1887-88 in addition to reflection, refraction, diffraction, and polarization of EM waves [2]. In the radar-domain, its principle was first accidentally observed by Russian physicist Alexander Stepanovich Popov, who experienced the interference caused by the nearby ships while transmitting the radio waves in 1897 [3]. The first radar application experiment of detecting a metallic object (ship) using radio waves at 650 MHz was carried out in 1904 by the German scientist Christian Hülsmeyer for the application of collision avoidance with the device called "Telemobiloskop" [1]. Although the first experiment was conducted at the beginning of the 20th century, the concept of radar gained popularity in the 1930s in the defense sector. The research was being conducted simultaneously in many countries. Most of the radar systems developed at an early stage (before the 1940s) were operating at a carrier frequency below 1 GHz with a transmit power in the range of a few KW and are based on analog electronic components [1]. The acronym *Radar* was defined in 1940 by U.S. Navy [3] and since 1945 it is widely used worldwide [1].

Early radar usage was restricted only to the defense sector with limited applications such as velocity estimation, and detection and ranging of moving or stationary objects. In this technique, a known waveform is transmitted with a particular polarization, and the reflected received signal is a time-shifted variant of the original signal. The recorded reflection, delay, and frequency shift based on the Doppler effect define the target's presence, position, and velocity, respectively [4, 5]. The radar systems at radio or microwave spectrum majorly benefit from long propagation range and suitability in all-weather conditions such as cloudy and foggy environment, where the optical technology such as camera at the visible spectrum might not provide any useful information. In contrast, the camera offers very high-resolution images in the range of  $\mu m$  [6].

In the 1950s, the need for surveillance around the clock led to the development of

*Synthetic Aperture Radar* (SAR) as an imaging radar in alternative to the optical systems [4, 5, 7]. The major constraint in using a typical radar such as real aperture radar for imaging is the requirement of enormous antenna aperture or diameter for high azimuth (also known as cross-range or angular) resolution given by  $-3$  dB beamwidth of an antenna at a reference range [8]. American mathematician Carl Atwood Wiley first reported the SAR principle in 1951, where he demonstrated high-angular resolution using a coherent mobile radar system [7].

## 1.1 Synthetic Aperture Radar

SAR is a remote sensing technique that synthesizes a large aperture to provide high angular resolution. The principle of SAR 2D imaging can be well explained from Fig. 1-1. In this approach, the SAR high-frequency sensors are mounted on a flying (or mobile) platform, which transmit EM waves towards the target along the range direction at discrete azimuth sampling positions  $u \in (u_1, u_N)$ , where  $N$  is the total number of azimuth positions. The platform follows a particular trajectory along the azimuth direction at a certain height, which leads to the formation of a synthetic aperture. For image reconstruction, backscattered signals from the illuminated space are captured at each aperture position and processed with an image reconstruction algorithm.

SAR sensors configuration could be a monostatic, bistatic, or multistatic. In the monostatic case, the transmitter and receiver are collocated and are generally driven by the same reference oscillator [9]. It is achieved by using a transceiver device that can perform both transmission and reception operations. Whereas in the bistatic case, the transmitter and receiver are spatially separated, and the multistatic is the combination of both mono- and bi-static configurations [10, 11]. The separation in bistatic or multistatic could range from a few cm to many Km [12].

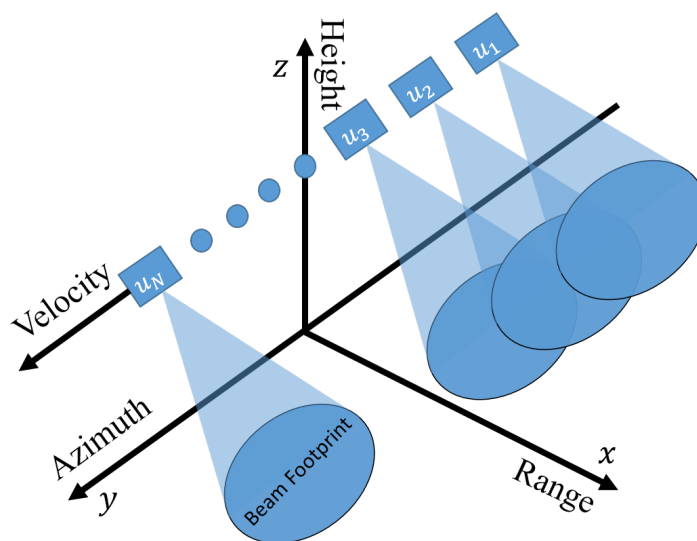


Figure 1-1: Generic SAR imaging scene.

Although SAR was developed primarily for the defense sector, its applications are widely extended to the commercial domain. Topographic imaging, air traffic control, meteorology, underground resource exploration, land and vegetation structure observation are some of the well-established SAR applications [4, 5, 8].

## 1.2 Motivation

State-of-the-art SAR is widely used at the microwave spectrum (below 30 GHz), which offers long penetration depth and range but lacks spatial resolution (range and cross-range). The resolution defines the minimum resolvable distance between two scatterers. In general, the higher the resolution, the more detailed and accurate information of the imaging target can be extracted. The spatial resolution is directly related to the system bandwidth, carrier frequency, and antenna diameter. Therefore, higher frequency regions are being investigated to achieve sub-mm resolution. Visible and infrared (IR) spectrums provides very high-resolution but are considered non-penetrating. The THz spectrum lying between the microwave and visible/IR spectrums offers both the traits, good penetration depth, and high-resolution due to large available bandwidth, compact antenna and shorter wavelength.

The THz spectrum is under investigation for many decades [13] such as in astronomy [14]. In the past, the complexity of the electronic hardware modules and cost of the devices limits the large-scale adoption of its application [15]. Another drawback of the THz spectrum is the high free space path loss (FSPL) [16] and atmospheric absorption [17] that limits the propagation range. However, there are specific spectral windows with less atmospheric attenuation that can be utilized [17].

Nowadays, the THz spectrum has emerging short-range applications [18, 19]. Many novel THz SAR testbeds are being actively proposed in the literature and the research is being carried out for different potential applications such as defense and security [20], automobile [21, 22], non-destructive testing (NDT) [18, 23], and road mapping [24]. This dissertation focuses on the application of high-resolution indoor environment mapping.

An example application scenario could be an indoor hazardous environment and rescue mission, where different types of sensors are utilized for environment sensing and mapping. Based on the sensors operating frequency range, they are usually classified into the microwave/radio, THz, visible, and IR groups. The visible/IR sensors benefit from shorter wavelengths and provide very high spatial resolution but lack penetration depth. Therefore, they might not offer any useful information when a target of interest is obscured by smoke, fire, or hidden by other objects. For example, environment mapping using visible/IR sensors is shown in [25, 26]. The resulting images are of very high-resolution but non-penetrating as nothing is mapped behind the indoor and outdoor objects in [25]. Similarly, in the case of considered indoor objects in [26], only the object's front surface is mapped. In contrast, the microwave sensors offer higher penetration depth but with a limited resolution. This is demonstrated in [27] and [28], where indoor environment mapping with microwave sensors around the center frequency of 1.35 GHz and 5.8 GHz,

respectively, are shown.

However, the THz SAR sensors, for example, mounted on a unmanned aerial vehicle (UAV) can provide a sub-mm resolution room profile as this spectrum lies between the IR and microwave spectra. Therefore, it offers the advantages of higher penetration depth than the IR/visible and higher resolution compared to the microwave spectrum. The achieved map can be further analyzed for material characterization, and object localization, detection, and classification. Detecting and localizing the unconscious human beings covered by smoke or estimating the danger from high-voltage electrical cables are common examples. Besides, the THz SAR technique's indoor environment mapping creates the base for many other applications such as health monitoring and support to household robotics.

Object detection and classification using machine learning primarily belongs to the field of computer vision and has a wide variety of applications, for example, detection and classification of environmental objects to avoid collision in self-driving cars or with service robots [29]. The applications are mainly based on optical systems due to the available very high-resolution. Therefore, this technique is not explored widely in radar-domain and especially concerning to indoor environment. However, the THz spectrum provides a new paradigm of adapting this technique in radar-domain by providing image quality in good compliance to optical systems.

Most of the state-of-the-art THz SAR demonstrations with electronics transceiver modules (radar- [20, 21, 30] or vector network analyzer-based [23, 31]) are limited either with bandwidth (sub-100 GHz) or propagation range (sub-m). Besides, in terms of high-resolution environment mapping, the prime focus is on outdoor applications in the sector of automobile [22] and security [30]. This dissertation focuses on long-range and investigation of the spectrum up to 1.5 THz with a maximum bandwidth of 400 GHz. UAV-based indoor environment mapping with autonomous object detection and classification, and accelerating imaging is in the foreground in this work.

Moreover, based on the SAR technique, imaging at THz frequencies can also be realized with the photonics system such as time-domain spectroscopy [13, 32]. It provides very high spatial resolution due to much larger bandwidth ( $>1$  THz) and shorter wavelength ( $<0.1$  mm), but the systems are limited to very short-range ( $<30$  cm) and low signal to noise ratio [33]. This dissertation addresses the THz SAR imaging based on electronic transceiver modules, although similar algorithms and methods can be applied to photonics-based THz imaging.

To summarize, from theoretical analysis, it can be concluded that the THz SAR has vast potential for indoor applications.

### **1.3 Research Project: SFB/TRR 196 MARIE**

The work in this dissertation was supported by the Deutsche Forschungsgemeinschaft (DFG, German Research Foundation) Project-ID 287022738 - SFB/TRR 196 MARIE, where MARIE stands for *Mobile Material Characterization and Localization by Electro-*

*magnetic Sensing.*

MARIE's objective is to characterize and localize stationary and non-stationary objects in a dynamic environment. The vision is to build a novel compact sensor to extend human senses or support to the industrial environment. Generating an indoor relief map in case of emergency scenarios and expanding the map with localization, classification, and characterization of materials is one of MARIE's novel sensor's application cases. This vision is well-supported by 3 project pillars: Models from measurements ( $M$ ), Chips for technology ( $C$ ) and Systems from Concepts ( $S$ ), where  $M$  focuses on models and validation with measurements,  $C$  provides the technology and  $S$  addresses the signal processing. The project is planned for 3 phases with each duration of 4 years. In Phase 1 (2017-2020), static-lab environment and spectrum up to 1.5 THz is in the foreground. Phase 2 (2021-2024) considers a dynamic environment with an extended-spectrum range of up to 4 THz. Finally, Phase 3 (2025-2028) realizes the MARIE vision with a fusion of technologies and principles [34].

In this thesis, the work is conducted under two associated-projects  $M01$  (work package 4) and  $S05$  in phases 1 and 2, respectively. The project goal is to generate a 3D indoor material map based on the THz SAR technique and to expand the map with autonomous object detection, characterization and classification in "*Minimum flight time*" and with "*Maximum on-board computation*" [34].

Therefore, the indoor THz SAR with high-resolution and accelerated imaging, motion compensation, and objection detection and classification is in the foreground in this dissertation.

## 1.4 Outline and Contributions

The dissertation structural workflow is shown in Fig. **1-2**. To briefly describe the workflow, first and foremost, a novel simulation framework is developed to investigate the THz SAR technique and generate a comparable result to the measurements. Supported by the framework, a novel UAV-based indoor THz simultaneous localization and mapping (SLAM) system is presented. It is extended by investigating non-linear SAR trajectories and motion compensation (MOCO) at the THz spectrum.

Further, the long-range 2D and 3D THz imaging of indoor objects are demonstrated. In this work, the spectrum up to 1.5 THz is addressed. The demonstration is extended with high-resolution multi-object environment mapping with autonomous object detection and classification using machine learning. Another major challenge of the THz SAR, real-time imaging is also addressed in this work, and an optimized signal processing scheme is presented. Lastly, as one of the future research projects on THz SAR advancement, an experimental demonstration of long-range non-line of sight (N-LoS) THz sensing is presented.

Following is the detailed description of the contributions along with the outline of the dissertation and associated publications:

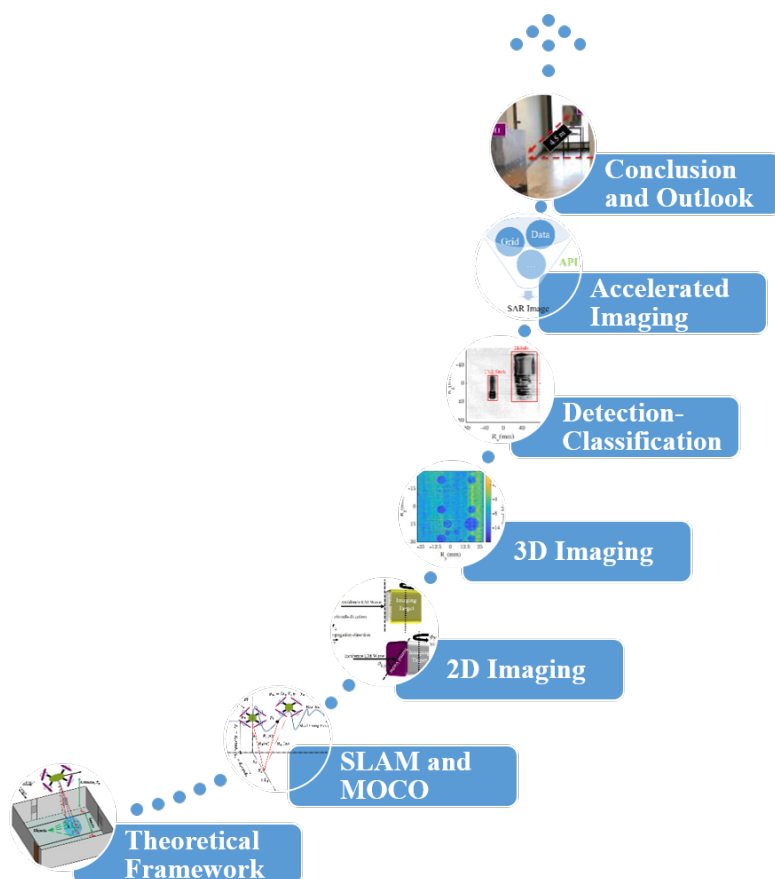


Figure 1-2: Schematic structure and contribution of the dissertation.

- **Chapter 2:** Theoretical Framework

In traditional SAR such as airborne or spaceborne [4, 5, 8], the space surveillance stations such as German Aerospace Center [35], and Fraunhofer Institute for High Frequency Physics and Radar Techniques [36] in Germany are generally the source of providing measured raw data generated by satellites systems or high-profile missions. The data is commonly in the microwave spectrum range due to well-established microwave SAR sensors and required special permissions to use. Besides, due to the unavailability of a complete commercial THz SAR simulation platform that includes both raw data generation and image reconstruction, a simulation framework is required to investigate small-scale THz SAR. One major challenge is to generate raw data with simulations that should be comparable to the measurements. Therefore, in this dissertation, a THz SAR simulation framework is investigated and developed using CST studio [37] to virtualize a measurement environment.

Firstly, the chapter presents the fundamentals of SAR signal processing and UAV-based indoor imaging geometry. Further, the system parameters in comparison to the lower frequency spectrum are evaluated. Based on the estimated parameters and geometry, an imaging environment is simulated with different materials and shapes of objects. The raw data is generated for the frequency band of 220-330

GHz with calculations of 3D EM waves in the imaging space. The results are presented for high-resolution 2D imaging and validated based on the considered object's properties.

Following are the supported publications for the work presented in this chapter:

- **A. Batra**, M. El-Absi, M. Wiemeler, D. Göhringer and T. Kaiser, “Indoor THz SAR Trajectory Deviations Effects and Compensation With Passive Sub-mm Localization System,” in *IEEE Access*, vol. 8, pp. 177519-177533, 2020.
  - **A. Batra**, M. Wiemeler, D. Goehringer and T. Kaiser, “Simulation Validation of High Resolution Indoor Terahertz Synthetic Aperture Radar Imaging,” 2020 14th European Conference on Antennas and Propagation (EuCAP), Copenhagen, Denmark, pp. 1-5, 2020.
- **Chapter 3: Impact of Motion Errors and Compensation**

SAR technique requires precise localization information of the mobile radar sensor, which in conventional SAR is achieved using an existing localization infrastructure, such as a global positioning system (GPS) and inertial measurement unit (IMU). For the indoor UAV-based THz SAR, the GPS does not provide coverage in complex indoor environments, and also, the state-of-art compact IMU does not provide the required sub-mm accuracy. These limitations can be overcome by utilizing an indoor localization system. Therefore, this chapter presents an indoor THz simultaneous localization and mapping (SLAM) system. The method comprises of passive tags-based radio frequency identification (RFID) localization system and SAR that provides the localization and mapping of the in-room objects. Another challenge for the UAV-based indoor THz SAR that is addressed here is motion compensation (MOCO). At the THz spectrum, MOCO requires special consideration because of the minimal trajectory deviation is in the range of carrier wavelength. Therefore, to study the effects of the sub-mm translational errors, a testbed has been set up. The measurement results are presented in this chapter along with the 3D electromagnetic simulation results with the developed framework in Chapter 2 for a carrier frequency of 275 GHz and bandwidth of 50 GHz. Further, to compensate for these error's impact, the sub-mm localization system is used, and the results are presented to validate the proposed solution for the indoor THz SAR MOCO.

The author would like to acknowledge here Dr. Mohammed El-Absi from the Institute of Digital Signal Processing, University of Duisburg-Essen for providing the UAV estimated coordinates based on the localization system presented in [38]. The author would also like to clarify that the UAV estimated coordinates with RFID-based localization system presented in this chapter are provided by Dr. El-Absi. The same statement is also provided at the beginning of this chapter.

Following are the supported publications for the work presented in this chapter:

- **A. Batra**, M. El-Absi, M. Wiemeler, D. Göhringer and T. Kaiser, “Indoor THz SAR Trajectory Deviations Effects and Compensation With Passive Sub-mm Localization

System,” in *IEEE Access*, vol. 8, pp. 177519-177533, 2020.

- **A. Batra**, M. Wiemeler, T. Kreul, D. Goehringer and T. Kaiser, “SAR Signal Processing Architecture and Effects of Motion Errors for mmWave and THz Frequencies,” 2019 Second International Workshop on Mobile Terahertz Systems (IWMTS), pp. 1-6, 2019.

- **Chapter 4: 2D Imaging and Analysis**

State-of-the-art THz SAR demonstration with a bandwidth of more than 100 GHz is mainly limited by the propagation distance of sub-m. Also, the material of the imaging object is primarily metal. The technique must be explicitly evaluated with non-metallic indoor items and at higher ranges to realize the indoor THz SAR applications. Therefore, in this chapter, a testbed with a long reference range has been set up to demonstrate and study the THz SAR imaging of indoor objects made of different materials such as plastic, wood, glass, paper, and foam. Imaging configurations based on specular and diffuse reflections are presented. Both configurations provide valuable information about the measured object, and, therefore, an optimum configuration for a specific application can be retrieved. Based on the optimized configuration, 2D imaging of indoor objects is investigated. Additionally, the impact of object surface roughness at the THz spectrum is analyzed, and the geometric properties of the mapped objects are extracted. Furthermore, a comparative analysis of small and large bandwidth for 2D imaging in the spectrum range of 220-330 GHz is presented.

The chapter also addresses the THz EM waves penetration capabilities using hidden object imaging. Lastly, an analytical model for defining the considered object’s maximum sensing range based on the measurement setup is proposed and validated.

Following are the supported publications for the work presented in this chapter:

- F. Sheikh, Y. Zantah, **A. Batra**, I. Mabrouk, M. Al-Hasan and T. Kaiser, “Far-Distance VNA-based Measurements of Indoor Materials at 300 GHz,” 2021 IEEE-APS Topical Conference on Antennas and Propagation in Wireless Communications (APWC), pp. 064-064, 2021.
- D. Damyanov, **A. Batra**, B. Friederich, T. Kaiser, T. Schultze and J. C. Balzer, “High-Resolution Long-Range THz Imaging for Tunable Continuous-Wave Systems,” in *IEEE Access*, vol. 8, pp. 151997-152007, 2020.
- **A. Batra**, M. Wiemeler, D. Goehringer and T. Kaiser, “Comparison Analysis of Small and Large Bandwidth Indoor SAR Multi-Object Imaging at Low Terahertz Spectrum,” 2020 45th International Conference on Infrared, Millimeter, and Terahertz Waves (IRMMW-THz), Buffalo, NY, USA, pp. 1-2, 2020.
- D. Damyanov, **A. Batra**, B. Friederich, K. Kolpatzeck, X. Liu, T. Kaiser, T. Schultze, J. C. Balzer, “High Resolution VNA THz Imaging for Large Distances,” 2020 45th International Conference on Infrared, Millimeter, and Terahertz Waves (IRMMW-THz), Buffalo, NY, USA, pp. 01-02, 2020.

- **A. Batra**, Y. Zantah, M. Wiemeler, V. T. Vu, M. I. Pettersson, D. Goehring and T. Kaiser, “Experimental Analysis of High Resolution Indoor THz SAR Imaging,” WSA 2020; 24th International ITG Workshop on Smart Antennas, Hamburg, Germany, pp. 1-5, 2020.
- **A. Batra**, V. T. Vu, Y. Zantah, M. Wiemeler, M. I. Pettersson, D. Goehring and T. Kaiser, “Sub-mm Resolution Indoor THz Range and SAR Imaging of Concealed Object,” 2020 IEEE MTT-S International Conference on Microwaves for Intelligent Mobility (ICMIM), pp. 1-4, 2020.

- **Chapter 5:** 3D Imaging and Object Detection-Classification

This chapter addresses the 3D THz SAR imaging. From theoretical analysis, it can be summarized that the higher frequency spectrum provides better resolution. Still, a comparative study on the impact on the image quality for the frequency spectrum ranging from GHz to THz has not been presented. Besides, as of the THz devices hardware complexity, the spectrum’s optimum range is constantly under investigation. The optimum range is defined, where no strong improvements in image quality are achievable with further increases in the frequency spectrum. Therefore, this chapter firstly presents an analysis of 3D imaging using the SAR technique for the frequency spectrum ranging from GHz to THz. Six frequency bands: 5-10 GHz, 75-110 GHz, 0.22-0.33 THz, 0.325-0.5 THz, 0.85-1.1 THz, and 1.1-1.5 THz are selected for comparative analysis.

State-of-the-art imaging based on SAR technique with electronics transceiver modules has only been demonstrated up to the sub-0.75 THz to the best of author’s knowledge. In this chapter, the spectrum up to 1.5 THz is addressed.

The demonstration of multi-object environment mapping further enriches the contribution. Based on the mapped environment, a method is proposed for autonomous object detection and classification using machine learning techniques. The detection provides information about the number of objects and their respective locations in the imaging scene. The classification supported by the detection provides the information, for example, that the detected object is a mobile phone.

Following are the supported publications for the work presented in this chapter:

- **A. Batra**, J. Barowski, D. Damyanov, M. Wiemeler, I. Rolfes, T. Schultze, J. C. Balzer, D. Göhringer, T. Kaiser, “Short-Range SAR Imaging From GHz to THz Waves,” in IEEE Journal of Microwaves, vol. 1, no. 2, pp. 574-585, April 2021.
- V. T. Vu, M. I. Pettersson, **A. Batra**, T. Kaiser, “Fourier Transform of SAR Data Cube and 3D Range Migration Algorithm,” in IEEE Transactions on Aerospace and Electronic Systems (correspondence), 2021 (accepted on Nov. 25, 2021).
- **A. Batra**, M. Wiemeler, D. Göhringer and T. Kaiser, “Sub-mm Resolution 3D SAR Imaging at 1.5 THz,” 2021 Fourth International Workshop on Mobile Terahertz Systems (IWMTS), pp. 1-5, 2021.

- **Chapter 6:** Hardware-Software Accelerated Imaging

This chapter addresses the objective of “minimum computation time” for SAR image reconstruction. At the THz spectrum, many pixels (in case of 2D imaging) and voxels (in case of 3D imaging) have to be processed that drastically increase the computational time. The chapter presents the signal processing architectures and the design methodology for accelerated imaging. Based on the methodology, the prominent architectures, central processing unit (CPU), (graphics processing unit) GPU and (field-programmable gate arrays) FPGA, are analyzed for 2D and 3D imaging. A detailed comparison of computational time on these architectures is provided. Based on the analyzed results, an optimized hybrid processing technique is proposed and validated with results.

The author would also like to acknowledge the collaboration with bachelor and master thesis in [39, 40, 41] for the initial results of investigating different architectures.

Following are the supported publications for the work presented in this chapter:

- **A. Batra**, A. Kamaleldin, L. Y. Zhen, M. Wiemeler, D. Göhringer and T. Kaiser, “FPGA-Based Acceleration of THz SAR Imaging,” 2021 Fourth International Workshop on Mobile Terahertz Systems (IWMTS), pp. 1-5, 2021.
- **A. Batra**, M. Wiemeler, T. Kreul, D. Goehring and T. Kaiser, “SAR Signal Processing Architecture and Effects of Motion Errors for mmWave and THz Frequencies,” 2019 Second International Workshop on Mobile Terahertz Systems (IWMTS), pp. 1-6, 2019.
- **A. Batra**, M. Wiemeler, T. Kreul, D. Goehring and T. Kaiser, “A Massive MIMO Signal Processing Architecture for GHz to THz Frequencies,” 2018 First International Workshop on Mobile Terahertz Systems (IWMTS), pp. 1-6, 2018.

- **Chapter 7:** Conclusion and Outlook

This chapter presents a conclusive summary of the the achieved results and an outlook on the future trends for the THz SAR. Additionally, initial results on one of the future trends, long-range N-LoS THz sensing, are presented.

Following is the supported publication for the work presented in this chapter:

- **A. Batra**, J. Alam, M. Wiemeler, D. Goehring and T. Kaiser, “Long-Range Non-Line of Sight THz Sensing,” 2021 46th International Conference on Infrared, Millimeter and Terahertz Waves (IRMMW-THz), pp. 1-2, 2021.

## Theoretical Framework

The chapter addresses the THz SAR signal processing and presents the developed simulation framework in this thesis. A novel framework is crucial to investigate THz SAR technology as there is no such commercial platform available that provides the complete solution. SAR simulation framework includes generating the raw data and processing this data with an image reconstruction module to form the image. The primary concern is the generation of raw data, and there are two possible generic methods. The first is to mathematically model transmit and receive signals in consideration of wireless channel properties and targets as point scatterers. In contrast, the other method includes virtualization of the measurement setup concerning actual target properties such as material, shape and dimensions, including the calculations of 3D EM fields based on Maxwell equations [42]. The chapter focuses on this virtualization scheme. However, the system modeling with point scatterers is also considered to explain SAR signal processing and evaluate system parameters.

Basically, the modeled SAR data simulation approach with point scatterers provides detailed information on the workflow and imaging geometry in consideration of the continuous UAV movement. The evaluated imaging geometry and system parameters are the basic building block of the 3D EM simulation approach. The objective is to provide comparable imaging results depending on the fundamental properties of the transceiver system, imaging environment, and target.

The chapter is organized as follows. Firstly, Section 2.1 explains the SAR signal processing and system model. Section 2.2 describes the indoor SAR geometry and evaluates the system parameters. In Section 2.3, the simulation framework is presented. Section 2.4 presents the results of SAR image reconstruction based on the presented geometry and evaluated parameters. Lastly, in Section 2.5, a conclusive remark is provided.

### 2.1 Signal Processing and System Model

The general principle for an indoor SAR in the monostatic configuration is illustrated in Fig. 2-1 (left). In this approach, a transceiver as radar sensor is mounted on a mobile

platform such as a UAV and transmits EM waves towards the ground targets. As shown in Fig. 2-1 (left), the flying direction is along the azimuth or  $y$ -axis, the propagation direction is along the  $x$ -axis,  $X_c$  is the swath center, and swath length along the  $x$ -axis is  $2X_0$ . The length is defined by the antenna beamwidth or beam footprint [4] and provides the illuminated space. To form a 2D image of the ground targets in the  $x$ - $y$  plane, the backscattered signals are received and recorded by the sensor providing the raw data.

To model the system, let's consider  $p(t)$  as a transmit signal in time-domain and  $P(\omega)$  in frequency-domain. The received signal from a single scatterer  $k$  at a range  $R_k$  is given by

$$s_k(t) = A_k p\left(t - \frac{2R_k}{c}\right). \quad (2-1)$$

It is a time shifted version of  $p(t)$ , where  $A_k$  is the amplitude of scatterer  $k$  reflectivity and  $c$  is the speed of light [4]. For multiple scatterers  $k \in (1, K)$ , where  $K$  is the number of scatterers, the received signal is the summation of all individual returns and given by

$$s(t) = \sum_{k=1}^K A_k p\left(t - \frac{2R_k}{c}\right). \quad (2-2)$$

The transmit signal could be a single/multi-tone, Gaussian or a chirp [4, 5]. The chirp signal majorly benefits in providing high signal energy over a short duration and the bandwidth  $B_w$  is inversely proportional to signal duration  $T_D$ . Hence, the chirp signal leads to increasing the range resolution in short duration. Let's consider a chirp signal, which is given by

$$p(t) = w_r(t) \cos(2\pi f_0 t + \pi \kappa_r t^2), \quad (2-3)$$

where  $w_r(t)$  is the signal envelope and  $w_r(t) = 1$  for  $0 \leq t \leq T_D$ . Further,  $f_0$  is the starting frequency, and  $\kappa_r = B_w/T_D$  is the chirp rate. At each azimuth sampling position  $\mathbf{P} = (0, u, Z_0)$ , where  $u \in (u_1, u_N)$  and  $N$  is the total number of aperture positions, the signal in (2-3) is transmitted, and similar to eq. (2-1 and 2-2), the time-shifted version is received. The demodulated received signal from  $K$  scatterers along  $(x, y)$  and sensor at position  $\mathbf{P}$  is expressed as

$$s(t, u) = \sum_{k=1}^K A_k w_r(t - t_d) w_a(u - u_{c,k}) \times \exp(-j2\pi f_0 t_d) \exp(j\pi \kappa_r \{t - t_d\}^2), \quad (2-4)$$

where  $t_d = 2R_k(u)/c$  is the time of flight and  $R_k$  is the slant range between sensor position and  $k^{\text{th}}$  scatterer,  $w_a(u)$  is the square of received signal strength in association with the time of zero Doppler plane  $u_{c,k}$  [5]. The received echoes from all the azimuth positions  $u$  are accumulated and form a 2D raw data matrix. In the 2D matrix, rows correspond to time bins, and columns correspond to azimuth sampling position.

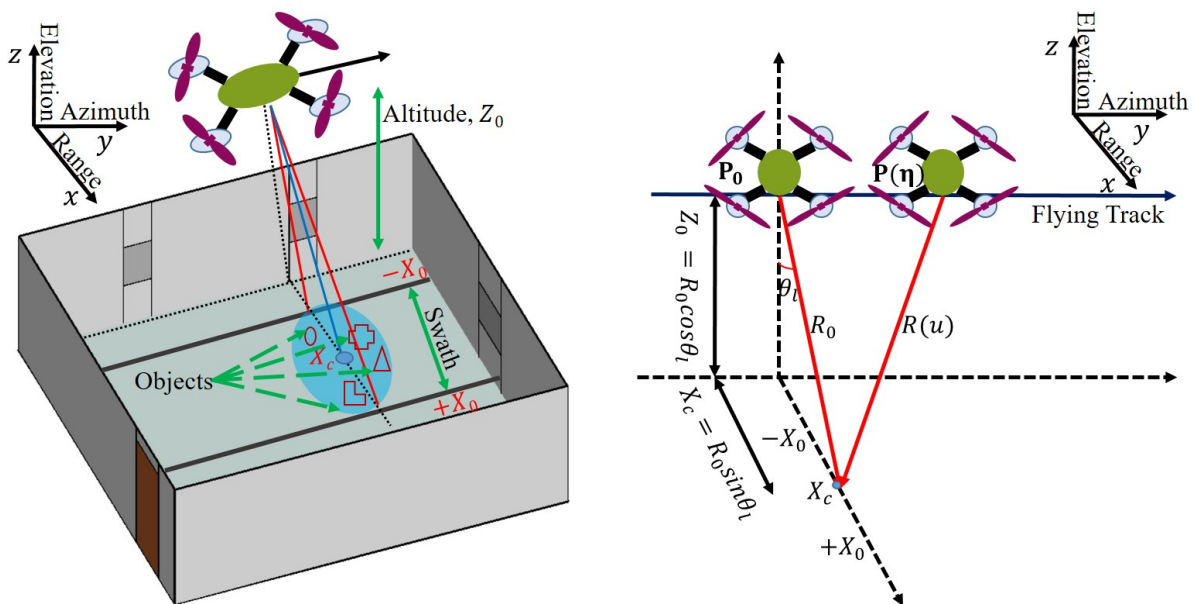


Figure 2-1: UAV based indoor SAR imaging (left) scene, and (right) geometry.

## 2.2 Indoor SAR Geometry and System Parameters

Considering the indoor SAR imaging scene shown in Fig. 2-1 (left), a UAV is flying with velocity  $V_r$ , and correspondingly imaging geometry is shown in Fig. 2-1 (right). The transceiver looks at the ground surface with the look angle  $\theta_l$ , where  $\theta_l$  is the angle between the transceiver antenna pointing direction and nadir. In Fig. 2-1 (left),  $R_0$  is the slant range of the nearest approach to the  $X_c$ . If the variables  $\theta_l$  and  $R_0$  are known,  $Z_0 = R_0 \cos \theta_l$  and  $X_c = R_0 \sin \theta_l$  can be calculated, respectively. The slant range for the UAV (or transceiver) position  $\mathbf{P}_0 = (0, V_r \eta_{N/2}, Z_0)$ , where  $V_r \eta_{N/2} = u_{N/2} = 0$  as a azimuth reference position and a target  $k$  at position  $(X_c, 0, 0)$  is given by

$$R_0 = \sqrt{X_c^2 + Z_0^2}. \quad (2-5)$$

Here, the time  $\eta \in (\eta_1, \eta_N)$  is associated with the UAV movement along the  $y$ -axis that is much smaller than the speed of light and called slow-time, whereas the time  $t$  corresponding to EM signal propagation with speed  $c$  is called fast-time [4]. Moreover, the slant range  $R_0$  can also be termed as reference range  $R_{\text{ref}} = R_0$  between the transceiver and the target. Similarly, the slant range between the same target position but varying UAV positions can be given by

$$R(u) = \sqrt{X_c^2 + (V_r \eta)^2 + Z_0^2}. \quad (2-6)$$

To generalize the slant range equation for the target located  $(x_k, y_k, z_k)$  anywhere in the swath, where  $\pm x_k \in (X_c - X_0, X_c + X_0)$ ,  $\pm y_k \in (-L_s/2, +L_s/2)$ , and  $L_s$  is the

synthetic aperture length, the slant range is given by

$$R_k(u) = \sqrt{(X_c + x_k)^2 + (V_r \eta + y_k)^2 + (Z_0 + z_k)^2} \quad (2-7)$$

Here,  $x_k$  and  $y_k$  can be positive or negative with respect to the reference location  $X_c$  and  $L_s/2$ , respectively. For 2D imaging with  $x - y$  plane, no information about the height can be extracted and therefore,  $z_k = 0$  or constant.

Following are the most important parameters that have to be evaluated to design the simulation system compared to the lower frequency region:

- **Beamwidth:** It decreases at higher frequencies and increases with smaller antenna length. The antenna length is inversely proportional to the frequency. For example, dipole antenna length is  $\lambda/2$ . The antenna  $-3$  dB beamwidth [43] with antenna length or diameter  $L_r$  is given by

$$\theta_{-3 \text{ dB}} \approx 0.886 \frac{\lambda}{L_r}, \quad (2-8)$$

where  $\lambda$  is the high-frequency signal wavelength and  $\theta_{-3 \text{ dB}}$  is given here in radians.

- **Doppler bandwidth:** Motion of the platform corresponds to the Doppler bandwidth. It is given by

$$f_D \approx 0.886 \frac{2V_r}{L_r} \cos \theta_{r,c}. \quad (2-9)$$

For a very low squint case, the beam center's squint angle can be approximated as  $\theta_{r,c} = 0$ . However, in a realistic environment, the squint is always present because of the flight motion. For a pulse-based radar, where pulse of duration  $T_D$  is transmitted at each aperture position with a certain pulse repetition frequency (PRF), the PRF should be between an oversampling factor of 1.1 to 1.4 of the Doppler bandwidth [5].

- **Range resolution:** The slant range resolution is directly proportional to the  $B_w$  and given as

$$r_x = \frac{c}{2B_w}. \quad (2-10)$$

At the THz spectrum, hundreds of GHz of bandwidth is available which provides a resolution in sub-mm. Moreover, the ground range resolution for the presented imaging scene and geometry in Fig. **2-1** is  $r_{gr} = \frac{r_x}{\sin \theta_1}$ .

- **Azimuth (cross-range) resolution:** It is directly proportional to beamwidth [5, 44] and given by

$$r_y = \frac{\lambda R_{\text{ref}}}{2L_s}, \quad (2-11)$$

- **Synthetic aperture length:** In indoor scenarios, it decreases at higher frequencies because of shorter wavelengths and distances. It is given by

$$L_s \approx 0.886 \frac{\lambda}{L_r} R_{\text{ref}} \quad (2-12)$$

For simplicity,  $L_s$  can be approximated as  $L_s = \frac{\lambda}{L_r} R_{\text{ref}}$  and using this in eq. (2-11),  $r_y$  can be derived as

$$r_y = \frac{L_r}{2} \quad (2-13)$$

It is defined as the maximum achievable azimuth resolution and independent of platform range and height [4, 5, 44]. The THz spectra offers compact antennas and hence enhances the azimuth resolution.

## 2.3 Raw Data Generation with 3D Electromagnetic Field Calculations

This section aims to virtualize the actual test environment and have comparable simulation results to the measurements. The imaging environment's major entities are transceiver, atmosphere, and targets, as shown in Fig. 2-2. The entity properties to be considered in virtualization are also summarized in Fig. 2-2. These properties and their dependencies are briefly explained below.

- **Transceiver:** It transmits and receives a specific EM signal such as chirp or Gaussian with a certain transmit power, polarization, receiver sensitivity defining the noise floor, and radiation pattern expressing the beamwidth.
- **Atmosphere:** The EM waves propagate in the atmosphere with specific polarization and attenuate over the distance due to FSPL [16] and atmospheric absorption [17]. Additionally, the environment provides either free space propagation as line of sight (LoS) or N-LoS due to the cluttered objects.
- **Targets:** The target material, shape, and dimension define the radar cross-section (RCS), and the reflected power is directly proportional to it. Moreover, phenomena such as reflection, transmission, and absorption from the target are dependent on its material. The material is characterized by its various properties, such as electrical and magnetic.

Therefore, to virtualize the imaging environment, a simulation system has been designed that generates the raw data in considering these entities using CST Studio Suite [37]. CST studio is an EM solver, and the fields are calculated with Maxwell equations in 3D-space.

### 2.3.1 Target Design

The target design includes the specification of the target shape, dimensions, and material, which influence the backscattered power. Its material can be defined based on a general parameter such as permittivity or specific parameters, for example, conductivity (electrical, magnetic, and thermal) and dispersion (dielectric and magnetic). These properties

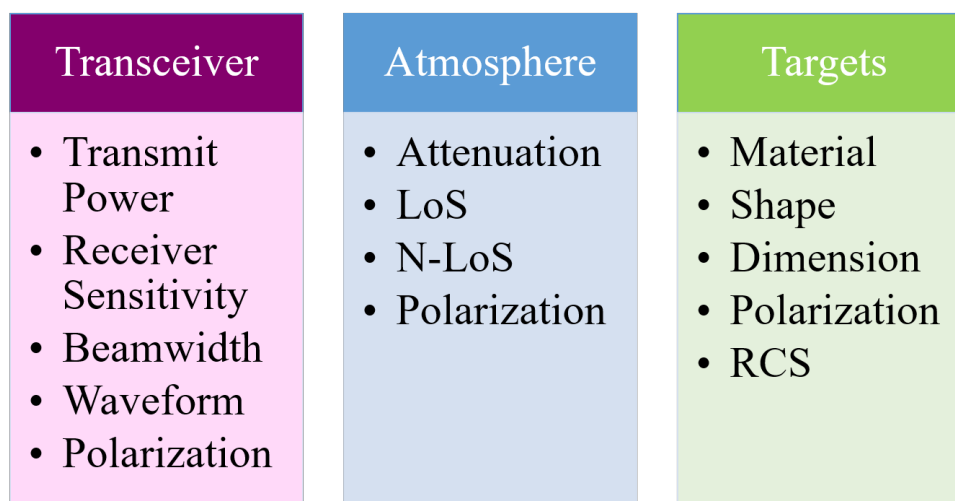


Figure 2-2: Imaging environment entities.

are generally frequency-dependent. So, if the properties of the material are known, any target can be designed. Also, CST provides a materials library that includes a set of materials with defined parameters for a specific frequency range.

In this work, four different shapes and dimensions of targets are considered to validate the simulation design. The target shapes are shown in Fig. 2-3, where (top-left) is a sphere of radius  $r = 11 \text{ mm}$  ( $\sim 10\lambda_c$  for the band of 220-330 GHz), (top-right) is a rectangular prism of dimension (length  $\times$  width  $\times$  height)  $2.5 \text{ mm} \times 60 \text{ mm} \times 80 \text{ mm}$ , and lastly (bottom-left) and (bottom-right) are random shapes. These random shapes are composed of independent bricks in the shape of rectangular prism, and the number of bricks in Fig. 2-3 (bottom-left) and (bottom-right) are 3 and 4, respectively. The designed objects based on these shapes in CST are shown in Fig. 2-4. The material of objects 1-3 shown in Fig. 2-4.a-c is the perfect electric conductor (PEC). So, objects 1-3 can be considered of a metallic material. As defined earlier, the object of any material can be designed if the material properties are known in the interested frequency range. Therefore, objects 4-5 shown in Fig. 2-4.d-e are of material similar to glass with a refractive index of 2.58 as defined in [45]. Moreover, a multi-material object can also be designed. Therefore, object 6 is a cluster of PEC and glass material, where cyan and gray color represent glass and PEC, respectively. These targets are considered to observe the shape and material-oriented information in the resulting SAR images.

### 2.3.2 Excitation Waveform and Probe

The designed target is excited or illuminated with a specific signal waveform, and the default excitation waveform in CST is Gaussian. However, other types of signals such as

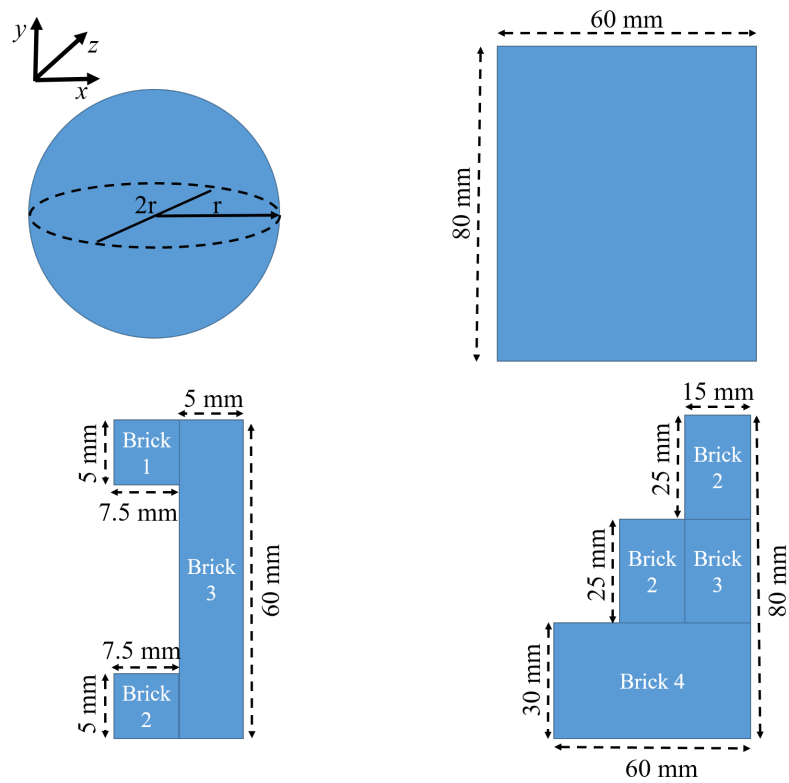


Figure 2-3: Shape of imaging objects: (top-left) sphere, (top-right) rectangle, (bottom-left) and (bottom-right) random shapes.

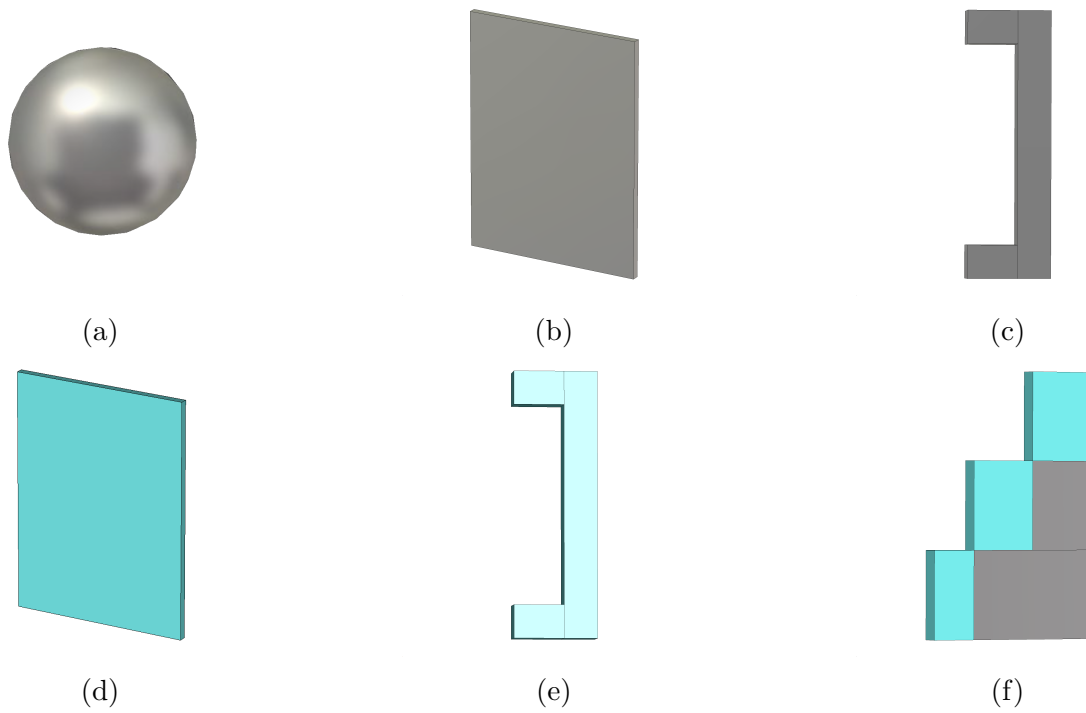


Figure 2-4: Pictures (a-f) of designed object 1-6 in CST.

chirp or a single-tone can also be generated. For example, it can be designed in MATLAB based on the requirements and imported in CST to be used as an excitation signal. In this simulation framework, the Gaussian signal is used, and the target is excited by plane waves.

The plane waves exist in the far-field region and the far-field condition is defined by

$$R > \frac{2L_r^2}{\lambda}, \quad (2-14)$$

where  $R$  is the propagation distance from the antenna phase center [43]. In consideration of  $L_r = 6$  mm and  $\lambda = 1.1$  mm at 275 GHz, the far field region begins with  $R > 6.6$  cm. In reference to the coordinate system shown in Fig. 2-3, the propagation and azimuth direction is along the  $x$ - and  $y$ -axis, respectively.

The backscattered signal from the target is recorded using a set of probes. The probe is a term defined in CST which measures the electrical field strength in a 3D-space. In comparison to a practical scenario, it can be considered as a receiver. To form the synthetic aperture, they are placed at equidistant  $\Delta u = u_N - u_{N-1}$  for the complete aperture length  $L_s$  along the azimuth or  $y$ -axis. This configuration is analogous to stop-and-go approximation SAR system. Each probe contains the phase-shifted data in respect to others depending on their respective positions.

### 2.3.3 Raw Data and Power Flow

The imaging is performed for frequency spectrum of 220-330 GHz and the object is positioned at  $R_0 \approx 0.5$  m. The imaging parameters are summarized in Table 2-1 and the generated raw data in frequency-domain is shown in Fig. 2-5. The recorded data from each probe is extracted in complex form and further processed in MATLAB [46] to form a 2D raw data matrix. The generated raw data for the objects 1-6 are shown in Fig. 2-5.a-f, respectively and it is processed further for image reconstruction.

Concerning the flow of EM waves within the material, the waves do not penetrate the PEC material and the energy is reflected from the object's surface. Whereas, in case

Table 2-1: CST based SAR imaging parameters.

Symbol	Parameter	Value
$f_c$	center frequency	275 GHz
$B_w$	bandwidth	110 GHz
$L_s$	synthetic aperture length	8.4 cm
$r_x$	range resolution	1.36 mm
$R_{\text{ref}} = R_0$	reference range	50 cm
$\Delta u$	step size	1 mm
$N_f$	number of frequency bins	1001
$N$	number of azimuth sampling points	85
$P_T$	transmit power	0 dBm

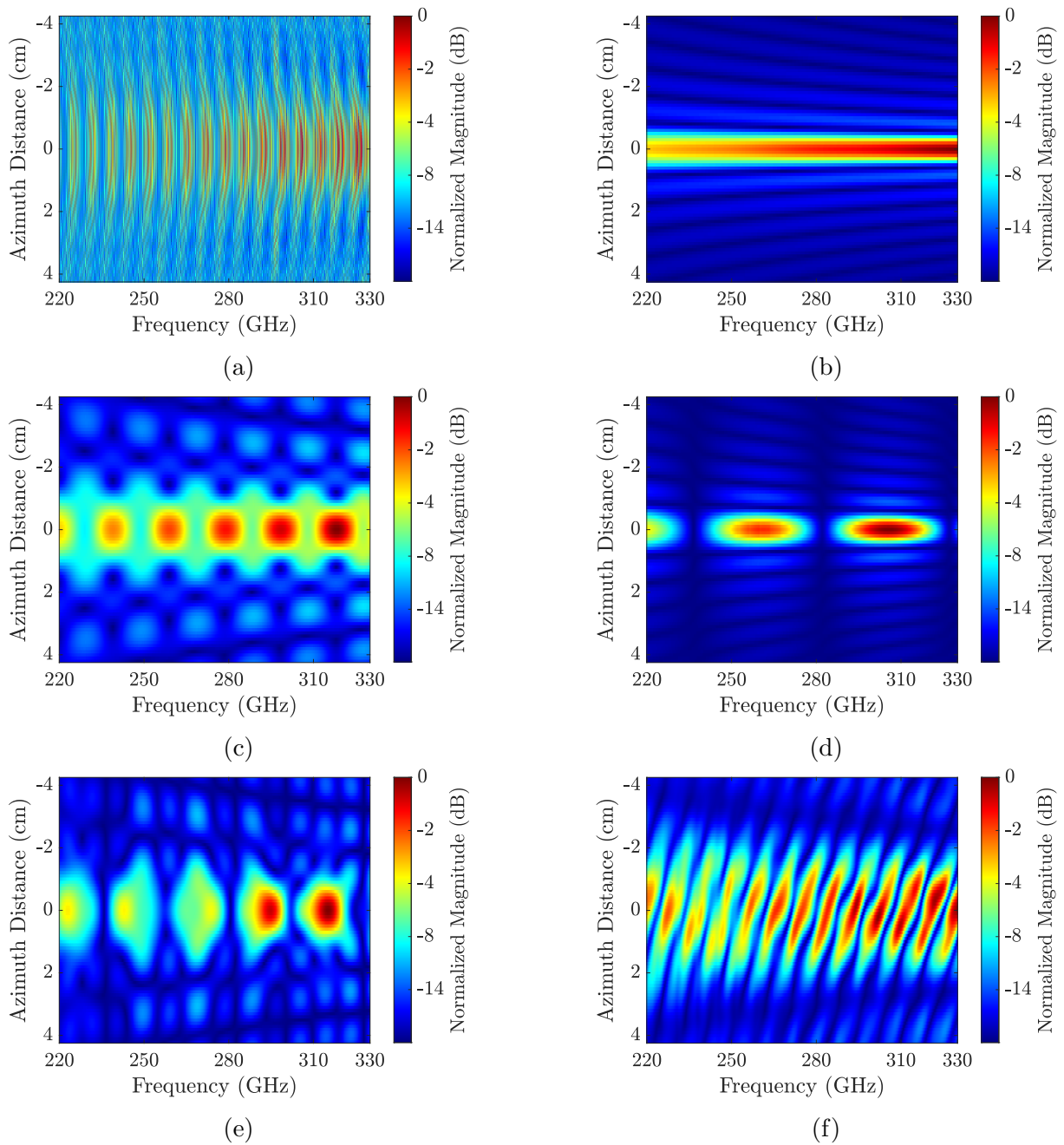


Figure 2-5: Frequency domain raw data (a-f) for object 1-6.

of glass, along with the reflection, refraction and absorption also takes place [42, 47]. The EM waves penetrate the surface, and the power decreases exponentially along with the material's length, which results in absorption and a certain power propagates out of the glass material. This behavior can be well explained by considering the power flow diagrams.

The EM wave power flow represented by the power density given in  $\text{VA}/\text{m}^2$  at  $f_c$  for metallic and glass material objects is shown in Fig. 2-6. The flow of power for the metallic sphere from the front (illuminated space) and back is shown in Fig. 2-6.a and b,

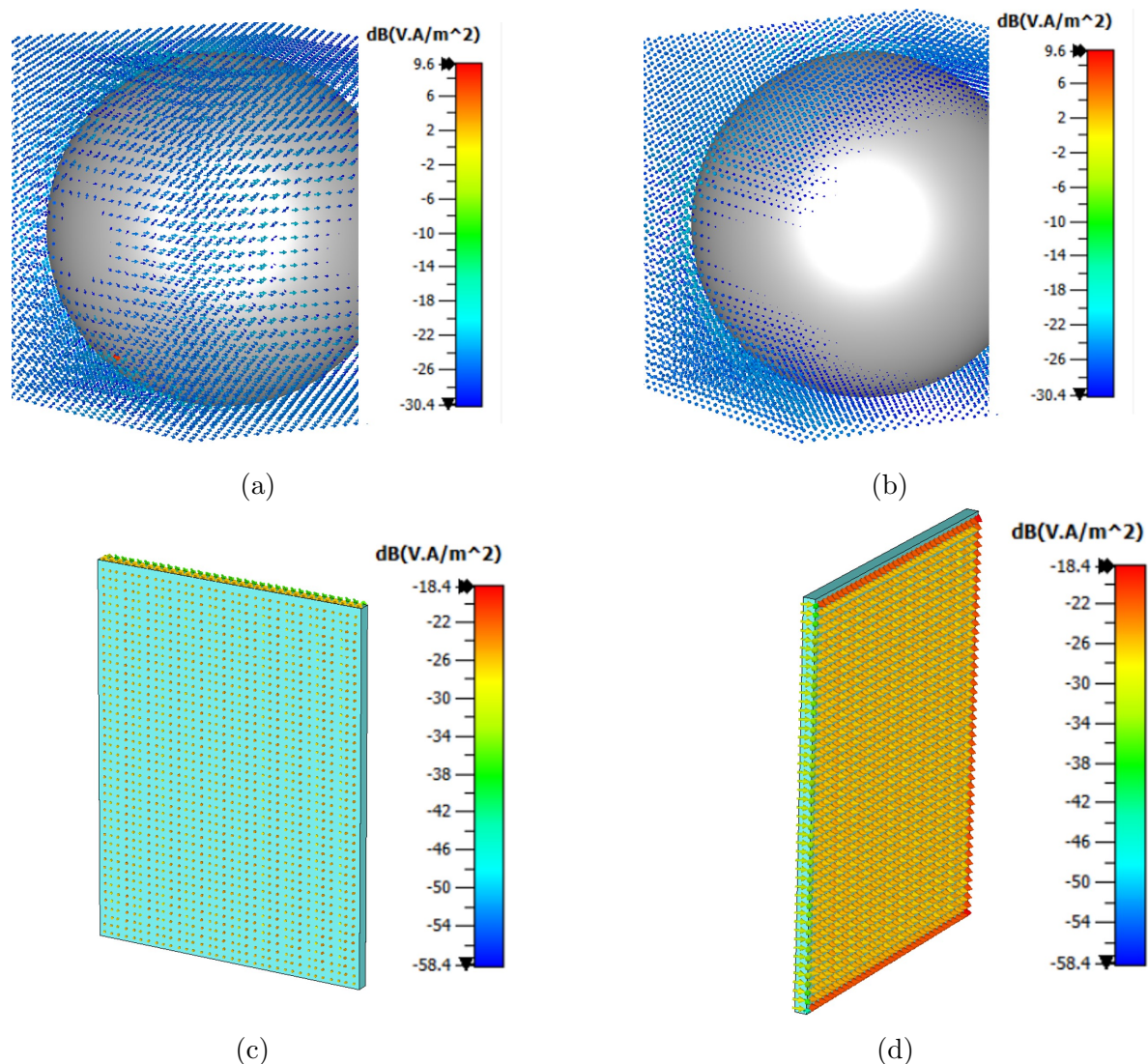


Figure 2-6: Power flow with metallic and glass objects at  $f_c$ , where (a-b) and (c-d) are the front and back view of metallic sphere and glass flat plate.

respectively. It can be seen that the waves do not penetrate the sphere. Therefore they do not appear at the rear of the sphere in Fig. 2-6.b. The power flow in the flat glass plate from the front (illuminated space) and back is shown in Fig. 2-6.c and d, respectively. The EM propagation out of the glass can be seen in Fig. 2-6.d, which is not the case with the metallic object.

## 2.4 Image Reconstruction

To generate the target's SAR image, the raw data is processed in terms of range and azimuth compression. The reconstruction can be performed in time domain with Back-projection Algorithm (BPA) or frequency domain such as Omega-K and Range Doppler Algorithm (RDA) [4, 5]. In this work, BPA is used due to its simplicity and accuracy.

### 2.4.1 Backprojection

Based on BPA, a SAR target reconstruction function at pixel location  $(x_i, y_j)$  is given by

$$f(x_i, y_j) = \int_u s_{\text{cm}}(t_{ij}, u) du, \quad (2-15)$$

where  $t_{ij} = 2R_{ij}(u)/c$ ,  $s_{\text{cm}}(t, u) = s(t, u)p^*(-t)$  is a range compressed signal,  $p^*(-t)$  is the inverse Fourier transform of  $P^*(\omega)$ , and  $R_{ij}(u)$  is the slant range for the aperture position  $u$  [4]. This algorithm can more easily handle motion compensation in comparison to frequency domain algorithms but requires high computational power [48]. However, the algorithm lacks data dependencies and inherit massive parallelism to support real-time imaging [49]. The target function  $f(x, y)$  can be calculated independently for different image pixel locations. In this work, the raw data in frequency domain defined by  $S(\omega)$  is firstly zero-padded by a factor of 8 to have high sampling frequency before transforming into time domain  $s_z(t)$ . Additionally, the zero-padding also provides compatibility with the 2D imaging grid  $\mathbf{I}$ . Based on BPA, the pixel value at location  $(x_i, y_i)$  is calculated by

$$I(x_i, y_j) = \sum_{n=1}^N s_z(t_{ij}, u_n) \exp(-j4\pi f_{\text{min}} R_{ij, u_n}/c), \quad (2-16)$$

where  $f_{\text{min}}$  is the minimum frequency of zero-padded raw data.

### 2.4.2 Resulting SAR Images

The raw data of all the objects 1-6 shown in Fig. 2-5 are processed with BPA and the generated SAR images using eq. (2-16) are summarized in Fig. 2-7.

For the metallic sphere of radius  $\sim 10\lambda_c$ , the resulting SAR image is shown in Fig. 2-7.a and it matches well with the physics of scattering from spherical surfaces by forming an image close to a reference point target. The spherical surface scattered the EM waves uniformly in all directions [50]. Further, the SAR image of object 2 is shown in Fig. 2-7.b, and it is well focused. As for PEC material, only the reflection from the front surface is captured. In Fig. 2-7.c, SAR image of object 3 is shown. It can be seen that all the bricks of the object are well focused, and the shape of the object shown in Fig. 2-4.c is obtained.

Further, Fig. 2-7.d shows the resulting SAR image of the object 4. For glass material, the flat plate's front and back surfaces are expected to appear in the SAR image, and the same has been observed. The front surface appears because the reflection occurs due to the change in refractive index  $n$  at the surface interface. In this case, the EM waves traveling in vacuum with  $n_1$  is incident on glass with  $n_2$ . The EM waves penetrate the glass, and a second focused plane of reflection is observed for the wave traveling out of the glass, basically at the back interface due to change of propagation medium from  $n_2$  to  $n_1$ . In addition, the medium with  $n_2$  also results in change of propagation speed of the EM waves. In a medium with  $n_2$ , the EM wave phase velocity is given by  $c_{n_2} = c_0/n_2$  [51]. So, the speed of propagation decrease with an increase in  $n$ . The compensation of the change

of speed in the SAR image processing can only be applied if the object material is known in advance. In the other case, the object dimension along the propagation direction will appear extended in the resulting image. The same has been observed with glass material objects.

Furthermore, the SAR image of object 5 is shown in Fig. 2-7.e. The shape of the object and all front and back surfaces of the brick are well observable. The discontinuity in the case of the back cover of brick 1 and 2 relative to brick 3 is observed because of the the delay in the interaction of the EM wave with the brick front surface. Also,

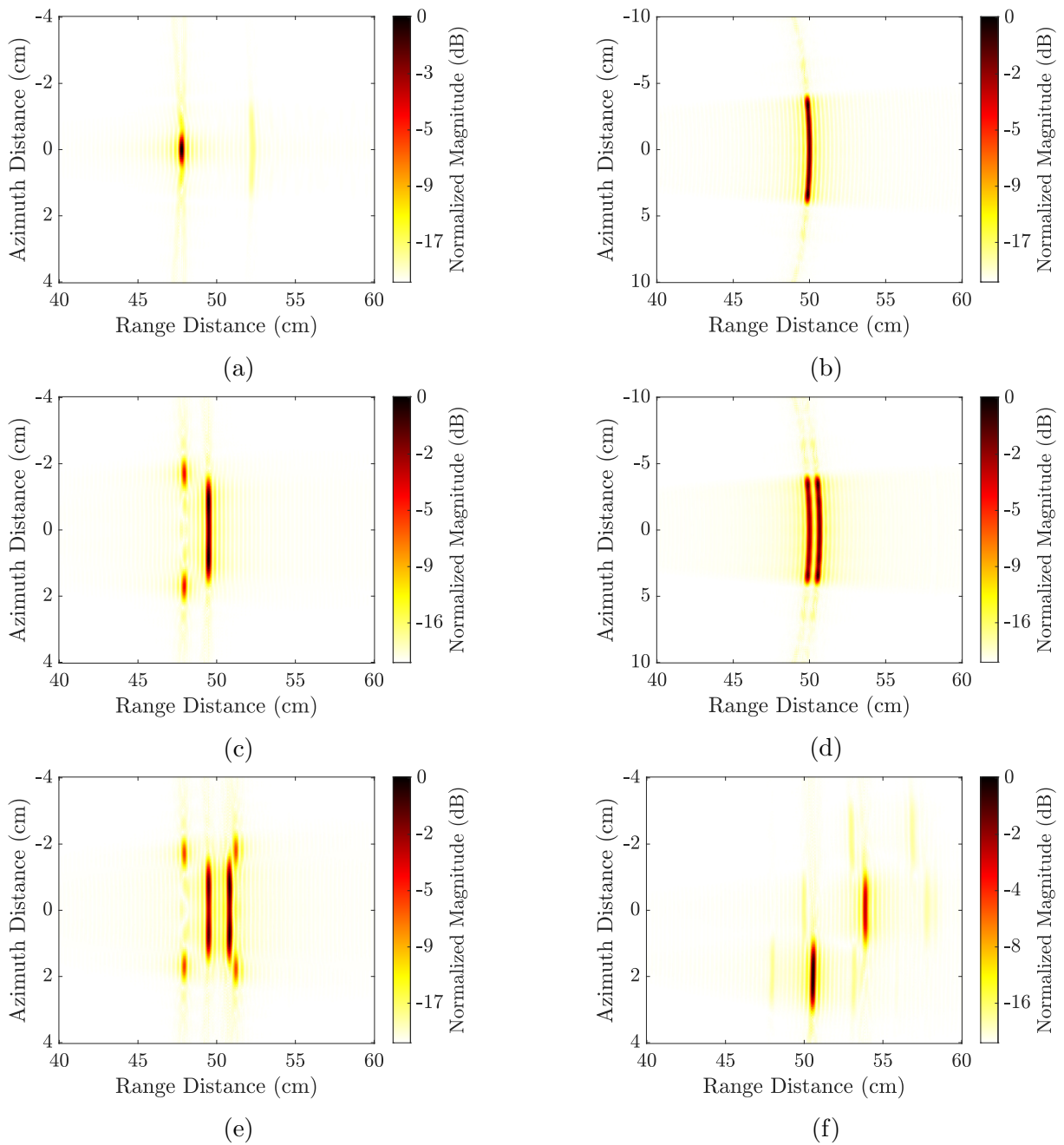


Figure 2-7: SAR image (a-f) for object 1-6.

the difference in brick length contributes to the discontinuity, as the length defines the duration of  $c_{n_2}$  within the brick.

Lastly, Fig. 2-7.f shows the SAR image of object 6, where the bottom two layers along  $y$ -axis are composed of two materials. Both of the materials along each layer can be seen in the resulting image. The PEC has much stronger reflectivity than the glass. Therefore, the magnitude of the PEC material-focused part is much higher. Moreover, in similar to other objects focusing, the shape of this object is also well obtainable.

## 2.5 Conclusive Remark

The chapter has summarized the fundamentals for SAR signal processing in consideration of indoor imaging geometry. Based on the presented geometry and evaluated THz SAR parameters, SAR imaging is realized with the developed THz SAR simulation framework. The framework to virtualize the measurement setup is crucial to investigate THz SAR at a larger scale. The presented framework considers all the required three entities and their respective properties to provide comparable results to the measurements. The presented results are validated by considering different shapes, materials, and dimensions of objects. This framework is used for all the simulation results presented in this dissertation.

Moreover, the presented results and signal processing takes an ideal trajectory and geometry into consideration. In practical applications, the trajectory deviates due to internal or external factors such as atmospheric disruptions or mechanical errors, resulting in phase errors. It has several impacts on the generated SAR image, such as blurring or de-focusing. Especially at the THz, motion errors required special consideration due to the minute change in the trajectory is in the range of the wavelength. Therefore, the next chapter addresses this challenge and extends the framework to investigate it.



## Impact of Motion Errors and Compensation

For the indoor THz SAR, precise localization information of the UAV trajectory in 3D space is required with sub-mm accuracy. In conventional outdoor GHz SAR, this is usually achieved with a global positioning system (GPS) aided inertial navigation system (INS) and inertial measurement unit (IMU) [4, 52, 53]. The IMU consists of gyroscopes and accelerometers to provide a measurement of relative position and altitude. In combination with the IMU, the GPS-aided INS provides navigation information such as a position in 3D space with respect to the global reference frame [52]. However, the GPS does not work in an indoor environment, and also the 3D positioning accuracy offered by the compact INS/IMU is not sufficient at the THz. This chapter proposes the THz SAR with an indoor localization system providing sub-mm accuracy to overcome this challenge. The chipless RFID-based localization system proposed in [38] is utilized to enable the UAV's self-localization using the infrastructure composed from the reference chipless tags.

In SAR operation, the basic assumption is that the mobile platform follows an ideal or nominal trajectory with constant velocity and maintains a constant angular geometry with the target area. However, internal and external factors such as platform vibrations and turbulence influence the altitude, velocity, and geometric angles, which results in deviations from the ideal path and is known as motion errors. These errors introduce variation in the received signal phase history that results in image quality degradation, blurred images, and wrong range and azimuth estimations [54, 55, 56, 57]. The errors are usually classified into rotational and translation errors. The rotational errors are along the roll, pitch, and yaw axis and result in the antenna beam's squinting. On the other hand, the translational errors are along upward-downward, forward-backward, and left-right directions resulting in unequal spatial sampling and target to sensor range errors. [58]. This chapter focuses on translational errors. Compared to sub-30 GHz SAR, the THz SAR system is sensitive to very small platform deviations because of the wavelength in the range of sub-mm. In this chapter, we will analyze the effects of sub-mm deviations. We will come to a certain conclusion regarding the constraint on the amplitude of deviation

concerning the image quality for object-level THz SAR imaging. The effects will be studied with both the 3D electromagnetic simulations framework developed in Chapter 2 and measurements for the carrier frequency  $f_c = 250$  GHz and bandwidth  $B_w = 50$  GHz. To the best of our knowledge and at the time of our publication [19], the effects are not studied for this wide bandwidth. Most of the available THz SAR testbeds are limited with the system bandwidth and follow either an ideal trajectory or equipped with high weighing IMU/INS systems that cannot be mounted on the UAV [22, 31, 59, 60].

Moreover, as of commercial THz radar frontend unavailability for this wide bandwidth, a vector network analyzer (VNA) with the THz extenders is used as a radar sensor or transceiver. The effects of all three types of translational errors, “upward-downward,” “left-right,” “forward-backward,” has been studied individually and in combination by designing the trajectories associated with these errors. Furthermore, the motion compensation (MOCO) is commonly achieved by using IMU/INS defined as gross nonlinear MOCO [4] and for residual error correction, the trajectory is estimated using raw data [56, 57, 61, 62, 63] or in-scene targets [4]. In IMU/INS-based MOCO, the IMU/INS provides the vehicle’s coordinates during the SAR trajectory. However, the coordinates lack precision. Therefore, in a conventional SAR, firstly, the image is compensated using IMU/INS coordinates, and then the residual correction is performed using estimations from in-scene targets or raw data. In the in-scene targets-based MOCO, the mapping environment is equipped with known targets such as omnidirectional reflectors and their positions. The MOCO is achieved with the measurement of the sharpness of these targets in the imaging scene. Generally, the SAR signature of these targets is estimated to calculate the relative error with respect to the known location [4]. Moreover, current research with raw data trajectory estimation is demonstrated experimentally primarily for  $B_w$  of sub-5 GHz. As already stated, the available commercial compact IMU/INS lacks precision and therefore cannot be used at THz spectrum with high  $B_w$ . This chapter proposes a method for MOCO using a passive sub-mm indoor localization system, and the same has been investigated.

To summarize, the following are the main contribution of this chapter. Firstly, the chapter validates the indoor THz simultaneous localization and mapping (SLAM) system. The localization is here referred to the localization of the UAV throughout the SAR trajectory and mapping is room profiling with SAR such as 2D imaging of the in-room object with the positioning accuracy close to mm based on the spatial resolution provided by the SLAM system. Secondly, the chapter investigates the impact of the sub-mm motion errors on the SAR image to define the amplitude constraint. Lastly, the compensation of these errors with the localization system is proposed. The MOCO based on the proposed method can be considered as an application of SLAM.

The chapter is organized as follows. Firstly, Section 3.1 describes the system model. Section 3.2 presents the indoor THz SLAM. In Section 3.3, the non-ideal trajectories are realized to study to effects of sub-mm translational errors. Section 3.4 presents the results of MOCO with the localization system. Lastly, in Section 3.4, a conclusive remark is provided.



ideal slant range is calculated using eq. (3-1). With the introduction of translational motion errors along all the axes  $\pm(x_e, y_e, z_e)$ , the real position of the UAV is  $\mathbf{P}_m$  and therefore,  $R_i$  gets modified. The modified or real slant range is given by

$$R_m(u) = \sqrt{(X_R + x_e)^2 + (Y_R + y_e)^2 + (Z_0 + z_e)^2}, \quad (3-2)$$

where  $X_R = X_c + x_i$ ,  $Y_R = Y_r + y_i$  and  $Y_r = V_r \eta$ . The change in the slant range modulates the echo phase. The phase is given by  $\phi = (2\pi R)/\lambda$ , where  $R$  is a two-way path length. In case of ideal trajectory, for position  $\mathbf{P}_i$ ,  $R = 2R_i(u)$  and for position  $\mathbf{P}_m$  with trajectory deviations,  $R = 2R_m(u)$ . The deviations result in a phase error of  $\Delta\phi = (2\pi\Delta R)/\lambda$ , where  $\Delta R = 2(R_m(u) - R_i(u))$  is the relative change in the slant range. Based on the far-field condition [55, 64, 65], the impact of phase error on SAR image can be neglected if

$$\Delta\phi \leq \frac{\pi}{8}. \quad (3-3)$$

Therefore, this chapter focuses on the effect of sub-mm slant range deviations because  $\lambda$  is in close proximity to mm.

### 3.1.2 Localization System

A chipless RFID-based localization system operated at THz band described in [38] is used in this work to fulfill the requirement of the sub-mm localization system for the SAR process. The localization system is briefly described here.

In this approach, the transceiver mounted on a UAV acts as a reader for the RFID-based system and records the excited reference nodes (chipless tags) response. Based on the round-trip time-of-flight (RToF), the reader's position (UAV) is estimated. Due to the large available  $B_w$  at the THz spectrum, RToF is preferred for ranging even in a cluttered environment. Considering the imaging scene shown in Fig. 3-1 (left), the room is equipped with  $N_{\text{tag}}$  tags, and each tag has known parameters  $\mathbf{P}_{k,\text{tag}} = (\bar{x}_k, \bar{y}_k, \bar{z}_k)$  and  $f_k$ , where  $k \in 1, 2, \dots, N_{\text{tag}}$ ,  $f_k$  is the resonance frequency and  $\bar{x}_k, \bar{y}_k$  and  $\bar{z}_k$  are x-, y- and z-coordinates of the tag, respectively. The tags are designed as a combination of a dielectric resonator and spherical lens to enhance the RCS of the chipless tag, extending its range [38]. The objective is to estimate the UAV coordinates  $\mathbf{P}_{\text{uav}} = (\bar{x}, \bar{y}, \bar{z})$  by self-localization, which is fulfilled in three phases.

In the first phase, the reader performs fast and rough scanning to detect the reference tags that are allocated at the predefined locations. The tags backscattered the signal toward the reader position based on the retrodirectivity property of the tag. As an outcome, the reader/UAV established a connection with several tags. The second phase is carried out to perform ranging, where UAV sequentially transmits signals centered at the connected tag's resonance frequency covering the resonance bandwidth. The backscattered data from the corresponding tags are processed using a matched filter to estimate RToFs and associated distances between the UAV and tags. In the last phase, the UAV positions are estimated using the linear least square algorithm.

Based on this localization system, the UAV can localize itself on the predefined trajectory that is required for SAR processing.

## 3.2 Simultaneous Localization and Mapping

The SAR framework designed in Chapter 2 is used in this section, and the localization system is realized with the signal processing model explained in Section 3.1. This section demonstrates the THz SLAM and evaluates the SAR imaging results based on the localization system's UAV position estimations. The SAR operation in this section is realized with an ideal trajectory.

Due to high spatial resolution and short-range applications at the THz band, the imaging can be realized with both side-looking and down-looking ( $\theta_1 = 0$ ) configurations [8]. Therefore, an analogous to the imaging geometry of the THz SLAM shown in Fig. 3-1 (left), inside a room with the dimension (length  $\times$  width  $\times$  height) of 5 m  $\times$  5 m  $\times$  7 m is considered with  $\theta_1 = 0$ . For a uniform  $x$ -axis propagation direction and range resolution in this dissertation, following change of the direction of Cartesian coordinates with respect to Fig. 3-1 are considered. The altitude is referred along the  $x$ -axis, UAV movement along the  $y$ -axis, and the width along the  $z$ -axis. Further two simultaneous beam footprints are considered, one along the ground targets and the other along the tags. The beams can be generated using the Multiple-Input-Multiple-Output (MIMO) beamforming technique. In SLAM, the THz SAR is realized with a conventional single antenna system, whereas the localization system with the MIMO technique. Furthermore, the SLAM operation can be summarized as the transceiver mounted on a UAV that flies at a constant altitude  $R_{\text{ref}} = 50$  cm along the azimuth or  $y$ -axis and radiates towards the ground targets and tags.

For localization and SAR imaging, the transceiver radiates a Gaussian waveform at each aperture position. It is analogous to a stop-and-go approximation system. The target center is at nadir to aperture position, therefore  $R_0 = R_{\text{ref}}$ . Considered center of imaging scene is (0.5, 2.5, 2.5) m and an initial position for UAV is  $\mathbf{P}_1 = (R_0, u_1 = 2.5 + L_s/2, 2.5)$ , the UAV flies for a synthetic aperture length  $L_s \approx (\lambda R_0)/L_r$ , where  $L_r$  is the real aperture length of the antenna and the end position is denoted by  $\mathbf{P}_N = (R_0, u_N = 2.5 - L_s/2, 2.5)$ . The azimuth trajectory could be left to right (from  $u_1$  to  $u_N$ ) or right to left (from  $u_N$  to  $u_1$ ), both presents the same results. Furthermore, the step size between two aperture positions is  $\Delta u$ . During the trajectory, the localization system evaluates all the azimuth positions and provides input to the SAR system.

The SAR system based on these positions further processes the raw data with BPA and returns the target's focused image. The SLAM is carried out at  $f_c = 275$  GHz with  $B_w = 50$  GHz. The simulation parameters are summarized in Table 3-1. For localization, the MIMO antenna area is 10  $\times$  10 cm<sup>2</sup>. It is assumed that the transceiver antenna aperture for localization is constant and has an area of 10  $\times$  10 cm<sup>2</sup>. The numbers of antennas integrated into this area can be calculated based on  $\lambda/2$  spacing between the antennas. Also, it is assumed that only one antenna structure for localization and one input is enough for the MIMO to send a localization waveform. To generalize, it is

considered that a certain array of antennas are mounted on the UAV, and localization is achieved by using the MIMO technique, whereas the SAR is performed with a single antenna in the monostatic configuration.

Table 3-1: Localization and simulation-based SAR imaging parameters.

Symbol	Parameter	Value
$f_c$	center frequency	275 GHz
$B_w$	bandwidth	50 GHz
$L_s$	synthetic aperture length	8.4 cm
$r_x$	range resolution	3 mm
$R_0 = R_{\text{ref}}$	minimum range (equals to altitude)	50 cm
$\Delta u$	step size	1.5 mm
$N_f$	number of frequency bins	3001
$N_u$	number of azimuth sampling points	57
$P_T$	transmit power	0 dBm
$N_{\text{tag}}$	number of tags for localization	16
$\alpha$	noise figure for localization	20 dB
$\sigma_{\text{tag}}$	tag radar cross section for localization	-35 dBsm
$A$	antenna area for localization	$10 \times 10 \text{ cm}^2$

The designed imaging object/target shape and dimensions shown in Fig. 3-2 (left) and Fig. 3-2 (right) represents the actual object image in the simulation framework. The target material is PEC. The imaging object can be divided into 4 bricks and following are the dimensions ( $x, y, z$ ) in mm scale: Brick 1 (2, 50, 4), Brick 2 (6, 8, 4), Brick 3 (6, 5, 4) and Brick 4 (6, 8, 4).

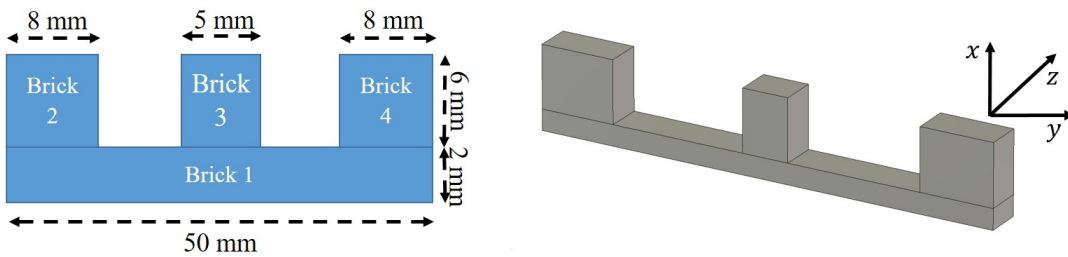


Figure 3-2: Imaging object (left) shape and dimensions, and (right) object image in CST.

The target is illuminated with plane waves, and EM fields are measured at each aperture position in the far-field region. The generated raw data is processed with the BPA algorithm. The SAR image without considering the localization estimations is shown in Fig. 3-3.a. It is provided for reference to evaluate the results with SLAM. From the image, the calculated  $-3$  dB distance below the maximum azimuth scatterer localization is  $\sim 5.5$  mm, and this corresponds to azimuth resolution  $r_y$  for this case.

Moreover, the brick's dimensions along the  $x$ -axis (propagation direction) and  $y$ -axis can be extracted directly from the resulted image. An important note for the range axis dimension is that the extracted value has to be divided by two because of two-way propagation. Further ahead, the obtained image with SLAM is presented in Fig. 3-3.b. The image is generated with the estimated UAV positions and the normalized errors in estimation is shown in Fig. 3-3.c. Basically, Fig. 3-3.c shows the relative errors in all three dimensions w.r.t. actual UAV positions along the SAR trajectory. The SLAM SAR image closely matches the reference image Fig. 3-3.a and also defines the positioning of the target in the room. For the PEC material, the EM wave does not propagate inside the material. Therefore, the connecting edges of the object do not appear in the resulted image. The resulted image is also comparable to the optical quality. A similar image can be generated in the event of smoke and fire in the room where the optical technology might not be helpful. Additionally, the object dimensions in the image and its positioning accuracy are based on offered spatial resolution  $r_x$  and  $r_y$ .

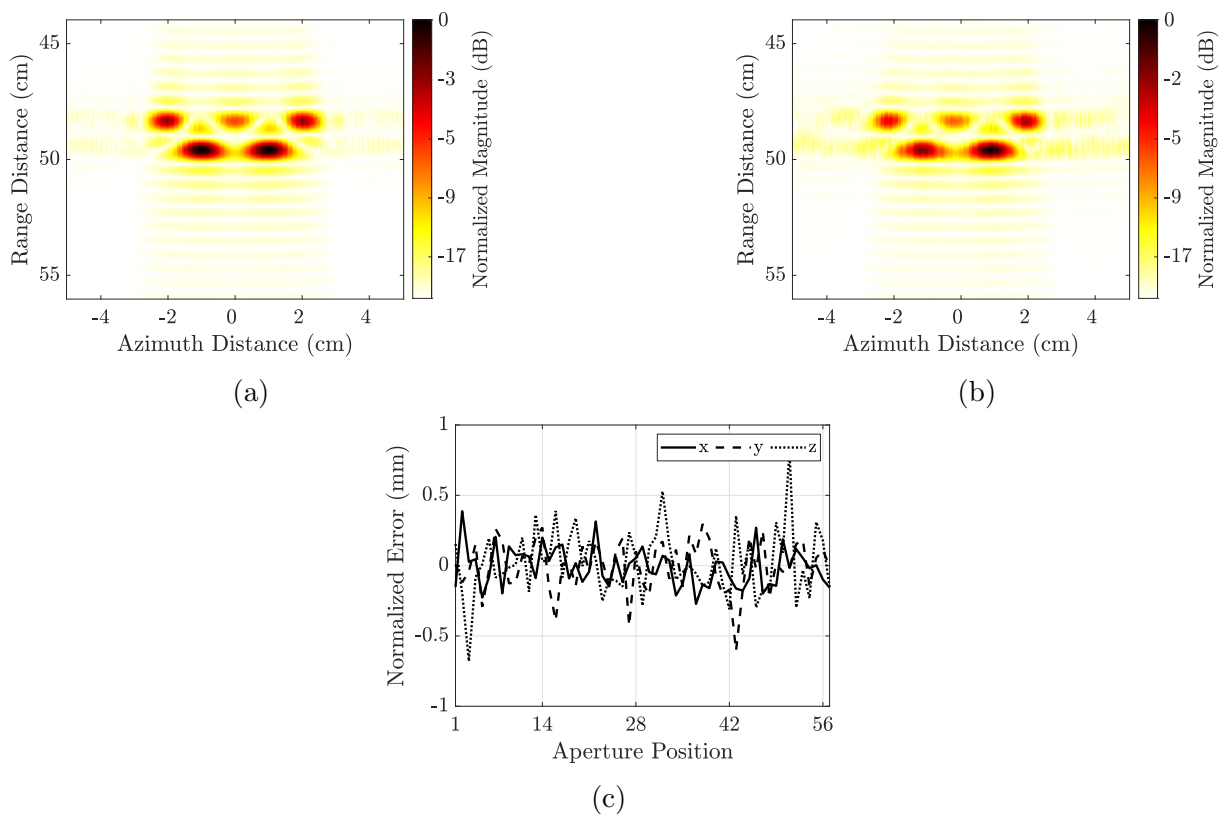


Figure 3-3: SAR image with idle trajectory, (a) without and (b) with using sub-mm localization system, (c) relative UAV position estimation errors.

### 3.3 Translational Trajectory Deviations Effects

In Section 3.2, the THz SAR is investigated for an ideal trajectory. However, in reality, it deviates along the three axes i.e. “upward-downward” (U-D), “forward-backward” (F-B),

and “left-right” (L-R). This section presents the effects of these errors in the range of sub-mm on the SAR image using the EM wave simulation and experimental results.

### 3.3.1 Simulation Analysis

To investigate the impact of the motion errors, the trajectories are designed first for three individual errors and lastly with their combination. For comparison, the simulation setup of Section 3.2 is used here to examine the error effects better. It is to be noted that multiple internal and external factors influence the UAV dynamics, such as weather conditions, wind speed, vehicle properties, payload, rotor speed and vibrations. These factors lead to change in flight dynamics, such as drift in velocity and altitude. Designing the UAV trajectories in consideration of these influencing factors is not the focus of this chapter. The chapter emphasizes the impact of sub-mm trajectory deviation and positioning error on the THz SAR image. Besides, the objective is to find the required localization accuracies in the 3D space to compensate for these effects. The strict accuracy requirement is defined by the phase error condition defined in eq. (3-3), and it is tough to achieve at the THz. Therefore the task is to evaluate the impact with higher phase error than eq. (3-3), to define the new amplitude constraint on the phase error or relative change in slant range.

To begin with, a trajectory with U-D errors is designed with a maximum deviation  $x_{e,\max}$  in the range  $\pm 0.25$  mm ( $\lambda/4$ ), where  $\lambda = 1$  mm is defined for 300 GHz that is the maximum frequency in the considered band of 250-300 GHz. The UAV follows this trajectory, and the sensors mounted on the UAV record the backscattered echoes at each aperture position. In the ideal case of Section 3.2, a constant altitude of 0.5 m is maintained throughout the trajectory, but for this case, deviation  $x_e \in (-0.25$  mm, 0.25 mm) leads to the altitude varying between 499.75 mm to 500.25 mm. The recorded raw data set is processed using BPA without any information/consideration for these deviations. The generated image is shown in Fig. 3-4.a and it is not completely degraded. Although some additional artifacts appear in the center along the range edges but the bricks are still distinguishable. This amplitude of deviation could be considered a cut-off amplitude of motion error along the range if minor artifacts are acceptable. Moreover, the effect has also been studied for the phase constraint of  $\Delta\phi \leq \pi/8$  and  $\Delta\phi \leq \pi/4$  by designing the trajectories with  $x_{e,\max} = \pm 0.0625$  mm ( $\lambda/16$ ) and  $x_{e,\max} = \pm 0.125$  mm ( $\lambda/8$ ) but no major impact has been observed in the resulted SAR image. Therefore,  $\lambda/4$  is defined here as the cut-off limit for U-D errors in this case with phase constraint of  $\Delta\phi \leq \pi/2$ .

Furthermore, it is also important to investigate the maximum positioning deviation, where the target is completely washed out, as in some cases, the accuracy of 0.25 mm is very hard to achieve. Therefore, the amplitude of deviation is increased to  $\pm 0.5$  mm ( $\lambda/2$ ), and the resulted SAR image for  $x_e \in (-0.5$  mm, 0.5 mm) is shown in Fig. 3-4.b. The image is highly degraded, although some of the bricks are still observable. The impact is further analyzed for the amplitude of deviation in close proximity to the  $\lambda$ , and

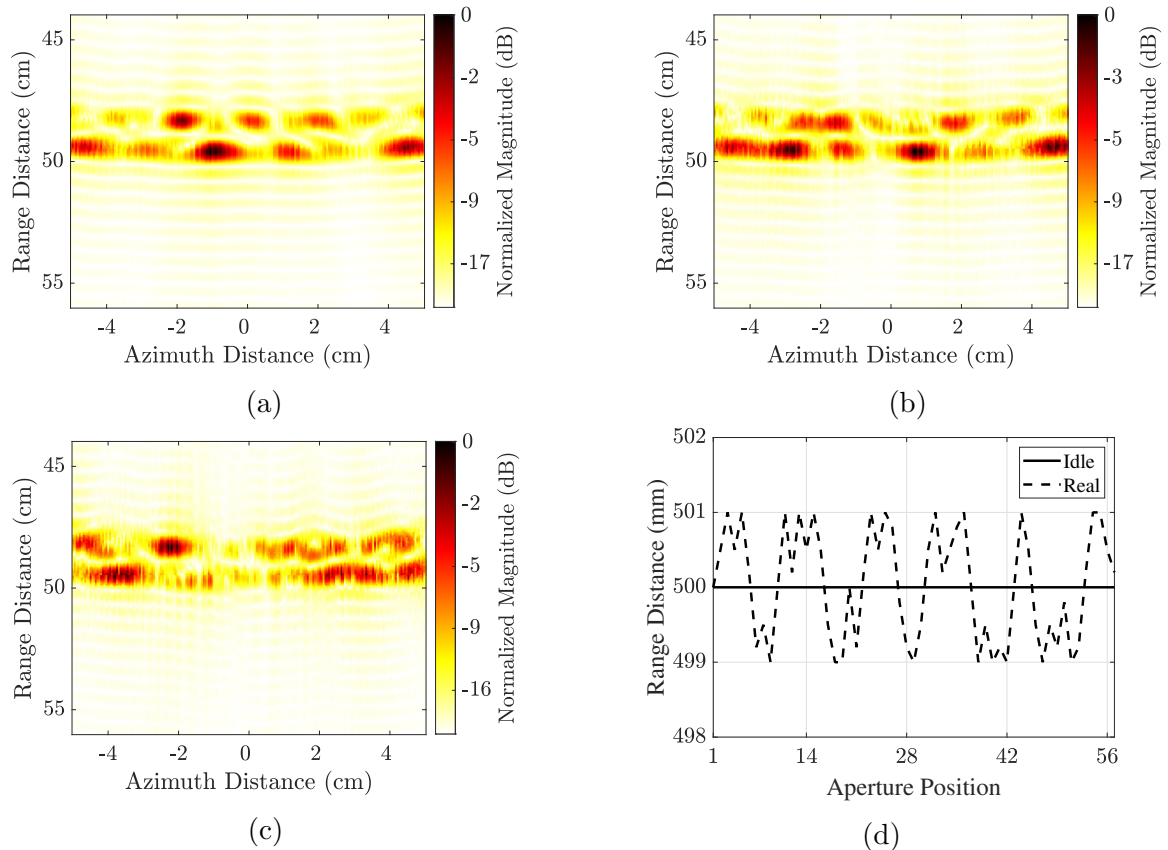


Figure 3-4: Effect of errors on SAR image along x-axis/U-D with  $x_{e,\max} =$  (a)  $\pm 0.25$  mm, (b)  $\pm 0.5$  mm and (c)  $\pm 1$  mm, and (d) comparison of ideal and real trajectory  $x$ -axis positions for  $x_{e,\max} = \pm 1$  mm.

therefore the trajectory is designed for  $x_e \in (-1 \text{ mm}, 1 \text{ mm})$ . The resulted SAR image for  $x_{e,\max} = \pm 1$  mm is presented in Fig. 3-4.c. It can be noted from this figure that the image is completely destroyed, and no information about the object can be obtained in comparison to Fig. 3-3.a. To conclude, the sub-mm errors along the  $x$ -axis have a very drastic effect on the focused image. Moreover, the relative error comparison between the ideal and non-ideal trajectory  $x$ -axis positions with  $x_{e,\max} = \pm 1$  mm is shown in Fig. 3-4.d and for  $x_{e,\max} = \pm 0.25$  mm and  $x_{e,\max} = \pm 0.5$  mm, this relative error comparison is exactly downscaled by a factor of 4 and 2, respectively. The solid curve represents the idle scenario, and the dotted curve represents the real trajectory  $x$ -axis positions with  $x_e$ .

Further, to analyze F-B errors impact, a trajectory is designed with unequal azimuth aperture sampling with maximum forward  $y_{e,\max}$  deviation in the range of 1 mm and as shown in Fig. 3-5.a. The unequal azimuth aperture sampling is defined here as the sensors transmit and receive from a shifted aperture position along the  $y$ -axis, and  $\Delta u = 1.5$  mm spacing between aperture positions is not followed. The shift could be positive or negative and represent forward or backward deviation, respectively. Therefore, the new step size is  $\Delta u_s = \Delta u \pm \delta u$ , where  $\delta u$  is forward or backward deviation. In general, one reason for

this deviation could be a change in the UAV velocity. In Fig. 3-5.a, the right movement from the azimuth reference position  $\mathbf{P}_c = (R_0, u_c = 2.5, 2.5)$  m is represented by positive values and left movement with negative values. Furthermore, with  $y_{e,\max} = \pm 1$  mm, it is found out that the error does not degrade the image quality to a greater extent as the object, and its shape with correct dimensions are observable in the generated image provided in Fig. 3-5.b. There might be additional artifacts along azimuth, but the impact is negligible. To obtain the amplitude of deviation along azimuth degrading the image, the deviation in azimuth sampling positions is increased to  $y_{e,\max} = \pm 5$  mm. The comparison of the idle and real trajectory  $y$ -axis positions is shown in Fig. 3-5.c and the resulting image is shown in Fig. 3-5.d. These motion errors degrade the image along azimuth and generate artifacts that might emerge as additional or ghost targets leading to altering the target's shape, such as enlargements of bricks.

For L-R errors, the initial trajectory is designed in the same way as in previous cases of U-D and F-B errors. For  $z_{e,\max} = \pm 1$  mm, the effect on the quality of the SAR image is negligible. Therefore, for further investigation, the range of  $z_{e,\max}$  is increased to  $\pm 1$  cm, where the deviations throughout the trajectory along the  $z$ -axis are shown in Fig. 3-5.e. In the presented THz SLAM geometry for 2D image generation, there is no movement along the  $z$ -axis. Hence, its values are defined as 0 represented by the solid curve in Fig. 3-5.e. As performed in all the other cases, the data collected with the trajectory deviation along  $z_e$  is processed with the BPA algorithm, and the resulted image is shown in Fig. 3-5.f. It is observed that a large deviation  $z_{e,\max} = \pm 1$  cm does not significantly impact image quality. The beginning of image degradation is observed at  $z_{e,\max} = \pm 2$  cm. The error comparison is shown in Fig. 3-5.g and the resulting degraded image in Fig. 3-5.h. Additional minor artifacts are observed for this case, and also the image is not well focused. It is further analyzed that the impact is much higher with a further small increase in the amplitude of deviation such as 2 mm.

The effects of the errors are presented with individual contributions along all three axes till now in this section to illustrate the effect and the impact of the different amplitude of deviations on the THz SAR image. To understand the effect with combined errors, a trajectory with errors along all the three axes i.e.  $x_e, y_e, z_e$  and  $x_{e,\max} = \pm 1$  mm,  $y_{e,\max} = \pm 5$  mm,  $z_{e,\max} = \pm 2$  cm is implemented. The resulting SAR image is presented in Fig. 3-6. The target is completely washed out and does not reveal any information about the object. This trajectory has the highest impact on image degradation in comparison to other cases. The cut-off limits defined in this section are from the general concept of achieving some information about the target even though with some minor artifacts, where the target is not completely washed out.

The results in Fig. 3-4 reveals that the impact of errors along the range is susceptible and requires the highest positioning accuracy. The effect of errors along the other two axes is less sensitive due to the high modulation of the slant range dependent phase with minimal deviation along range compared to the other axes deviations. The L-R is the least dominant in modifying the phase.

### 3.3 Translational Trajectory Deviations Effects

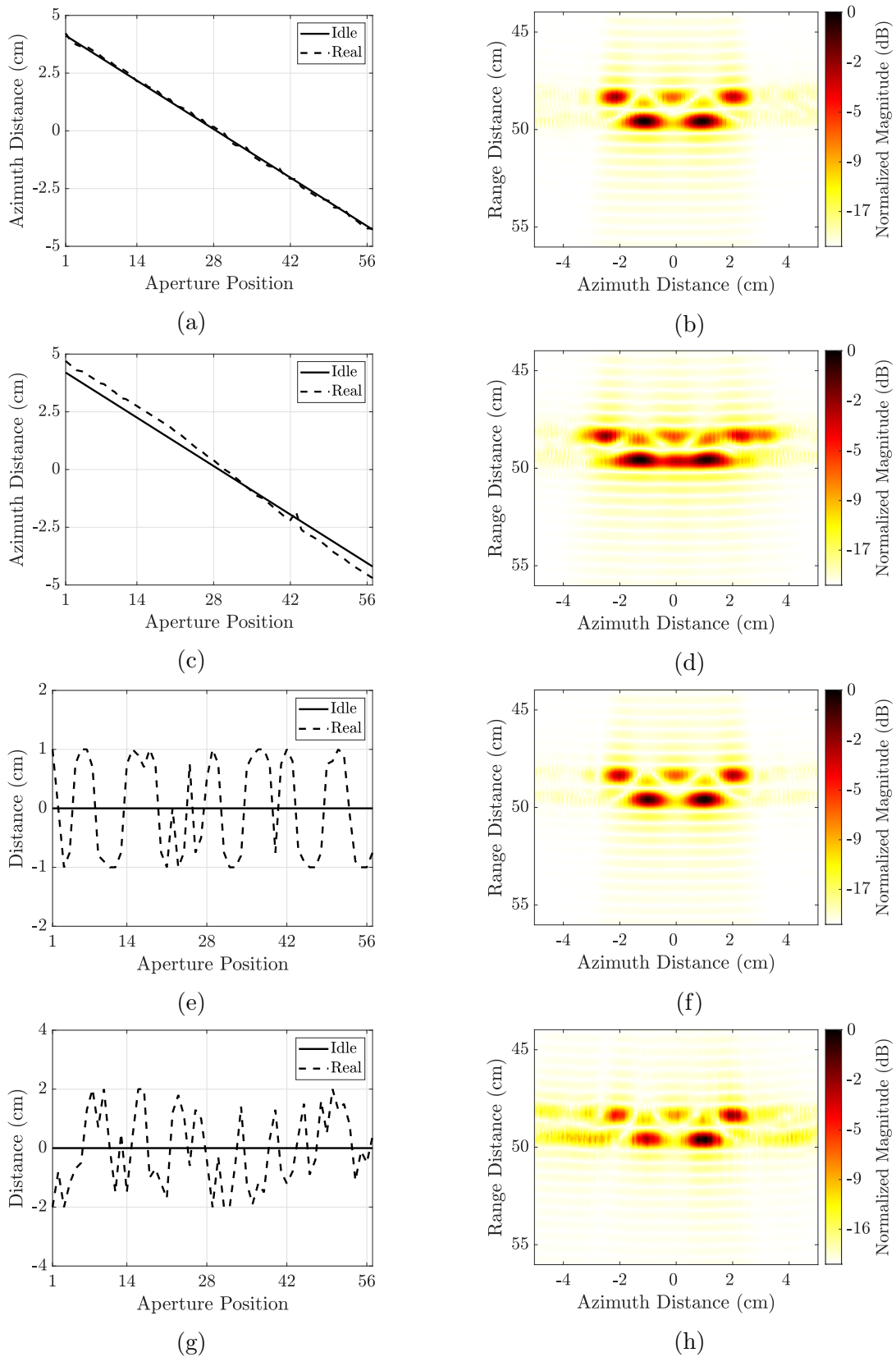


Figure 3-5: Errors comparison and effects of individual errors on SAR image: along y-axis/F-B (a) and (b) with  $y_{e,\max} = \pm 1$  mm, (c) and (d) with  $y_{e,\max} = \pm 5$  mm, and along z-axis/L-R (e) and (f) with  $z_{e,\max} = \pm 1$  cm, and (g) and (h) with  $z_{e,\max} = \pm 2$  cm.

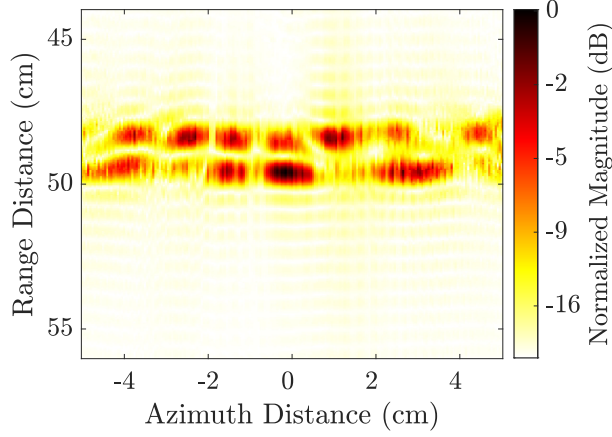


Figure 3-6: Effect of trajectory deviation along all the three axes i.e. U-D, F-B and L-R.

### 3.3.2 Analysis of Different Localization Cut-off Requirement in 3D Space

To analyze the different localization requirements along different axes, let's consider a point target at  $(x_c, y_c)$  and this target is illuminated from the reference altitude at  $X_0 = R_{\text{ref}}$ . The UAV follows an ideal path described in Section 3.2 with an aperture length of  $L_s$ . The slant range for each aperture position  $y(u)$ , where  $y(u) \in (-L_s/2, L_s/2)$  is given by

$$R(u) = \sqrt{(X_0 - x_c)^2 + (y_c - y(u))^2 + Z_0^2}, \quad (3-4)$$

and the slant range vector for the complete trajectory is denoted by  $R$ . In an ideal trajectory, there is no UAV movement along the  $z$ -axis and therefore  $Z_0 = 0$ . With the consideration of the point target at the center of origin,  $x_c = y_c = 0$ ,  $R(u)$  calculation for each aperture position with eq. (3-4) is shown in Fig. 3-7.a. Further, the impact on the  $R$  with introducing the U-D trajectory errors with  $x_e \in (-1 \text{ mm}, 1 \text{ mm})$  similar to Fig. 3-4.d is shown in Fig. 3-7.b and the modified slant range vector is denoted by  $R_{m,x}$ . The relative slant range error comparison  $\Delta R_x = R_{m,x} - R$  is shown in Fig. 3-7.c. This slant range has a maximum deviation  $\Delta R_{x,\text{max}} \approx \pm 1 \text{ mm}$ . Similarly,  $\Delta R_{x,\text{max}} = \pm 0.25 \text{ mm}$  and  $\Delta R_{x,\text{max}} = \pm 0.5 \text{ mm}$  is observed for  $x_{e,\text{max}} = \pm 0.25 \text{ mm}$  and  $x_{e,\text{max}} = \pm 0.5 \text{ mm}$ , respectively.

In the case of F-B errors as shown in Fig. 3-5.a and c with  $y_e \in (-1 \text{ mm}, 1 \text{ mm})$  and  $y_e \in (-5 \text{ mm}, 5 \text{ mm})$ , the relative slant range error comparison along the  $y$ -axis  $\Delta R_y$  is shown in Fig. 3-7.d and e. For the trajectory error of  $y_e = \pm 1 \text{ mm}$  and  $\pm 5 \text{ mm}$ ,  $\Delta R_{y,\text{max}}$  is approx. 0.09 mm and 0.44 mm, respectively. With L-R errors, the trajectory deviation of  $z_e \in (-10 \text{ mm}, 10 \text{ mm})$  and  $z_e \in (-20 \text{ mm}, 20 \text{ mm})$  similar to Fig. 3-5.e and g are introduced in the slant range calculation. The relative error  $\Delta R_z$  are shown in Fig. 3-7.f and g, respectively. Here,  $\Delta R_{z,\text{max}}$  comes out approximately to be 0.1 mm and 0.4 mm for  $z_e = \pm 10 \text{ mm}$  and  $z_e = \pm 20 \text{ mm}$ , respectively. Lastly, for the combined errors with  $x_{e,\text{max}} = \pm 1 \text{ mm}$ ,  $y_{e,\text{max}} = \pm 5 \text{ mm}$ ,  $z_{e,\text{max}} = \pm 2 \text{ cm}$  same as of Fig. 3-6 case, the relative slant range deviation is shown in Fig. 3-7.h. The deviations are the summation of

the individual errors and hence, the slant range is highly modulated and has the highest impact in degrading the SAR image.

From Fig. **3-7** results of slant range calculations, it is observed that the errors along the propagation have the highest impact on modifying the slant range. With a slight deviation of  $\pm 1$  mm along the range, the slant range is also modified by  $\pm 1$  mm whereas, in the other two cases for F-B and L-R errors, to achieve even  $\sim 0.4$  mm of modification in slant range, the required deviations are close to  $\pm 5$  mm and  $\pm 20$  mm in F-B and L-R cases, respectively. To summarize the results from Section 3.3.1 and these slant range calculations provide the following constraint on the amplitude of deviation along the individual axes:  $x_e \leq \lambda/4$ ,  $y_e \leq 5\lambda$  and  $z_e \leq 20\lambda$ . With these constraints, the SAR image is acceptable with some minor artifacts.

In terms of novelty, one of the biggest challenges with UAV-based THz SAR is the very high requirement of positioning accuracy, the knowledge that is being carried from conventional GHz SAR. The results in this and previous Section 3.3.1 define the positioning accuracy requirements are different along the U-D, F-B, and L-R directions. It can reach up to  $5\lambda$ ,  $20\lambda$ , and maybe much more depending on the imaging geometry and plane, and target symmetry. Therefore, this is a need to define an analytical model, and it can be well represented with the acceptable amplitude constraint  $\Delta R \leq \lambda/4$  or  $\Delta\phi \leq \pi/2$ .

To find the model for U-D errors or along propagation range, let's define an ideal slant range  $R_i(u)$  from eq. (3-4) for the target at the center of origin  $x_c = y_c = 0$  and therefore  $R_i(u) = \sqrt{X_0^2 + y(u)^2 + Z_0^2}$ . Due to the no-movement along the  $z$ -axis,  $Z_0 = 0$  and the range can be further simplified as  $R_i(u) = \sqrt{X_0^2 + y(u)^2}$ . Further, the modified slant range due to U-D error can be defined by  $R_{m,x}(u) = \sqrt{(X_0 + x_e)^2 + y(u)^2}$ ,  $x_e$  can be positive or negative based on the shift direction. It will be positive for upward and downward shifts, respectively. Based on the  $\Delta R \leq \lambda/4$ , and the amplitude constraint on  $x_e$  can be calculated by solving the following inequality  $\sqrt{(X_0 + x_e)^2 + y(u)^2} - \sqrt{X_0^2 + y(u)^2} \leq \lambda/4$ . This leads to a quadratic polynomial given as

$$x_e^2 + 2X_0x_e - \frac{\lambda(\lambda + 8R_i(u))}{16} \leq 0. \quad (3-5)$$

The solution of this quadratic polynomial is

$$x_e \leq \frac{-4X_0 \pm \sqrt{16X_0^2 + \lambda(\lambda + 8R_i(u))}}{4}. \quad (3-6)$$

As of quadratic polynomial, two roots of  $x_e, x_{e,1}$  and  $x_{e,2}$  will be generated by (3-6), the minimum root defines the amplitude constraint on  $x_e$ ,  $|x_e| \leq \min(|x_{e,1}|, |x_{e,2}|)$ . Similarly, in consideration of the modified slant range due to F-B error,  $R_{m,y}(u) = \sqrt{X_0^2 + (Y_0 + y_e)^2}$ , where  $Y_0 = \max(y(u)) = L_s/2$ , the constraint on  $y_e$  will be given by

$$y_e \leq \frac{-2L_s \pm \sqrt{4L_s^2 + \lambda(\lambda + 8R_i(u_{\max}))}}{4}, \quad (3-7)$$

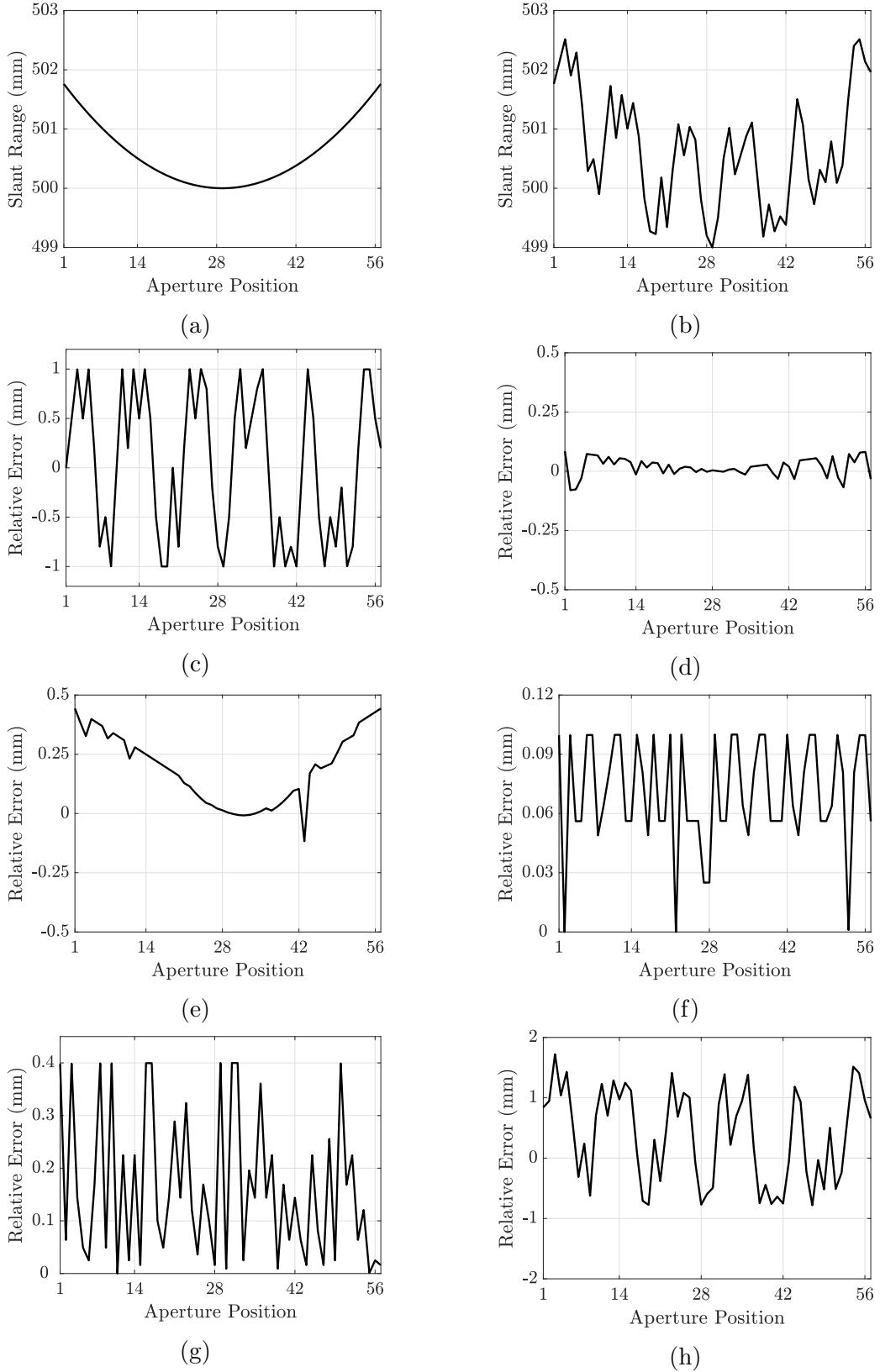


Figure 3-7: (a) Ideal slant range, (b) slant range with U-D errors,  $x_{e,\max} = \pm 1$  mm, and relative slant range error comparison for (c)  $x_{e,\max} = \pm 1$  mm, (d)  $y_{e,\max} = \pm 1$  mm, (e)  $y_{e,\max} = \pm 5$  mm, (f)  $z_{e,\max} = \pm 1$  cm, (g)  $z_{e,\max} = \pm 2$  cm and (h) combined ( $x_{e,\max} = \pm 1$  mm,  $y_{e,\max} = \pm 5$  mm,  $z_{e,\max} = \pm 2$  cm).

where  $R_i(u_{\max}) = \sqrt{X_0^2 + (L_s/2)^2}$  is derived from eq. (3-4) with  $x_c = y_c = Z_0 = 0$  and based on the roots of (3-7),  $|y_e| \leq \min(|y_{e,1}|, |y_{e,2}|)$ . Taking the parameters from Table 3-1,  $L_s = 0.084$  m,  $\lambda = 0.001$  m and  $R_i(u_{\max}) \approx 0.501761$  m, the corresponding constraint is  $y_e \lesssim 2.9$  mm that corresponds to  $\sim 3\lambda$ .

Lastly, to derive the constraint for  $z_e$ , the modified slant range is given by  $R_{m,z}(u) = \sqrt{X_0^2 + y(u)^2 + z_e^2}$  and finding a solution by using a similar approach. The constraint is given by

$$z_e \leq \frac{\sqrt{\lambda(\lambda + 8R_i(u))}}{4}. \quad (3-8)$$

In the case of  $x_e$  (U-D) and  $z_e$  (L-R) amplitude constraint, the ideal slant range has to be evaluated with an aperture position with a reference or lowest slant range. It is in contrast to the maximum aperture consideration in the case of  $y_e$  calculation. For the target at the center of origin, the minimum slant range will be at center aperture position, that is  $y(u) = 0$  and  $u = N/2$ , where  $N$  is the number of azimuth aperture position and  $y(u) \in (-L_s/2, L_s/2)$ . With the same parameters as defined above and consideration of reference slant range, the amplitude constraint on  $x_e$  and  $z_e$  are 0.25 mm ( $\lambda/4$ ) and 1.5 cm ( $15\lambda$ ) respectively.

The analytical model findings are well suited to the results and cut-off values presented in Section 3.3.1.

#### 3.3.3 Experimental Analysis

To validate the simulation results of Section 3.3.1 and 3.3.2 and carry out a comparative analysis with measurements, a THz SAR testbed has been set up to investigate the motion errors impact (similar to Fig. 3-4, Fig. 3-5 and Fig. 3-6) on the THz SAR image. The sketch and optical picture of the testbed are shown in Fig. 3-8 (top) and (bottom), respectively. The imaging target is shown in Fig. 3-8 (bottom-right), and it is an ‘‘L’’ shape metallic wrench. The measurement setup consists of a Rhode and Schwarz ZVA67 VNA [66] that operates up to a frequency range of 67 GHz and a THz extender that can up-convert the RF signal from the VNA in the range of 220-330 GHz [67]. A horn antenna is connected to the extender waveguide flange. The extender is mounted on a vertical rail to perform the SAR operation as shown in Fig. 3-8 and moved along  $y^m$ -axis with the step size of  $\Delta u = 1.5$  mm in the ideal case. It is to be noted here that the direction of the Cartesian coordinate is different from 3D EM wave simulations. In the simulation, the UAV moves along  $y$ -axis at an altitude of  $R_{\text{ref}}$  and excites the target from the top, similar to downward-looking SAR. In contrast, in the measurement, the target is excited from the front, similar to the parallel-looking SAR configuration. To make the imaging plane similar to the simulation, the target is mounted vertically, whereas in simulation the target is lying horizontally. The vertical mounting of the target can also be considered as illuminating the target from the top. Therefore, the geometry of EM field simulation and measurement is similar. The Cartesian coordinates of both the approaches are related by  $x^m = y$ ,  $y^m = x$ , and  $z^m = z$ , where  $(x^m, y^m, z^m)$  are the Cartesian coordinates for the measurement imaging space.

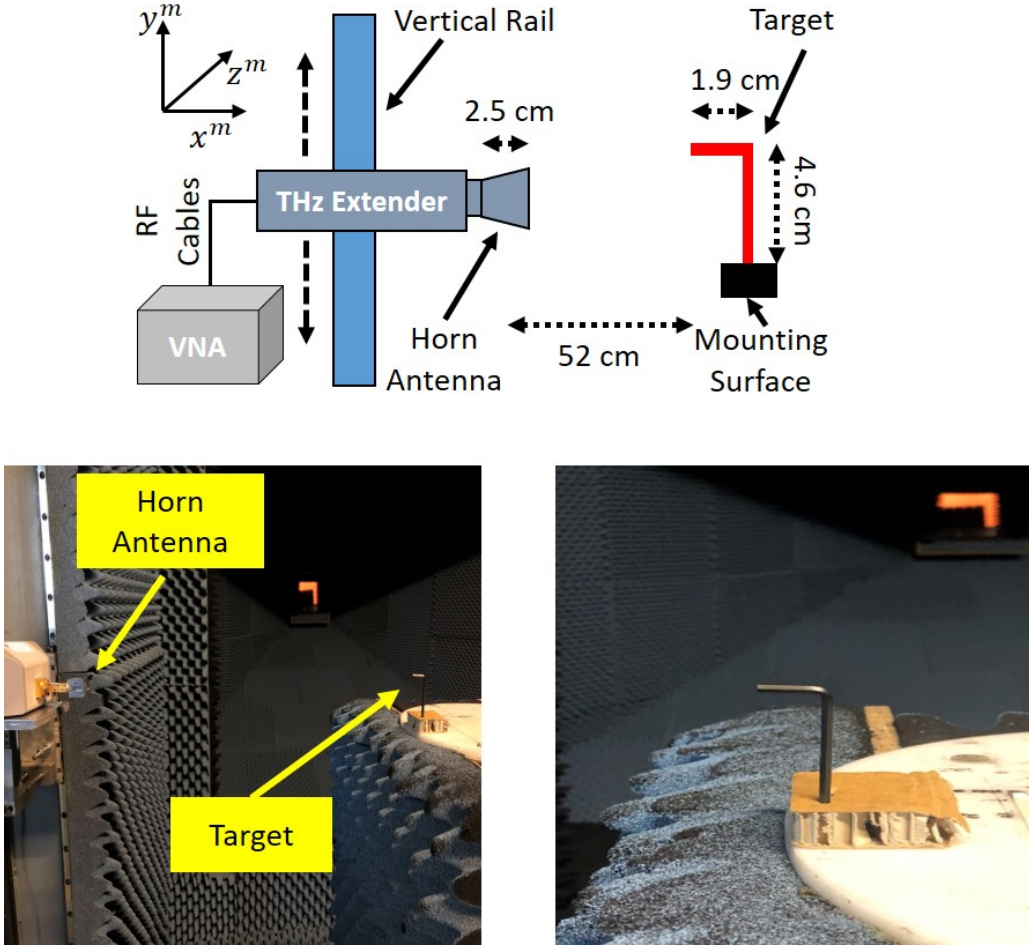


Figure 3-8: (top) Testbed sketch, (bottom) picture of the testbed: (bottom-left) side-view and (bottom-right) target, target is a L-shaped metallic wrench tool.

For the measurement,  $S_{11}$  reflection coefficients are measured for the frequency range of 250-300 GHz. The base power from the VNA port 1 is  $-10$  dB and the noise floor for different intermediate frequency (IF)  $B_w$  is provided in [68]. The IF filter  $B_w = 10$  KHz is considered and the resulting noise level is approx.  $-100$  dB. In Table 3-2, the measurement parameters are summarized and a detailed description of THz SAR operation with VNA is provided in [18]. The measurement results are presented in Fig. 3-9. SAR image of the target with an ideal trajectory is shown in Fig. 3-9.a. It is a high-resolution SAR image, where the object shape is clearly observable, and its dimensions can be approximated with respect to the spatial resolution defined in Table 3-2.

To analyze the effects of motion errors and to validate the simulation model with measurements, firstly, the F-B error trajectory with  $y_{e,\max} = \pm 1$  mm is implemented similar to Fig. 3-5.a. The generated SAR image within proximity to this trajectory is shown in Fig. 3-9.b. Similar to the simulation results of Fig. 3-5.b, the errors do not highly alter the image. Due to the hardware limitations, further trajectories are not exactly similar to Fig. 3-5, but fulfill the maximum relative error deviation such as  $y_{e,\max}$  and  $z_{e,\max}$ . For  $y_{e,\max} = \pm 5$  mm, the resulting image is shown in Fig. 3-9.c. The image

Table 3-2: THz SAR measurement parameters.

Symbol	Parameter	Value
$L_r$	antenna length	6 mm
$R_{\text{ref}}$	reference range	52 cm
$f_c$	center frequency	275 GHz
$B_w$	bandwidth	50 GHz
$L_s$	synthetic aperture length	8.4 cm
$r_x$	range resolution	3 mm
$r_y$	azimuth resolution	3 mm
$\Delta u$	step size	1.5 mm
$N_f$	number of frequency bins	3001
$N$	number of azimuth sampling points	57

has degraded, but the target shape is still observable and proves the cut-off motion error provided by simulation for the y-axis. Secondly, for analyzing the effects of L-R errors, the imaging with the trajectory for  $z_{e,\text{max}} = \pm 1$  cm is performed, and the results are presented in Fig. 3-9.d. These deviations alter the image, but still, the shape of the object is observable. In reference to the simulation results, for  $z_{e,\text{max}} = \pm 1$  cm, the resulting image differs a bit. In the simulation, the azimuth positions are exactly parallel to the object center, whereas in measurement, due to hardware imperfections, there might be a slight variation in illuminating the object exactly parallel to its center. Further, the error amplitude is increased to  $z_{e,\text{max}} = \pm 2$  cm. The effects of this trajectory are observed from the generated image shown in Fig. 3-9.e, and the result matches with the simulation results.

To investigate the impact of U-D errors, the testbed currently does not have a linear rail to shift the sensors along the  $x$ -axis with sub-mm accuracy. Therefore, to study such errors along the propagation direction for  $x_e \in (-1 \text{ mm}, 1 \text{ mm})$ , the errors in aperture positions as shown in Fig. 3-4.d are introduced in the image generation with an ideal trajectory in post-processing. The resulted image is shown in Fig. 3-9.f. Lastly, for combined errors, the trajectory with only F-B and L-R errors is realized, and the resulting image is shown in Fig. 3-9.g. The target is completely washed out.

The measurement results reveal a close match with the findings of the simulations and the analytical model. Therefore, it validates the results.

### 3.4 Motion Compensation with Passive Localization System

This section presents the motion error compensation results by utilizing the trajectory estimations with the proposed sub-mm passive localization system. The position estimations are introduced in the slant range calculation under BPA processing, and position

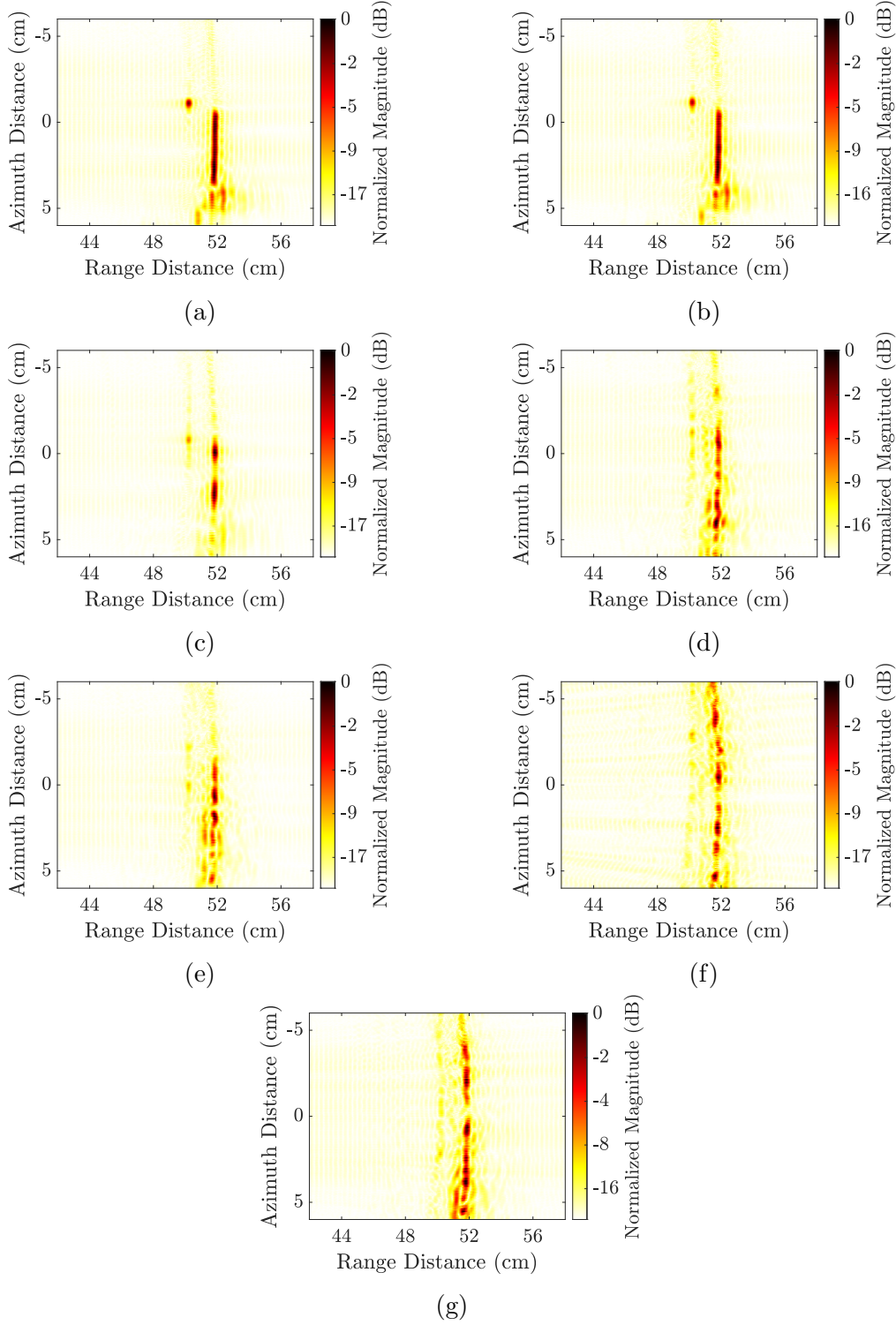


Figure 3-9: SAR image with (a) idle trajectory, and with motion errors: along  $y^m$ -axis/F-B (b) with  $y_{e,\max} = \pm 1$  mm, (c) with  $y_{e,\max} = \pm 5$  mm, along  $z^m$ -axis/L-R (d) with  $z_{e,\max} = \pm 1$  cm, (e) with  $z_{e,\max} = \pm 2$  cm, along synthesized  $x^m$ -axis/U-D (f) with  $x_{e,\max} = \pm 1$  mm, and (g) combined along F-B with  $y_{e,\max} = \pm 5$  mm and L-R with  $z_{e,\max} = \pm 2$  cm.

estimations along  $(x, y, z)$  are represented by  $(X_E, Y_E, Z_E)$ . Furthermore, it is to be noted that the estimations are considered individually for the U-D, F-B, and L-R error cases and lastly all together for combined errors case.

The modified slant range to compensate for the effect of the U-D errors in Fig. 3-4.a, b, and c at pixel location  $(i, j)$  is given by

$$R_{(i,j)}^{E_x}(u) = \sqrt{(x_i - x_e(u))^2 + (y_j - y(u))^2 + Z_0^2}, \quad (3-9)$$

where  $x_e(u) = X_E(u) - X_0$  is the error relative to the ideal trajectory along range at azimuth position  $u$ . As defined in Section 3.3, in the ideal case  $X_0 = 0.5$  m, and with U-D error  $x_e \in (-0.25 \text{ mm}, 0.25 \text{ mm})$ , the relative error estimations  $x_e(u)$  from the localization system is presented in Fig. 3-10.a and the achieved compensation in the SAR image is shown in Fig. 3-10.b. In comparison to Fig. 3-4.a, the resulted SAR image in Fig. 3-10.b is well compensated. Similarly, the relative errors estimations and MOCO SAR image for the case  $x_e \in (-0.5 \text{ mm}, 0.5 \text{ mm})$  and  $x_e \in (-1 \text{ mm}, 1 \text{ mm})$  is shown in Fig. 3-10.c and Fig. 3-10.d, and Fig. 3-10.e and Fig. 3-10.f, respectively. These images are also well-compensated with respect to. Fig. 3-4.b and Fig. 3-4.c.

Furthermore, for the F-B error compensation, the  $x_e(u) = 0$  and the modified slant range is given by

$$R_{(i,j)}^{E_y}(u) = \sqrt{x_i^2 + (y_j - Y_E(u))^2 + Z_0^2}, \quad (3-10)$$

where  $Y_E(u) = y(u) - y_e(u)$ . With the relative trajectory error  $y_{e,\max} = \pm 5$  mm similar to Fig. 3-5.c, the relative error estimations  $y_e(u)$  at all aperture positions is shown in Fig. 3-11.a and the motion compensated image is presented in Fig. 3-11.b. Similarly, to compensate for the L-R errors, the modified slant range is

$$R_{(i,j)}^{E_z}(u) = \sqrt{x_i^2 + (y_j - y(u))^2 + z_e(u)^2}, \quad (3-11)$$

where  $z_e(u) = Z_E(u) - Z_0$ . In L-R analysis  $x_e(u) = y_e(u) = 0$ , and relative position estimations  $z_e(u)$  to compensate for the errors in Fig. 3-5.g are presented in Fig. 3-11.c. Achieved compensation in comparison to Fig. 3-5.h is shown in Fig. 3-11.d. Lastly, to compensate for the effects of the combined errors as shown in Fig. 3-6, the modified slant range to be considered for image reconstruction with BPA algorithms is

$$R_{(i,j)}^{E_{x,y,z}}(u) = \sqrt{(x_i - x_e(u))^2 + (y_j - Y_E(u))^2 + z_e(u)^2}. \quad (3-12)$$

The relative position estimations acquired with the localization system, i.e.  $(x_e, y_e, z_e)$ , are shown in Fig. 3-11.e. All the estimations are approximately in the order of sub-mm accuracy w.r.t the trajectory deviations and fit very well for THz SAR MOCO as the same can be seen with the compensated image in Fig. 3-11.f.

In all the above cases, either with individual or combined errors, the proposed MOCO technique based on the sub-mm passive localization system is validated with the results. Moreover, increase in the accuracy estimations especially along the range direction will

further enhance the image quality. One of the potential methods is to increase the bandwidth. Fig. 3-12 shows the cumulative distribution function (CDF) of localization error for the bandwidth of 10, 50, and 100 GHz of the proposed localization system. The major contribution in the increase of accuracy is due to overlap reduction of the line of sight and non-line of sight paths with the increase in bandwidth. The deep insight into this localization system algorithms and methods are available in [38]. With 50 GHz of bandwidth, localization error is less than 2.5 mm ( $\lambda/4$ ) at 99.99% confidence. Moreover, the proposed solution also supports further higher frequency spectrum for SAR imaging such

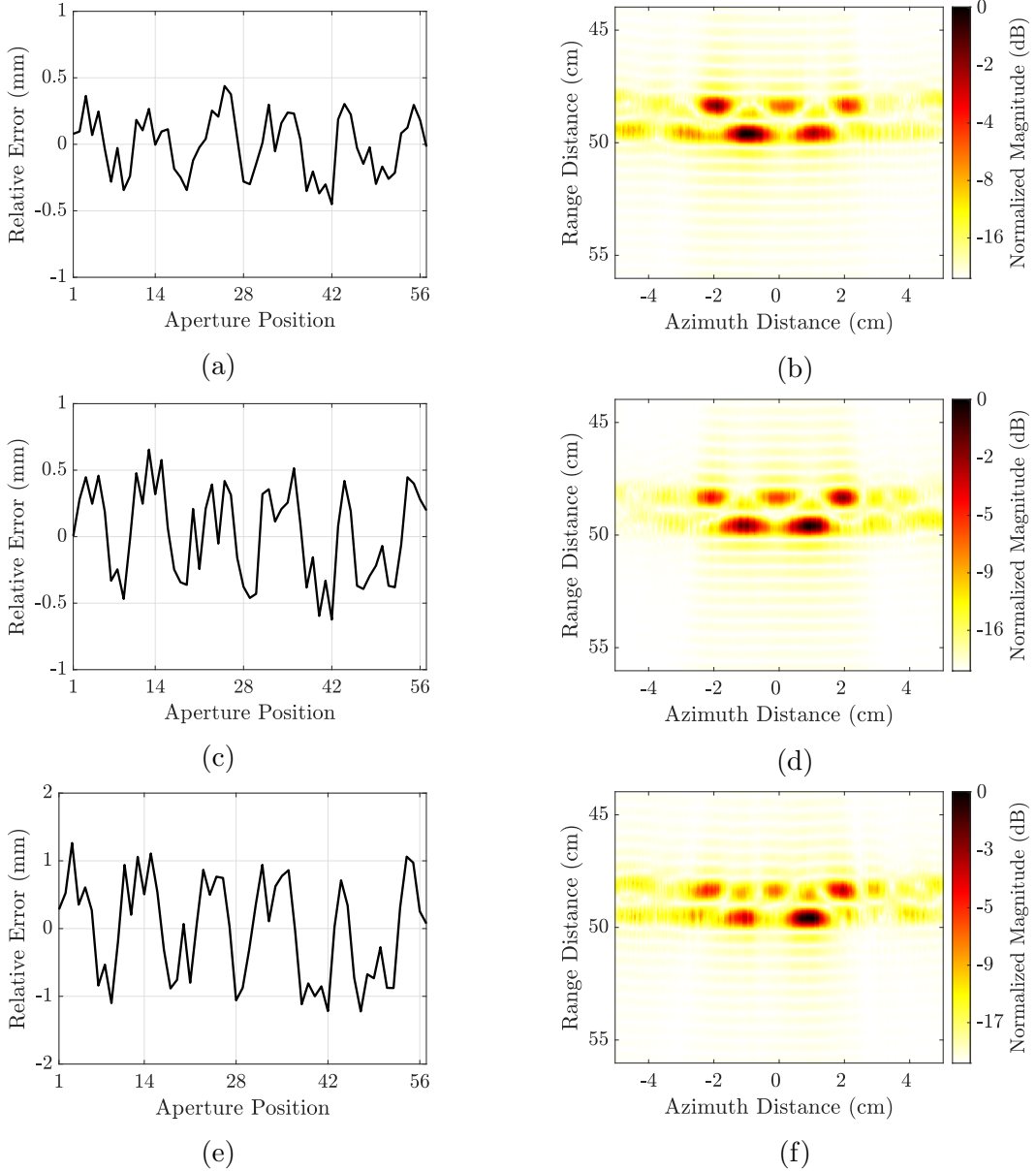


Figure 3-10: Relative error estimation and motion compensated SAR image: for U-D errors (a) and (b) with  $x_{e,\max} = \pm 0.25$  mm, (c) and (d) with  $x_{e,\max} = \pm 0.5$  mm, and (e) and (f) with  $x_{e,\max} = \pm 1$  mm

### 3.5 Conclusive Remark

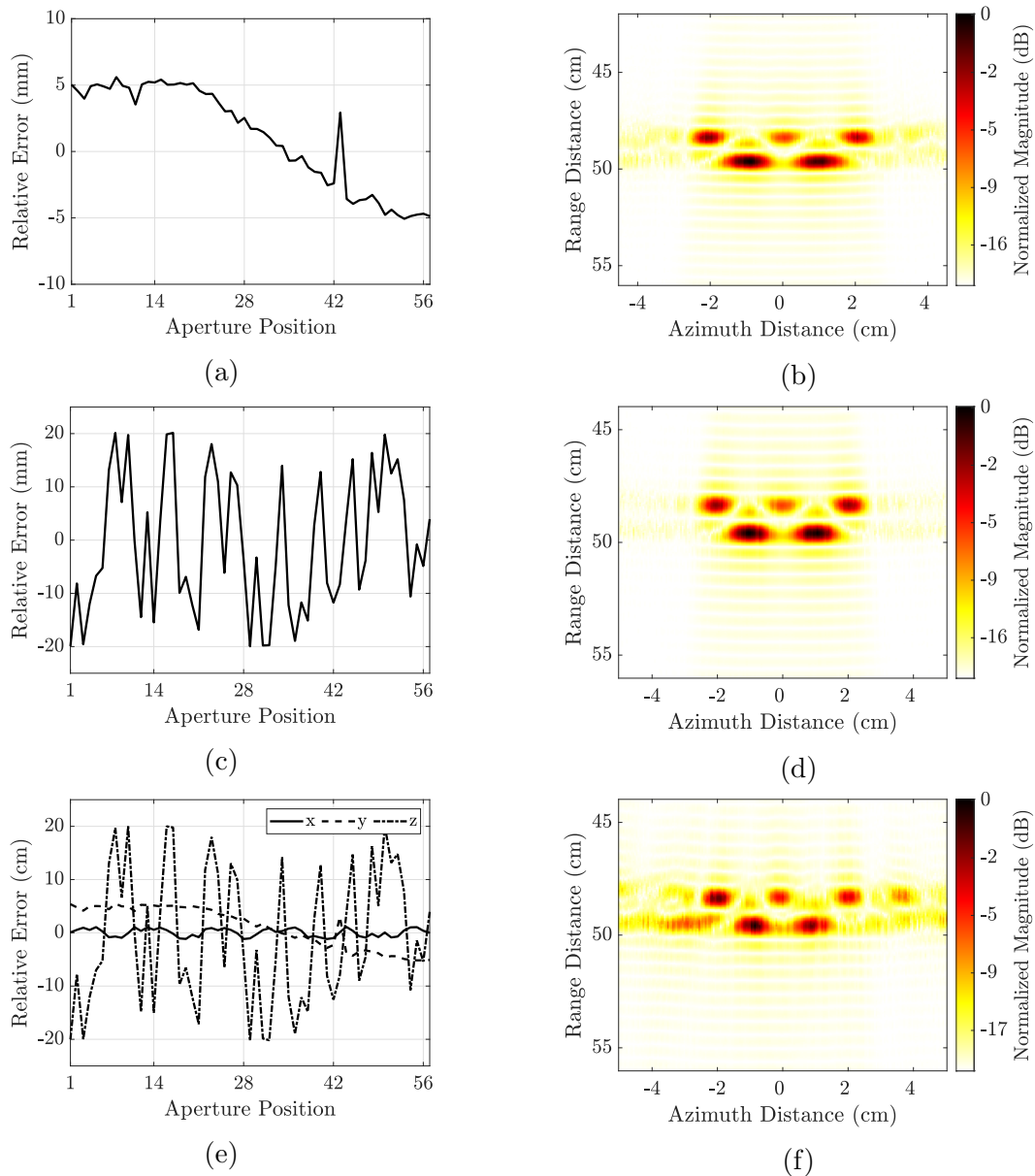


Figure 3-11: Relative error estimation and motion compensated SAR image: for F-B errors (a) and (b) with  $y_{e,\max} = \pm 5$  mm, for L-R errors (c) and (d) with  $z_{e,\max} = \pm 2$  cm, and combined errors (e) and (f) with  $x_{e,\max} = \pm 1$  mm,  $y_{e,\max} = \pm 5$  mm and  $z_{e,\max} = \pm 2$  cm.

as 1 THz as the localization error is less than  $70 \mu\text{m}$  at the confidence of approx. 90% with 100 GHz of bandwidth.

### 3.5 Conclusive Remark

This chapter presented UAV-based indoor THz SLAM in which the localization of UAV is provided using the sub-mm passive localization system and mapping with the SAR

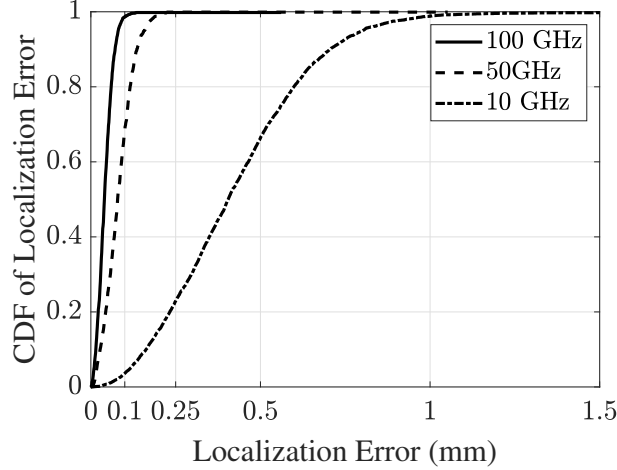


Figure **3-12**: CDF of localization error of the proposed localization system for the bandwidth of 10, 50 and 100 GHz.

technique. The THz SLAM results signify the high-resolution object mapping and its position in the room using SAR and the UAV position estimations along the SAR trajectory using the RFID-based localization system. The THz SAR mapping is very sensitive to translational motion errors, and the same has been studied and compensated with the localization system. The MOCO utilizing the localization system can be considered as an application of the THz SLAM. The impact of the errors has been demonstrated with simulations and measurements in detail. The errors along all three axes are analyzed individually and jointly.

As sub-mm positioning accuracy is difficult to achieve for UAV-based THz SAR, this chapter's findings reveal the required accuracy is not the same along all three axes in 3D space. The impact of U-D errors is the most sensitive. Whereas F-B errors are comparatively less, and the L-R errors effects are the least sensitive. For presented 300 GHz SAR results, the accuracy of 0.25 mm ( $\lambda/4$ ), 5 mm ( $5\lambda$ ), and 20 mm ( $20\lambda$ ) would be acceptable with minor artifacts along the propagation direction (U-D), flying direction (F-B), and perpendicular to the other two (L-R), respectively. To generalize the amplitude of deviations or cutoff motion error, we define the acceptable constraint on the phase error  $\Delta\phi \leq \pi/2$ . It is described in this chapter as a relaxed constraint compared to the strict constraint of  $\Delta\phi \leq \pi/8$  or  $\Delta R \leq \lambda/16$  that is hard to achieve at THz. An analytical model is presented to calculate the cutoff motion error for different dimensions based on the relaxed phase constraint. For proposed imaging geometry and system parameters, the cutoff limits are defined by the models for different coordinates. These cutoff limits are well supported by the simulation and measurement results. It is a well trade-off solution if some minor artifacts are acceptable compared to hard achievable accuracy along the propagation range.

To compensate for the impact, the trajectory estimation from the localization system is applied. The proposed method of THz SAR MOCO with the indoor localization system is proved with the presented results.

## 2D Imaging and Analysis

This chapter addresses the THz SAR 2D imaging, especially with indoor objects. Mapping and analysis of indoor objects at a long reference range are in the foreground in this chapter. The long-range plays a crucial role as the THz spectrum is always concerned about the dynamic range. State-of-the-art THz SAR demonstration with a  $B_w > 100$  GHz is mostly limited to a propagation distance of sub-m and mainly with metallic targets.

For example, demonstrations with bandwidth  $B_w < 100$  GHz, in [22], imaging of an outdoor environment is addressed with  $B_w = 40$  GHz. In [60], a metal target is imaged by a system with  $B_w = 42$  GHz. The study presented in [30] focuses on concealed object imaging from security/defense perspective with  $B_w = 28$  GHz. Another example of SAR imaging with metallic targets at  $B_w > 100$  GHz can be found in [31]. To summarize, the THz SAR imaging of indoor objects with  $B_w > 100$  GHz and at a long reference range of  $> 1$  m is not widely explored. Therefore, this chapter provides a detailed analysis of 2D indoor THz SAR imaging primarily with a wide bandwidth of 110 GHz and at a long range of  $> 1$  m.

The chapter is organized as follows. Firstly, in Section 4.1, imaging configurations are proposed based on planar aperture and type for reflection, specular and diffuse. The configurations are of significant relevance to obtain a different imaging plane in a 3D coordinate system. The findings of the imaging plane are validated with simulations and measurements. Based on the results, a method is provided to optimize SAR configuration that can be applied to different applications such as look-through and surface imaging. Supported by the optimized configuration, 2D imaging of objects commonly found in the indoor environment is demonstrated in Section 4.2. Indoor objects made of different materials such as plastic, wood, glass, foam, and metal are considered in this chapter.

Further, in Section 4.3, the chapter presents an analysis addressing the following terms.

- Geometric properties: The retrieved 2D SAR images are further processed for geometric properties extraction such as length, width, height, shape, and thickness of a target.

- Surface roughness: The received power depends on the surface roughness. Therefore, the impact of surface roughness in the THz imaging is analyzed.
- Small and large bandwidth: A comparative analysis of small and large bandwidth 2D imaging within the frequency band of 220-330 GHz is presented.

To further investigate the potential of the THz spectrum, the 2D imaging is addressed in Section 4.4 for concealed and hidden object scenarios. Besides defining the maximum sensing range of the considered objects, an analytical model based on transceiver sensitivity is proposed and validated with measurements in Section 4.5. Lastly, in Section 4.6, a conclusive remark is provided.

Also to be noted, the chapter presents the figures in various color coding scheme. The color coding is selected to show the best possible information of the mapped target.

## 4.1 Planar Aperture 2D Imaging Configurations

SAR imaging relies on the principle of image reconstruction via received reflected waves from the illuminated target. Based on the surface roughness, the reflection is generally classified into specular and diffuse reflection as shown in Fig. 4-1 [69, 70]. In case of specular reflection, laws of reflection state that the angle of reflection  $\theta_r = \theta_i$ , where  $\theta_i$  is the angle of incidence. Whereas in diffuse reflection, the incident ray is scattered along different angles. This phenomenon of specular and diffuse reflection is well validated for visible light rays. However, it is also valid for other EM waves such as radio waves and even at the THz spectrum [70]. The specular reflection occurs if the surface is smooth, as shown in Fig. 4-1. (left), and Fig. 4-1 (right) shows the diffuse reflection where the surface is rough.

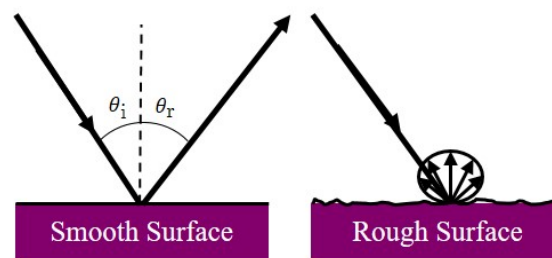


Figure 4-1: Types of reflection: (left) specular on smooth surface and (right) diffuse on rough surface.

Based on the Fraunhofer criterion, a target can be characterized as smooth or rough depending on the standard deviation of target surface irregularities  $h$ . For an angle of incidence  $\theta_i$  and the signal wavelength  $\lambda$ , the surface of the target is considered rough if

$$h > \frac{\lambda}{32\cos\theta_i}. \quad (4-1)$$

Otherwise, it is considered smooth [65]. The requirement of  $h$  to define whether the surface is rough or smooth for frequency spectrum from 10 GHz to 1 THz with different  $\theta_i$  is summarized in Fig. 4-2. There are also other models of surface scattering such as the Rayleigh criteria [8, 65]. However, in general, it can be concluded that the higher the frequency, the more precise surface roughness and smoothness can be analyzed.

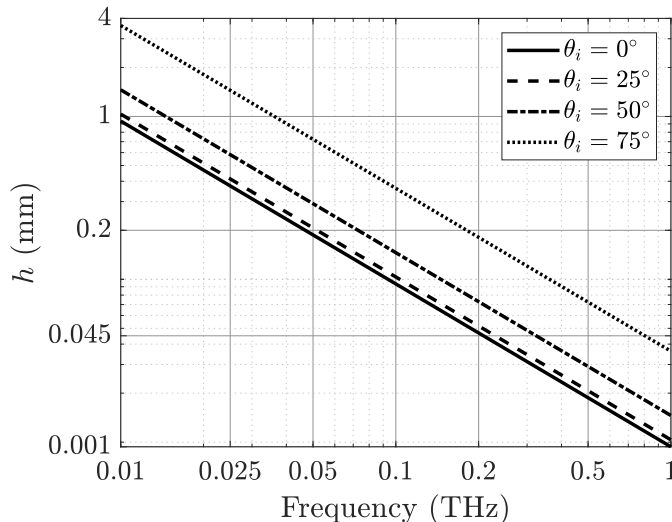


Figure 4-2: Relationship of  $h$  and frequency from 10 GHz to 1 THz.

Conventional SAR imaging such as side-looking SAR [8, 65] in monostatic transceiver geometry is realized mostly based on the diffuse reflection. In this case, the backscattered EM waves along the propagation direction are recorded. In contrast, the specular reflection travels away from the transceiver and hence is not being captured. The impact of surface roughness at the THz spectrum on diffuse reflection is shown in [71]. The diffuse reflection can be further characterized based on the phase variation. Moreover, in case of a slightly rough surface both specular and diffuse reflection exists [69, 70]. Based on these reflection principles, this chapter presents two imaging configurations for the THz SAR imaging .

The first configuration is based on both specular and diffuse reflections termed SDR. In this case, the target is positioned parallel to the transceiver with  $\phi_y = 0^\circ$  as shown in Fig. 4-3 (top), where  $\phi_y$  is a yaw-rotational shift along the  $y$ -axis. In another configuration, the target is positioned the same as in the case of SDR but with  $0^\circ < \phi_y < 90^\circ$  as shown in Fig. 4-3 (bottom). This configuration refers to imaging only with diffuse reflections (DR) or scattering. The rotational shift leads to a change in the incident plane and normal vector direction, as shown in Fig. 4-3 (bottom). The corresponding incidence angle is represented by  $\theta_{i,y}$ . For the incident plane formed in DR configuration with  $0^\circ < \phi_y < 90^\circ$ , corresponds to  $\theta_{i,y} = \phi_y$ .

In the case of SDR, the objective is to capture maximum specular and diffuse reflection based on the object's smoothness or roughness. In the DR case, it has to be guaranteed that the imaging is only realized with diffuse reflection. Therefore, with a certain rotational shift  $\phi_y$ , specular reflection is excluded from the receiving sensor if it

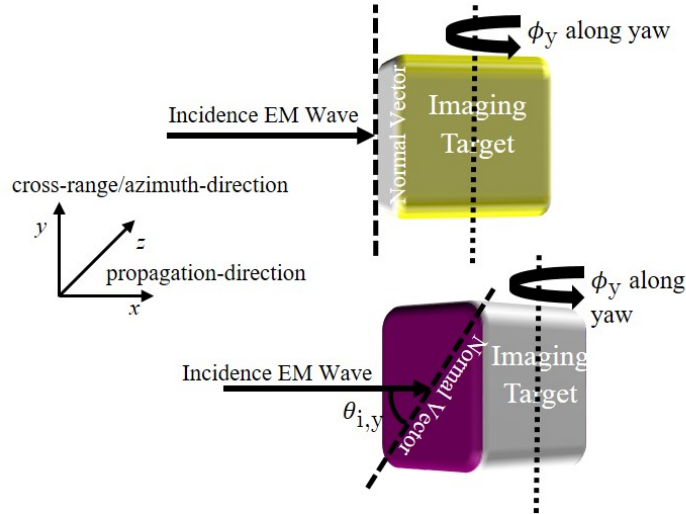


Figure 4-3: Imaging geometry of (top) SDR and (bottom) DR configurations.

exists.

The applications of both configurations relate to the requirement of the imaging plane. In 2D imaging with SDR configuration, the imaging plane is the  $x - y$  plane, as shown in yellow in Fig. 4-3 (top). Whereas the DR configuration imaging plane is the  $y - z$  plane relative to the target center as shown in magenta in Fig. 4-3 (bottom). The imaging with SDR and DR will be investigated with a developed simulation system and measurements in this chapter. It can be expected that the SDR will be beneficial for look-through imaging, while the DR configuration will be more suitable for surface imaging.

#### 4.1.1 Simulation Analysis of Imaging Plane with SDR and DR

This section evaluates the imaging with both configurations based on simulations. Analysis of both configurations is required for validating the defined imaging plane and assess the  $\phi_y$  for surface scanning, where the DR is maximum. The simulation framework from Chapter 2 is used in this section.

The designed imaging target shape and dimensions are shown in Fig. 4-4. The target consist of 3 bricks with the following dimensions (length  $\times$  width  $\times$  height) in mm: brick 1 ( $5 \times 2 \times 5$ ), brick 2 ( $4 \times 2 \times 20$ ) and brick 3 ( $7 \times 2 \times 5$ ), where brick 1 and 2 are attached to each other and brick 3 is separated from brick 2 by 1 mm along the  $x$ -axis. The target material is a PEC. The target shape and material is a well-fit to evaluate the configurations. From theoretical analysis, it can be concluded that the third brick will not be observable for SDR imaging as the EM waves cannot penetrate the PEC material. In the case of surface imaging, where the imaging plane is the  $y - z$  plane, for a certain range of  $\phi_y$ , all the bricks are expected to be observable. However, as the optimum range of  $\phi_y$  is unknown, an evaluation for different values of  $\phi_y$  is performed.

For 2D imaging, the target is illuminated by plane waves propagating along the  $x$ -

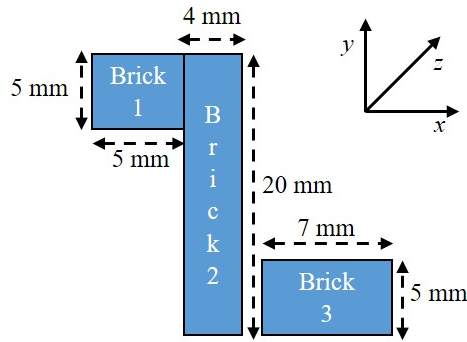


Figure 4-4: Imaging object shape and dimensions.

axis, and the electric and magnetic fields are along the  $y$ -axis and  $z$ -axis, respectively. The imaging parameters are summarized in Table 4-1. The imaging is performed at a reference slant range  $R_{\text{ref}}$  of 25 cm. In case of SDR imaging, the target is positioned parallel to the sensors as shown in Fig. 4-3 (top). Fig. 4-5.a-d shows the imaging scene with  $\phi_y = 0^\circ, 15^\circ, 45^\circ$  and  $90^\circ$ , respectively. The propagation plane is represented by red, and it shows the directly illuminated target components. The arrow represents the propagation direction. The generated SAR images for different  $\phi_y$  are summarized in Fig. 4-6.

Table 4-1: Simulation parameters for THz SAR imaging.

Symbol	Parameter	Value
$f_c$	center frequency	275 GHz
$B_w$	bandwidth	110 GHz
$L_s$	synthetic aperture length	6 cm
$r_x$	range resolution	1.36 mm
$R_{\text{ref}}$	reference range	25 cm
$\Delta u$	step size	1 mm
$N_f$	number of frequency points	3001
$N$	number of azimuth points	61
$P_T$	transmit power	0 dBm

Fig. 4-6.a shows the SAR image for  $\phi_y = 0^\circ$ , i.e. SDR configuration. Bricks 1 and 2 are observed in the presented result, but no information about brick 3 is available. As a result of PEC material, the EM waves do not propagate inside the material. Therefore, brick 3 is not illuminated on a larger scale. The achieved results provide the imaging plane along  $x - y$ . Brick 3 can be mapped if the imaging plane is along  $y - z$ . Therefore, based on DR configuration, the target is rotated around the  $y$ -axis. For  $\phi_y = 5^\circ$  and  $\phi_y = 15^\circ$ , the SAR images are shown in Fig. 4-6.b and c, respectively. Still, no information about Brick 3 is obtainable from the resulting images. With a further increase in  $\phi_y = 25^\circ$ , brick 3 is observed but with a low magnitude, as shown in Fig. 4-6.d. The image of brick 3 gets sharper and the magnitude increases for the range of  $\phi_y = 35^\circ$  up to  $\phi_y =$

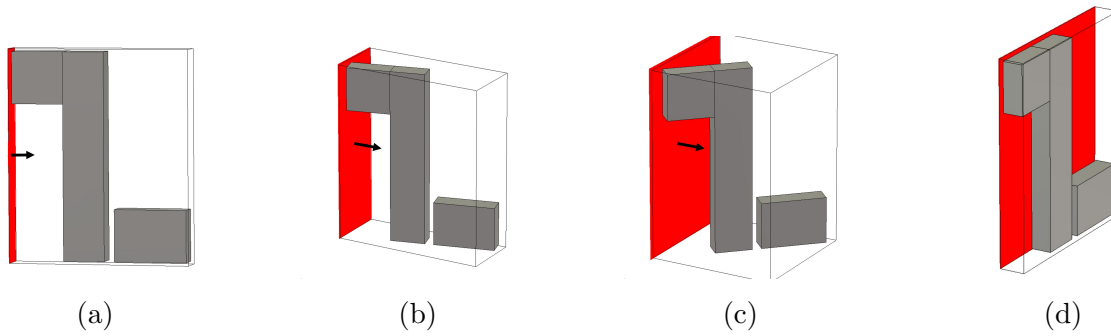


Figure 4-5: Imaging scene for different  $\phi_y =$  (a)  $0^\circ$ , (b)  $15^\circ$ , (c)  $45^\circ$  and (d)  $90^\circ$ .

$55^\circ$ . In this range, the target and all the composite bricks are well observable with a high magnitude as shown for the case of  $\phi_y = 35^\circ, 45^\circ$  and  $55^\circ$  in Fig. 4-6.e, f, and g, respectively.

With a further increase in  $\phi_y = 65^\circ$  and  $75^\circ$ , the SAR image is degraded as shown in Fig. 4-6.h and i, respectively, and no useful information regarding target shape is obtainable for  $\phi_y = 90^\circ$  as shown in Fig. 4-6.j. To summarize the results, for the increase in  $\phi_y$  from  $0^\circ$  to  $45^\circ$ , from the laws of reflections [70], the incidence angle increases due to the change in normal vector plane, and the specular reflected signal travels away from the sensor. Especially, at  $45^\circ$ , the specular signal is perpendicular to the sensor position. With further increase in  $\phi_y$  up to  $90^\circ$ , the main contributions come from the specular reflection of the target and the maximum detected power due to the RCS of the target is recorded.

The EM wave power flow at  $f_c$  represented by the power density given in VA/m<sup>2</sup> for  $\phi_y = 0^\circ, 5^\circ$  and  $45^\circ$  is shown in Fig. 4-7 (left, middle and right), respectively. It shows the flow of power at  $f_c$  in the boundary box. It can be seen that in the case of SDR for  $\phi_y = 0^\circ$ , EM waves do not penetrate the target and therefore cannot excite the brick 3. With a rotational shift  $\phi_y \neq 0^\circ$ , a small and large area of brick 3 is excited in case of  $\phi_y = 5^\circ$  and  $\phi_y = 45^\circ$ , respectively.

In evaluating the imaging with DR, the objective is to have well-received power, and detailed and accurate information about the target. Based on the obtained simulation results, the best-suited range of  $\phi_y$  for DR is from  $35^\circ$  to  $55^\circ$ .

### 4.1.2 Measurement Analysis of Imaging Plane with SDR and DR

In this section, a testbed has been set up to validate the simulation results from the previous section with measurements. The sketch and a picture of the testbed are shown in Fig. 4-8 and Fig. 4-9, respectively. The imaging targets are two cylindrical metal post (M-P) P1 and P2, with a diameter of around 13 mm, and height 15.5 cm and 11.5 cm, respectively, as shown in Fig. 4-8. The posts also consist of a small screw at the top of the cliff 0.5 cm, as shown in Fig. 4-8 and Fig. 4-9. Similar to the simulations target,

## 4.1 Planar Aperture 2D Imaging Configurations

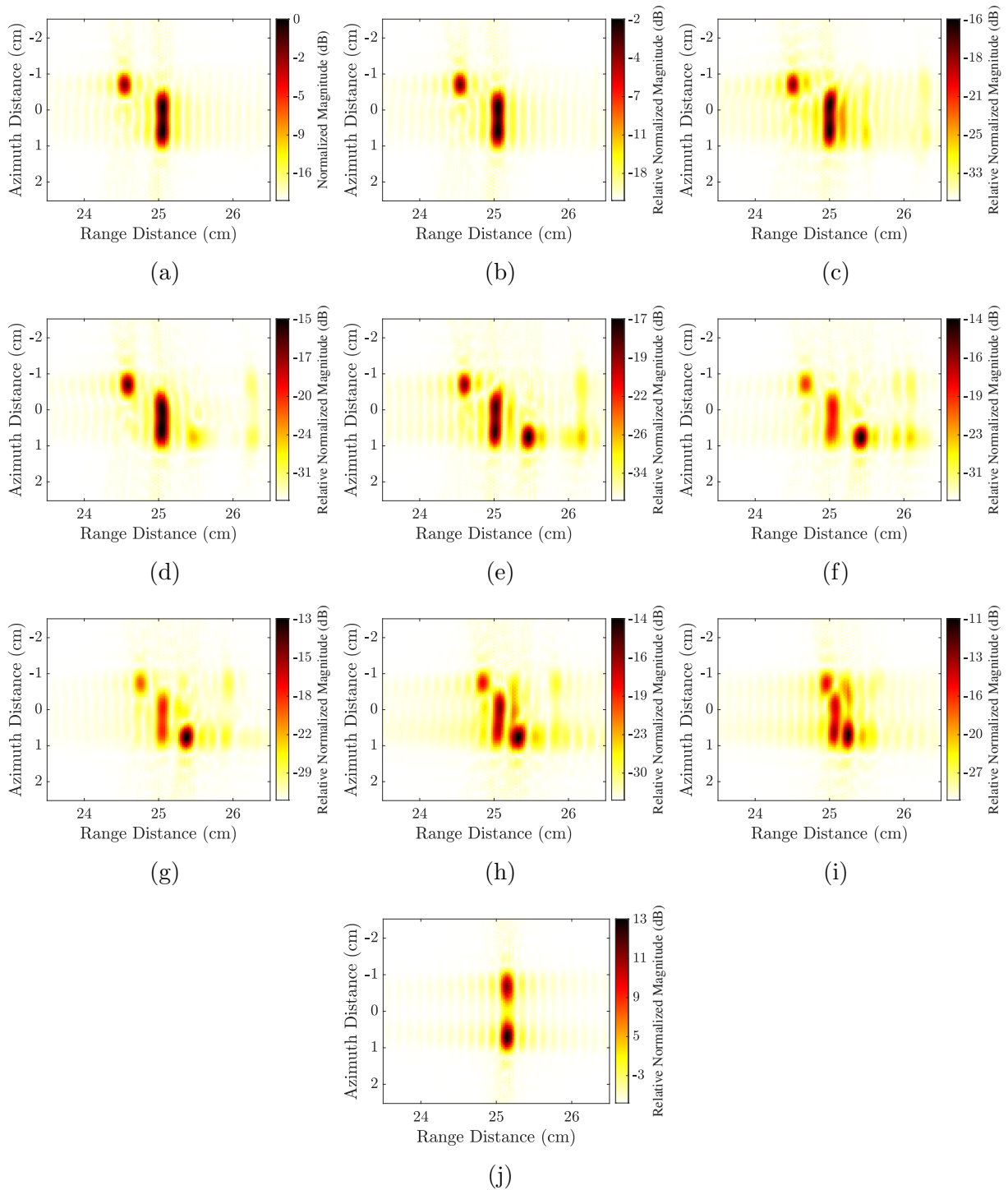


Figure 4-6: Resulting SAR images based on simulations for different  $\phi_y =$  (a)  $0^\circ$ , (b)  $5^\circ$ , (c)  $15^\circ$ , (d)  $25^\circ$ , (e)  $35^\circ$ , (f)  $45^\circ$ , (g)  $55^\circ$ , (h)  $65^\circ$ , (i)  $75^\circ$  and (j)  $90^\circ$ .

posts can be considered an object composed of two Bricks (P1 and P2). These posts are mounted next to each other with a spacing of  $\delta_d = 5$  mm. In the SDR configuration, it is expected that P2 will not be observable. The objective is to investigate the optimum range of  $\phi_y$  in DR configuration, where the complete target shape is obtainable, based

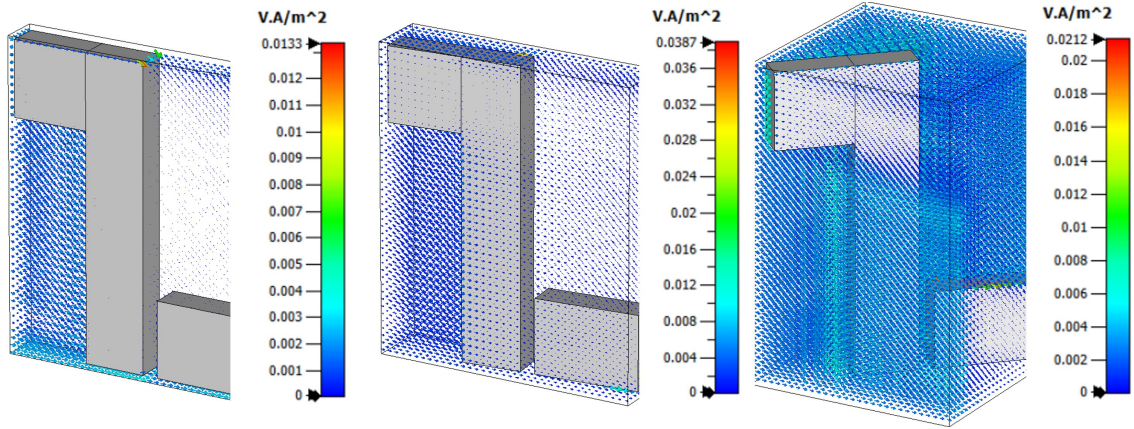


Figure 4-7: Power flow at  $f_c$ :  $\phi_y =$  (left)  $0^\circ$ , (middle)  $5^\circ$ , and (right)  $45^\circ$ .

on the measurements. The measurement setup consists of a Rohde and Schwarz ZVA67

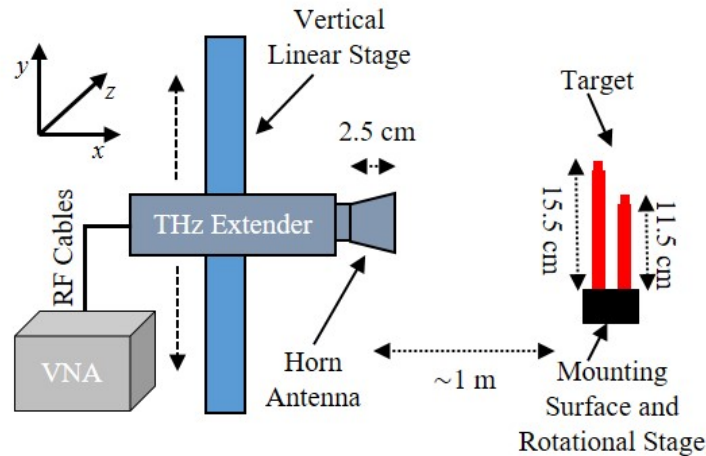


Figure 4-8: Measurement sketch.

VNA, a THz frequency extender (Rohde and Schwarz ZC330), and a horn antenna with a gain of around 24.8 dB, which is connected to the extender waveguide flange. To form the synthetic aperture, the extender is mounted on a vertical stage, as shown in Fig. 4-8 and Fig. 4-9, and moved along the  $y$ -axis with a step size of  $\Delta u = 1$  mm. The target is mounted on a rotation stage to provide  $\phi_y$  along the  $y$ -axis. In the measurement,  $S_{11}$  reflection coefficients are measured and the reference range is  $R_{\text{ref}} \approx 1$  m. The base power from the VNA port 1 is around  $-10$  dBm. For the measurements in this chapter, the IF filter  $B_w = 10$  KHz is selected, and the associated noise floor is  $\sim -100$  dB. The SAR parameters are summarized in Table 4-2 and the measurement results are provided in Fig. 4-10.

For  $\phi_y = 0^\circ$ , the resulting image is shown in Fig. 4-10.a. The post P1 is well focused, and even the tiny screw on the top is visible, but no information about P2 is available as P2 is perfectly aligned vertically to P1. Therefore, it has not been illuminated due to the non-penetration of EM waves through P1. It is similar to the simulation result of Fig. 4-

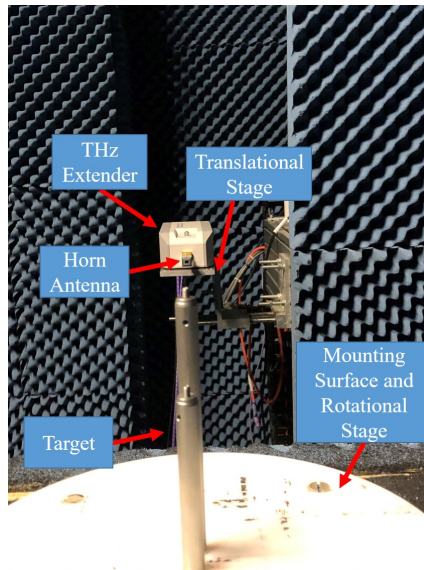


Figure 4-9: Picture of testbed.

Table 4-2: Measurement parameters for THz SAR imaging.

Symbol	Parameter	Value
$f_c$	center frequency	275 GHz
$B_w$	bandwidth	110 GHz
$L_r$	antenna length	6 mm
$L_s$	synthetic aperture length	16.8 cm
$r_x$	range resolution	1.36 mm
$r_y$	azimuth resolution	3 mm
$R_{\text{ref}}$	reference range	1 m
$\Delta u$	step size	1 mm
$N$	number of azimuth positions	169
$N_f$	number of frequency points	3001
$P_T$	base transmit power	-10 dBm

6.a, where brick 3 is not observed due to the same reason. To investigate further, the imaging results with  $\phi_y = 5^\circ$  and  $15^\circ$  are shown in Fig. 4-10.b and c, respectively. Still, P2 is not observable. Moreover, due to the cylindrical shape of the target, the received power has not been reduced due to the rotation, and the same can be seen in the relative normalized magnitude scale. In simulation results, brick 3 starts appearing for the case of  $\phi_y = 25^\circ$ , but it is not well focused, and the same has been observed in the measurement results shown in Fig. 4-10.d. For the case of  $\phi_y = 35^\circ$ ,  $45^\circ$  and  $55^\circ$ , the resulting SAR images are shown in Fig. 4-10.e, f, and g, respectively. In these cases, both the posts P1 and P2 are very well focused, and also the relative magnitude in comparison to  $\phi_y = 0^\circ$  is higher due to the captured reflection from both posts.

However, some additional artifacts are also observed due to the bouncing of EM

waves between the posts. With the further increase in the  $\phi_y$ , the image starts defocusing and introduces additional artifacts, which can be seen in the resulting SAR images for  $\phi_y = 65^\circ, 75^\circ$  and  $90^\circ$  shown in Fig. 4-10. h, i and j, respectively.

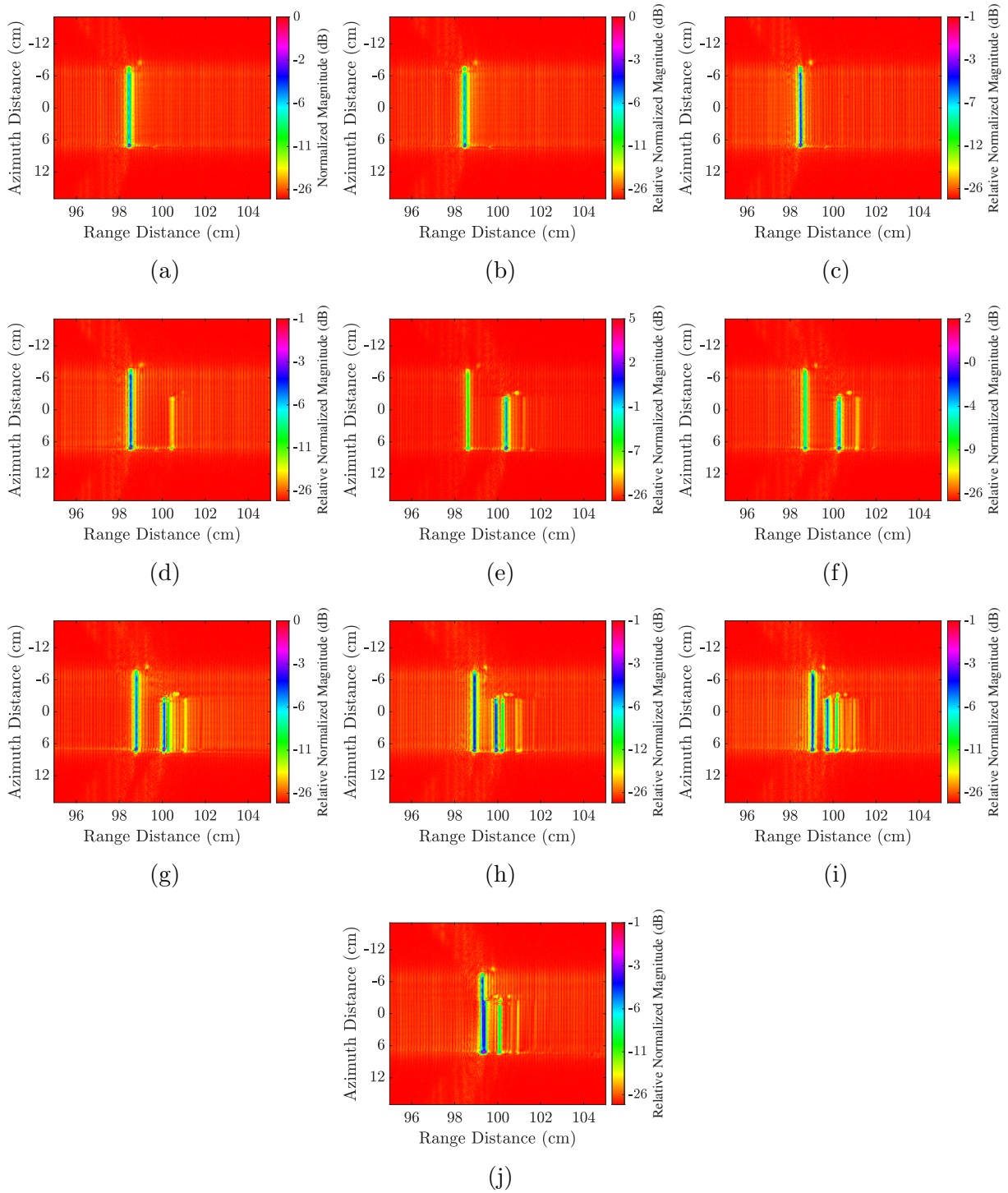


Figure 4-10: SAR images based on measurements for different  $\phi_y =$  (a)  $0^\circ$ , (b)  $5^\circ$ , (c)  $15^\circ$ , (d)  $25^\circ$ , (e)  $35^\circ$ , (f)  $45^\circ$ , (g)  $55^\circ$ , (h)  $65^\circ$ , (i)  $75^\circ$  and (j)  $90^\circ$ .

To summarize, the presented measurement results are in good compliance with simulation results and validate the imaging plane's concept for SDR and DR configuration and the optimum range of DR configuration that is  $35^\circ \leq \phi_y \leq 55^\circ$ .

## 4.2 Imaging of Indoor Objects

The findings from the previous section regarding the imaging plane for SDR and DR configuration are used in this section for 2D imaging of indoor objects. Additionally, the previous results show that the optimum range for the rotational shift is  $35^\circ \leq \phi_y \leq 55^\circ$ . Therefore, imaging in DR configuration is realized with the  $\phi_y$  specified in this range.

The standard indoor materials and their corresponding objects considered for imaging are summarized in Table 4-3. The reference range is also provided in this table. Based on the range,  $L_s \approx \lambda_c R_{\text{ref}}/L_r$  can be calculated, and all the other measurement parameters are the same as the ones given in Table 4-2. The reference range is considered selected in accordance with materials, and the objective of the 2D imaging range in this chapter of  $\geq 1$  m is fulfilled in all the cases.

Table 4-3: Imaging material, object and reference range.

Material	Object	$R_{\text{ref}}$ (m)
Plastic	Water bottle	1.5
Plastic	Human face model 1	1.4
Plastic	Electrical wire mount	1.2
Glass	Water bottle	1.8
Metal	Compass	1.05
Foam	Human face model 2	1.15
Foam with	Human face model 3	2
Metallic Paint		
Wood	Box	2

Fig. 4-11.a shows the plastic bottle (P-B) optical picture, and the generated 2D SAR image is shown in Fig. 4-11.b at  $R_{\text{ref}} \approx 1.5$  m under SDR configuration. The results show that the bottle shape is well observable. The bottle is composed of a plastic body in white color and a closing lid in blue color as shown in Fig. 4-11.a. The lid is rougher than the body and therefore provides higher scattering than the body. This is also seen in the generated SAR image, where the body is well focused, and also the magnitude is higher than that of the lid. The additional artifacts along the  $y$ -axis are observed due to the symmetric circular shape and the bouncing of EM waves inside the bottle. In Fig. 4-11.c, the picture of the glass bottle (G-B) is shown, and the corresponding generated SAR image at  $R_{\text{ref}} \approx 1.8$  m is shown in Fig. 4-11.d. In the resulting image, the front and back surface of the bottle body is well observable. The EM wave penetrates the glass, and this results in absorption losses. Due to the absorption and change of refractive index, the magnitude of the back part of the bottle in the SAR image is comparatively less than the

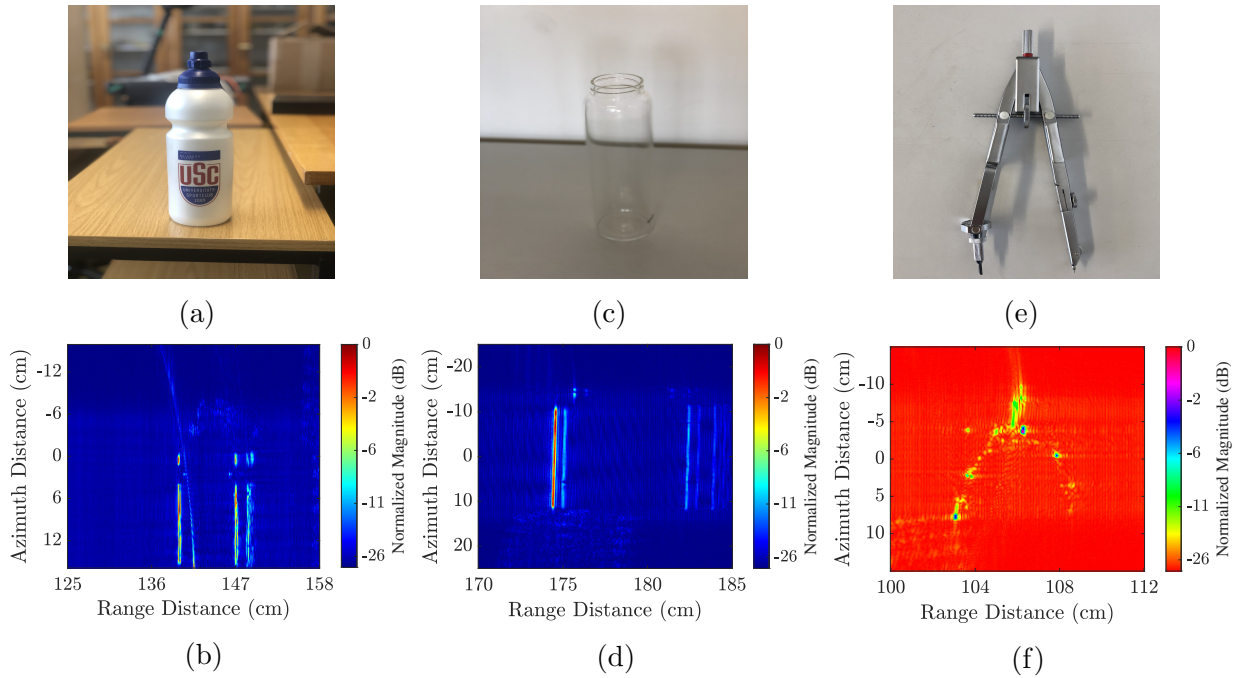


Figure 4-11: Pictures (a-c), and SAR image (d-f) of P-B, G-B and M-C for the case of SDR with  $\phi_y = 0^\circ$ .

front surface. Moreover, similar to the artifacts in Fig. 4-11.b, they are also observed in this image due to the same symmetric circular shape and bouncing of waves.

Furthermore, a metallic target considered for imaging is shown in Fig. 4-11.e. It is a metallic compass (M-C). The resulting SAR image is shown in Fig. 4-11.f, and the shape is well observable. Even tiny components of the compass, like a screw or tip, in the beginning, are distinguishable.

So-far the imaging of P-B, G-B, and M-C is performed in SDR configuration. The reason is self-evident that with these objects, the imaging surface along  $x - y$  provides more information about the object's shape and structure. As also defined before, the choice of configuration depends on the interested imaging plane. However, to validate this theory, two objects for imaging have been selected, where one of them provides more information about the object shape only in the DR configuration, and the other provides various useful information in both SDR and DR configurations.

For DR configuration, the first object is a wooden box (W-B) shown in Fig. 4-12.a. It is mounted for imaging precisely in similar to as shown in the figure. The EM waves propagate along the  $x$ -axis, and transceiver movement is along the  $y$ -axis. The resulting SAR image of W-B in SDR configuration is shown in Fig. 4-12.b. It can be seen that no information about the box shape is obtainable. In the resulting image, only the first interacted surface of the box is observed with high magnitude, as the EM wave penetration into the wood results in high absorption losses. Therefore, the reflections from inside the box are not detected. However, in the DR configuration with  $\phi_y = 40^\circ$ , the resulting SAR image is shown in Fig. 4-12.c, and the rectangular object shape is well observable.

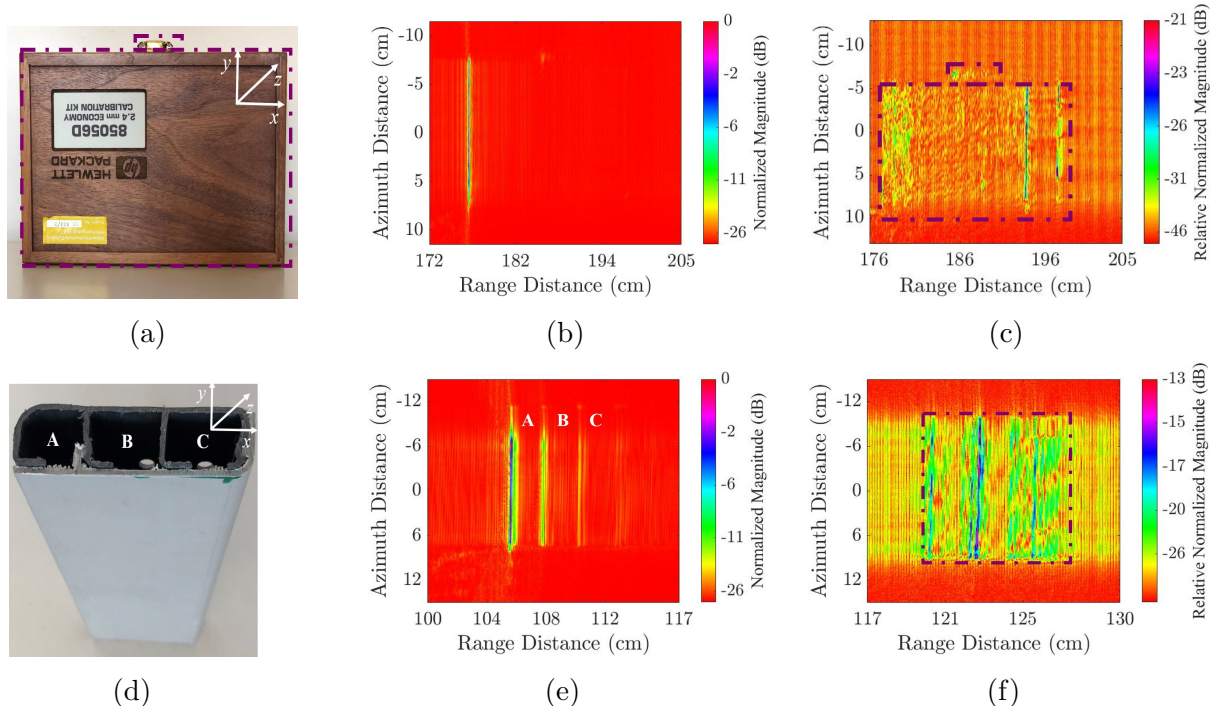


Figure 4-12: W-B (a) picture, and SAR image for (b) SDR ( $\phi_y = 0^\circ$ ) and (c) DR ( $\phi_y = 40^\circ$ ) configurations; P-EWM (d) picture and SAR images for (e) SDR ( $\phi_y = 0^\circ$ ) and (f) DR ( $\phi_y = 40^\circ$ ) configurations.

Even the metal clip on the top of the box is also well focused. In this case, only DR configuration provides valuable information about the target shape.

In the second case, the object is a plastic electrical wire mount (P-EWM) shown in Fig. 4-12.d. For imaging, it is mounted in similar geometry to W-B. The generated SAR image in SDR configuration is shown in Fig. 4-12.e. The EWM consists of 3 holes or spacing for wires marked with letters A, B, and C in Fig. 4-12.d and the interfaces between these holes. In the resulting SAR images, the holes and interfaces are well observable, but the object's rectangular shape cannot be observed in this configuration. By increasing the angle to  $\phi_y = 40^\circ$  in the DR configuration, the rectangular shape of the P-EWM can now be seen as shown Fig. 4-12.f. It is the shape of the backside of the P-EWM. It is an uneven surface, and the same has been observed in the resulting image. In this case, both the configurations are applicable as it offers various information about the object.

It can be concluded that SDR and DR provide look-through and surface imaging, respectively.

## 4.3 Analysis

This section presents the method of geometric parameter extraction from the resulting SAR image, and evaluates the impact of surface roughness and bandwidth at THz imaging.

### 4.3.1 Geometric Parameters Extraction

SAR images can be further analyzed for various geometric properties such as shape and dimensions extraction of imaging objects. This section focuses on the extraction of length  $L$ , height  $H$ , and the surface thickness  $T$  of the first material illuminated of the object. An object is generally composed of heterogeneous materials. To be precise, the first material is defined here as the surface of the illuminated object with a refractive index  $n_2$  that is interacted with incident EM wave, where the medium before this object is air with the refractive index  $n_1 = 1$ .

Based on eq. (2-16), the resulting 2D SAR image pixels are defined by the elements of the 2D matrix  $\mathbf{I}_{A \times B}$ , where A is the number of rows, and B is the number of columns. The parameters  $L$  and  $H$  can be roughly calculated directly from the SAR image. Still, to find precise estimations,  $\mathbf{I}$  has to be processed further to create a range and azimuth vector. Let's define  $\mathbf{G} = |\mathbf{I}|$  and the azimuth vector can be determined by

$$v_{az}(i) = \max(\text{row}_i \mathbf{G}), \quad (4-2)$$

where  $\text{row}_i \mathbf{G}$  is a row vector of  $\mathbf{G}$  with the length B, and  $i \in (1, B)$ . The estimated azimuth vector from the SAR image of the glass bottle shown in Fig. 4-11.c is shown in Fig. 4-13.a. Based on it,  $H$  can be retrieved. The first reflection point is defined as  $x_{az,1}$  and the last reflection point from the target along azimuth is defined by  $x_{az,2}$  and therefore,  $H = x_{az,2} - x_{az,1}$ . Similarly, the range vector can be defined by

$$v_r(j) = \max(\text{col}_j \mathbf{G}), \quad (4-3)$$

where  $\text{col}_j \mathbf{G}$  is a column vector of  $\mathbf{G}$  with the length A, and  $j \in (1, A)$ . This vector provides the estimations of  $L$  and  $T$ . The calculated  $v_r$  from the SAR image of glass bottle shown in Fig. 4-11.c is given in Fig. 4-13.b. Here,  $L$  can be calculated similar to  $H$  i.e.  $L = x_{r,3} - x_{r,1}$ , where  $x_{r,1}$  and  $x_{r,3}$  are the first and last reflection point from the target, respectively. Furthermore,  $T = x_{r,2} - x_{r,1}$  is the difference between the first  $x_{r,1}$  and second peak  $x_{r,2}$ .

The calculation of  $T$  can be explained by considering a refractive index of the glass (material of bottle) as  $n_2$  and air as  $n_1$  and generally,  $n_2 > n_1$ . The change of  $n$  causes reflection. The first reflection point  $x_{r,1}$  occurs when EM wave propagating in medium  $n_1$  is incident on the surface with  $n_2$ . So, in this case, the EM wave is incident on the glass. The second reflection point  $x_{r,2}$  takes place at the interface where the EM wave propagation medium changes from  $n_2$  to  $n_1$ . The duration of propagation in the medium with  $n_2$  depends on the glass  $T$ . In general, to precisely evaluate  $T$ , the refraction angle needs to be known and also the change of speed of EM wave in the glass. This approach requires the advance knowledge of the material  $n_2 = \sqrt{\epsilon_r}$ , where  $\epsilon_r$  is the relative permittivity of the material, and it varies with the frequency. This section focuses on the rough thickness evaluation without any prior information about the imaging object material  $n_2$ . Furthermore, the estimated  $T$  can be further validated from Fig. 4-13.b, wherein the highlighted region in magenta color, the same two peaks appeared due to the same homogeneous material of the bottle in the beginning and at the end.

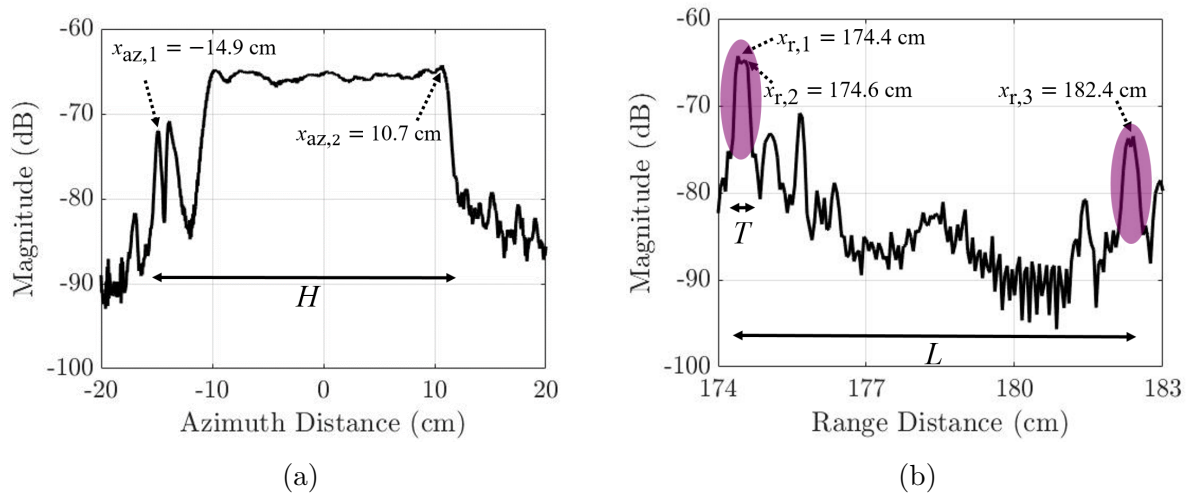


Figure 4-13: (a) Azimuth and (b) range vector of G-B SAR image to estimate  $L$ ,  $H$  and  $T$ .

Based on this approach of calculating  $L$ ,  $H$ , and  $T$ , the estimated parameters for various objects are summarized in Table 4-4. Only in the case of a wooden box,  $T$  can not be assessed because the box is imaged in DR configuration, which corresponds to surface scanning. The  $T$  can only be evaluated in the look-through SDR configuration. To make a comparative analysis with the real and extracted parameters,  $L$  and  $H$  of the object are measured with a measuring scale. Although it is susceptible to scale and human errors, it is given here only for reference. Moreover, it has to be considered that some parts of the objects are not perfectly focused due to heterogeneous material, bouncing EM waves, and low RCS, such as the P-B closing lid, which causes certain deviations. However, the estimations are close approximations to the real values and provide the accuracy based on the spatial resolution.

Table 4-4: Comparison of real and extracted geometric parameters of objects.

Object	Real		Extracted		
	$L_R$ (cm)	$H_R$ (cm)	$L$ (cm)	$H$ (cm)	$T$ (mm)
Plastic bottle	7.47	24.4	7.6	24	2
Glass bottle	8	26.6	8	25.6	2
EWM	7	18.3	7.2	18.6	2
Wooden box	22.3	15.9	21	15.65	-

### 4.3.2 Comparison of Small and Large Bandwidth Imaging

In this section three SAR systems with different  $f_c$  and  $B_w$  are studied. These systems are set up with  $f_c = 230$  GHz, 245 GHz, and 275 GHz and associated  $B_w = 20$ GHz, 50 GHz and 110 GHz, respectively. This section presents the comparison between these systems

w.r.t. the focused SAR image quality associated with the spatial resolution.

The picture of the targets is shown in Fig. 4-14. As shown in the figure, three different-sized metal screws are taken as targets and mounted on white foam. The targets are placed at  $R_{\text{ref}} \approx 39$  cm. The measurement parameters of the three configurations are summarized in Table 4-5.

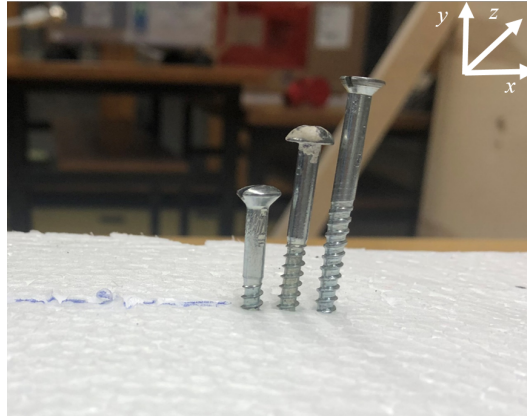


Figure 4-14: Picture of metal screws.

Table 4-5: System parameters for comparison analysis.

Symbol	Parameter	Configuration 1	Configuration 2	Configuration 3
$f_c$	center frequency	230 GHz	245 GHz	275 GHz
$B_w$	bandwidth	20 GHz	50 GHz	110 GHz
$r_x$	range resolution	7.5 mm	3 mm	1.36 mm
$L_s$	synthetic aperture length	8.7 cm	8.7 cm	8.7 cm
$r_y$	azimuth resolution	3 mm	3 mm	3 mm
$N_f$	no. of frequency points	201	501	1101

The generated results are summarized in Fig. 4-15. For configuration 1, the focused SAR image is shown in Fig. 4-15.a. All the three targets are visible, but their separation is difficult to distinguish, and the pixel spread is large. Further, Fig. 4-15.b shows the focused image for configuration 2. In this, the objects are distinguishable, and the image is also much sharper that reveals more accurate information about the targets, such as height, in comparison to configuration 1. Lastly, the result for configuration 3 is shown in Fig. 4-15.c. Due to the highest resolution of the other two configurations, the image offers very sharp visibility of target edges and the lowest pixel spread. Compared to the other two, it provides better image quality in terms of target shape and dimensions. Moreover, it is also observed that the backscattered power is highest in configuration 3 because of the smallest beamwidth.

To summarize, it can be concluded that image quality or focusing significantly improves with the increase in bandwidth, but the resulting image with configuration 2 is also in good compliance.

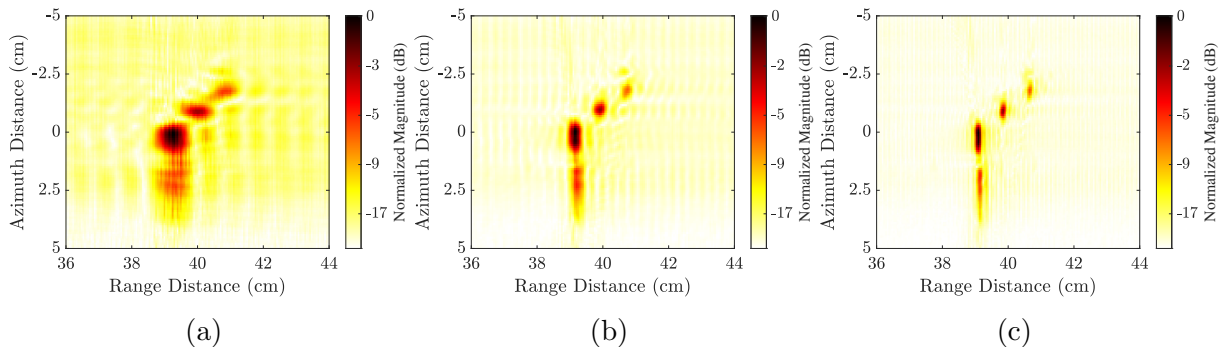


Figure 4-15: SAR image  $B_w =$  (a) 20 GHz, (b) 50 GHz and (c) 110 GHz.

### 4.3.3 Impact of Surface Roughness

This section evaluates the impact of surface roughness on the THz SAR imaging. Based on eq. (4-1), a surface is considered rough at 330 GHz with  $\theta_i = 0^\circ$ , if  $h$  is  $\geq 28.4 \mu\text{m}$ , which is difficult to measure or require special measurement equipment such as a profilometer. Moreover, the irregularity can also be measured over 2D or 3D surface [72]. This section focuses not on considering the materials based on different  $h$  but based on relative roughness to study the impact of roughness in the THz SAR imaging. In addition to the roughness impact analysis and the consideration of this chapter's objective, i.e., high-resolution imaging of an indoor environment, the focus is also on the THz imaging of human face models. This provides insight information on the possible achievement of the high-resolution human face imaging at the THz.

Therefore, in this chapter, three human face mannequins are selected that differ in surface roughness. The relative surface roughness is defined here as smoothest (ST), intermediate between smooth-rough (SR), and roughest (RT). Fig. 4-16 shows the picture of all the three human face mannequins, where Fig. 4-16.a defined as ST is built-up of plastic material and Fig. 4-16.b is SR made up of foam material. Lastly Fig. 4-16.c is RT made of foam material, but painted with metallic paint to make it rough. The imaging is performed with the same parameters defined in Table 4-2, except  $L_s$  which can be calculated based on  $R_{\text{ref}}$  defined in Table 4-3. The SAR image of the ST mannequin is shown in Fig. 4-16.d. Here, the complete face shape is well observable, and also the body parts such as nose, neck, eyes are distinguishable. However, the forehead is not well focused due to the curvature of this part in the mannequin. Therefore, the reflected waves, mostly specular due to smoothness, go away from the transceiver.

Further, Fig. 4-16.e shows the resulting SAR image of the SR mannequin. The shape of the face, including the forehead, is observable. However, the body parts are indistinguishable, like the one given in Fig. 4-16.d. It is not due to the surface roughness but actually due to the foam material. The backscattered energy, in this case, is deficient compared to the plastic material. Therefore, to increase the backscattering with the same material, as mentioned earlier, it is painted with metallic paint, and the resulting SAR image is shown in Fig. 4-16.f. The results demonstrate a significant improvement in the image quality. The complete face shape, including neck and forehead, are observable. The

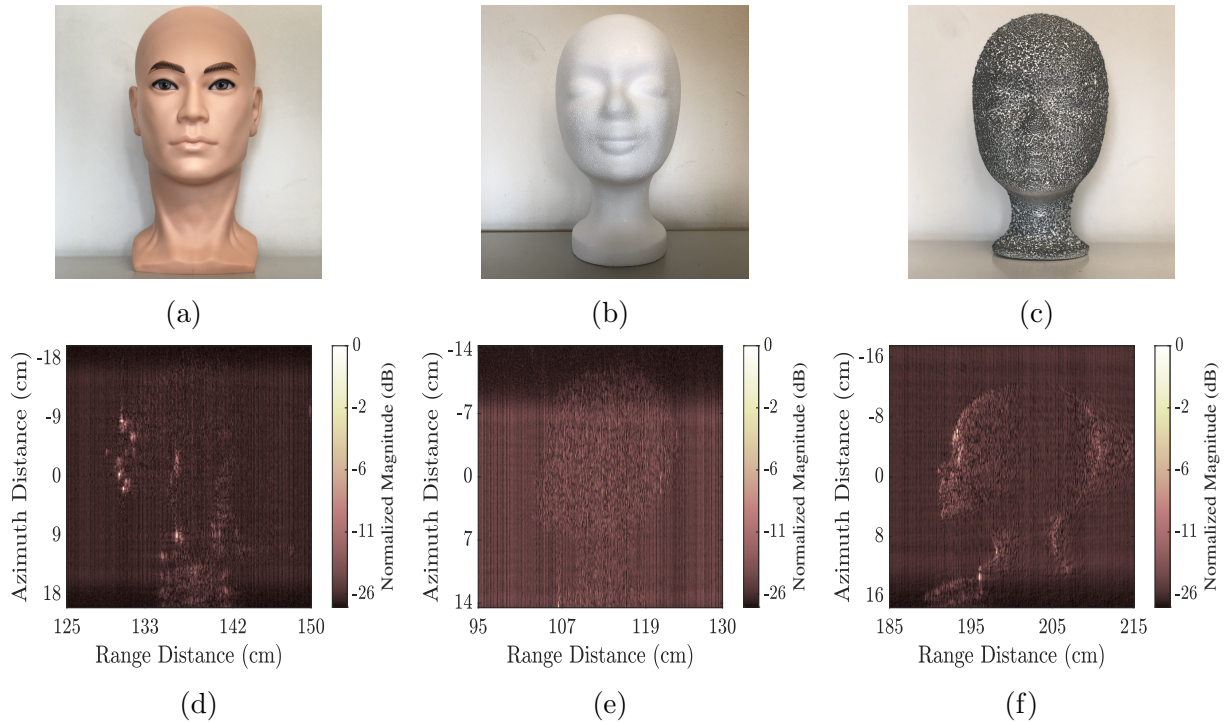


Figure 4-16: Picture (a-c), and SAR image (d-f) of ST, SR and RT human face mannequins.

body parts of the face are also sharply visible.

It has been seen that the higher the roughness of the material is, the more information about the object can be revealed. The EM waves can be captured from the entire illuminated surface of the material, not the case with smooth objects such as the curved face region. Additionally, this section's objective is not to compare the results with a real human face that consists of human tissues but to provide a glimpse of the possibility of high-resolution human face sensing at the THz spectrum. In general, the human face skin surface is also rough, and roughness can range up to sub-mm based on the measurement results, and methods [73], [74]. It increases with the facial hairs and varies with the nature of the skin [75].

## 4.4 Concealed and Hidden Object Imaging

So-far the chapter evaluated the high-resolution imaging in free space without any obstruction. Another important application of SAR is the concealed and hidden object sensing, where this technique dominates in comparison to IR and visible sensors. For this application, the IR and visible spectrum lacks in providing any relevant information about the target. Therefore, this section aims to evaluate the high-resolution THz SAR mapping of concealed/hidden objects. The evaluation is significantly relevant at THz because of the sub-mm wavelength and EM waves experience high penetration losses in addition to the high atmospheric attenuation and FSPL. Moreover, this application is look-through

imaging, and therefore, the imaging will be performed in SDR configuration. The system parameters will be the same as defined in Table 4-2 except  $R_{\text{ref}}$  and correspondingly  $L_s$ . Four cases of concealed/hidden object imaging are considered.

#### 4.4.1 Metallic Structure in Cardboard Box

In this case, a metallic structure as an imaging target is packed inside a cardboard box. The front view with the opened and sealed box is shown in Fig. 4-17.a and b, respectively. The metallic object surface is rectangular. It consists of a metal plate at the back denoted by M1, and additional 20 metal plates denoted by M2 are attached to the M1 with inter-spacing of 2 cm between each other. The box is placed at  $R_{\text{ref}} \approx 1$  m, and the resulting SAR image is shown in Fig. 4-17.c. The box surface can be seen at a range distance  $R \approx 1$  m and the metallic structure at  $R \approx 1.1$  m. In the SAR image reconstruction algorithm, the imaging plane is truncated by the time-gating window to focus mainly on the target. The resulting focused SAR image of the metallic object is shown in Fig. 4-17.d. The magnitude is relatively normalized in respect to the reflection from the box surface. So, the box surface results in attenuation of  $\sim 8$  dB. In the resulting image, 20 M2 metal plates and M1 are well-observed.

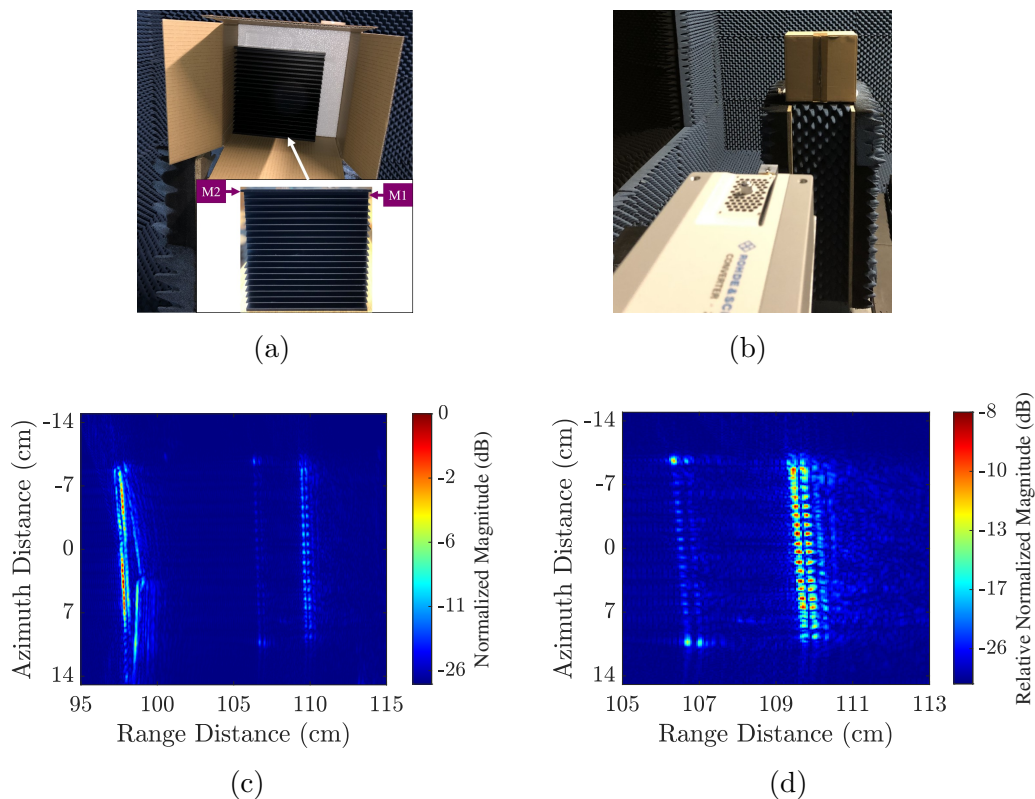


Figure 4-17: Picture of (a) open and (b) sealed box with target inside the box, and (c) complete (box+target) and (d) truncated (target in focus) SAR image.

#### 4.4.2 Small Components covered with Foam in Plastic Box

In this case, three small metallic components of height  $\approx 2$  cm are packed inside a plastic box. The box also consists of two foam layers in the front and back of the components. The opened box picture is shown in Fig. 4-18.a, and components are labeled as 1, 2, and 3. Fig. 4-18.b. shows the closed box picture, which is considered for imaging. The imaging is performed at  $R_{\text{ref}} \approx 1.1$  m, and the resulting SAR image is shown in Fig. 4-18.c.

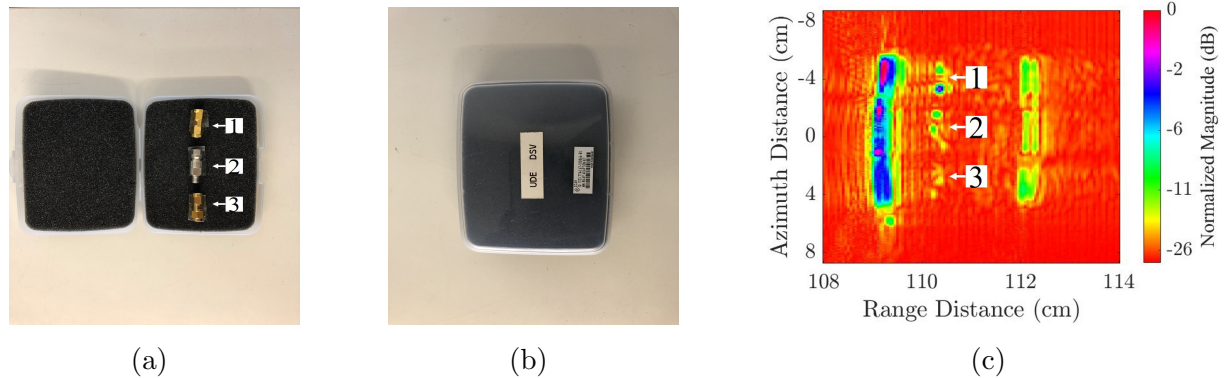


Figure 4-18: Picture of (a) open and (b) closed box with components inside the box, and (c) SAR image of mapped box and inside components.

All the three components are observable and distinguishable from each other. The image also shows these components positions inside the box based on the offered spatial resolution defined in Table 4-2. In addition to the box front cover at  $R \approx 1.09$  m, the rear cover is also mapped and visible in the resulting image at  $R \approx 1.12$  m.

#### 4.4.3 Electrical Cables in Plastic Mount

This section focuses on the imaging of the electrical cables inside the mount. The look-through imaging result of empty P-EWM is already shown in Fig. 4-12.e. In this case, three electrical wires of yellow, black, and white color shown in Fig. 4-19.a are mounted in the P-EMW as shown in Fig. 4-19.b. The yellow cable is usually used in electrical installation for main supply and earthing, and black and white are coaxial cables generally used for television connection. These are ubiquitous cables found in the EWM in the indoor environment.

The resulting SAR image for a measurement performed at  $R_{\text{ref}} \approx 1.05$  m is shown in Fig. 4-19.c. Similarly to Fig. 4-12.e, all the three compartments A, B, and C are visible, but the electrical cable is only observed in A. To enhance the image similar to the previous method of truncating the imaging plane by the time window, the generated image is shown in Fig. 4-19.d. Here, the yellow cable in A is well observed, and even its position and twisting shape inside the mount is well definable. In B, minor information such as detecting the cable is obtainable, but the shape cannot be focused due to the low received energy. For the third black cable in C, no information can be obtained.

Moreover, it can be seen in the relative magnitude scale that the reflected power from the yellow cable is  $\sim 13$  dB less in comparison to the reflection from the first surface of the P-EWM. Also, to be noted here, the first yellow cable focusing is better in comparison to the other because the cables consist of metal wires inside the outer jacket. In addition to the attenuation from the mount, the transmitted and received energy to and from the second and third cable is further attenuated due to the cables in the front.

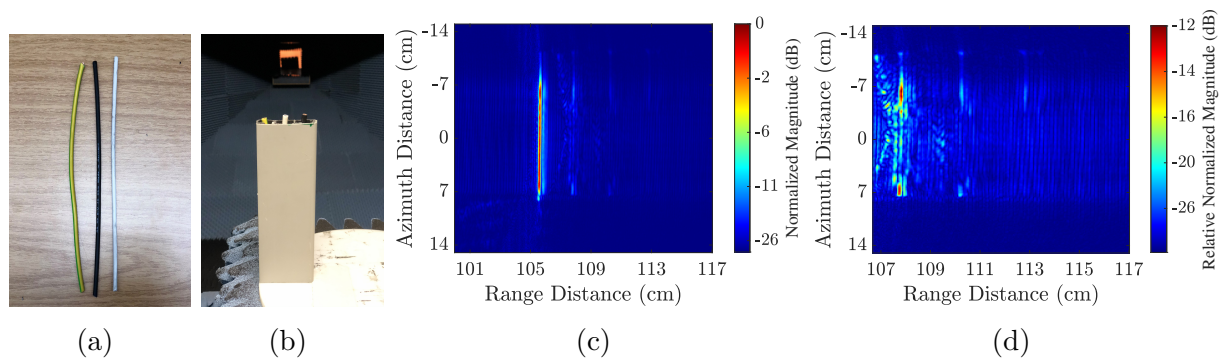


Figure 4-19: Picture of (a) cables, (b) cables inside vertical mounted P-EWM, and (c) complete and (d) truncated (cables in focus) SAR image.

Therefore, to map all the cables inside the mount, imaging should be performed in which the wires are not covering each other. This can be achieved by mounting the P-EWM in the horizontal configuration as shown in Fig. 4-20.a. This configuration in the 2D imaging is only suitable when the application only detects the number of cables inside the mount instead of mapping along height to obtain the shape and information related to the defects. The resulting SAR image is shown in Fig. 4-20.b. All cables are mapped perfectly, and the front surface of the mount appeared without any discontinuities, whereas the back surface of the P-EWM is not continuous because of the cables covering that specific area of the rear surface.

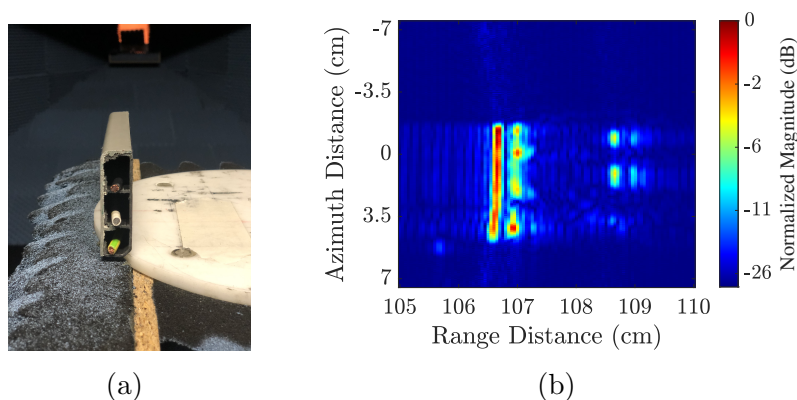


Figure 4-20: Picture (a) and (b) SAR image of cables inside horizontal mounted P-EWM

#### 4.4.4 Plastic Mount in Cardboard Box and Post behind the Box

This section focuses on the imaging of multiple concealed/hidden targets of interest of different materials. There are also multiple targets of interest in the previous three subsections, but they are close to the same material. Here, two targets P-EWM and M-P, of height 11.5 cm, are considered for imaging.

The P-EWM without cables is packed inside a cardboard box as shown in the opened box image in Fig. 4-21.a. The box is placed at  $R_{\text{ref}} \approx 1.6$  m and behind this box, the M-P is mounted at  $R_{\text{ref}} \approx 1.74$  m as shown in Fig. 4-21.b. The resulting SAR image is shown in Fig. 4-21.c. The front and back surface of the box and P-EWM are observable. Additionally, it can be seen that the box placement is not straight. It is in a slanting position, which can also be seen in Fig. 4-21.b. Moreover, the box is placed in this position to demonstrate the further application of SAR to define object placement, such as bending angle prediction with very high accuracy.

Furthermore, in the generated image, the P-EWM shape is not perfectly distinguishable, and additionally, there is no sufficient information about the M-P at  $R_{\text{ref}} \approx 1.74$  m. Therefore, firstly to enhance the EWM image, the imaging plane has been truncated, and the generated SAR image is shown in Fig. 4-21.d. The P-EWM and its shape are much better visible. Regarding the relative reflected power of P-EWM, the box surface only provides the attenuation of  $\sim 3$  dB as shown in the normalized magnitude scale. Further, to gain information about the post, the imaging plane is truncated close to the  $R_{\text{ref}}$  range of the M-P, and the resulting image is shown in Fig. 4-21.e. The metal post is observable but not entirely, and the relative magnitude difference to the box and P-EWM first surface is  $\sim -24$  dB and  $\sim -21$  dB, respectively. The M-P is of height 11.5 cm, and only  $\sim 2$  cm is observable. Only that specific part of the M-P is observed, which is not hidden by the P-EWM. The P-EWM offers very high attenuation. Therefore, the EM waves to the M-P is highly attenuated in the forward and return paths.

Moreover, the complete shape can be obtainable by either increasing the transmit power or improving the receiver sensitivity. The current system has  $P_{\text{T}} \approx -10$  dBm and receiver sensitivity defined by the noise floor is around  $-100$  dB. The increase in  $P_{\text{T}}$  has to deal with other challenges, and also increasing the receiver sensitivity at THz is still a major challenge to be addressed by the semiconductor industry. Nevertheless, this section evaluated THz waves penetration capabilities, and the finding reveals the spectrum at 300 GHz supports concealed and hidden object imaging. However, it is highly dependent on the type of material and its properties. In this chapter, the materials commonly found in the indoor environment, such as warehouses, logistics centers and residence places are considered.

## 4.5 Maximum Sensing Range

To provide a complete outlook of the 2D THz SAR imaging of indoor objects, it is relevant to define the maximum sensing range. Therefore, this section describes the maximum

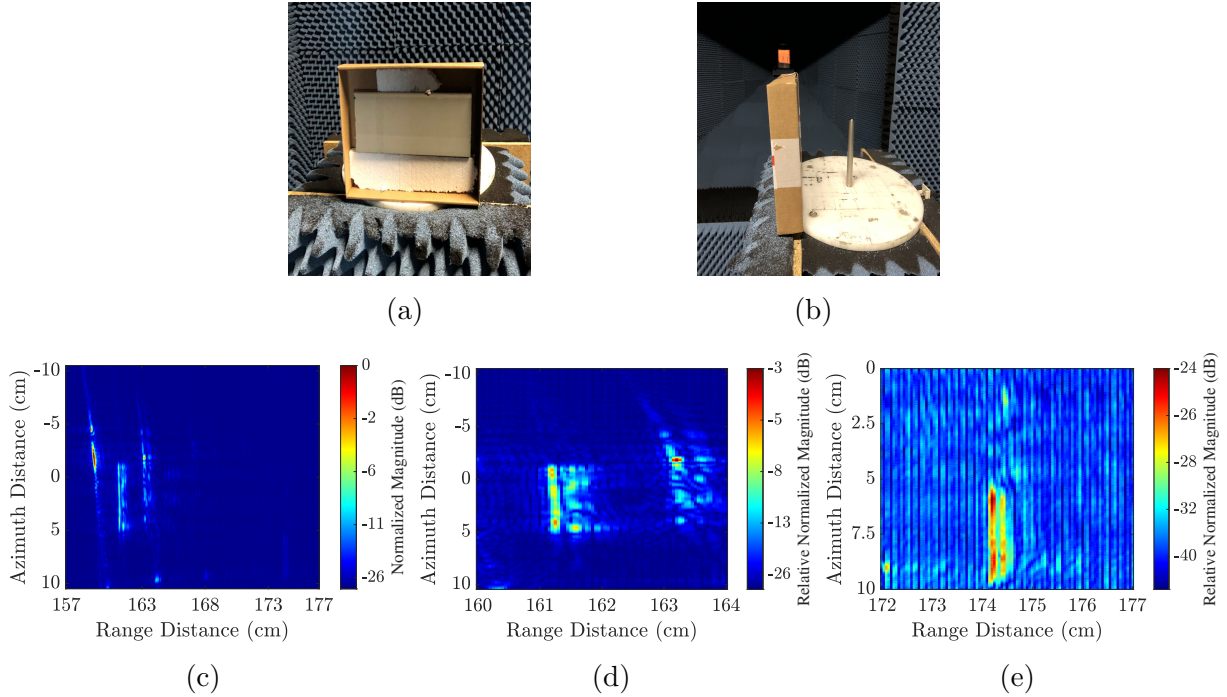


Figure 4-21: Picture of (a) open and (b) sealed box with mount inside the box and post behind the box, and (c) complete (box+mount+post), (d) truncated (mount in focus) and (e) truncated (post in focus) SAR image.

sensing range  $R_{\max}$  of the imaging targets of various materials presented so-far based on the receiver sensitivity and RCS. The ideology is that if the target can be sensed above the receiver noise floor, then their respective image can be generated using the SAR technique. Therefore, in this section, a methodology is first defined for predicting the  $R_{\max}$ , and then it is validated with measurement results.

### 4.5.1 Methodology

The radar equation provides the relation between the received power  $P_r$  and transmitted power  $P_t$ . In a monostatic system configuration and direct line of sight between the transceiver and the target, the radar equation defined in [65] is given by

$$P_r = \frac{P_t G^2 \lambda^2 \sigma}{(4\pi)^3 R^4}, \quad (4-4)$$

where  $G = G_t = G_r$  is the transceiver antenna gain,  $\sigma$  is the RCS, also defined as the backscattering coefficient, and  $R$  is the range between the transceiver antenna phase center and the target. Based on the minimum detectable received power  $P_{r,\min}$  and using (10), the maximum detectable range  $R_{\max}$  is

$$R_{\max} = \sqrt[4]{\frac{P_t G^2 \lambda^2 \sigma}{(4\pi)^3 P_{r,\min}}}. \quad (4-5)$$

For a particular  $\lambda$ , all the parameters in eq. (4-5) are constant except  $\sigma$  and eq. (4-5) can be further defined as

$$R_{\max}(\sigma) = \sqrt[4]{W\sigma}, \quad (4-6)$$

where  $W = \frac{G^2\lambda^2}{F_{\min}(4\pi)^3}$  and  $F_{\min} = P_{r,\min}/P_t$ . It shows that with a radar system with known  $W$ ,  $R_{\max}$  of the target can be calculated if  $\sigma$  is known.

In the presented VNA based testbed, a single port reflection measurement  $S_{11} = S$  is performed analogous to monostatic radar configuration with  $|S|^2 = P_r/P_t$ . Hence,  $F_{\min} = |S_{\min}|^2$  is defined by the noise floor of the VNA based on the IF filter  $B_w$ . Here,  $F_{\min} = -100$  dB, for the used VNA-based testbed with IF filter  $B_w = 10$  KHz [68]. For the calculation of  $W$ , the system parameters used for the imaging of the object are considered with  $G \approx 24.8$  dB, and  $0.9 \text{ mm} \leq \lambda \leq 1.4 \text{ mm}$ .

For estimating the maximum range with eq. (4-6), the RCS of various objects/targets  $\sigma_{\text{tgt}}$  is calculated. Due to the complexity of the objects and hardware modules,  $\sigma_{\text{tgt}}$  is calculated in respect to the reference object with known RCS  $\sigma_{\text{ref}}$ . The measured reflection coefficient for the reference target can be given as

$$|S_{\text{ref}}|^2 = \frac{P_{r,\text{ref}}}{P_{t,\text{ref}}} = \beta\sigma_{\text{ref}}, \quad (4-7)$$

where  $\beta = \frac{G^2\lambda^2}{(4\pi)^3R^4}$ . The target reflection coefficient for the same range and parameters is given by  $|S_{\text{tgt}}|^2 = \beta\sigma_{\text{tgt}}$ . Therefore,  $\sigma_{\text{tgt}}$  in logarithm scale can be given [76] as

$$\sigma_{\text{tgt}} = |S_{\text{tgt}}|^2 - |S_{\text{ref}}|^2 + \sigma_{\text{ref}}, \quad (4-8)$$

where,  $\beta$  is calculated for the whole frequency spectrum, and the reflection coefficient and RCS are in logarithm scale i.e. dBm and dBsm, respectively. To calculate,  $|S_{\text{ref}}|^2$ , a sphere of radius  $a = 15$  mm is considered with  $\sigma_{\text{ref}} = \pi a^2 = -31.51$  dBsm for the geometric optic region [76].

For the frequency spectrum of 220-330 GHz,  $\sigma_{\text{tgt}}$  of the different objects from Table 4-3 including roughest face mannequin (R-FM), rough-smooth face mannequin (RS-FM), and M-P of 11.5 cm height is calculated with eq. (4-8) at  $R = R_{\text{ref}} \approx 1.098$  m. Fig. 4-22.a and b show the frequency-domain response  $|S_{\text{ref}}|^2$  and  $|S_{\text{tgt,P-B}}|^2$  of the reference target sphere and P-B as one of the target, respectively. Similar measurements are performed with all other objects. Although, the RCS is frequency dependent, the mean value of  $\sigma_{\text{tgt}}$  in the frequency region 220-330 GHz is considered.

Fig. 4-23.a summarizes the calculated  $\sigma_{\text{tgt}}$  of all the considered objects. Based on the  $\sigma_{\text{tgt}}$  calculations and system parameters, the estimated  $R_{\max}$  is presented in Fig. 4-23.b using eq. (4-6). It can be seen that  $R_{\max} \propto \sigma_{\text{tgt}}$ .

## 4.5.2 Validation

This section focuses on the validation of the findings shown in Fig. 4-23 by predicting the reflection coefficient  $S_P = P_{r,P}/P_{t,P}$  in consideration of the presented  $\sigma_{\text{tgt}}$  and  $R_{\max}$ . The

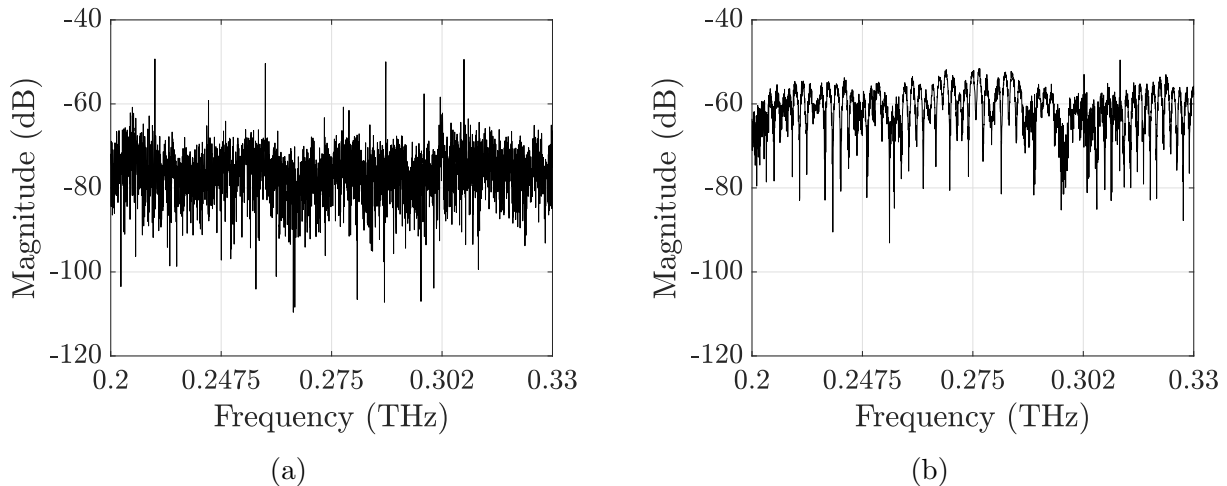
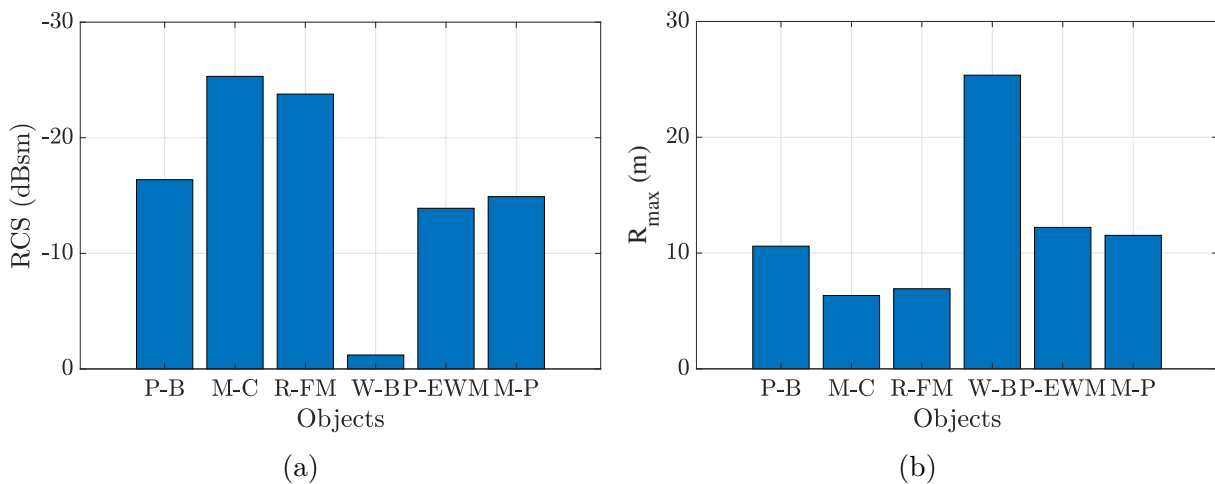


Figure 4-22: Reflection coefficient of (a) reference target and (b) plastic bottle.

Figure 4-23: Summary of (a) RCS and (b) maximum sensing range of different objects with  $F_{\min} = -100$  dB.

validation is being achieved by comparing the calculated  $S_P$  to the measured reflection coefficient  $S_M = |S|^2 = P_{r,M}/P_{t,M}$ .

Firstly, the measurements have been performed with the reference object metallic sphere (M-S) and target P-B for the frequency spectrum of 220-330 GHz at  $R \approx 1.098$  m. Fig. 4-24.a and b shows the time-domain response after inverse-Fourier transform of  $S_M$  for M-S and P-B, respectively. For comparison analysis, the first reflection's measured magnitude from the target is considered. Therefore, from Fig. 4-24.a and b the values for  $S_M$ , for M-S and P-S are  $S_{M,M-S} = -83.59$  dB and  $S_{M,P-B} = -65.97$  dB, respectively. Based on the system parameters  $G = 24.8$  dB,  $\lambda = 1.1$  mm, reference target  $\sigma_{\text{ref}} \approx 31.51$  dBsm, and calculated  $\sigma_{P-B} \approx 16.37$  dBsm from Fig. 4-23.a, the predicted reflection coefficient is  $S_{P,M-S} = -75.76$  dB and  $S_{P,P-B} = -60.62$  dB. The predicted coefficients  $S_{P,M-S}$  and  $S_{P,P-B}$  are in close approximation to the  $S_{M,M-S}$  and  $S_{M,P-B}$ . The difference could be appeared because of the change of  $G$  with frequency and due to the hardware

impairments such as losses at the waveguides connectors and antenna. Similarly, the

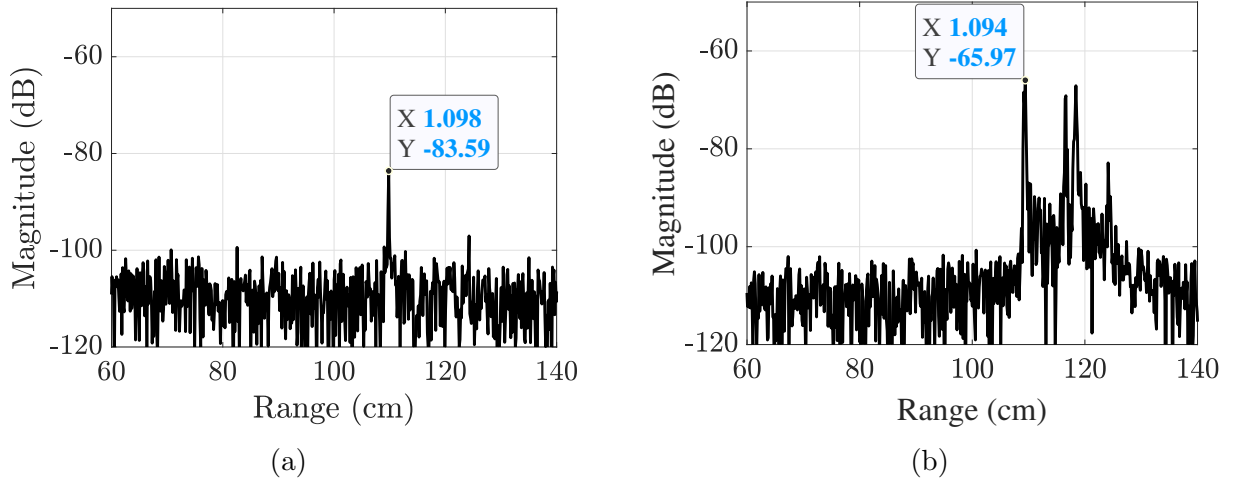


Figure 4-24: Time domain response of (a) reference target and (b) plastic bottle.

values for  $S_P$  and  $S_M$  have been calculated for all objects with  $\sigma_{\text{tgt}}$  defined in Fig. 4-23.a and are summarized in Fig. 4-25. For all the cases, the predicted coefficient  $S_P$  is in close approximation to measured coefficient  $S_M$  and hence, validates the findings of Section 4.5.1.

To further validate the presented approach, new measurements are conducted at different  $R$  with M-P and P-B as targets. The measurement setup is shown in Fig. 4-26, where the target as P-B is mounted on a cylindrical structure of a foam material.

The time-domain response from the two targets M-P and P-B, after channel normalization are shown in Fig. 4-27.a and b, respectively. The M-P is measured at  $R = 6.59$  m and P-B at  $R = 9.42$  m. From the figures, the values for the reflection coefficients of the two targets M-P and P-B are  $S_{M,M-P} = -95.45$  dB, and  $S_{M,P-B} = -98.35$  dB. Based on the similar approach as explained above, these measured values are compared to the predicted  $S_{P,M-P} \approx -90.3$  dB and  $S_{P,M-P} \approx -98$  dB. The results here also demonstrate

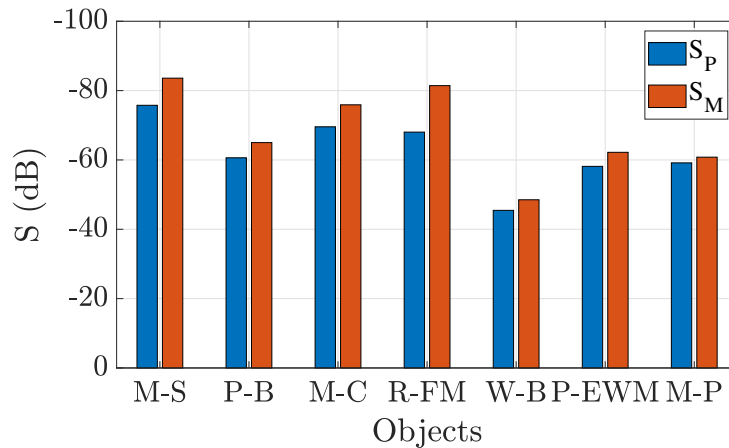


Figure 4-25:  $S_P$  and  $S_M$  of different objects at  $R \approx 1.098$  m.

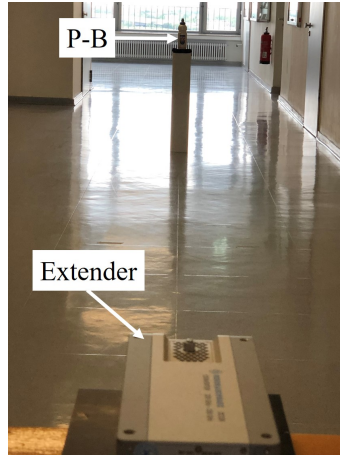


Figure 4-26: Testbed setup for long range sensing.

the close approximation between the predicted and measured coefficients.

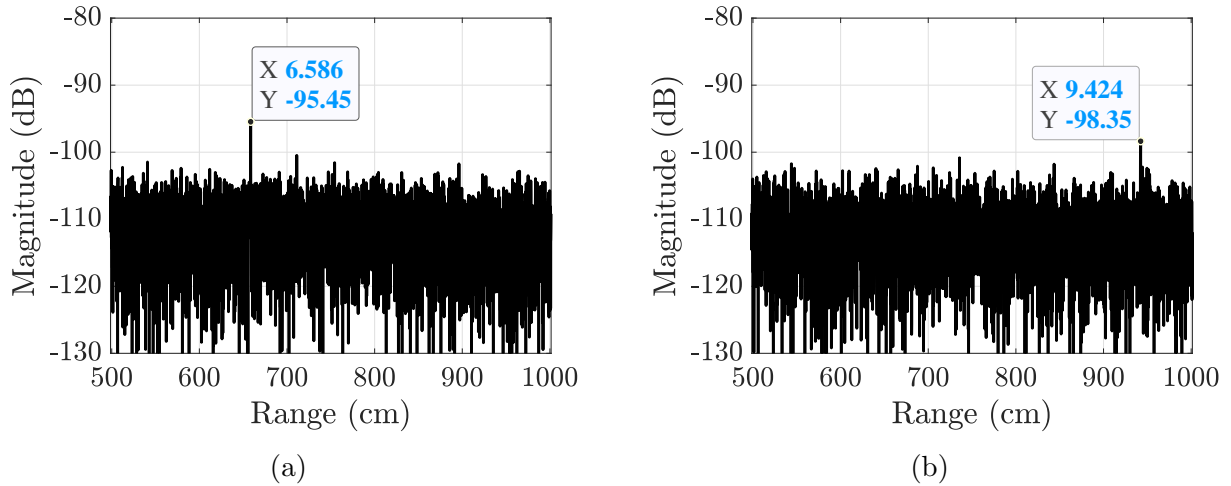


Figure 4-27: Time domain response of (a) metallic post at  $R \approx 6.59$  m and (b) plastic bottle at  $R \approx 9.42$  m.

To summarize, for all the considered cases in this section,  $S_P$  is well-matched with the  $S_M$ . Hence, validates the presented  $\sigma_{tgt}$  and  $R_{max}$ .

## 4.6 Conclusive Remark

The chapter has provided a comprehensive outlook of the indoor THz SAR 2D imaging. Two configurations based on the type of reflection, SDR and DR, have been presented. The configurations have been evaluated to define the imaging plane and applications. The SDR is more suitable for look-through and DR for surface imaging. The chapter's finding provides the optimized range of  $35^\circ \leq \phi_y \leq 55^\circ$  for the DR configuration. The same range can be adapted to map the indoor environment in the case of side-looking SAR, where the transceiver forms a certain look angle, and  $\phi_y$  is analogous to this angle

and hence the range. This range has been validated with simulations and measurements. The applications of these configurations have been demonstrated in consideration of the common indoor objects of materials metal, wood, plastic, foam, paper and glass.

Further, the chapter presented the application of geometric properties extraction from the generated 2D image. The length, height, and first surface thickness of the imaging target have been evaluated and validated. In terms of comparative analysis with the increase in bandwidth, significant improvement in the imaging quality is observed at large bandwidth. The chapter also presented the impact of surface roughness at the THz spectra. In comparison to the smooth surface imaging, the rough surface lacks reflected power but provides substantial reflections from different angles. Therefore, it offers more information about the target.

Additionally, the chapter demonstrated the concealed and hidden objects imaging at the long range. Four cases are presented: metallic structure in the cardboard box, small metallic components in the plastic box, electrical cables in the plastic mount, and multi-materials targets. In all the cases, the loss in receiver power due to concealing/hidden surface has been presented, and targets are well imaged.

Lastly, to define the maximum sensing range of the indoor objects, the chapter presented the range calculation methodology based on the used transceiver properties and estimated RCS. The predicted reflection coefficient  $S_P$  has been estimated based on the method, and it has been validated with the measured reflection coefficient  $S_M$ . The  $S_P$  and  $S_M$  are in close approximations, and the sensing range of presented objects ranges from  $6 \text{ m} \leq R_{\max} \leq 25 \text{ m}$ .

## 3D Imaging and Object Detection-Classification

The chapter addresses the THz SAR 3D imaging along with autonomous object detection and classification.

State-of-the-art SAR imaging testbeds are based on radar frontends [20, 21, 22, 30], and VNA with extension modules [23, 31]. The radar-based testbed benefit with compactness but has limited bandwidth and lower dynamic range compared to the VNA-based. For example, testbeds in [21, 22, 30] have system bandwidth of 6 GHz, 40 GHz, and 28.8 GHz with a center frequency of around 150 GHz, 290 GHz, and 590.5 GHz, respectively. On the contrary, the VNA-based testbed is bulky but provides an enormous bandwidth and high dynamic range. The testbeds in [23, 31] operate at a center frequency of 272.5 GHz and 412.5 GHz, and corresponding bandwidths are 105 GHz and 175 GHz, respectively. The radar-based testbed is the first approach in a practical environment, whereas the VNA-based testbed is suitable for experimental evaluation and validation of methods.

It is important to analyze the potential and limitations of SAR at different frequency bands. So, this chapter firstly presents an overview of 3D SAR imaging from GHz to THz waves. The selected frequency bands are 5-10 GHz (Band 1), 75-110 GHz (Band 2), 0.22-0.33 THz (Band 3), 0.325-0.5 THz (Band 4), 0.85-1.1 THz (Band 5) and 1.1-1.5 THz (Band 6). Moreover, the results for NDT using THz SAR technique with frequency modulation continuous wave radar-based frontends for the frequency band 68-92 GHz and 0.122-0.168 THz in a joint collaboration with MARIE sub-projects *M04* and *M05* [34] are available in [18]. Additionally, to the best of the author's knowledge, electronic-based SAR imaging has been presented for frequencies up to 750 GHz [77], whereas in this chapter and supported publications [18, 78] one of the first results up to 1.5 THz are presented.

Further, the chapter presents the multi-object environment mapping by considering objects in a group of 2 and 4. The map is extended with object detection and classification using machine learning techniques. For object detection, speeded up robust features (SURF) [79] are extracted and clustered based on the density-based spatial clustering of

applications with noise (DBSCAN) algorithm [80]. Finally, the classification of detected object is addressed with k-means clustering and a supervised machine learning-based support vector machine model .

The chapter is organized as follows. Firstly, Section 5.1 presents the 3D imaging system model. Section 5.2 demonstrates the imaging from GHz to THz waves. In Section 5.3, multi-object environment mapping is presented. Section 5.4 and 5.5 addresses object detection and classification. Lastly, in Section 5.6, a conclusive remark is provided.

## 5.1 System Model

The 3D imaging requires a 2D trajectory. In this chapter, planar aperture configuration is considered, and the trajectory is implemented along the azimuth and elevation direction. Fig. 5-1 presents the 3D imaging geometry, where  $x$ -,  $y$ - and  $z$ -axis are range, azimuth, and elevation directions, respectively. The transceiver located at  $\mathbf{P}_n$ , where  $n \in 1, N$  and  $N$  is the total number of positions in the 2D scanning track, transmits and records the backscattered EM wave at each aperture position. The parameter  $(u, v)$  are the azimuth and elevation coordinates based on the presented geometry, where  $u \in (1, U)$ ,  $v \in (1, V)$ , and  $U$  and  $V$  are the total number of aperture positions along  $u$  or  $y$ -axis and  $v$  or  $z$ -axis, respectively.

Extending the signal processing explained in Section 2.1 to 3D imaging case, for the transceiver at position  $\mathbf{P}_n$  and the received signal from  $K$  scatterers can be given by

$$s(t, u, v) = \sum_{k=1}^K A_k p\left(t - \frac{2R_k}{c}\right), \quad (5-1)$$

where,  $R_k = \sqrt{(x_k + R_{\text{ref}})^2 + (y_k + u)^2 + (z_k + v)^2}$  is the slant range between the  $k^{\text{th}}$  scatterer and transceiver, and  $A_k$  is the amplitude of reflectivity from the  $k^{\text{th}}$  scatterer. The coordinates of the scatterer position  $(x_k, y_k, z_k)$  and transceiver can be positive or negative from the considered reference center of origin.

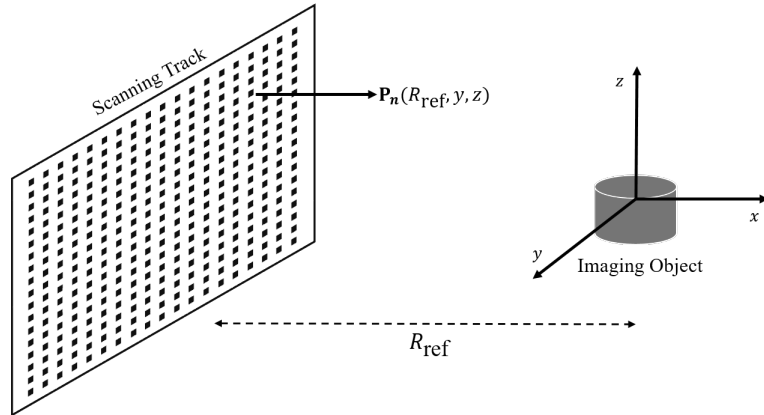


Figure 5-1: 3D imaging geometry.

For the image reconstruction with VNA-based testbed, similar to BPA process explained in Section 2.5, the eq. (2-16) can be extended to 3D imaging. In the 3D image reconstructed grid  $\mathbf{I}$ , voxel value at location  $(x_i, y_j, z_k)$  is given by

$$I(x_i, y_j, z_k) = \sum_{p=0}^U \sum_{m=0}^V s_z(t_{ijk}, u_p, v_m) \exp(-j4\pi f_{min} R_{ijk, u_p, v_m} / c), \quad (5-2)$$

where  $t_{ijk}$  is round the trip delay for the scatterer at the voxel position  $(x_i, y_j, z_k)$  in  $\mathbf{I}$ . Moreover, the spatial resolution can be given as per eq. (2-10) and (2-11). The azimuth and elevation directions are orthogonal to the range, and hence the respective resolution is associated with eq. (2-11). The maximum achievable cross-range resolution, if condition for  $L_s$  is fulfilled, along elevation ( $r_z$ ) and azimuth ( $r_y$ ), can be given by eq. (2-13).

## 5.2 Analysis of Imaging up to 1.5 THz

This section presents the result of 3D SAR imaging from 5 GHz to 1.5 THz. Firstly, the testbed is presented along with a brief explanation of all associated components.

### 5.2.1 Testbed

As explained in Chapter 2, in SAR, the transceiver is mounted on a mobile platform. However, due to the high load and positioning accuracy requirements for mounting the transceiver module for the VNA-based testbed, a lightweight imaging object is mounted on the mobile platform instead of the transceiver module in this section. Very high positioning accuracy is required at the THz, as described in Chapter 3. Especially for the case of vertical movement against gravity, the mounting load is of critical importance.

For a planar aperture formation, the imaging object is mounted on a linear motorized YZ-stage. The object is moved along the  $y$ -axis and  $z$ -axis, and at every position, a frequency sweep is transmitted and received. It is a stop-and-go approximation system, and this configuration where the imaging object forms a trajectory, and the transceiver system is stationary is called inverse-SAR (ISAR) [4]. It provides the same results as in the case where the transceiver is mobile, if the imaging object movement is always under the antenna's beam footprint. Also, the imaging and movement planes are parallel to each other. In this section, it has been taken into consideration. Therefore, the testbed is analogous to SAR.

The VNA-based testbed can be divided into two configurations. In the first configuration, the VNA is directly connected to an antenna via radio frequency (RF) cables whereas, in the other configuration, a frequency extender is used to up-convert the low-frequency signal from the VNA into the desired frequency range such as THz. Similar to the other testbed in this dissertation, a Rohde&Schwarz ZVA67 VNA [66] is employed. Based on the VNA specification, it operates in the frequency range from 10 MHz to 67 GHz. Therefore, first configuration is suitable for Band 1, and Band 2-6 are addressed with the second configuration.

## Antennas

For Band 1-4 and 5-6, rectangular and diagonal horn antennas are used, respectively. The parameters of all the antennas are summarized in Table 5-1, where  $L_{a,y}$  and  $L_{a,z}$  corresponds to antenna width and height, respectively.

Table 5-1: Antennas parameters.

Band	Freq. Range (GHz)	Type	Gain (dB)	$L_{a,y}$ (mm)	$L_{a,z}$ (mm)	$\theta_{-3 \text{ dB,E}}$	$\theta_{-3 \text{ dB,H}}$
1	5-10	Rectangular	25	243	143	16°	9.4°
2	75-110	Rectangular	25	26.8	20.8	9°	7°
3	220-330	Rectangular	25	8	6	10.4°	7.8°
4	325-500	Rectangular	20	2.89	1.93	21.6°	14.4°
5	850-1100	Diagonal	26	1.6	1.6	10°	10°
6	1100-1500	Diagonal	26	1.1	1.1	10°	10°

To provide a physical overview, the pictures of the antennas are shown in Fig. 5-2. From left to right, the antennas are shown for the corresponding Band 1-5. The reference dimension of the antennas can be compared with the 1 Euro coin shown in Fig. 5-2. For Band 6, the antenna looks similar to Band 5 but with a smaller dimension specified in Table 5-1.



Figure 5-2: Picture of horn antennas for (from left to right) Band 1-5, and 1 Euro coin for dimension reference.

The horn antenna has a beamwidth along E-plane ( $\theta_{-3 \text{ dB,E}}$ ) and H-plane ( $\theta_{-3 \text{ dB,H}}$ ). The E-plane and H-plane beamwidth are associated with the direction of the electric and magnetic field. In the considered geometry, the electric and magnetic field is along the horn antenna height or  $z$ -axis and width or  $y$ -axis, respectively. From eq. (2-8), the beamwidth varies with frequency. In Table 5-1, it is defined for a wavelength of center frequency in the presented band. Additionally, most of the antennas specified in Table 5-1

have approximately identical gain and the received power is directly proportional to the gain as defined in eq. (4-4).

### Frequency Extenders

To investigate imaging for the Band 2-6, frequency extenders are coupled with VNA, which performs the frequency multiplication and up-converts the low-frequency signal from VNA into the desired spectrum. Rohde&Schwarz extender series ZC110, ZC330, and ZC500 are used for Band 2-4. The extenders ZC110 and ZC330 have a dynamic range above 100 dB, and ZC500 has around 85 dB [67]. As defined in Chapter 4, the dynamic range defines the maximum sensing range, and it highly depends on the IF filter  $B_w$ . For ZC330, the impact on the dynamic range for different IF filter  $B_w$  is shown in [68]. For Band 5-6, Virginia Diodes spectrum analyzer extender (SAX)-VDI Models: WR1.0SAX-M and WM-164 are used which have a dynamic range (IF  $B_w = 10$  Hz) of around 75-90 dB and 50-65 dB [81], respectively. At the THz spectrum, the extender's dynamic range is considerably less in comparison to the lower frequency region due to an increase in the hardware complexity.

For imaging, one port reflection measurement  $S_{11}$  is performed, and this configuration is analogous to monostatic radar. To compensate for the power losses from RF cables, dispersion of the frequency extender and shifting the reference plane at the extender waveguide flange, one short port calibration is performed in all the cases.

### 5.2.2 Imaging

For 3D imaging, two cases are considered. In case 1, a metallic object is considered, whereas in case 2, a dielectric object is considered. The measurement parameters are summarized in Table 5-2, and these parameters are the same for both cases except a minor change in  $R_{\text{ref}}$  and corresponding cross-range resolution. The maximum possible travel range of the used YZ stages is 150 mm. The measurements are performed on different days with the re-assembling of the tested. Therefore,  $R_{\text{ref}}$  is not exactly similar. The reference range in Band 1-4 and Band 5-6 is nearby.

However, to acquire the resolution based on eq. (2-13) either requires a large travel range, especially for the case of Band 1 and Band 4, which is not possible with the used stages or short  $R_{\text{ref}}$ . Besides, the change in dimension of the antenna with a change in the band as shown in Table 5-1, also restricted to have the same  $L_s$  at one reference range such as  $R_{\text{ref}} = 1$  m. The aperture length for Band 1-4 is 150 mm and it is the same along  $y$ - and  $z$ -axis. Therefore, the corresponding resolution  $r_y = r_z$  is given by eq. (2-11). Also, for Band 5, the aperture length along both azimuth and elevation are nearly the same. In the case of Band 6, the primary focus is along the elevation, and hence a lower aperture length is considered along the azimuth. This also corresponds to the change of resolution along azimuth and elevation at Band 6 as shown in Table 5-1.

Concerning the step size, the basic criteria is that it should be less than the resolution, and this is considered in all the cases, and it is equal along  $y$ -axis and  $z$ -axis, i.e.

Table 5-2: 3D imaging parameters.

Symbol	Parameter	Band 1	Band 2	Band 3	Band 4	Band 5	Band 6
$f_c$	centre frequency	7.5 GHz	92.5 GHz	275 GHz	412.5 GHz	925 GHz	1300 GHz
$B_w$	bandwidth	5 GHz	35 GHz	110 GHz	175 GHz	250 GHz	400 GHz
$L_{s,y}$	synthetic aperture length along $y$ -axis	150 mm	150 mm	150 mm	150 mm	89 mm	58 mm
$L_{s,z}$	synthetic aperture length along $z$ -axis	150 mm	150 mm	150 mm	150 mm	90 mm	105 mm
$r_y \approx r_z$	cross-range resolution	174 mm	13.8 mm	4.2 mm	3 mm	0.8 mm	0.77 mm ( $r_y$ ), 0.7 mm ( $r_z$ )
$r_x$	range resolution	30 mm	4.3 mm	1.4 mm	0.86 mm	0.6 mm	0.375 mm
$R_{\text{ref}}$	reference range	1.31 m	1.28 m	1.16 m	1.22 m	0.44 m	0.39 m
$\Delta u_y$	step size along $x$ -axis	1 mm	1 mm	1 mm	1 mm	0.7 mm	0.7 mm
$\Delta u_z$	step size along $y$ -axis	1 mm	1 mm	1 mm	1 mm	0.7 mm	0.7 mm
$N_f$	no. of frequency bins	201	801	3001	3001	1201	1201
$P_T$	base transmit power	-10 dBm	-10 dBm	-10 dBm	-10 dBm	-10 dBm	-10 dBm

$\Delta u_y = \Delta u_z$ . For simplicity,  $\Delta u_y = 1$  mm is considered for Band 1-4 whereas for Band 5-6,  $\Delta u_y = 0.7$  mm is selected to meet the criteria. In a stop-and-go approximation SAR, the cross-range resolution cannot be smaller than the step size. Moreover, stages provide

the position accuracy of  $< \pm 0.005$  mm. Therefore, the positioning accuracy requirement as per strict and relaxed constraint defined in Chapter 3 is fulfilled for all the bands.

The measurements are performed with the testbed explained in Section 5.2.1, and the SAR image has been generated using eq. (5-2). Moreover, the measurements are performed in a cluttered environment without any prior wireless channel subtraction to remove the cluttered noise. The noise in this scenario is the reflections from all the objects existing in the environment except the imaging object. Most of the reflections from the non-interested objects will not be focused because the synthetic aperture is only formed by the considered object's movement.

### Metallic Object

The picture of the imaging object is shown in Fig. 5-3. The imaging object is a metallic plate of dimension (length  $\times$  width  $\times$  height) 6 mm  $\times$  90 mm  $\times$  100 mm that consist of many open circular holes of different dimensions and also some closed holes with a small screw in it as shown in Fig. 5-3. The maximum and minimum diameter of the hole in the plate is 12 mm and 3 mm, respectively. The object is well suited for the imaging comparison for the GHz to THz spectrum due to the variable circular shapes within the object.

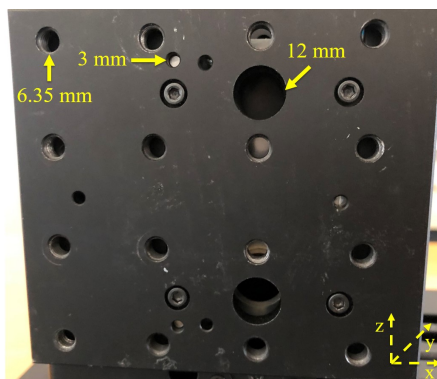


Figure 5-3: Picture of metallic object.

SAR images of the object for the Band 1-4 are summarized in Fig. 5-4. The resulting images are given in 2D-plane along  $y - z$  plane, where  $y$ -axis and  $z$ -axis are along the imaging object's width and height, respectively. As for metallic material, EM waves do not penetrate the material. So, no useful information is acquired along the range or  $x$ -axis. Therefore, the 3D image plane is truncated into a 2D plane to represent the object surface, and the range  $R_{\text{ref}}$  of this plane is given in Table 5-2. For Band 1, no information about the object's rectangular shape and holes within the object is obtainable as shown in Fig. 5-4.a due to the low spatial resolution specified in Table 5-2 in this band. However, the target is focused, which represents the imaging object's presence, and the dimension of the object is also achievable in accordance with the spatial resolution.

For Band 2, the SAR image is shown in Fig. 5-4.b. Compared to the previous band image, more information can be acquired as the rectangular shape of the object

is observable and the object's dimension is more accurate. However, the holes are not observable. Due to the spatial resolution in this band, it seems that holes are overlapping, and therefore, their boundaries are not visible. The image quality is highly improved at Band 3, which can be seen in the resulting SAR image in Fig. 5-4.c. The complete shape and most of the holes are visible. However, the boundaries of the rectangular shape and holes are not sharp or well focused. Also, the holes of diameter 6.35 mm and 3 mm are not correctly imaged as perfect circles. With further increase in the frequency and bandwidth to Band 4, much better image quality is observed in Fig. 5-4.d. The dimension and the shape have been drastically improved in comparison to Band 1-3.

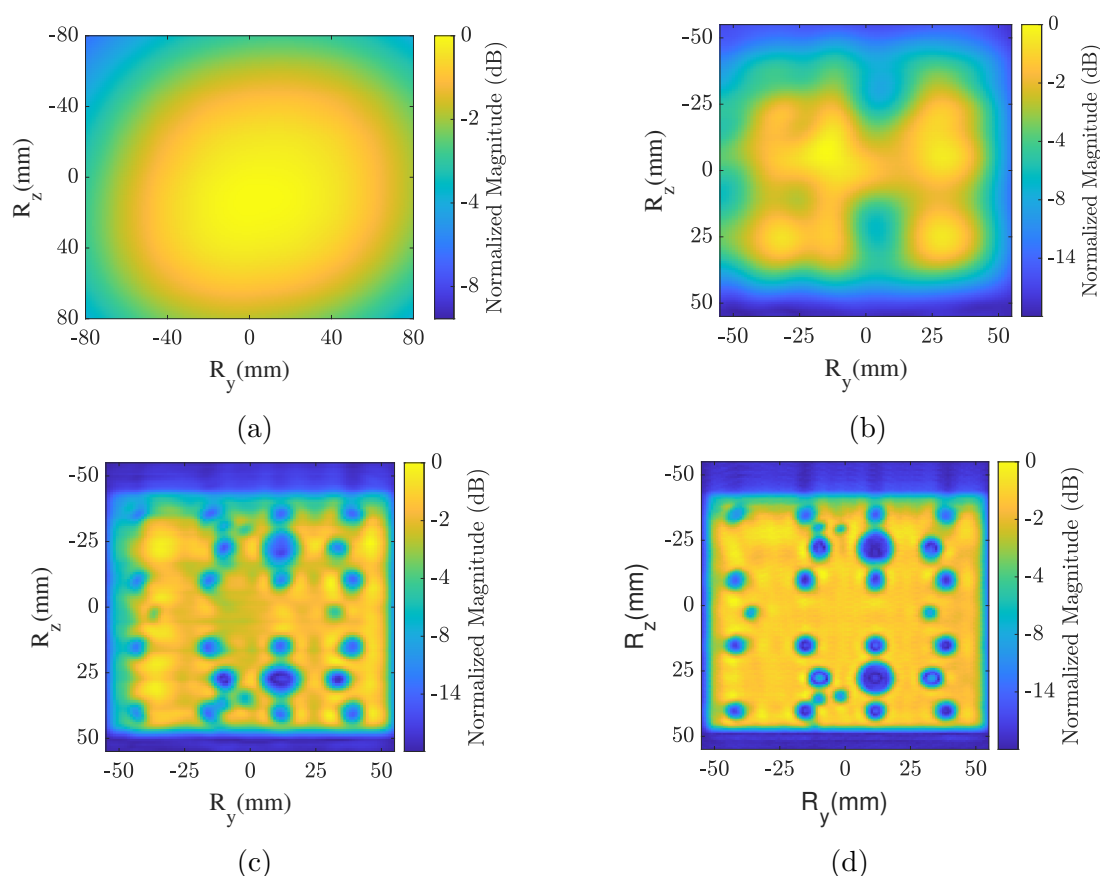


Figure 5-4: (a-d) SAR image of metallic object for Band 1-4.

Imaging at Band 5-6 requires special consideration as the atmospheric absorption is very high and the electronic transceiver module has a low dynamic range because of the hardware complexity. To provide stability and better noise level, the local oscillator (LO) input to frequency extender has to be provided using an external source instead of internally by the VNA as is the case for the Band 2-4 setup. So, two SMA100B signal generators from Rohde&Schwarz [82] are used as an external LO input source. Due to the external source and reduced step size, the measurement time has been drastically increased. Therefore, instead of illuminating and reconstructing the complete object, only a certain area of the object is illuminated and reconstructed. The part of the object is selected which consists of the smallest holes and are not sharply observable in Band 5.

For comparison analysis, the enlarged image of Fig. 5-4.d of this specific part is shown in Fig. 5-5.a. It can be seen that the smallest holes of diameter 3 mm have overlapping edges and are out of focus.

The generated SAR image for Band 5 is shown in Fig. 5-5.b. The enhancement concerning to Band 5 which is the highest quality image in Band 1-4 can be easily seen in the resulting image. All the holes appear with more sharp edges and without any overlap. The imaging object has minor scratches/defects in the bottom that is also observable which was not the case in Band 4 image. Furthermore, due to the higher complexities at

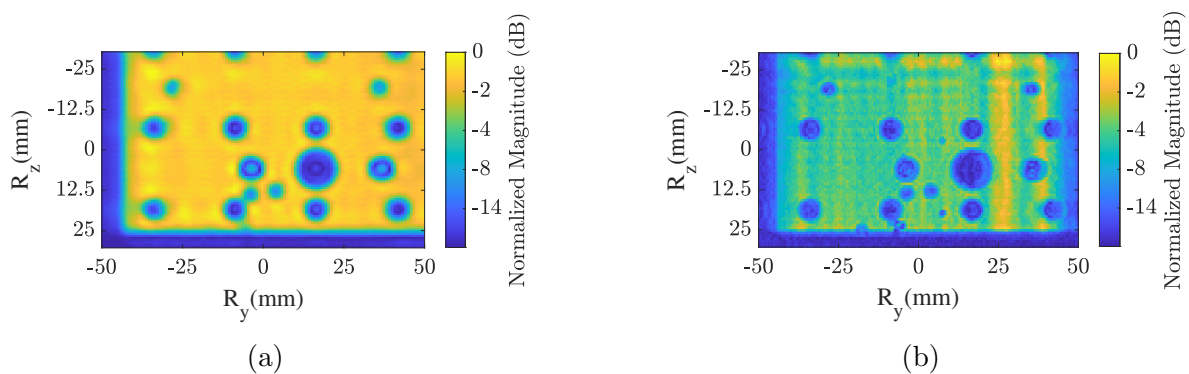


Figure 5-5: SAR image of metallic object for Band (a) 4 (enlarged) and (b) 5.

Band 6 (measurement time, path loss, atmospheric absorption, and hardware impairments in terms of losses associated with the waveguides) with imaging at Band 6 in comparison to 5 as listed above, only a specific part of the object is mapped. For contrast, the enlarged image of Fig. 5-5.b specific area, which is also mapped at Band 6, is shown in Fig. 5-6.a. The enhancement in the image quality at Band 6 can be seen in the resulting image shown in Fig. 5-6.b. The shape of the holes is much more accurate and sharper than Band 5. Hence, Band 6 provides the highest image quality through out the considered bands.

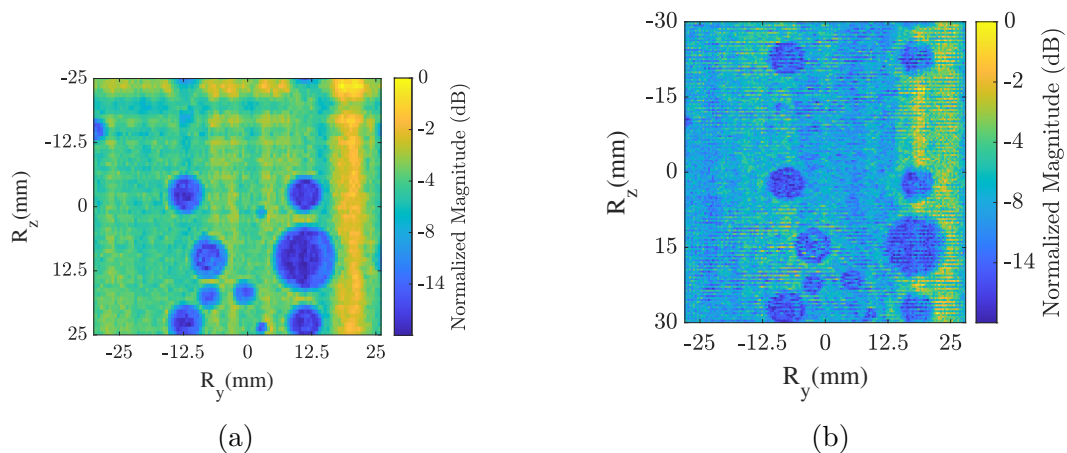


Figure 5-6: SAR image of metallic object for Band (a) 5 (enlarged) and (b) 6.

## Dielectric Object

With metallic object imaging, the dominant spatial resolution are cross-range resolution  $r_y$  and  $r_z$ . So, to evaluate the imaging also from range resolution  $r_x$  perspective, a 3D printed object of high impact polystyrene sheet, which is a type of plastic material is considered. The object is shown in Fig. 5-7. The object shape is similar to stairs which consist of 10 steps. Each step along the  $z$ -axis is of height 1 cm and separated by 1 mm from adjacent step along  $x$ -axis. The steps have constant width along the  $y$ -axis of 10 cm. Apart from these variations in dimension for spatial resolution comparison analysis, the object also has air inclusions inside it due to improper filling in the 3D printing. The air inclusions are visible as dark irregular holes or patches in the picture shown in Fig. 5-7. As for plastic material, the EM waves can penetrate the object surface and the air inclusions within the object results in a change of refractive index which results in reflection. So, it is the case of a multi-layered object concerning the change of refractive index at many different instances inside the material. With SAR, these layers can be analyzed based on the spatial resolution.

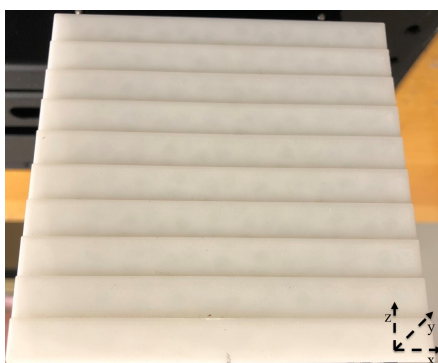


Figure 5-7: Picture of plastic object.

In the previous case of 3D metallic object imaging at Band 6, it is achieved with extenders provided by VDI [81] for initial measurements and are only available at DSV for a short time-span. Therefore, for dielectric object imaging, Band 1-5 are considered and the resulting images are summarized in Fig. 5-8. The range resolution in this case will be the same as specified in Table 2. However, there will be a minor shift in the cross-range resolution based on  $R_{\text{ref}}$ , which can be estimated directly from Fig. 5-8.

Similar to the metallic object images for Band 1-2, no useful information about the object shape with variation in dimension and air inclusion layering is obtained as shown in Fig. 5-8.a and b, respectively. The drastic improvement in the image quality is shown at Band 3 and the corresponding SAR image of stair shape is shown in Fig. 5-8.c. Focusing is performed on 8 steps (instead of 10 due to limited beamwidth) and are well-focused. The stair shape is observed along with multi-layering. The plane of the object with printing artifacts (air inclusions) is clearly observable behind the object surface. However, the stairs step are overlapping due to the spatial resolution at this band whereas it is not the case at Band 4 as shown in Fig. 5-8.d. The shape of the steps is much sharper and

## 5.2 Analysis of Imaging up to 1.5 THz

the plane of artifacts is more precise. To be noted, the plane of artifacts in both Band 3 and 4 appeared with a shifted range position due to the change of speed of EM waves inside the material. This can be compensated with signal processing but requires a-prior knowledge of object material electromagnetic properties such as relative permittivity  $\epsilon_r$  and dimension of each material of a multi-layered object.

Finally, same as case with the metallic object at Band 5, only a limited area from the center of the object is focused and the resulting SAR image is shown in Fig. 5-8.e. The

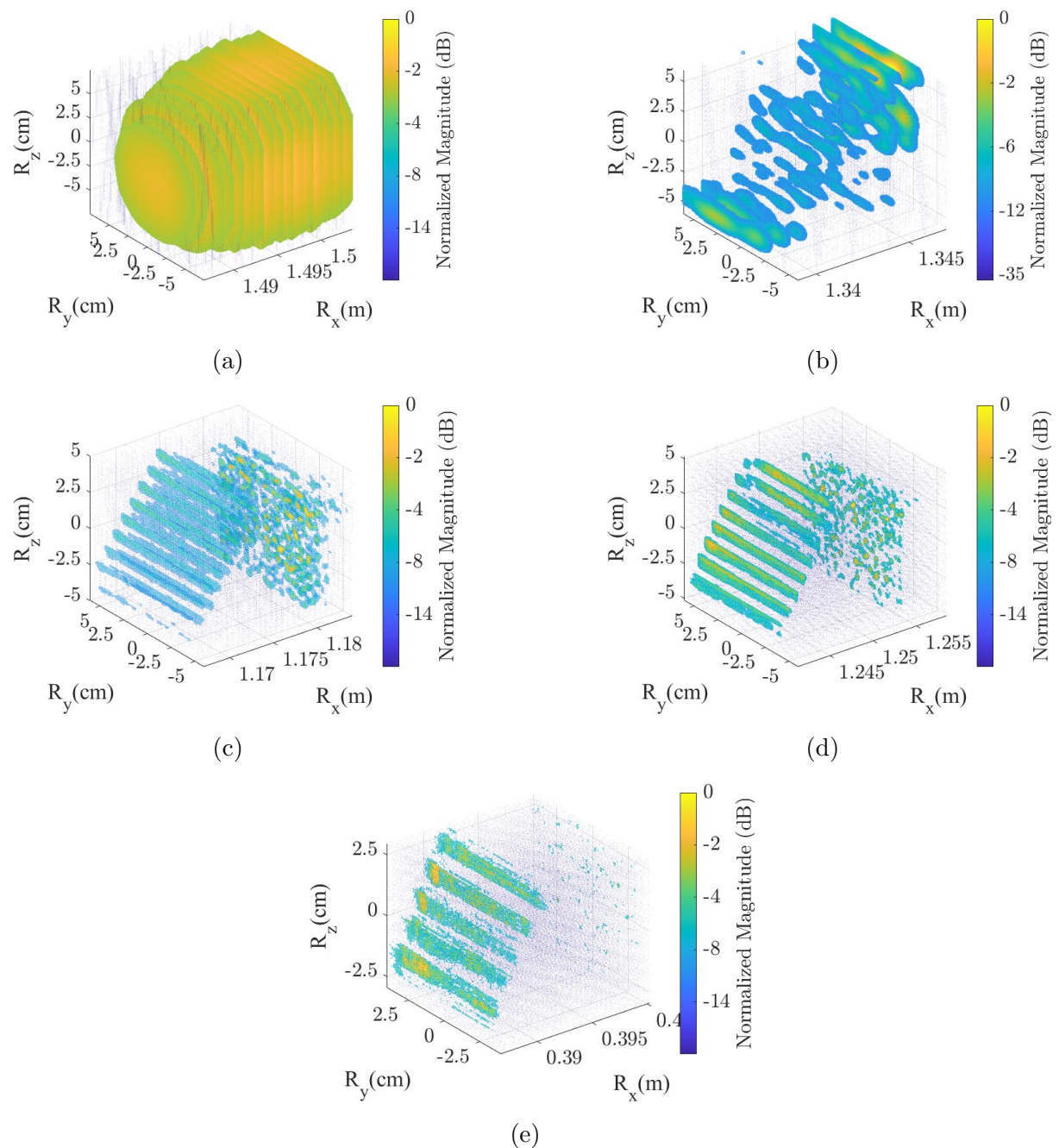


Figure 5-8: SAR image of plastic object for Band 1-5.

object surface shape is highly improved in comparison to the rest of the band. However, due to the smaller wavelength, a high noise level of frequency extender, high atmospheric absorption and path loss, and low penetration depth, the inner-layer of artifacts is not observed.

### 5.3 Multi-Object Environment Mapping

This section addresses 3D multi-object environment mapping. It is the base for autonomous object detection and classification in a cluttered environment. The objective is to first demonstrate a THz SAR-based 3D multi-object mapping, especially with indoor objects. Secondly, to generate a high-resolution map that can be extended for object detection and classification.

To realize this objective, three cases are considered. In case I and II, two objects are considered, which are displaced horizontally and vertically as shown in Fig. 5-9 (left) and (middle). Case III combines both the other cases with scattered four objects horizontally and vertically as shown in Fig. 5-9 (right). The considered objects are keyboard, calculator, mobile phone, and universal serial bus (USB) stick or flash drive. The distribution of these objects in the three cases is provided in Table 5-3 along with the measurement parameters, which are quite analogous to Band 4 (325-500 GHz) presented in Table 5-2. In case 3, a set of two  $L_y$  is considered to optimize the measurement time based on the imaging space. To form the synthetic aperture, the frequency extender for the range of 325-500 GHz is mounted in a monostatic configuration on the YZ stages.



Figure 5-9: Picture of objects in (left) case 1, (middle) case II and (right) case III.

The generated raw data is processed with BPA, and inverted 3D imaging plane scattered plots of resulting SAR images for the case I-III is shown in Fig. 5-10.a-c. Visualization of the 3D images in a 2D plane is also one of the concerns. Therefore, scattered and truncated volumetric plots are considered for presentation. The scattered plots shown in Fig. 5-10 provides the information in the context of the position in 3D space and magnitude scale, but the object's shape is challenging to observe. In contrast, the truncated

Table 5-3: 3D multi-object imaging parameters.

Symbol	Parameter	Case I	Case II	Case III
$f_c$	center frequency	412.5 GHz	412.5 GHz	412.5 GHz
$B_w$	bandwidth	175 GHz	175 GHz	175 GHz
$L_{s,z}$	synthetic aperture length along $z$ -axis	240 mm	340 mm	284 mm
$L_{s,y}$	synthetic aperture length along $y$ -axis	200 mm	150 mm	300 mm ( $0 \leq L_z \leq 233$ mm) and 270 mm ( $234 \leq L_z \leq 284$ mm)
$R_{\text{ref}}$	reference range	1.31 m	1.28 m	1.05 m
$\Delta u_y = \Delta u_z$	step size along $y$ - and $z$ - axis	1 mm	1 mm	1 mm
$N_f$	number of frequency bins	3001	3001	3001
$P_T$	base transmit power	-10 dBm	-10 dBm	-10 dBm
-	imaging objects	mobile, USB stick	calculator, USB stick	keyboard, mobile, cal- culator, USB stick

volumetric view of the SAR images shown in Fig. 5-11 provides a nice visualization of the object's surface in a 2D plane.

For case I, both the objects are well mapped as shown in Fig. 5-11.a. The keys of the mobile phone are well visible. The right side of the mobile phone is left intentionally un-focused in this imaging case. The aim for object detection and classification is that the object should be detected and classified even though the image consists of artifacts. As an example to show better focusing of the mobile phone, it is also mapped individually for the same frequency band, and the resulting SAR image is shown in Fig. 5-12.a. Moreover, in case I, the USB stick shape is also well observable in Fig. 5-11.a. The metallic component and the plastic material of the body are well distinguishable. Also, the tiny rectangular holes in the metallic component are observable.

Fig. 5-11.b shows the SAR image for case II. Similar to the previous case, both objects are well mapped, and the complete shape of the calculator is observable. Further Fig. 5-11.c shows the resulting SAR image for case III with four objects. Also, in this case, a well-focused SAR image showing all the four objects is generated. The high-resolution image clearly displays the tiny components of the objects, such as keys to complete shape are well distinguishable. Besides, the inside components of the object's body are suitably mapped. As an example, Fig. 5-12.b shows the expected mapped inside components of the USB stick, which could be a microcontroller. It is extracted with a penetration depth of  $\sim 6$  mm from the front surface, and the relative magnitude difference from the outer body (maximum magnitude) is  $-7$ dB as shown Fig. 5-12 (right).

To conclude, the resulting SAR images are in good compliance with the optical systems. In addition, the THz SAR technique also benefits from possessing penetration capabilities.

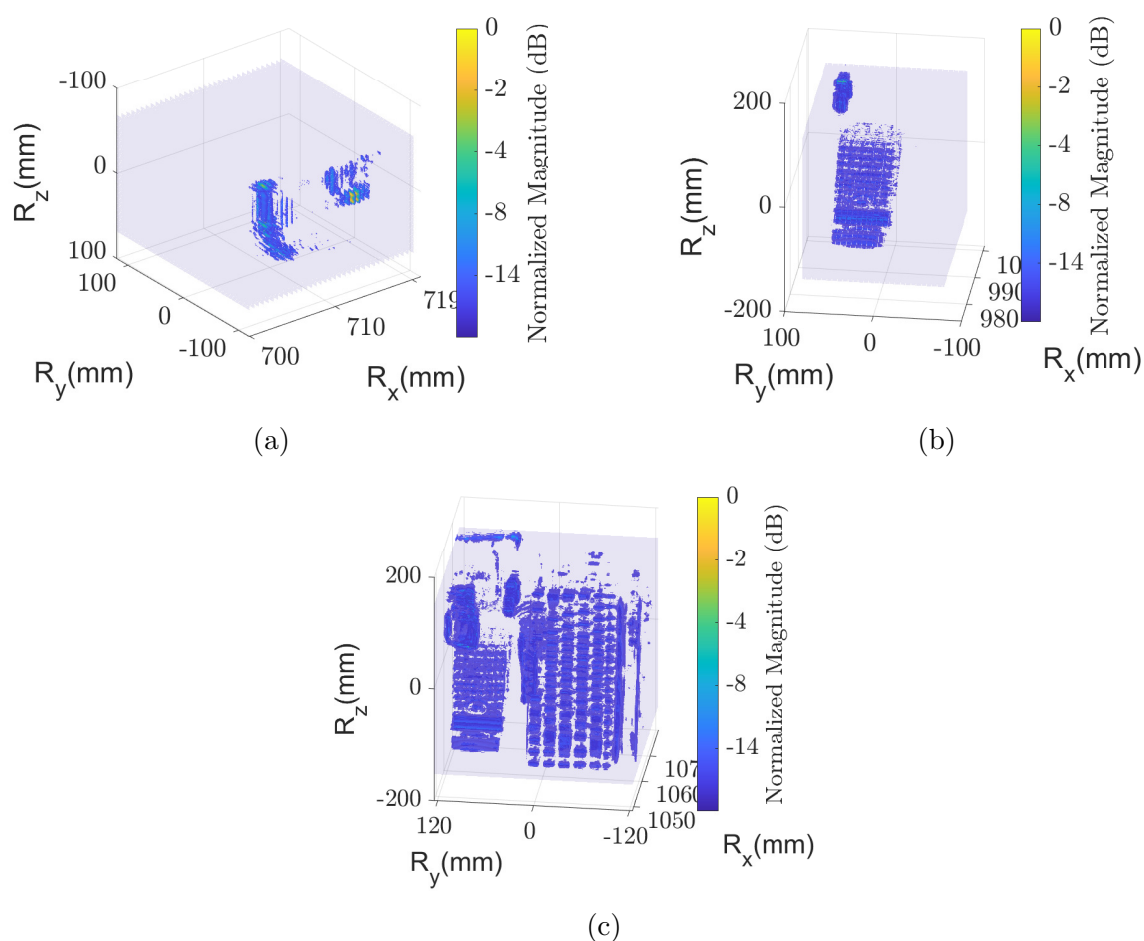


Figure 5-10: SAR image scattered plot of (a-c) case I-III.

## 5.4 Object Detection

The generated SAR image for case I-III are processed in this section for object detection. Most of the state-of-the-art object detection applications, such as face detection in smartphones and street objects detection in autonomous cars, are implemented mainly at visible or infrared spectrum due to the offered high-resolution [29]. Based on the results demonstrated in this dissertation, the THz spectrum provides high-resolution images in good compliance with optical systems, for example, camera at visible spectrum and infrared systems such as light detection and ranging (LiDAR).

For the presented THz SAR imaging (case I-III), object detection provides the identification in terms of the number of mapped objects and their respective location. The localization information is provided in reference to the transceiver position. Besides creating a base for classification, the detected objects can also be analyzed for geometric properties extraction as presented in Chapter 4.3.1. The workflow of the proposed method for object detection is shown in Fig. 5-13 and described below.

- Input image: It is the SAR image considered for object detection as shown in Fig. 5-14 (top-left) for the case I.

## 5.4 Object Detection

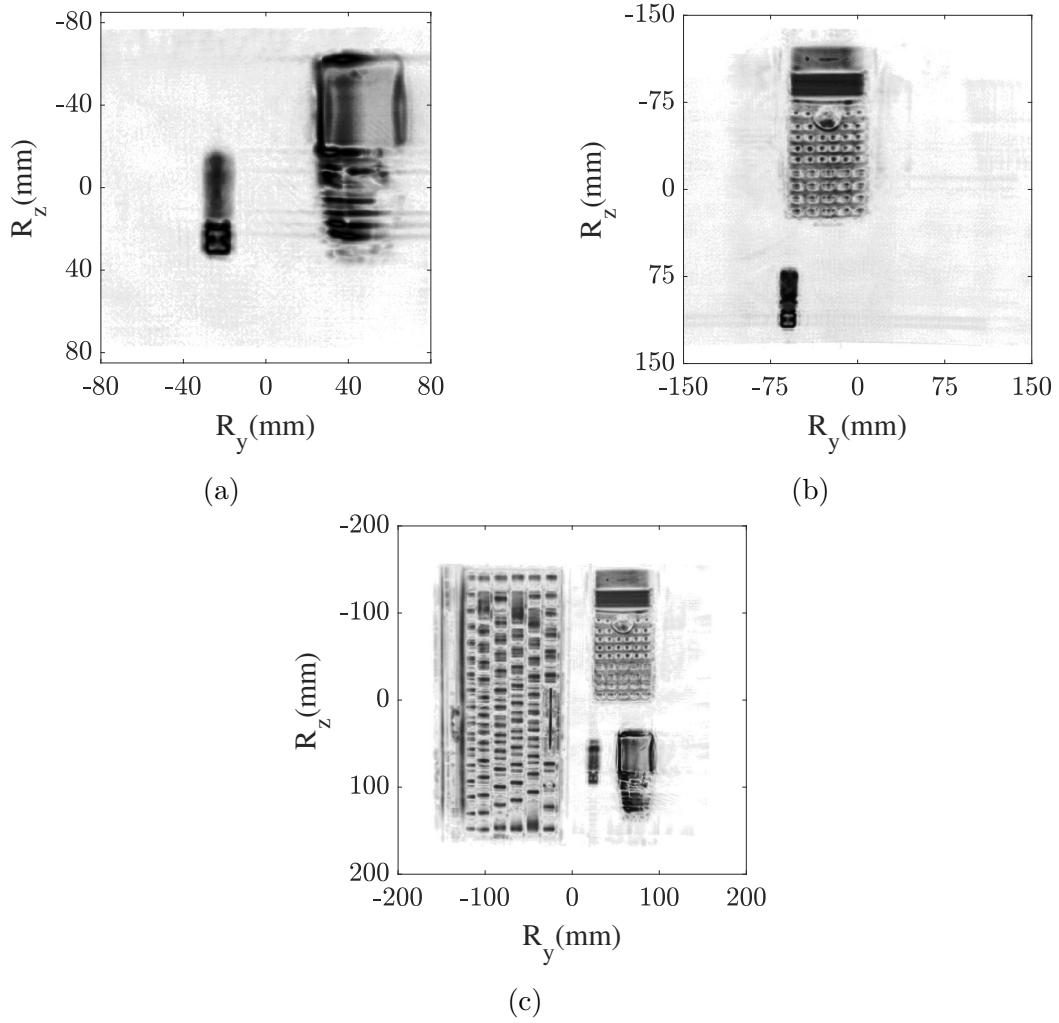


Figure 5-11: SAR image of 2D truncated volume plot of (a-c) case I-III.

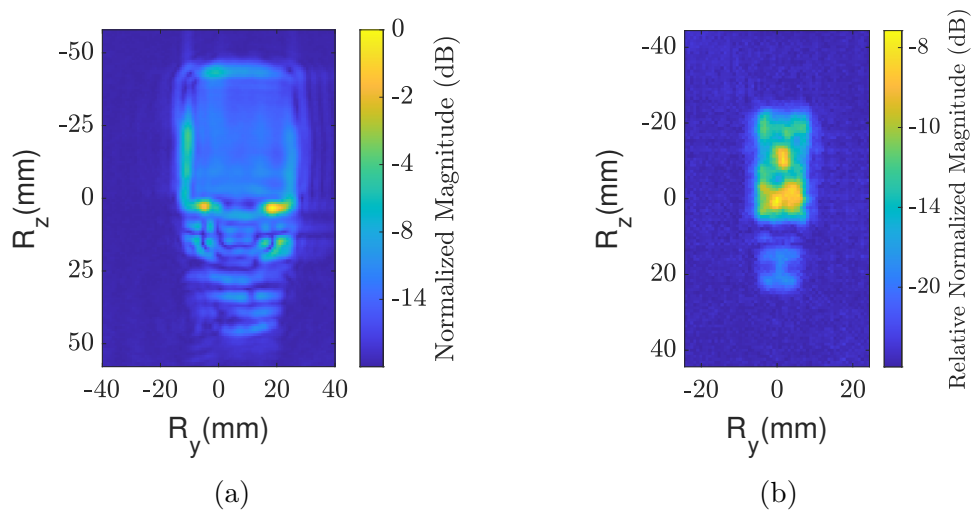


Figure 5-12: SAR image of (a) individually mapped mobile phone (b) mapped microcontroller inside USB stick.



Figure 5-13: Object detection workflow.

- **Image formation:** A gray-scale SAR image (input image) is processed to reduce the clutter and artifacts. Here, the continuous shape of objects is in the foreground instead of their components or parts. This is achieved by suppressing the image with a certain threshold. The gray-scale SAR image consists of values between 0-255, where 0 is considered black, and 255 represents white. The values within this range represent each pixel intensity in the gray-scale SAR image. For image formation (referred here as image formation for object detection), pixels below 1 dB (in terms of field) or 0.5 dB (in terms of power) of the maximum pixel intensity (white color) are assigned to minimum gray-scale value (black color). Considering the case I SAR image as an input shown in Fig. 5-14 (top-left), the output of the image formation block is shown in Fig. 5-14 (top-middle). In the resulting image, only the continuous shape is in focus.
- **Speeded-up robust features (SURF) extraction:** After image formation, interest points and descriptors are extracted from the image using the SURF algorithm [79]. The algorithm is one of the state-of-art feature extraction algorithms in the domain of object detection and classification. It is invariant to the scale and rotation of the image and is based on the Hessian matrix to find the key points. The Hessian matrix elements are given by the convolution of image pixel position and the Gaussian second partial derivative. A detailed explanation of the algorithm is available in [79].  
 Fig. 5-14 (top-right) and (bottom-right) shows the extracted features key-points positions in the image. Most of the extracted features and key-points are within the boundary of the objects.
- **Density-based spatial clustering of applications with noise (DBSCAN):** The extracted key-points using SURF features are provided as an input to the DBSCAN clustering algorithm [80]. It works on the principle of identifying the data points within the specified region to a reference position. The clusters are formed by identifying the number of minimum neighboring points within a specified radius. The Euclidean distance between two key-points defines the radius. Following are the categories of the data points identified by DBSCAN.
  - **Core points:** The data points included within the specified radius are the core points.
  - **Border points:** The data points which lie on the edge of the specified radius are called border points.

## 5.4 Object Detection

- Noise: The data points which neither belong to core points nor border points are identified as noise by the algorithm.

Both the core points and border points make a dense cluster of an object in an image. For case I, seven minimum points for clustering and a radius parameter 34 are considered. The parameter is associated with Euclidean distance with pixels positions, whereas the corresponding Euclidean distance related to SAR mapped (or imaging) space can be estimated with each pixel of dimension  $(y \times z) \sim 0.25 \text{ mm} \times \sim 0.25 \text{ mm}$ . Fig. 5-14 (bottom-middle) shows the cluster of key points. It can be seen that two clusters associated with two objects are formed, which validates the cluster model.

- Detected objects: Finally, based on the key-points cluster grouping and coordinates of key-points with DBSCAN block, the detected objects are marked in the SAR image as shown in Fig. 5-14 (bottom-left). Both the objects in case 1 are perfectly detected, and their respective locations in the 2D coordinate system in the imaging space can also be extracted.

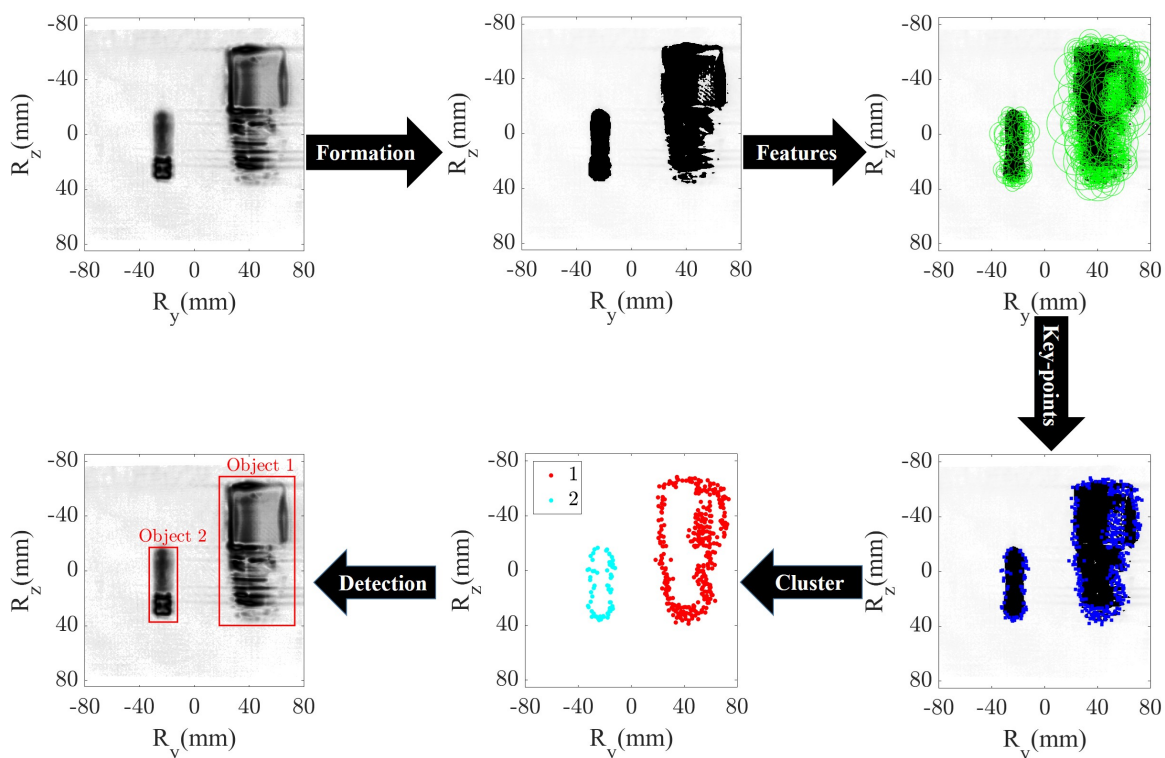


Figure 5-14: Output of object detection workflow for case I.

The complete workflow for object detection is implemented in MATLAB with SURF [83] and DBSCAN [84] functions. In a similar approach, the workflow is followed with the other two cases, and the results are summarized in Fig. 5-15. Only the change in respect to cluster radius parameter is adapted due to the different imaging grid size and pixel

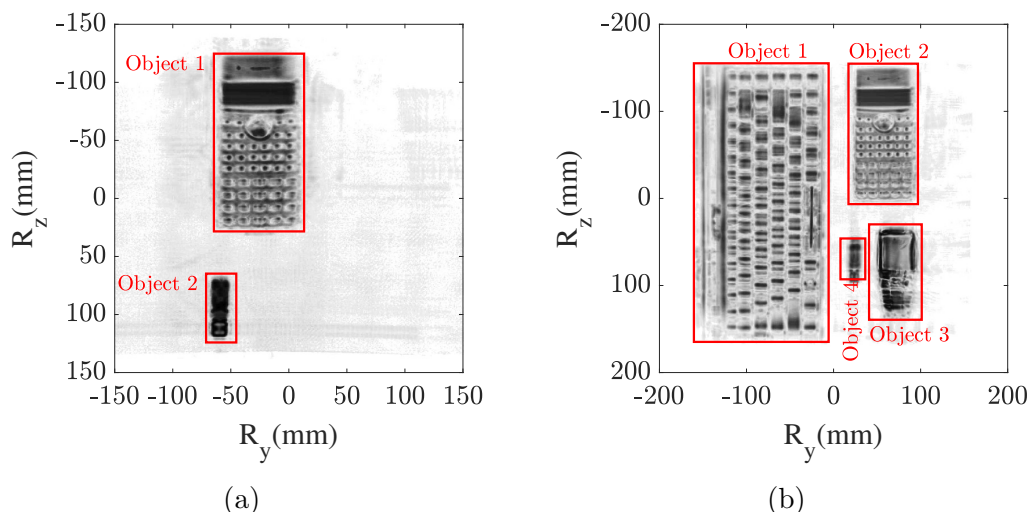


Figure 5-15: Detection of objects in case II and III.

dimensions. However, nearly similar euclidean distance to case I associated with imaging space is considered with the same minimum neighbouring points.

Fig. 5-15.a and b shows the detected objects in case II and III. All the objects (two in case II and four in case III) are well detected. Hence, validate the proposed method.

## 5.5 Object Classification

This section addresses the classification of the detected objects in Section 5.4. This scheme classifies the detected objects in SAR image into different classes. The workflow for object classification is presented in Fig. 5-16 and described below.

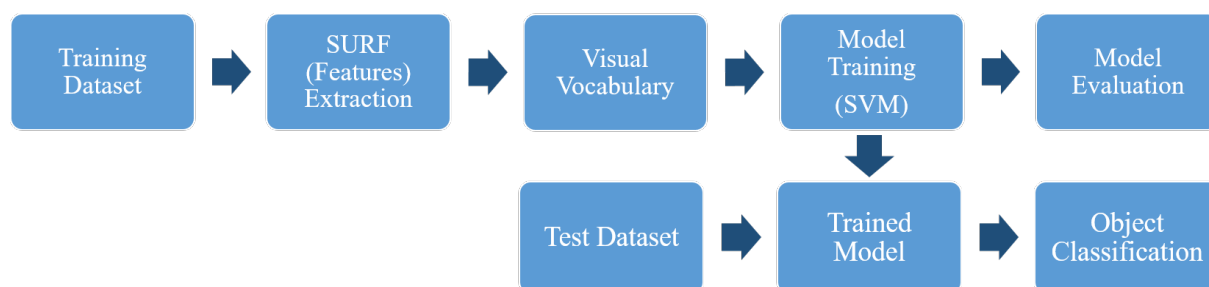


Figure 5-16: Object classification workflow

- Train and test split: In this technique, a complete training dataset is divided into two sub-parts to evaluate model performance during the training phase. The two sub-parts are described below.
  - Training set: The images in this set are used for training the model. The classifier knows the actual labels of the images during the training.

- Validation set: The classifier does not know the actual labels of images in this set. The validation images are provided to the trained model to evaluate model performance during a training phase.

In this work, 80% of provided data set is used for training, and the remaining 20% is used for validation. The input data set (training set + validation set) consists of SAR images of the detected objects in different dimensions, small and large, together with separately generated data of these objects by measurement campaigns. Generally, the test data (for final prediction) is different than the training data set, but it can be applied only in the case of the vast availability of the training data, which is not the case currently for emerging THz imaging. To the best of the author's knowledge, there is no public training data set available for THz images of indoor objects, especially for the considered objects. The SAR images provided in this work are one of the finest images of indoor objects. Therefore, to increase the training data set, the test data is also considered for training. The approach is to maximize the training data set for validation of the proof of concept. Following the approach, for the imaging object calculator, a SAR image of band 220-330 GHz is also provided in the data set due to image quality in reasonable compliance with the 325-500 GHz band.

To summarize, the training data set consists of four classes: keyboard, mouse, mobile and USB stick and the classes consist of multiple SAR images of the these objects.

- SURF extraction: The method is the same as explained in Section 5.4. Here, the training data set is provided as an input.
- Bag of visual words (BoVW) creation: The feature set extracted using the SURF method is given as input to the bag of features model. The bag of features model uses k-means clustering algorithm [80] to create a bag of visual words. As a result, k different clusters are formed, where features in one cluster are similar to each other and dissimilar to the features in other clusters. The center of each cluster is a visual word or feature. The BoVW model creates a visual dictionary of image features used to predict the class of test images.
- Model training: The feature vectors obtained through BoVW is used to train the classifier for object classification. In this work, the model is fitted using Support Vector Machine (SVM) classifier [80] which categorizes the data based on a best-fit hyperplane. The hyperplane can also be called decision boundary, which helps to classify the object into different classes. The features on one side of the boundary are different from features on the other side of the boundary. For example, features of the mobile image would be separated from features of the USB stick through this hyperplane.
- Model evaluation: The performance of the trained model is evaluated with validation and prediction accuracy. The accuracy is defined by the correct classification or

labeling over total instances.

- Validation accuracy: In this case the, the classifier does not know the actual labels and it is the validation set accuracy under test and split approach.
- Prediction accuracy: It is also defined as model accuracy and the accuracy obtained for the final test data set.

Basically, the higher is the accuracy of the model, the better is the model developed.

- Object classification: In the last step, the images from the test set are provided as input to the trained model for classification, and the respective predicted class or label is obtained.

The presented workflow is implemented as an extension of object detection in the same environment (MATLAB) and many functions available in MATLAB such as BoVW [85], k-means [86] and SVM [87] and predict [88] are used. Based on the workflow, the detected objects in all the cases are provided for classification, and results are summarized in Fig. 5-17. In all the cases I-III, all objects are correctly predicted as presented in Fig. 5-17.a-c and hence classify the object in the THz SAR image. For example, the detected object 1 in case II in Fig. 5-15.a is correctly classified as a calculator.

For the model robustness evaluation, truncated (incomplete) or modified SAR images of the objects are considered. These image are shown in Fig. 5-18 and are tested for classification. All these images are correctly classified, where (a-d), (e-h), (i-l) and (m-p) are the modified images considered in test set of keyboard, calculator, USB stick and mobile, respectively. This evaluation is beneficial as in many cases (for example, emergency situations or unintentional artifacts) generating a high quality focused SAR image in the practical applications might be complex. However, based on the proposed method, there is a possibility or opportunity of classifying the object in images with artifacts. For further evaluation, a mobile phone SAR image at a different frequency band of 220-330 GHz shown in Fig. 5-18.p is generated and tested. It is also correctly classified even though the training set consist of the mobile phone SAR images only of 325-500 GHz band. This achievement can be well explained due to spatial resolution at both the bands is in close proximity. Hence, the model is highly robust.

With the test and split philosophy of training set, the validation accuracy of 88% is achieved. Based on the predicted results, a prediction accuracy of 100% is achieved.

## 5.6 Conclusive Remark

The chapter has demonstrated 3D high-resolution imaging up to 1.5 THz with an extension to object detection and classification. The results are shown with a VNA-based testbed for the frequency spectrums: 5-10 GHz (Band 1), 75-110 GHz (Band 2), 220-330 GHz (Band 3), 325-500 GHz (Band 4), 850-1100 GHz (Band 5) and 1100 GHz-1500 GHz (Band 6). Detecting just the object's presence at Band 1 to resolving the minute

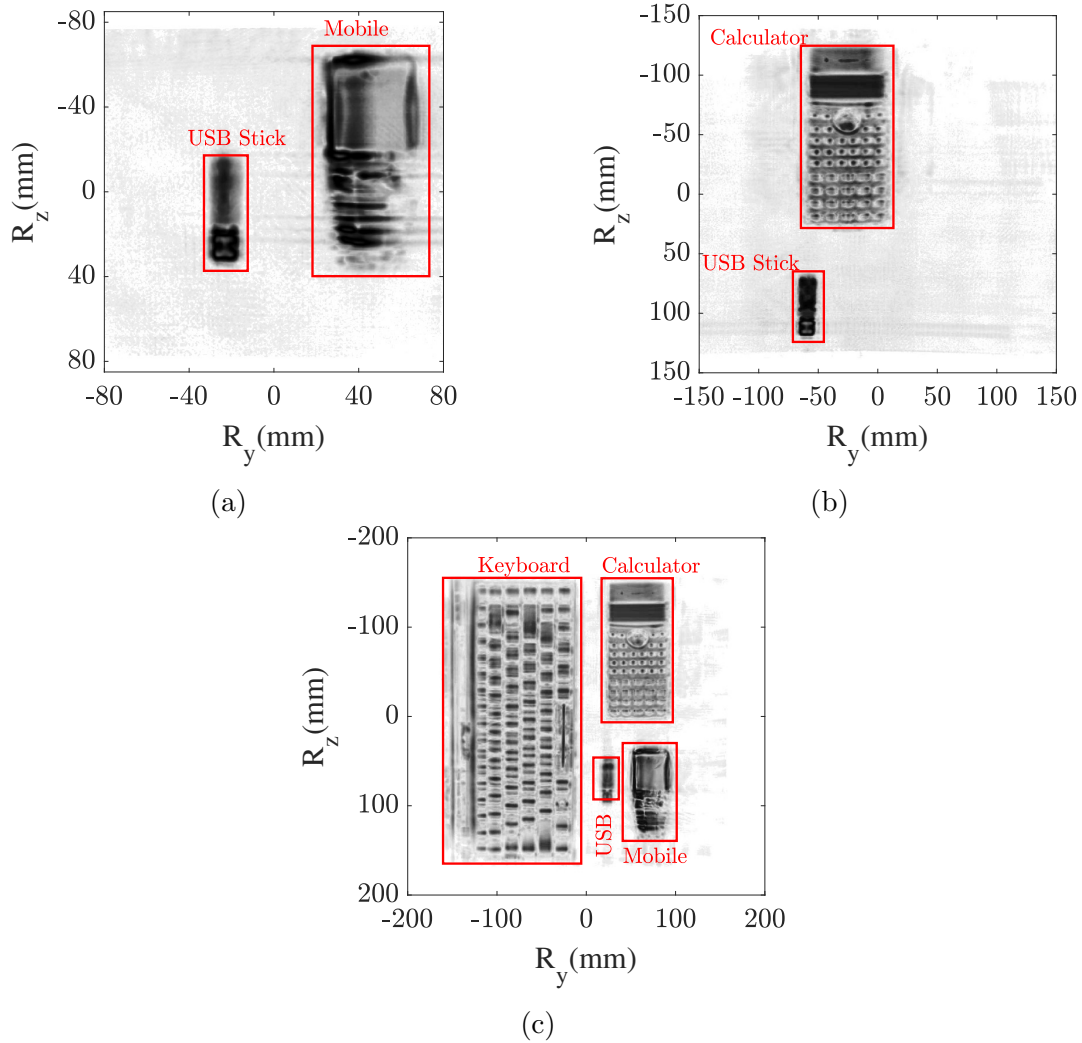


Figure 5-17: Classification of objects in (a-c) case I-III.

details and shape of the object with sub-mm accuracy at Band 6 (1100 GHz-1500 GHz) has been shown. The imaging objects are considered concerning both cross-range and range resolution. For cross-range evaluation, a metallic object consists of different sizes of circular holes is considered, whereas an object of dielectric material is considered, especially for range resolution. The imaging results of these objects show the enhancement of SAR image quality at the THz spectrum. In addition, the penetration capabilities of EM waves up to 1.1 THz are explored. Imaging at Band 4 is a well trade-off in terms of resolution and penetration depth. At Band 4, the SAR image has drastically improved compared to lower frequency spectrum Band 1-3. Besides, EM waves at Band 4 suffer lesser atmospheric absorption and path loss than higher frequency Band 5-6. In terms of imaging quality, Band 6 highly dominates, but Band 4 could also be a well trade-off depending on the requirements and applications.

For multi-object imaging, Band 4 is further explored, where three cases are considered with the indoor imaging objects: keyboard, mobile phone, USB stick and calculator. In all the respective cases, high-resolution images in good compliance to optical systems are

achieved, which creates the base for autonomous object detection and classification.

Therefore, these high-resolution images are firstly processed for object detection to identify the number of objects and their respective localization in the imaging space. A method is proposed based on the SURF and DBSCAN algorithm and is validated with correct detection of the objects in all the three cases. After the detection, the next step is the classification of the objects. Based on the classification chain with the SVM supervised machine learning classifier, all the objects are correctly classified. Besides, the considered modified objects are also correctly predicted. The validation and prediction accuracy of 88%, and 100 % is achieved, respectively. The proposed method is highly robust.

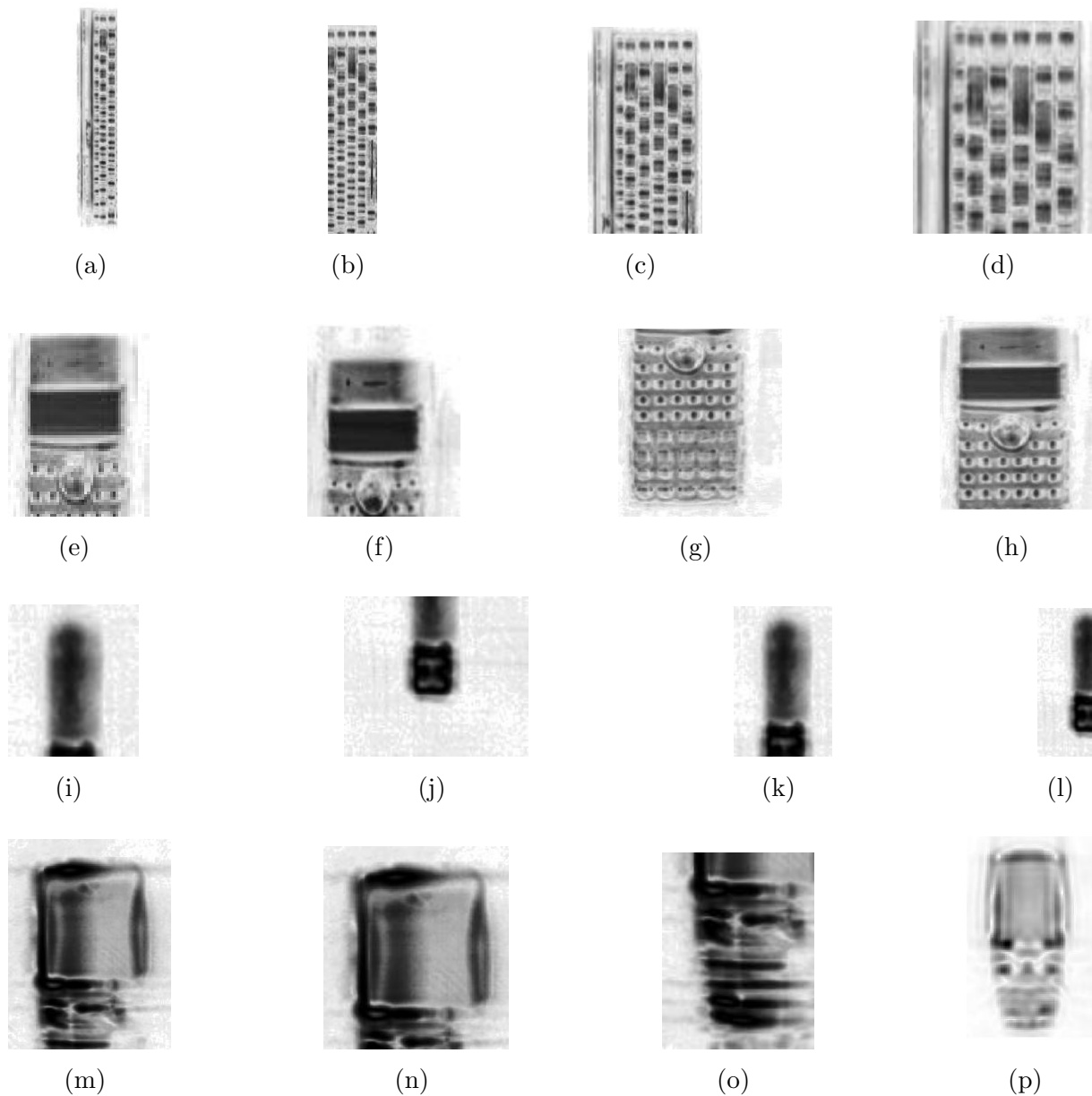


Figure 5-18: Modified SAR images test data set with different dimensions and focus plane (a-d) keyboard, (e-h) calculator, (i-l) USB stick and (m-p) mobile.

# Hardware-Software Accelerated Imaging

One of the other significant challenges of the THz SAR imaging is the requirement of very high computational power due to a large number of pixels (in case of 2D) or voxels (in case of 3D) to be processed ranging from billions to trillions. The pixel intensity is directly related to the imaging target's information, as shown in Fig. 6-1. The value or intensity at voxel  $\mathbf{V} = (i, j, k)$  in the mapped 3D space defines the target scatterer at position  $\mathbf{D} = (x, y, z)$  in the imaging or observation space. The pixel or voxel dimension should be less than the spatial resolution to avoid the scatterer's overlapping. It can be generalized that the higher the number of pixels/voxels, the more accurate information associated with the spatial resolution of the target can be obtained.

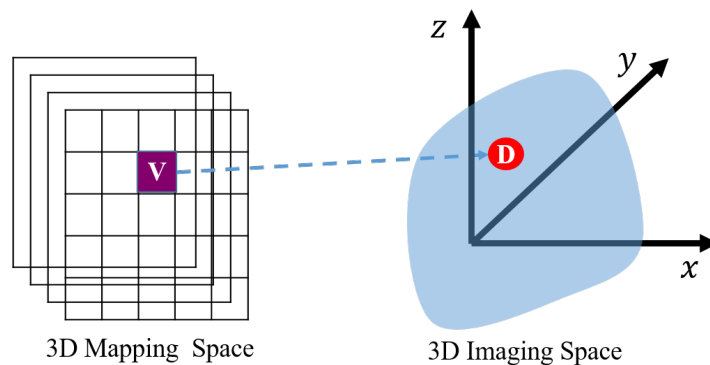


Figure 6-1: Graphical representation of relation between mapping and imagine space.

To estimate the number of pixels to be processed, let's consider firstly an example of generating a 2D image using *BPA* of an area of  $1 \text{ m}^2$  with the pixel dimension of  $0.1 \text{ mm} \times 0.1 \text{ mm}$  at frequency band 1100-1500 GHz and  $L_s = 1 \text{ m}$ . The reconstruction requires processing of  $N_{p,2D} = N_y \times N_i \times N_j = 1 \text{ billion } (10^{12})$  pixels, where  $N_i$  and  $N_j$  are the number of rows and columns in SAR image, and  $N_y = 10^4$  is the number of 1D aperture positions, for example, along  $y$ -axis. The processing requirement drastically increases

with 3D imaging as the number of voxels to be processed given by

$$N_{p,3D} = N_{p,2D} \times N_z \times N_k, \quad (6-1)$$

where,  $N_k$  is number of layers of 2D matrix to generate a 3D image matrix  $\mathbf{I}_{3D}$  of size  $N_i \times N_j \times N_k$  and  $N_z$  is the number of aperture positions, for example, along  $z$ -axis. Extending the same previous example of 2D to 3D image generation of volume  $1 \text{ m}^3$  with extended parameters of  $N_z = N_y$ . It requires  $N_{p,3D} = 100$  trillions ( $100 \times 10^{18}$ ) voxels to be processed. Also to be noted, each pixel/voxel is generated using multiple arithmetic logical floating point operations and therefore the number of pixels/voxels to be processed defined as  $N_p$  or  $N_{p,2D}$  (in case of 2D imaging) and  $N_{p,3D}$  (in case of 3D imaging), should not be confused with the computing industry standard units of floating operation per seconds (FLOPS) such as GFLOPS ( $10^9$ ) or TFLOPS ( $10^{12}$ ).

For a brief overview of the number of pixels to be processed for different imaging areas based on the same parameters from the previous example, Fig. 6-2 summarizes  $N_{p,2D}$  and  $N_{p,3D}$  for the imaging space length  $L$  ranging from 0.1 m to 5 m. Based on  $L$ , 2D area and 3D volume can be given by  $L^2$  and  $L^3$ , respectively. It can be seen in Fig. 6-2, the processing requirement drastically increases for the 3D case. Moreover, SAR image processing also consists of other functions than BPA, such as zero-padding, raw data extraction, inverse-Fourier transform, as explained in Chapter 2 and 5, which also contributes to the requirement of computational power. To generalize, the requirement increases with an increase of imaging area, frequency, bandwidth, and step size.

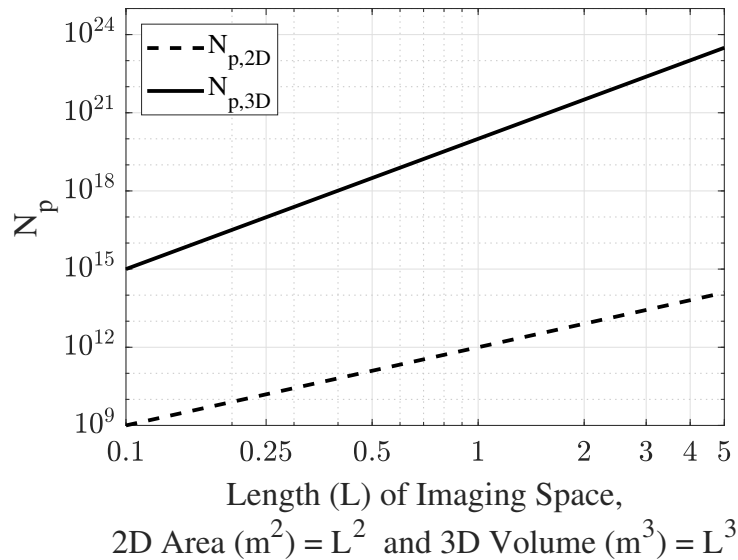


Figure 6-2: Number of pixel and voxel to be processed in 2D and 3D imaging for  $L$  ranging from 0.1 m to 5 m.

It is worth mentioning here that the presented example uses BPA as an image reconstruction algorithm. There are also other algorithms such as Omega-K, RDA [4], and Fast-BPA [89] which might require different computational power, but the algorithms are

well-established for the microwave spectrum. Besides computational requirement, the algorithms also differ in terms of motion errors, spatial resolution and side lobes as reported in [90]. In recent publication, [91], a comparison between algorithms in terms of imaging quality at THz is also reported. Therefore, in this chapter, we address accelerated imaging using BPA, which is self-tested and used throughout the dissertation for generating high-resolution THz images. However, the investigated acceleration scheme can be adapted to different algorithms.

The chapter aims to process the THz SAR 2D and 3D images in the shortest possible time span to address real-time imaging. Therefore, firstly, the CPU-, GPU- and FPGA-based architectures are investigated. Based on findings, a hybrid (optimized) architecture is proposed. For evaluation and comparison, a 2D image data set for the frequency band 220-330 GHz of Fig. 4-16.f and a 3D image data set for the frequency band 325-500 GHz of Fig. 5-4.d are considered.

The chapter is organized as follows. Firstly, Section 6.1 explains the serial and parallel processing techniques. Section 6.2 presents the signal processing architecture. Further, Section 6.3 defines the design methodology. Section 6.4-6.6 presents the CPU-, FPGA- and GPU-based accelerated SAR imaging, respectively. A hybrid processing scheme is proposed and validated in Section 6.7. Lastly, in Section 6.8, a conclusive remark is provided.

## 6.1 Processing Paradigm

Based on the data dependencies, the image reconstruction can be processed with sequential or parallel processing [92]. These techniques are briefly summarized below:

- Sequential processing: It is defined as processing of a single instruction at a time in a sequential order. For example, a computational task or problem consist of several sub-task P1-4 as shown in Fig. 6-3. These tasks are processed by the processing element (PE) one after another. In the presented figure, it shows that first P1 is handled by the PE at  $t_0$  and it is completed at  $t_1$ , where PE begins processing P2. In similar paradigm P3-4 are processed and the complete execution time is  $t_4$ .
- Parallel processing: In this scheme, multiple instructions are processed in parallel by many PE's either with shared or global memory [92] as shown in Fig. 6-3. In this case, the complete execution time is  $t_p$ , where in comparison to serial execution time  $t_1 < t_p < t_2$ . This scheme benefits in reducing the computational time, but it requires additional hardware resources such as multiple PEs and data independencies.

In the presented example, all the tasks P1-4 do not have any inter-dependency but this is not the case in practical scenario. Moreover, there are also many other challenges involved with parallel processing such as memory management and PEs synchronization.

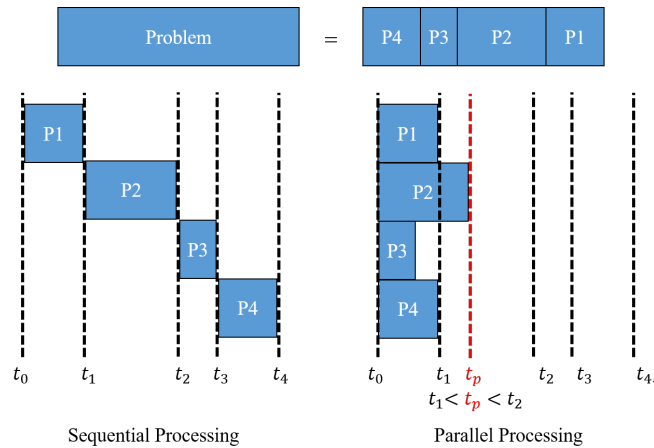


Figure 6-3: Block representation of sequential and parallel processing techniques.

## 6.2 Signal Processing Architecture

In this work, the THz SAR image reconstruction is investigated on three processing architectures CPU, GPU [93], and FPGA [94].

At the Institute of Digital Signal Processing (DSV), the University of Duisburg-Essen, a high-performance computing (HPC) platform is expected to be implemented in the year 2022, and the first design considerations of this testbed is published in [54, 95]. The testbed will consist of multiple computing nodes where each node, as shown in Fig. 6-4, will consist of CPU's, GPU and FPGA platform. This is one of the primary reasons for considering and investigating these three architectures in this work.

Although the main goal is to have real-time image processing for a UAV/drone-based THz SAR, radio frontends at these frequencies are commercially unavailable. Therefore, currently, we limit the real-time operations only for image reconstruction as off-line processing. The time for raw data generation is not taken into consideration. This section briefly presents the design consideration of the proposed architecture, which is the basis for the findings in this section.

The objective of the testbed is to support material characterization, sub-mm localization and imaging, and massive multiple-input multiple-output (MIMO) based millimeter Wave (mmWave) communication. Here, the testbed is described from the THz SAR imaging perspective. For other perspectives, it is described in [54, 95]. Regarding the THz SAR, the aim is to generate raw data and parallelize image processing at a larger scale to produce real-time results. The hardware modules of one of the nodes of the testbed are shown in Fig. 6-4. It is composed of a Signal Processing Platform (SPP) and a high-frequency frontend. The SPP for the testbed in Fig. 6-4 is the decentralized processing unit (DPU) as Node 1 and includes software-hardware accelerators as PEs such as FPGA, CPUs, and GPU. For data memory management, inter-node communication, and storage, the HPC platform includes infiniband and ethernet technology. The SPP follows the decentralized processing principle by distributing the processing task among several nodes to reduce the computational complexity. The transceiver module for the

presented testbed is a VNA (can also be a high-frequency radar frontend) with THz extenders mounted on a multi-dimensional motorized stage. To capture backscattering from different angles, the material under test is mounted on a circular stage.

The proposed architecture fits well for real-time imaging supported by a single DPU or multiple DPUs based on the requirements. It also supports image processing with cloud computing [96], which might be necessary for a realistic UAV-based 3D THz SAR imaging environment. As the payload carried by the UAV is limited, cloud computing can be performed on the SPP. Under this scheme, the low computational algorithms are performed on the energy efficient embedded platform linked with the UAV. Whereas the high computational algorithms are performed on the SPP (single or multiple DPUs), and only the computed results are sent back to the embedded platform.

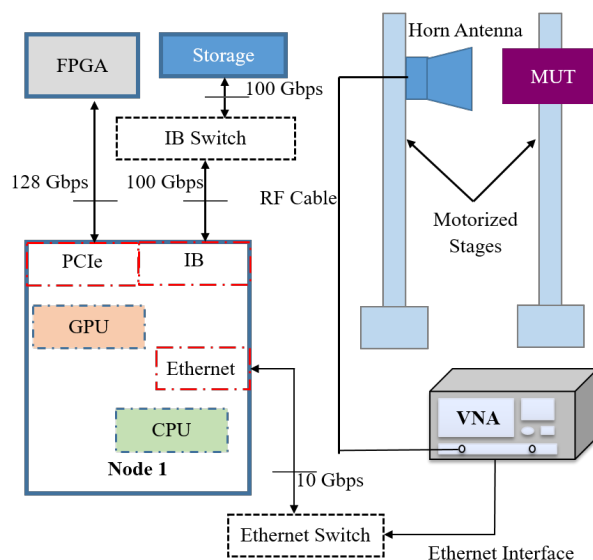


Figure 6-4: Hardware modules of signal processing architecture.

Supported by the above ideology, three systems are considered in this dissertation to investigate accelerated THz imaging. The system specifications are provided in Table 6-1. System 1 is a standard desktop with Windows 10 operating system (OS) and used in a remote server configuration. In contrast, system 2 and 3 is a cluster node and GPU server, respectively. Also, analogous to system 2, system 4 is a cluster node. Systems 2-4 are equipped with Linux distribution OS. Here, system 1 is considered mainly for two reasons. First, to use licensed applications such as MATLAB [46] and second for referencing the enhancement with the cluster computing. Moreover, systems 2 and 4 are nodes of the test cluster for the foreseen architecture described above.

For System 3, the author would like to thank the Faculty of Physics at the University of Duisburg-Essen for providing access to run some testbench on this HPC platform. In terms of usage, systems 1 and 2 are used for development, initial testing, and debugging, whereas systems 3 and 4 are primarily used for the final design.

Table 6-1: System specifications.

Parameter	System 1	System 2	System 3	System 4
Usage mode	Standard	Cluster node	GPU Server	Cluster node
Operating system	Windows 10	Linux centos 7	Linux centos 8	Linux centos 7
CPU product	Intel core i7-4790	Intel xeon CPU E5-2630 v4	2×AMD EPYC 7742	AMD Ryzen 3990X
CPU base frequency	3.60 GHz	2.20 GHz	2.25 GHz	2.9 GHz
# of CPU sockets	1	2	2	1
# of CPU cores/socket (CPUs)	1	10	64	64
RAM	24 GB	64 GB	1 TB	128 GB
Nvidia GPU product	GeForce GTX 750 Ti	Tesla K40C	6×Tesla V100S	RTX A6000
GPU memory	2 GB	12 GB	6×32 GB	48 GB

### 6.3 Design Methodology

The design methodology for accelerated THz SAR image reconstruction is shown in Fig. 6-5. The first fundamental parameter is the programming **Environment** selection, and the preference is to use license free sources such as Python [97], and CUDA [98]. Besides, the objective is to have a portable and scalable environment. The licensed sources such as MATLAB provide an easy high-level interface, but it lacks portability (as required license on each node) and scalability features in consideration of the HPC platform. A comparative analysis between MATLAB and Python is provided in this chapter from the SAR image reconstruction (iREC) perspective. The following selection is the **Architecture** which is described briefly in the previous Section 6.3. Therefore, iREC is investigated with all three architectures. Based on the findings, the best-suited architecture (or architectures) is considered for the final design.

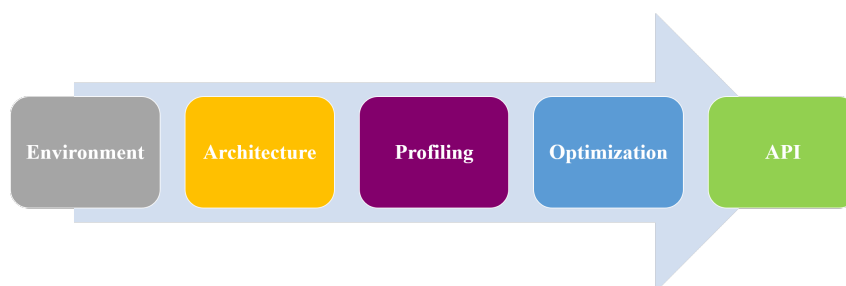


Figure 6-5: Design methodology workflow.

The signal processing of SAR 2D and 3D iREC is explained in detail in Sections 2.4 and 5.1, respectively. The reconstruction process can be summarized with four blocks

in a chain as shown in Fig. 6-6. The blocks are data extraction, zero-padding (Z-P), inverse-fast Fourier transform (i-FFT), and backprojection (BP). **Profiling** is performed on these blocks, and hot-spots are estimated in the 2D image reconstruction (2D-iREC) and 3D image reconstruction (3D-iREC). Especially for 3D-iREC, either a 3D data set is followed through the chain, or a 2D data set is iterated over the chain. The selection depends on the memory consumption and computation time supported by the profiling.



Figure 6-6: Block representation of SAR image processing chain.

The estimated hot-spots are optimized depending on the architecture and processing paradigm. The goal is to maximize the **Optimization** in accordance with the available hardware resources. Based on the final optimized design, an application-specific interface (**API**) for a 2D- and 3D-iREC is to be created. The API inputs are measurement data, imaging parameters, and output is a 2D/3D THz SAR image as shown in Fig. 6-7 (left). The developed API eases the design to be used by the vast majority of the users. It simplifies the complex accelerated image reconstruction modules and provides the necessary interface between the raw data and the SAR image.

The API will be implemented on SPP described in previous Section 6.3, and the block diagram of SPP is shown in Fig. 6-7 (right), which takes a stream of data from input modules and provides the output data. It handles the processing and memory management on cluster nodes.

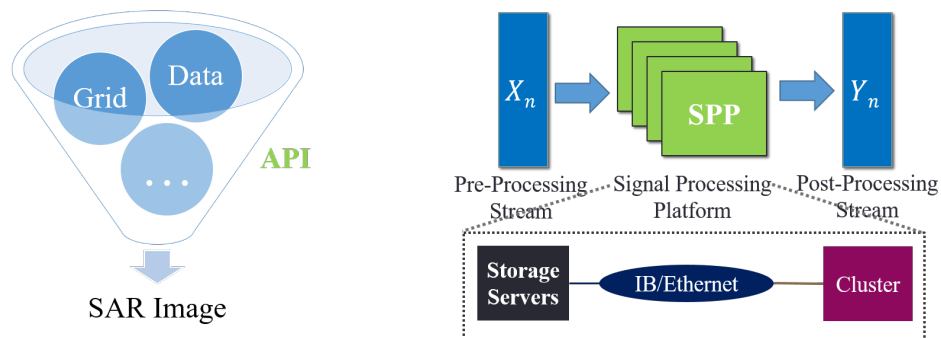


Figure 6-7: Overview of (left) API and (right) SPP.

## 6.4 CPU-based

This section presents the results of iREC based on CPU using both serial and parallel processing techniques. The considered environments are MATLAB and Python. For MATLAB as a licensed platform, the investigation is performed only for reference analysis

and system 1 is used. For the Python environment, systems 2 and 3 are used up to 10 and 64 cores, respectively. The objective is to use a high-performance cluster platform. The available cluster nodes (system 2) at the Institute of Digital Signal Processing motivate open-source environments to make proper usage of the cluster performance. For example, different MATLAB licenses [99] are required for individual or distributed cluster use of parallel computing toolbox [100].

The standard terms for serial and parallel processing on CPU are defined as single-core and multi-core processing, which are addressed in this section.

### 6.4.1 Single-core Processing

In this processing scheme, iREC blocks and their internal instructions are executed in a sequence. It is implemented in both MATLAB and Python. Five imaging area and surface area ranging from  $6.25 \times 100 \text{ cm}^2$  to  $225 \times 100 \text{ cm}^2$  and  $1.5 \times 100 \text{ cm}^2$  to  $37.5 \times 100 \text{ cm}^2$  in case of 2D- and 3D-iREC are considered, respectively. These areas and surface areas are associated with a square and cubic rectangular grid with a pixel and voxel volume dimension of  $0.5 \text{ mm} \times 0.5 \text{ mm}$  and  $0.5 \text{ mm} \times 0.5 \text{ mm} \times 0.5 \text{ mm}$ , respectively.

Fig. 6-8.a shows the logarithmic plot of 2D-iREC time (or 2D-iREC computation time) using MATLAB. The computation time  $T_c$  increases significantly with an increase in the imaging area. Traditionally, each pixel in the BP-block is processed in a singular form which is the most dominant factor in the  $T_c$ . The BP-block consists of 3 nested loops. Two of them are associated with estimating intensity of each pixel in a 2D imaging grid. The third loop is associated with iteration over the length of  $L_s$  as presented in eq. (2-16). It can be optimized by reducing the two loops for estimating each pixel intensity with the use of direct matrix operations. As a basic example, consider a 2D matrix multiplication  $\mathbf{C} = \mathbf{A} \times \mathbf{B}$ , where  $\mathbf{C}$ ,  $\mathbf{A}$  and  $\mathbf{B}$  are 2D matrices or arrays. It would require two loops with a length of rows and columns to estimate each index of  $\mathbf{C}$ . High-level optimized libraries can be used for direct multiplication from client-side (user) to cancel out the loops. Here, the input to the high-end computing library are the matrices  $\mathbf{A}$  and  $\mathbf{B}$  and the output is  $\mathbf{C}$ . MATLAB does the same thing at the back-end.

In Fig. 6-8.a,  $T_c$  is shown with traditional and optimized (indexed with subscript “op”) manner. The gain with  $2\text{D-iREC}_{\text{op}}$  increases with the area of the imaging grid. The mandatory condition for this optimization scheme in SAR processing is

$$\dim(\mathbf{X}) = \dim(\mathbf{Y}) = \dim(\mathbf{Z}), \quad (6-2)$$

where  $\mathbf{X}$ ,  $\mathbf{Y}$ ,  $\mathbf{Z}$  are associated with  $x$ -axis,  $y$ -axis, and  $z$ -axis for estimating range  $\mathbf{R}$  defined in eq. (2-7) (in case of 2D-iREC) and in Section 5.1 (in case of 3D-iREC), respectively.

Based on the  $2\text{D-iREC}_{\text{op}}$  scheme, the  $3\text{D-iREC}_{\text{op}}$  is implemented and results are presented in Fig. 6-8.b. Comparison to 2D,  $T_c$  is much higher which is well definable from the requirement analysis provided in eq. (6-1). To summarize MATLAB-based single-core results, for 2D-iREC and  $2\text{D-iREC}_{\text{op}}$ ,  $T_c$  is in the range of  $\sim 25\text{-}321$  sec and

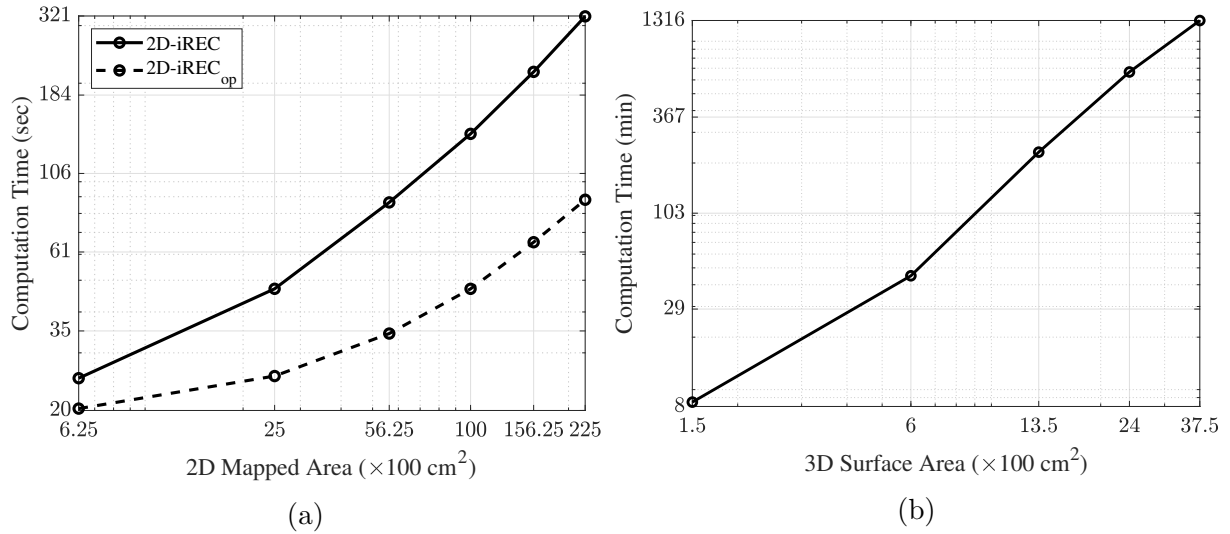


Figure 6-8: MATLAB-based execution time for (a) 2D-iREC and iREC<sub>op</sub> (indexed with subscript “op”), and (b) 3D-iREC<sub>op</sub>.

$\sim 22$ -88 sec, respectively. Whereas for 3D-iREC<sub>op</sub>,  $T_c$  is in the range of  $\sim 8$ -1361 min ( $\sim 0.13$ -22 hours) based on respective imaging surface area. The timings are calculated using tic-toc operation provided by MATLAB [101].

Further to address the open-source environment, the reconstruction chain is implemented with Python (version 3). Table 6-2 shows the list of high-end computing libraries used in the implementation. The computation time for Python-based implemented design 2D-iREC<sub>op</sub> and 3D-iREC<sub>op</sub> for the complete chain (indexed with subscript “cmp”) is shown in Fig. 6-9. For hot-spot estimation in the processing chain, profiling is performed. It is estimated that the BP-blocks consumes  $\sim 40$ -98% in 2D-iREC<sub>op</sub> and  $\sim 83.5$ -99.9% of the  $T_c$  or  $T_{cmp}$ , based on the imaging area as shown in the curve (indexed with subscript “bp”) in Fig. 6-9. Therefore, BP-block is further considered with parallel processing for optimization.

Table 6-2: List of python libraries used for single-core processing.

Library	Task
NumPy [102]	Provide N-dimensional arrays and numerical computing tools
SciPy [103]	Extract measurement data and for Fourier Transform operations
Cmath module [104]	Mathematics with complex numbers
Time module [105]	Time-stamp recording and conversions
Matplotlib [106]	Visualization

Moreover, Fig. 6-10.a and b represents the comparative analysis of the total execution time between MATLAB and Python-based implementation for the 2D and 3D case, respectively. Although the systems are different (system 1 for MATLAB) and (system 2 for Python), MATLAB seems to dominate with a larger area, and Python dominates

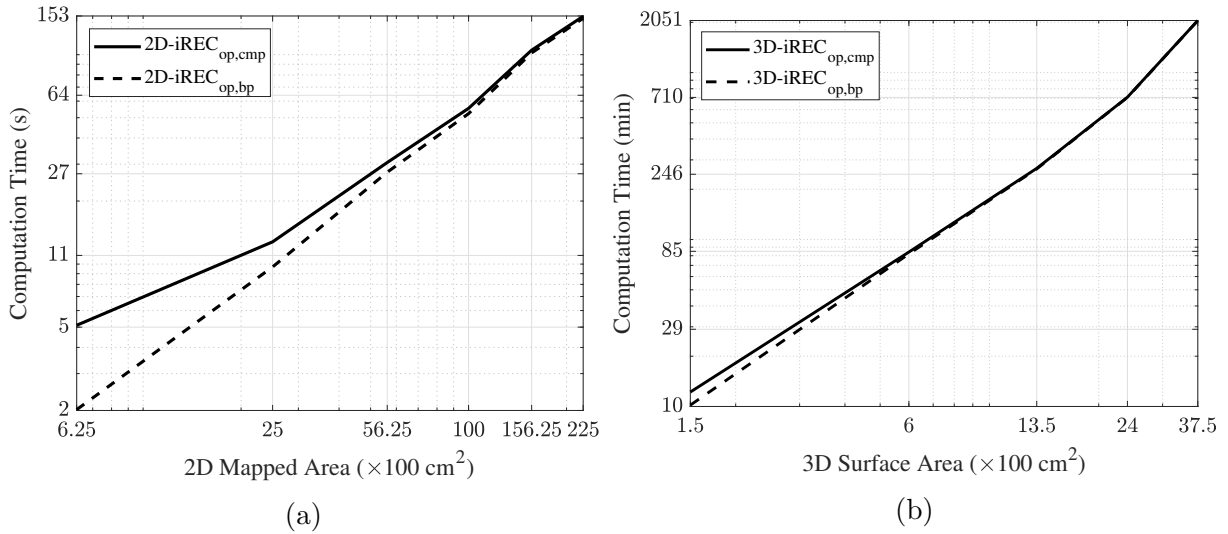


Figure 6-9: Python-based implementation: comparison with complete iREC chain execution time (indexed with subscript “cmp”), and profiling results of BP-block time (indexed with subscript “bp”) for (a) 2D and (b) 3D imaging.

with a smaller area for the 2D case. The data size to be processed is directly proportional to the imaging area as described in Section 6.1. In the case of 3D, MATLAB-based implementation is estimated to be more effective. It is well-defined from licensed source perspective as at the back-end (hidden from user/client) highly optimized logic, memory management, and libraries are used. In Python-based implementation, the user is the expert in optimizing the design using open-source libraries and also managing the logic and memory. The objective is to down-scale the computation time using parallel processing techniques. One of the methods, CPU-based multi-core processing, is addressed in the

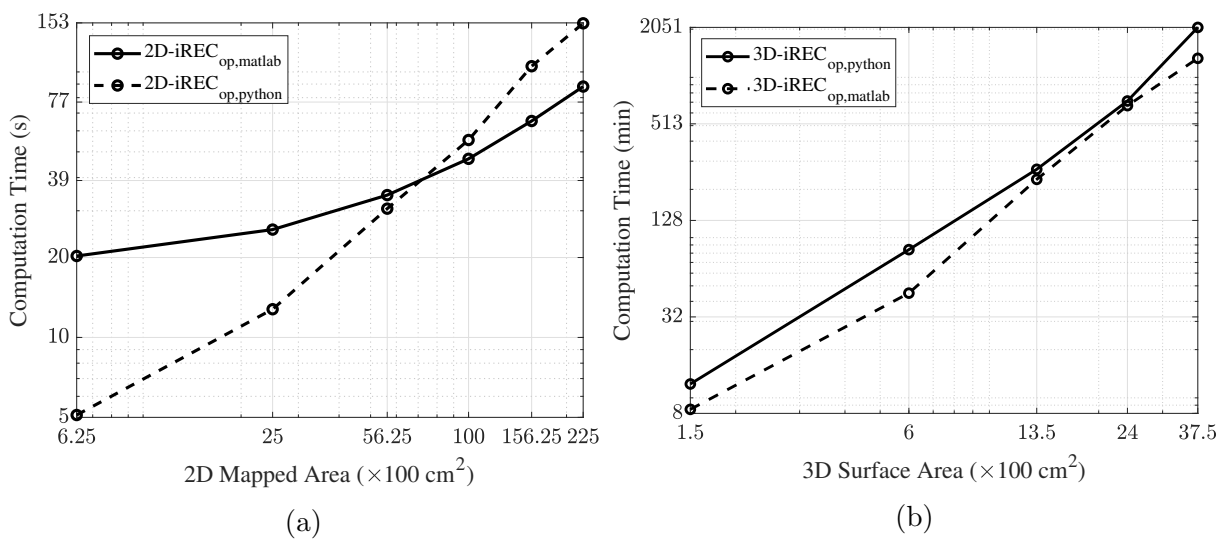


Figure 6-10: Comparison of single-core execution time with MATLAB and Python (a) 2D and (b) 3D imaging.

next section, which further clarifies the comparative analysis.

### 6.4.2 Multi-core Processing

To provide a brief explanation of multi-core processing workflow, the cores are actual available hardware resources, which can process an individual task or solve a common problem jointly. From the software perspective, the job assigned to the cores is handled by multiple processes, where each process further assigns the tasks or sub-tasks to numerous threads [93].

Based on the estimated hot-spot in the chain, BP-block is implemented with multi-core processing. As described in the iREC optimization concept in Section 6.4.1, the BP-block in 2D imaging after optimization only consists of one loop iterated  $N_y$  times, where  $N_y$  is the number of azimuth positions. In MATLAB based multi-core implementation, the  $N_y$  iterations are paralleled among 4 cores using *Parfor* [100] function. The BP-block in 3D imaging consist of  $N_y \times N_z \times N_k$  iterations, where  $N_z$  is the number of elevation positions, and  $N_k$  is number of 2D layers in  $\mathbf{I}_{3D}$  as also defined in the beginning of this chapter. Therefore, in this case,  $N_y \times N_z \times N_k$  iterations are distributed among 4 cores. The execution time based on this methodology (indexed with subscript “parallel”) for the 2D and 3D case is shown in Fig. 6-11.a and b, respectively. The figures also include the curve with serial processing execution time (indexed with subscript “serial”). As explained above, in CPU-based multi-core processing, each core generates multiple threads/processes that handle or process the task assigned to the core. Therefore, the thread generation, management, and synchronization for concurrent data are overhead in this processing scheme. In MATLAB-based results, it can be framed that the overhead dominates. Therefore, in the region of the smaller area of 2D and 3D, the multi-core processing time is higher than the serial (single-core) execution time. In this type of implementation, the multi-core looks effective only in processing big data sets associated with a large imaging area. Based on the achieved results, the speedup =  $\frac{T_{ser}}{T_{par}}$ , where  $T_{ser}$  and  $T_{par}$  are the computation time with sequential and parallel processing, in case of 2D and 3D imaging is in the range of  $\sim 0.78$ -1.06 and  $\sim 0.7068$ -1.42, respectively.

For Python-based multi-core implementation, message passing interface (MPI) standard is used with library MPI for Python *mpi4py* [107]. The standard defines the protocols to exploit multi-processing among a single node or cluster of nodes, and the library *mpi4py* provides the functions based on the standard for the Python environment. In this scheme, each processor or core is given a unique rank for identification. The rank remains constant throughout the execution of the program. Compared to another multi-processor standard Open Multi-Processing (OpenMP) [108], MPI is considered as it supports cluster computing with distributed memory, whereas OpenMP provides shared memory multi-processing. In this work, the objective is to develop an accelerated THz SAR imaging API, which is scalable to cluster of nodes.

Applying the same principle of hot-spot optimization, the BP-blocks iterations are scattered among the provided cores. For the 2D imaging case, the execution time is

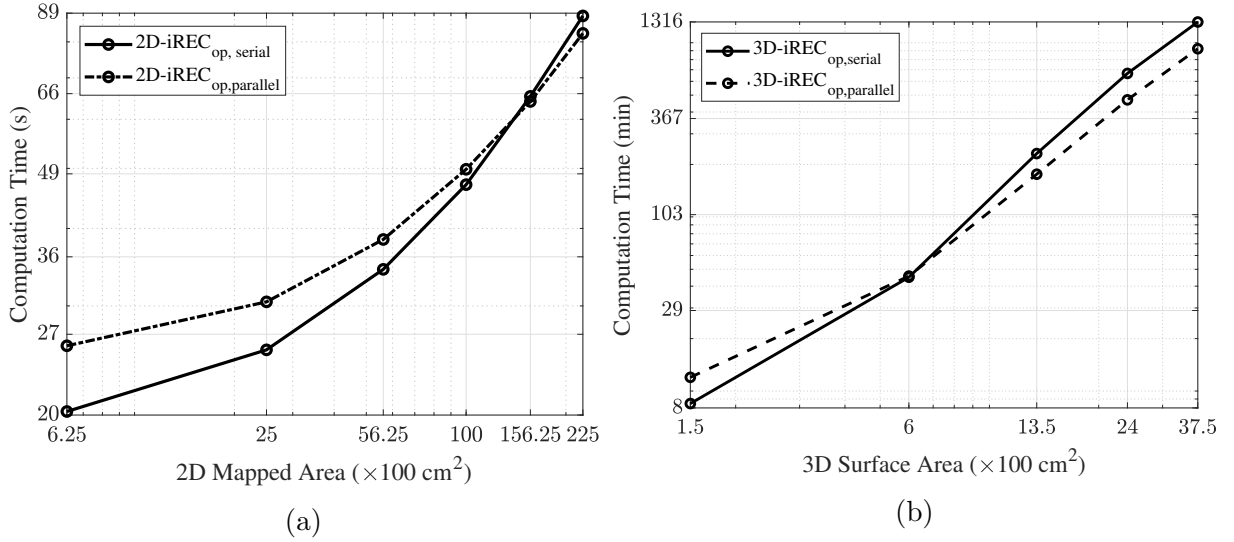


Figure 6-11: Comparison of MATLAB-based serial and parallel processing execution time for (a) 2D and (b) 3D imaging.

recorded with 1, 2, 4, 8, and 10 cores with system 2 and 64 cores with system 3. The results are summarized in Fig. 6-12.a, here the subscript “#core” defines the number of cores. The speedup with 64 cores in comparison to a single-core range from  $\sim 2.3$  to  $\sim 13.6$  with respect to the mapped area. Following the same optimization principle, the recorded 3D-iREC execution time with 1, 8, and 10 cores on system 2 and 64 cores on system 3 are shown in Fig. 6-12.b. With 64 cores, the speedup in the range  $\sim 4.8$ -9.11 is achieved with respect to the mapped area.

The multi-core Python-based design is much more effective than the MATLAB-based as a certain speedup is achieved even with 4 cores. Whereas, in the case of MATLAB-

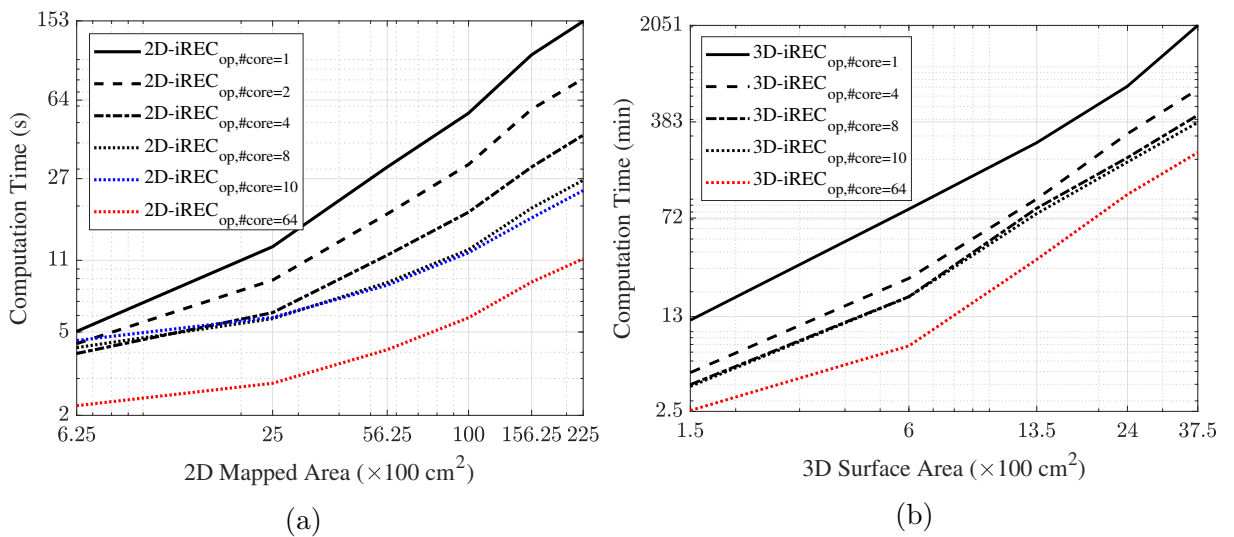


Figure 6-12: Comparison of Python-based serial and parallel processing execution time for (a) 2D and (b) 3D imaging.

based design, the execution decelerates for most of the SAR region in both cases of 2D and 3D. Therefore, the Python-based acceleration is considered further for the following sections involving CPUs.

## 6.5 FPGA-based

In this section, the acceleration is investigated with FPGA-based architecture, which is a reconfigurable architecture. Besides, some of the latest FPGA platforms support dynamic and partial configuration, which benefit in configuring the system at run-time [109]. It is used as a hardware accelerator and its applications are being extended from small scale to large scale computational environment such as in big data centers [110]. Based on the presented SPP in Section 6.2, the FPGA platform can support the other hardware resources such as CPU and GPU with offloading a computational task. However, these types of FPGA platforms are generally not suited for UAV-based THz SAR imaging due to limited payload and especially in terms of energy efficiency. To realize the UAV-based THz SAR imaging and MARIE applications, the objective is to build a high-performance embedded computing architecture with high-energy efficiency in **MARIE** project **S05** mainly based on FPGA and application-specific integrated circuit (both can be implemented with HDL) solutions. From the THz SAR imaging perspective, iREC involves extensive data set processing as presented in Section 6.4, which would require both on-board and off-board processing, such as cloud computing [96] to address real-time imaging. Therefore, the section investigates performance with hardware description language (HDL) based THz SAR iREC.

It is to be noted that the HDL-based design act as a hardware accelerator providing high performance, but the implementation is quite complex due to the low-level massive parallelization, very long (an optimized platform design can take several months to years depending on the scale of optimization), and requires a dedicated platform with large memory size. Therefore, in this section, it is only investigated for reference purposes to exploit the performance and a rough comparative analysis to other architectures discussed in this work.

The accelerator blocks of the chain are implemented using register transfer level (RTL) simulation in support of the bachelor thesis [41] and collaboration with Mr. Ahmed Kamaledin Atef from the Chair of Adaptive Dynamic Systems at the Technische Universitaet Dresden, Germany .

A similar data set to the presented 2D imaging in this chapter with the same frequency band and number of frequency points but a different object is considered for the implementation. The design is implemented using Verilog [111] as HDL with environment Xilinx Vivado design suite [112] and synthesized for a Xilinx Zynq-Ultrascale+ ZCU102 FPGA board [113]. The detailed implementation design is available in the publication [114]. Here, the execution time is reported for a computed image with grid and pixel dimensions of  $250 \times 250$  and  $1 \text{ mm} \times 1 \text{ mm}$ , respectively and resulting in an imaging area of  $625 \text{ cm}^2$ . The major issue experienced in HDL design in consideration of the selected

board is the limited memory size. Therefore, small-scale data is considered. The adaption makes the design synthesizable in reference to the considered board. The recorded execution time of RTL simulations is around 294 ms and 58.8 ms with a clock frequency of 100 MHz and 500 MHz, respectively. The computation time can be predicted based on the available clock frequency as shown in Fig. 6-13. The prediction is based on the analyzed number of required clock cycles for each block and complete chain. There will be additional overhead in the final executed design on FPGA due to the communication between the embedded processor and the FPGA platform. However, the number of required clock cycles for a particular kernel/block operation will be the same as in the testbench results.

To summarize, the investigation with the FPGA-based design, the recorded execution time shows a significant enhancement compared to other architectures, but the design is best suited with small-scale data sets. UAV-based THz SAR imaging fits well with the topology of sharing the computational task with on-board (energy-efficient FPGA) and off-board resources (CPU, GPU, and high-performance FPGA).

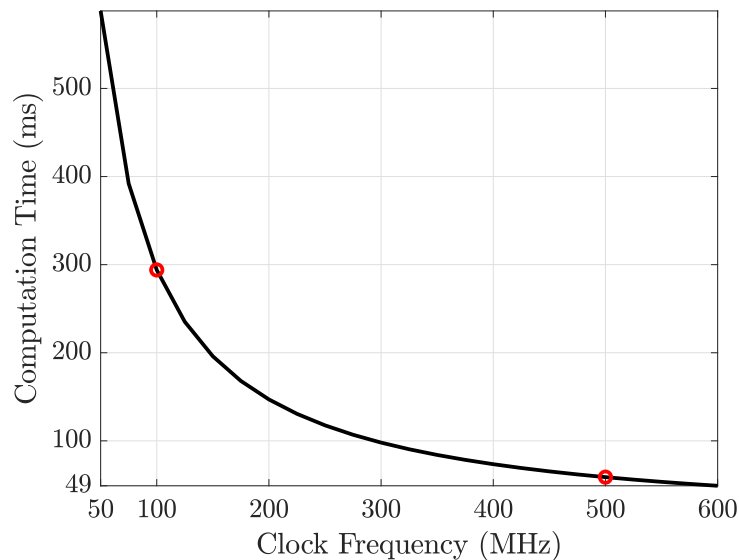


Figure 6-13: Computation time prediction at RTL simulation for HDL design with different clock frequency.

## 6.6 CPU-GPU-based

This section evaluates GPU-based THz imaging acceleration. In this scheme, GPU platform collaborates with CPU, where the CPU is defined as a host and GPU as a device. The host is responsible for scheduling jobs and providing necessary data to the GPU memory. In contrast, the device executes a computational task and handover the results to the user via CPU memory [93]. The primary difference between CPU-computation and GPU-computation is the existence of massive transistors for data processing in GPU. Therefore, GPU is specialized for parallel applications [115]

For task execution on Nvidia GPU, compute unified device architecture (CUDA) provides the required necessary parallel computing platform [98]. CUDA kernels are written in C++ [116] programming language, and CUDA threads execute these kernels. To integrate these kernels in a Python-based environment, an open-source PyCuda [117] library is used. It provides the necessary APIs to access CUDA computation [117].

The single-core Python-based model presented in Section 6.4 is extended with the GPU implementation of the BP-block. The block is the hot-spot in the total computation time in both 2D and 3D imaging cases. Therefore, the optimization is investigated by executing this block on GPU. Fig. 6-14.a presents the results of GPU-based implementation (indexed with subscript “gpu”) for the 2D imaging case executed on System 2. The computation time is in the range of  $\sim 5$ -7 sec based on the imaging area. The GPU-based provides good performance. For comparative analysis and to summarize the achieved results so-far, Fig. 6-14.a includes the curves of MATLAB-based serial and parallel execution (with 4 cores) and CPU-based serial and multi-core performance with 10 and 64 cores. In the smaller imaging region, the multi-core-based implementation with 64 cores seems to be efficient. In contrast, the GPU-based design shows better performance with a larger imaging region.

To further investigate the GPU-based design, profiling is performed, and the results are summarized in Fig. 6-14.b. The results present two dominating blocks: i-FFT (indexed with subscript “ifft”) and BP. The i-FFT block consumes around  $\sim 36$ -50% of the total computation time, but block time remains nearly constant throughout the mapped area due to the same i-FFT length. In contrast, the BP-block time increases with the imaging or mapped area. This is well defined by the increase in grid size computed by

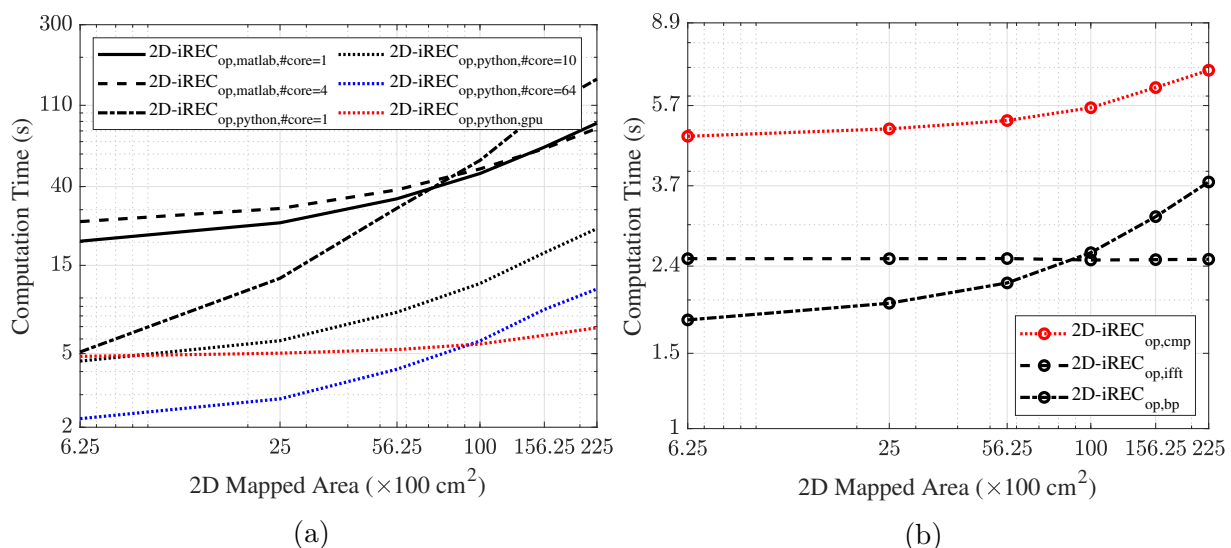


Figure 6-14: Comparison of 2D-iREC (a) execution time with CPU-GPU based design, single and multi-core CPU based design with MATLAB and Python environments, (b) profiling results of CPU-GPU-based design: total execution time, i-FFT (indexed with subscript “ifft”) and BP block time.

BP-block associated with imaging area.

Based on the achieved results, the CPU-GPU-based design seems promising and effective. Therefore, the design is further optimized to increase the speedup in the next section for both 2D and 3D imaging case.

## 6.7 Hybrid Multi-Processing-Threading CPU-GPU-based

This section presents the final optimized design based on the finding of the previous sections of this chapter. A processing scheme is proposed that includes the performance enhancement from both multi-processing (CPU) and multi-threading (GPU) architectures, termed in this work *Hybrid Multi-Processing-Threading*. This scheme focuses on hierarchy and data processing optimization.

The hierarchy includes MPI standard parallelization among CPU cores and CUDA kernels for GPU multi-threading. In a standard single-core CPU-GPU-based design presented in Section 6.6, around 40-50% of the computation time is consumed by the three blocks before BP. Although the BP is executed on GPU, there is additional overhead before the GPU job, such as kernel initialization, memory allocation, and transfer to the device. The approach is to parallelize the tasks before the GPU execution. This scheme can be well explained from the processing hierarchy presented in Fig. 6-15.

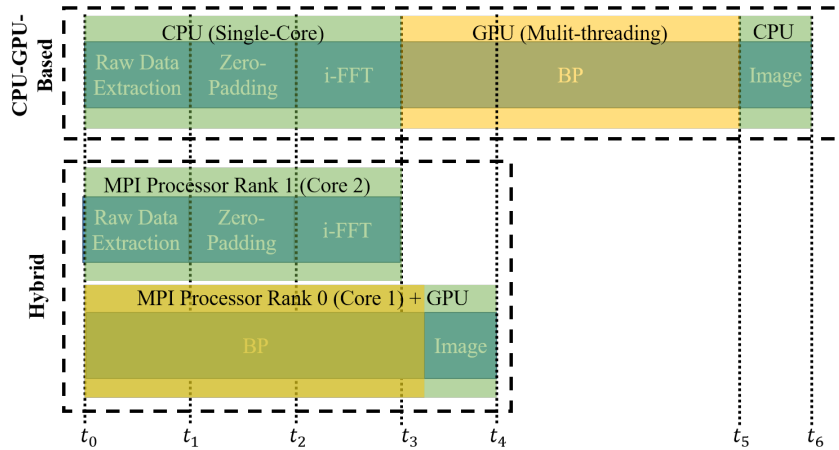


Figure 6-15: Hybrid processing hierarchy.

In the CPU-GPU, workflow chain presented in Section 6.6, the total execution time is  $t_6$  with assumption of  $t_0 = 0$ . Under the hybrid scheme, the task related to the first three blocks in the 2D-iREC chain is allocated to core 2 (MPI rank 1), and BP blocks are scheduled on core 1 as a root core with MPI rank 0. Both the blocks are initiated at same instant  $t_0$ . A time-gain is achieved with GPU-related task (before the GPU job) on CPU carried out simultaneously by the rank 0 processor, which then wait for the i-FFT block output for the GPU job. The MPI-based block communication occurs between the

i-FFT block and BP blocks, which again is an overhead, but the overhead is negligible compared to achieved high performance shown in Fig. **6-16.a** (indexed with subscript “hybrid,Sys2”). Here, the new indexed subscript “Sys#” defines the System# used for SAR iREC.

Further, in this scheme, the data processing is optimized from the memory management perspective at CPU and GPU. The data streams are handled more efficiently if the modulus of length or dimension of the data in respect to the size of a byte (= 8 bit) is 0. Therefore, the data associated with the most dominant blocks is arranged under this scheme. In the case of BP-block, the imaging grid size is increased by a minor dimension, for example,  $512 \times 512$  instead of the previous  $500 \times 500$  for the imaging area of  $6.25 \times 100 \text{ cm}^2$ . Also, the zero-padding and i-FFT length is reduced to  $\sim 64\text{K}$  from the previous case of  $\sim 72\text{K}$ . The CUDA block (different from SAR processing chain blocks) grid size is also considered in this arrangement for parallel processing. In the GPU job, the computation time is relatively less in the range of ms, but one of the primary bottlenecks is the memory management among the GPU threads.

To optimized this bottleneck, a shared memory approach is used. In this case, the memory is shared among the threads of a CUDA block, decreasing the latency associated with local or global memory access [118]. Fig. **6-16.a** presents the 2D-iREC based on this hybrid and optimized processing scheme. Significant improvement is achieved with this processing scheme as the execution time is reduced nearly to half in comparison to the previous best-case of CPU-GPU design presented in Section 6.6.

The enhancement is also recorded with the high-performance GPU (indexed with subscript “hp-GPU”) of System 3 and 4. The execution time results are shown in Fig. **6-16.a**. Besides, the figure also summarizes the performance with different architecture and

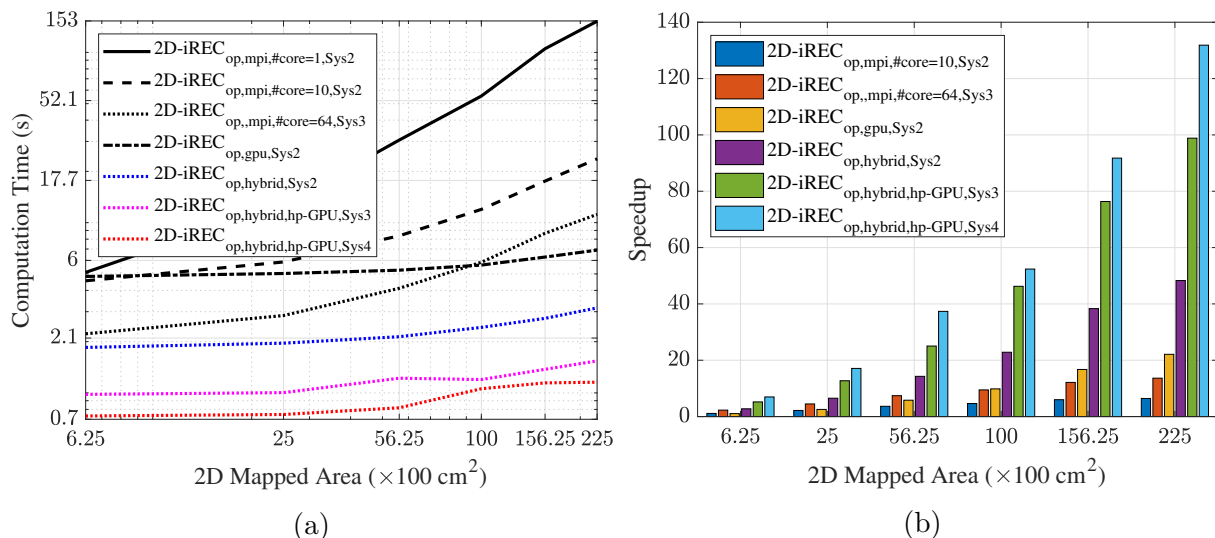


Figure **6-16**: Comparison of 2D-iREC (a) execution time with hybrid processing, CPU-GPU based design, single and multi-core CPU based design with python environment, and (b) speedup between different processing methods and architectures.

methods. Further Fig. 6-16.b presents the summary of the speedup in comparison to single-core CPU-based design with python environment. The proposed hybrid scheme and optimization is very efficient as a maximum speedup of around 132x is achieved for the imaging area of  $225 \times 100 \text{ cm}^2$  which is very promising. The hybrid scheme shows the best performance for all the imaging areas.

This scheme presents computing 2D-iREC chain in  $\sim 0.8$ - $1.156$  sec. Moreover, the BP-block (or Backprojection) computation on GPU is executed in  $\sim 0.5$  ms as shown in the profiling results of this scheme in Fig. 6-17 (indexed with subscript “gpuEXE”). It shows that the device to memory transfer time dominates (indexed with subscript “d2hMEM”).

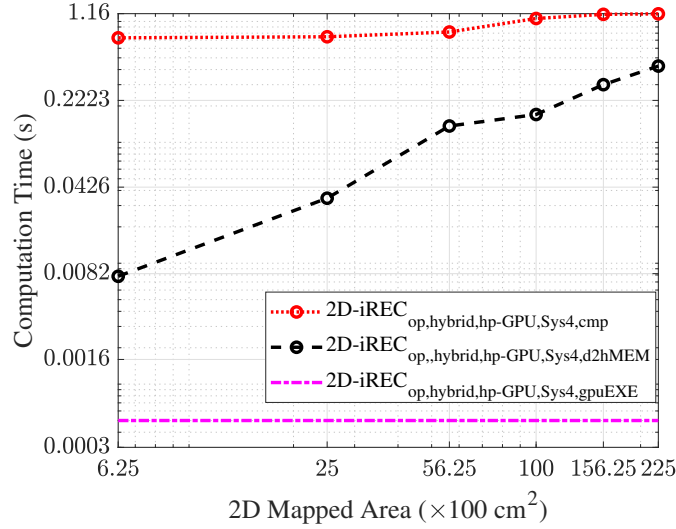


Figure 6-17: Profiling results of 2D-iREC BP-block with hybrid processing: total BP-block time, device to memory transfer time (indexed with subscript “d2hMEM”) and GPU computation time (indexed with subscript “gpuEXE”).

Based on this hybrid scheme, the 3D imaging is optimized. Managing the 3D data at GPU is quite complex than the case of 2D, and an additional minor change in the data set, such as imaging grid size, will highly influence the execution results. Therefore, unmodified data set without shared space is considered for fair evaluation. The execution times of 3D-iREC with hybrid processing with System 2-4 are presented in Fig. 6-18.a along with the curves of different architectures execution time for the comparative analysis. Fig. 6-18.b summarizes the speedup. The execution time has drastically reduced with the proposed scheme, and a speedup up to 64.5x is recorded in 3D-iREC.

Lastly, an API based on a hybrid processing scheme is generated using python modules [119], which takes the imaging parameters as an input and returns the accelerated computed image.

## 6.8 Conclusive Remark

This chapter presented the accelerated THz SAR imaging. Firstly, an analysis based on the number of pixels and voxels to be processed is presented, which defines the requirement

## 6.8 Conclusive Remark

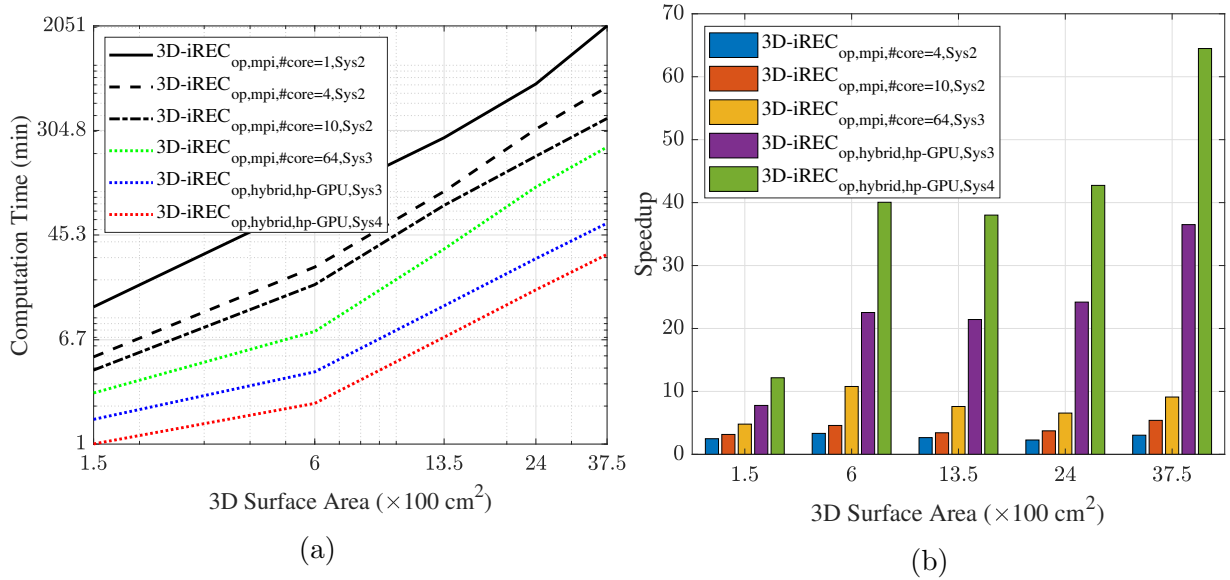


Figure 6-18: Comparison of 3D-iREC (a) execution time with hybrid processing, CPU-GPU based design, single and multi-core CPU based design with Python environment, (b) speedup between different processing methods and architectures.

of high computational power for THz iREC. Supported by the SPP and design methodology, three architectures: CPU, FPGA and GPU, for data processing are investigated. Single-core CPU-based results show the 2D-iREC processing time ranges up to 152.42 sec. A drastic exponential increment is observed with 3D-iREC, where the processing time ranges up to 2051 min (34.18 hours). Based on the findings of different architectures and the proposed hybrid processing scheme, the computation time reduced to 1.156 sec and 31.8 min for the 2D- and 3D-iREC. The maximum speedup of 132x (2D-iREC) and 64.5x (3D-iREC) is achieved. Hence, the proposed scheme shows a significant winning performance for all the different architectures and optimization investigated in this chapter. The method has been further realized into an API which simplifies the complex processing chain and eases the access to broad users by just providing a specific set of imaging parameters as an input.



# Conclusion and Outlook

This chapter concludes the work presented in this dissertation and provides an outlook with initial results on one of the future research topics.

## 7.1 Conclusion

The dissertation investigated SAR technique at the THz spectra, with a focus on the indoor environment. The study is conducted in regard to the novel extension of SAR applications to sub-mm resolution imaging and localization, material characterization, non-destructive testing, and autonomous object detection and classification. The dissertation is firstly supported by the development of the THz SAR simulation framework to virtualize a measurement environment.

**Simulation Framework** is based on calculating EM wave properties at the THz spectrum in 3D space and considering three major entity properties: transceiver, atmosphere, and targets. For validation, the targets of different materials, shapes, and dimensions are designed. The raw data is gathered for the simulated environment and processed with BPA for image reconstruction. The high-resolution reconstructed images validate the framework. Moreover, the framework is used for the investigation of the impact of motion errors and 2D imaging configurations. The simulation-based results are in good compliance with measurements, which further validates the designed framework. To summarize, the presented framework provides the virtualization of an experimental setup based on the properties of a target (for example, permittivity) and transceiver (such as transmit power, polarization and waveform).

Further, a THz simultaneous localization and mapping system (SLAM) is presented to achieve the UAV-based THz SAR environment mapping objective in a GPS lacking indoor environment.

**Simultaneous Localization and Mapping** system objective, to localize the UAV coordinates based on the passive localization system developed in the MARIE project *S04* and mapping the indoor environment, is achieved. The dissertation presents the integration of the sub-mm localization system and THz SAR. Based on the trajectory coordinates

provided by the *S04*, an object present in the room is mapped, and its respective position in the room is also derived using the THz SAR technique.

Minimal trajectory deviations highly modulate the phase at the THz spectrum. Therefore, motion compensation (MOCO) required special consideration for this frequency spectrum.

**Motion Compensation** is one of the primary concerns for UAV-based THz SAR. It is due to high instability in the flying platform and the high-positioning accuracy requirement because of the wavelength in the sub-mm range. Based on the far-field condition, the strict constraint on the amplitude of deviation is  $\lambda/16$ . This accuracy is tough to achieve at the THz spectrum, especially in the case of UAV-based SAR. Therefore, sub-mm translational deviations effects are analyzed, and the new threshold termed as relaxed constraint concerning the trade-off with the image quality is defined. The findings reveal the different positioning accuracy requirements along the range and cross-range directions. It has been found that the impact of errors along the propagation direction, U-D in the proposed geometry, is the most sensitive. On the other hand, the effects of L-R errors in the perpendicular direction to propagation and flying path is the least sensitive. For the presented case at 300 GHz with 50 GHz of bandwidth, the accuracy of 0.25 mm ( $\lambda/4$ ), 5 mm ( $5\lambda$ ), and 20 mm ( $20\lambda$ ) is acceptable with minor artifacts along U-D, F-B and L-R, respectively.

Regarding the generalization of the amplitude of deviation or the cutoff motion error, the relaxed constraint is defined by the condition of  $\Delta\phi \leq \pi/2$ . Based on it, an analytical model is presented to calculate the cut-off motion errors along different dimensions. The estimated cut-off limits are well supported by the simulation and measurement results. For MOCO, the integration solution of localization and SAR is used. MOCO can be considered as an application of SLAM, and the presented results regarding the compensation of the impact of the error validate the proposed method.

After realizing the UAV-based THz SAR and the compensation of non-linear trajectories, the dissertation addressed 2D imaging of indoor objects made of different materials. **2D Imaging** is presented based on two proposed planar aperture imaging configurations, SDR and DR. Firstly, the mapped imaging plane related to the configuration is validated with simulations and measurements. Based on the findings, an optimized mapping geometry is proposed for the case of DR. It is further validated that SDR configuration is more suitable for look-through imaging, whereas DR supports object's surface imaging. Indoor objects of material such as wood, plastic, foam, metal, cardboard, and glass are considered for validation. SAR-focused image is extended with the extraction of geometric properties of the object. Besides defining the maximum sensing range of the objects, an analytical model is presented and validated with measurements. The sensing range is derived from RCS and system parameters, and the model is validated by predicting the received power based on the estimated RCS. For most of the presented objects, the sensing range of  $\geq 10$  m is recorded.

Further, the impact of roughness for the THz SAR imaging is evaluated by considering face mannequins of different roughness indexes. The results present high-quality image

generation with the roughest material due to large backscattering. Nevertheless, the results also provide the theoretical validation of expected high-resolution image generation of an actual human face due to the roughness of the skin. Further analyses are derived in terms of image quality with different bandwidths at the frequency range of 220-330 GHz. As a result high-quality images are generated with 50 and 100 GHz of bandwidth.

In terms of penetration property at the THz spectrum, the concealed and hidden object imaging is addressed. Four different cases are considered, ranging from mapping tiny objects to large objects in concealed/hidden environments. Imaging objects are mapped effectively in most cases, and relative attenuation in the received power due to the concealing environment is also represented.

For volumetric information acquisition, 3D imaging is addressed in the dissertation. **3D Imaging** is addressed with planar aperture imaging configuration by implementing a 2D trajectory. It is of significant relevance to investigate the enhancement in imaging quality at different frequency bands at the THz spectra. Therefore, six frequency bands: 5-10 GHz, 75-110 GHz, 0.22-0.33 THz, 0.325-0.5 THz, 0.85-1.1 THz, and 1.1-1.5 THz are considered for comparative analysis. The band 5-10 GHz is considered only for the reference analysis in the imaging quality, for a shift from microwave (below 30 GHz) to THz region. Two imaging objects are considered in regard to the evaluation of spatial resolution and penetration properties. The results demonstrated a significant improvement in the imaging quality with the shift in the frequency band. However, from the penetration perspective, not much information is acquired above 0.5 THz for the considered object. As a suitable trade-off regarding imaging quality and penetration capabilities, the band of 0.325-0.5 THz dominates. Nevertheless, the quality in regard to surface imaging is significantly improved at 1.5 THz compared to the rest of the evaluated frequency bands.

Further, a multi-object environment with indoor objects, keyboard, calculator, USB stick, and mobile phone is considered to evaluate the highly close-range scattered rich environment imaging. This mapping also creates the base for object detection and classification. Three cases are considered, where in the first two cases, the objects are displaced horizontally and vertically. In case 3, a combination of these two cases is considered. In all three cases, the objects are very well mapped at the spectrum of 0.325-0.5 THz. Besides, the look-through imaging with all these objects is well obtained.

Thanks to the THz spectra and high-resolution imaging at this spectrum, the SAR-based mapped environment of small-scale objects can be extended to autonomous object detection and classification.

**Object Detection and Classification** is addressed using ML technique known in optical or infrared systems due to very high spatial resolution. In this dissertation, this technique is extended and validated to radar-domain. The three cases of the multi-object environment are first considered for object detection and localization in reference to transceiver position. Based on the SURF model, the features and key points are extracted from a grayscale optimized SAR image. The key points are clustered in groups based on the DBSCAN algorithm. Finally, the number of valid clustered groups based on the grouping conditions and group positions provides information on the detected objects.

In all the considered cases, the objects are well-detected.

Extracted objects are input to the SVM-based trained model for classification. For training of the model, supervised ML technique is used. The training data set is collected from many measurement campaigns. Based on the test and split approach, 80% of the data set is used for training and 20% for model validation. The trained model achieved the validation accuracy of 88%. All the objects in the test data set based on the considered three cases are correctly classified, and the prediction accuracy of 100% is obtained.

Moreover, the THz SAR imaging is a high computation task due to the large bandwidth, very high sampling rate, and large synthetic aperture positions.

**Accelerated Imaging** is investigated in consideration of three architectures, CPU, FPGA, and GPU. The results demonstrated the high processing requirement. In the case of 2D-iREC, the maximum recorded time is 152.42 sec with single-core CPU processing. For 3D-iREC, the execution time reaches 2051 min (34.18 hours). Following the presented design methodology and SPP, with multi-core architecture up to 64 cores, the computation time reduced to 11 sec and 225 min for the 2D- and 3D-iREC, respectively. Further, an FPGA-based architecture is also investigated, which seems to dominate with small-scale data set in consideration of energy efficient platform for a UAV-based SAR. The results define the requirement of on-board and off-board processing using technologies such as cloud computing. A significant improvement is achieved with the presented single-core CPU-GPU-based design.

In motivation with the findings of different architectures, topologies, and methods, a hybrid processing scheme is proposed based on multi-core-multi-threaded architecture. The proposed scheme acquired a maximum speedup of 132x in the case of 2D-iREC and 64.5x for 3D-iREC, respectively. The recorded execution time for the SAR processing chain is 1.156 sec and 31.8 min compared to traditional 152.42 sec and 2051 min for the case of 2D- and 3D-iREC, respectively. Especially for 2D-iREC, the achieved processing time of BPA (or BP-block in the presented SAR iREC chain) on GPU with proposed optimized hybrid processing is 0.5 ms with  $3K \times 3K$  pixels. The proposed scheme dominates throughout the presented imaging area. Moreover, based on the proposed method, an accelerated THz SAR imaging API is generated to ease user's access to a broad range.

To summarize, the dissertation addressed a broad range of challenges associated with the THz SAR technique. The presented results in the dissertation validate the THz SAR simulation framework, UAV-based THz SLAM and MOCO, and accelerated high-resolution 2D and 3D THz imaging of single and multi-object environments with extension to object detection and classification.

## 7.2 Outlook

In regards to further novel research in future projects, the following topics seem to be promising:

- MIMO THz SAR: To exploit beamforming gain, variable beamwidth and reduction

in SAR trajectory using arrays as aperture positions.

- THz SAR-based Vital Sensing: To exploit tiny body movements.
- THz SAR-based Non-Line of Sight Sensing: To look around corner or hidden objects.
- THz SAR-based Identification: To exploit the sub-mm resolution for identification of objects.

Initial results on one of the novel future research areas, Non-Line of Sight Sensing, are achieved for conceptual validation and published in [120].

### 7.2.1 THz Non-Line of Sight Sensing

State-of-the-art THz testbed demonstrations with bandwidth  $>100$  GHz are focused on a line of sight (LoS) sensing. In this work, the multipath propagation at the THz spectrum is exploited, and the first results of N-LoS THz sensing up to the fifth order of reflection at an extended range of  $>6$  m are presented.

Two cases of N-LoS sensing are considered. For case 1, with imaging scene shown in Fig. 7-1.a, the objective is to detect and range a metal plate M2 placed in a separate room next to the transceiver. To divert the beam towards M2, a metal plate M1 is mounted at  $45^\circ$  in front of the transceiver at a distance of 1.8 m. M1 also makes a similar angle with M2 at a length of 4.5 m. The expected propagation path is shown with a red arrow, and also, the distance between the objects is shown in Fig. 7-1.a. The metal plates provide specular reflection and follow the laws of reflection. Moreover, the measurements are performed with channel normalization. The time-domain response of the captured received signal in the absence and presence of the M2 is shown in Fig. 7-1.b and c, respectively. It validates the detection and ranging of long-range N-LoS object M2 at 6.3 m.

For case 2, with imaging scene shown in Fig. 7-2.a, the objective is to detect and range a corner reflector (CR) placed in the same room but outside the antenna beam footprint. Instead of one metal diverting the beam as in case 1, two metal plates M1 and M3 are used, which makes an angle of  $45^\circ$  to each other. Also, M1 and M3 make the same angle with transceiver and CR, respectively. Fig. 7-2.b and c shows the time-domain results with and without CR. The results validate the detection of CR at 7 m. The peak before the CR is from the cluttered environment close to the CR, and it also shows up in the case without CR in Fig. 7-2.b. Moreover, for transmission mode, the path length would be defined as doubled, 12.6 m and 14 m in accordance to case 1 and 2, respectively. Also, in cases 1 and 2, the third and fifth-order reflections are captured, respectively.

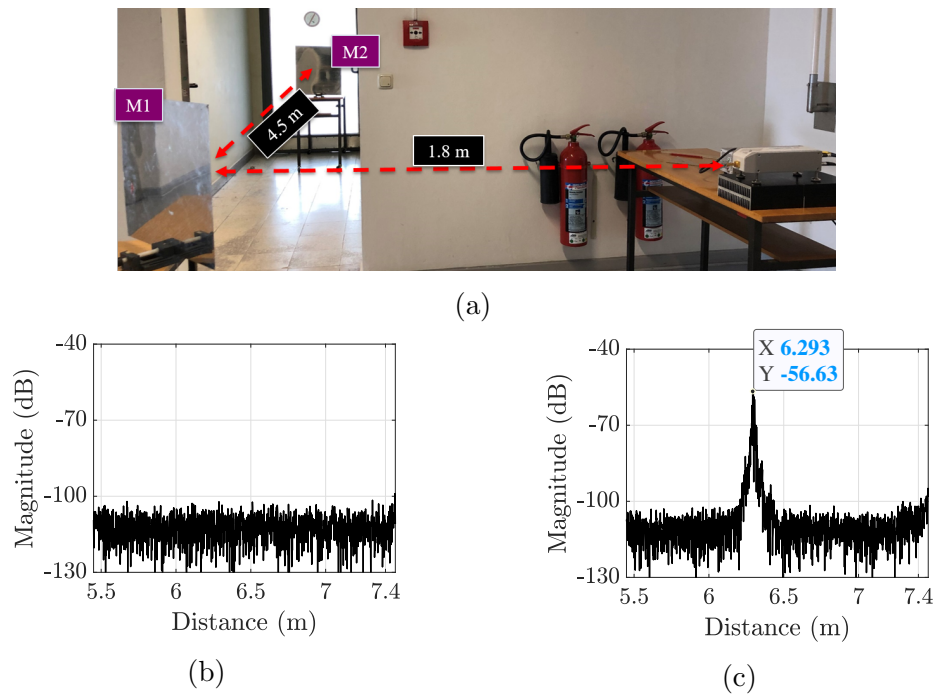


Figure 7-1: N-LoS detection and ranging (a) scene 1: metal plate M2 sensing (third order reflection) via reflection from M1, and measurements results: (b) time domain response of without M2 and (b) with M2 detected at 6.3 m.

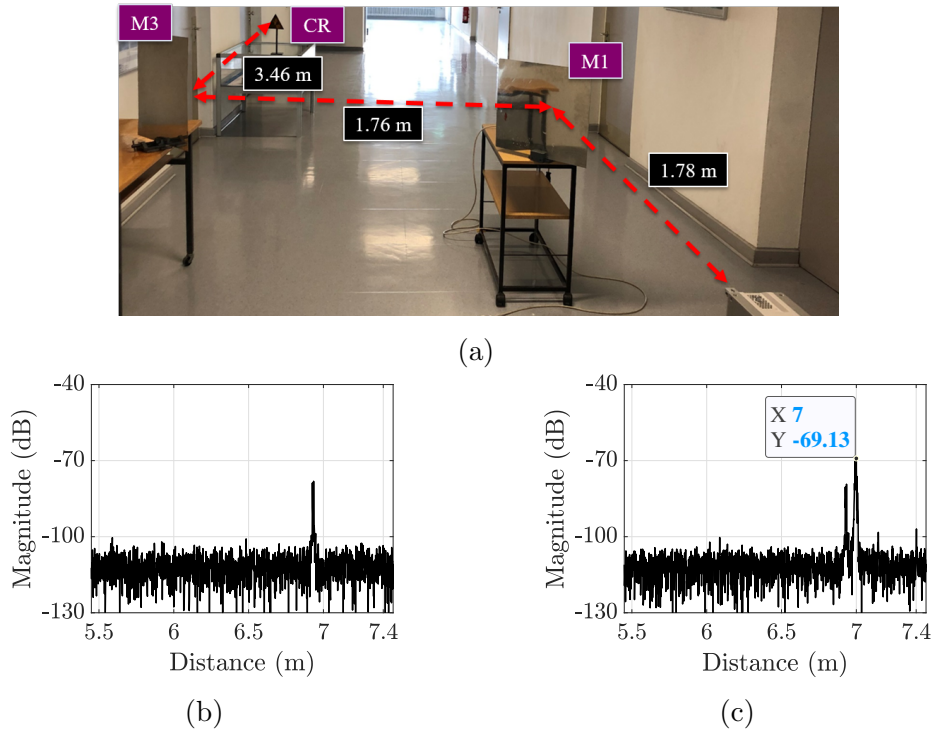


Figure 7-2: N-LoS detection and ranging (a) scene 2: corner reflector CR sensing (fifth order reflection) via reflection from M1 and M2, and measurements results: (b) time domain response of without CR and (d) with CR detected at 7 m.

# List of Publications

## Journal Papers

1. V. T. Vu, M. I. Pettersson, **A. Batra**, T. Kaiser, “Fourier Transform of SAR Data Cube and 3D Range Migration Algorithm,” in *IEEE Transactions on Aerospace and Electronic Systems* (correspondence), 2021 (accepted on Nov. 25, 2021).
2. **A. Batra**, J. Barowski, D. Damyanov, M. Wiemeler, I. Rolfes, T. Schultze, J. C. Balzer, D. Göhringer, T. Kaiser, “Short-Range SAR Imaging From GHz to THz Waves,” in *IEEE Journal of Microwaves*, vol. 1, no. 2, pp. 574-585, April 2021.
3. **A. Batra**, M. El-Absi, M. Wiemeler, D. Göhringer and T. Kaiser, “Indoor THz SAR Trajectory Deviations Effects and Compensation With Passive Sub-mm Localization System,” in *IEEE Access*, vol. 8, pp. 177519-177533, 2020.
4. D. Damyanov, **A. Batra**, B. Friederich, T. Kaiser, T. Schultze and J. C. Balzer, “High-Resolution Long-Range THz Imaging for Tunable Continuous-Wave Systems,” in *IEEE Access*, vol. 8, pp. 151997-152007, 2020.

## Conference Papers

5. **A. Batra**, J. Alam, M. Wiemeler, D. Goehringer and T. Kaiser, “Long-Range Non-Line of Sight THz Sensing,” 2021 46th International Conference on Infrared, Millimeter and Terahertz Waves (IRMMW-THz), pp. 1-2, 2021.
6. **A. Batra**, M. Wiemeler, D. Göhringer and T. Kaiser, “Sub-mm Resolution 3D SAR Imaging at 1.5 THz,” 2021 Fourth International Workshop on Mobile Terahertz Systems (IWMTS), pp. 1-5, 2021, .
7. **A. Batra**, A. Kamaleldin, L. Y. Zhen, M. Wiemeler, D. Göhringer and T. Kaiser, “FPGA-Based Acceleration of THz SAR Imaging,” 2021 Fourth International Workshop on Mobile Terahertz Systems (IWMTS), pp. 1-5, 2021.
8. F. Sheikh, Y. Zantah, **A. Batra**, I. Mabrouk, M. Al-Hasan and T. Kaiser, “Far-Distance VNA-based Measurements of Indoor Materials at 300 GHz,” 2021 IEEE-APS Topical Conference on Antennas and Propagation in Wireless Communications (APWC), pp. 064-064, 2021.

9. **A. Batra**, M. Wiemeler, D. Goehringer and T. Kaiser, "Comparison Analysis of Small and Large Bandwidth Indoor SAR Multi-Object Imaging at Low Terahertz Spectrum," 2020 45th International Conference on Infrared, Millimeter, and Terahertz Waves (IRMMW-THz), Buffalo, NY, USA, pp. 1-2, 2020.
10. D. Damyanov, **A. Batra**, B. Friederich, K. Kolpatzeck, X. Liu, T. Kaiser, T. Schultze, J. C. Balzer, "High Resolution VNA THz Imaging for Large Distances," 2020 45th International Conference on Infrared, Millimeter, and Terahertz Waves (IRMMW-THz), Buffalo, NY, USA, pp. 01-02, 2020.
11. **A. Batra**, M. Wiemeler, D. Goehringer and T. Kaiser, "Simulation Validation of High Resolution Indoor Terahertz Synthetic Aperture Radar Imaging," 2020 14th European Conference on Antennas and Propagation (EuCAP), Copenhagen, Denmark, pp. 1-5, 2020.
12. **A. Batra**, V. T. Vu, Y. Zantah, M. Wiemeler, M. I. Pettersson, D. Goehringer and T. Kaiser, "Sub-mm Resolution Indoor THz Range and SAR Imaging of Concealed Object," 2020 IEEE MTT-S International Conference on Microwaves for Intelligent Mobility (ICMIM), pp. 1-4, 2020.
13. **A. Batra**, Y. Zantah, M. Wiemeler, V. T. Vu, M. I. Pettersson, D. Goehringer and T. Kaiser, "Experimental Analysis of High Resolution Indoor THz SAR Imaging," WSA 2020; 24th International ITG Workshop on Smart Antennas, Hamburg, Germany, pp. 1-5, 2020.
14. **A. Batra**, M. Wiemeler, T. Kreul, D. Goehringer and T. Kaiser, "SAR Signal Processing Architecture and Effects of Motion Errors for mmWave and THz Frequencies," 2019 Second International Workshop on Mobile Terahertz Systems (IWMTS), pp. 1-6, 2019.
15. **A. Batra**, M. Wiemeler, T. Kreul, D. Goehringer and T. Kaiser, "A Massive MIMO Signal Processing Architecture for GHz to THz Frequencies," 2018 First International Workshop on Mobile Terahertz Systems (IWMTS), pp. 1-6, 2018.

# Bibliography

- [1] H. Rohling, “From Huelsmeyer’s Telemobiloskop to the Digital Radar,” in *2014 11th European Radar Conference*, pp. 33–36, 2014.
- [2] D. J. Cichon and W. Wiesbeck, “The Heinrich Hertz Wireless Experiments at Karlsruhe in the View of Modern Communication,” in *Proceedings of the 1995 International Conference on 100 Years of Radio*, pp. 1–6, 1995.
- [3] M. Guarnieri, “The Early History of Radar [Historical],” *IEEE Industrial Electronics Magazine*, vol. 4, no. 3, pp. 36–42, 2010.
- [4] M. Soumekh, *Synthetic Aperture Radar Signal Processing With MATLAB Algorithms*. NJ, USA: Wiley, 1999.
- [5] F. H. W. Ian G. Cumming, *Digital Processing of Synthetic Aperture Radar Data*. Artech House, 2005.
- [6] H. Kim, J. Park, I. Joe, D. Kwon, J. H. Kim, D. Cho, T. Lee, C. Lee, H. Park, S. Hong, C. Chang, J. Kim, H. Lim, Y. Oh, Y. Kim, S. Nah, S. Jung, J. Lee, J. Ahn, H. Hong, K. Lee, and H. Kang, “5.6 A 1/2.65in 44Mpixel CMOS Image Sensor with 0.7 $\mu$ m Pixels Fabricated in Advanced Full-Depth Deep-Trench Isolation Technology,” in *2020 IEEE International Solid-State Circuits Conference - (ISSCC)*, pp. 104–106, 2020.
- [7] C. W. Sherwin, J. P. Ruina, and R. D. Rawcliffe, “Some Early Developments in Synthetic Aperture Radar Systems,” *IRE Transactions on Military Electronics*, vol. MIL-6, no. 2, pp. 111–115, 1962.
- [8] H. Maître, *Processing of Synthetic Aperture Radar Images*. Wiley, 2008.
- [9] D. W. O’Hagan, S. R. Doughty, and M. R. Inggs, *Chapter 5 - Multistatic Radar Systems*. Academic Press, 2018.
- [10] G. Krieger, H. Fiedler, D. Houman, and A. Moreira, “Analysis of System Concepts for Bi- and Multi-Static SAR Missions,” in *IGARSS 2003. 2003 IEEE International*

- Geoscience and Remote Sensing Symposium. Proceedings (IEEE Cat. No.03CH37477)*, vol. 2, pp. 770–772 vol.2, 2003.
- [11] M. I. Skolnik, “An Analysis of Bistatic Radar,” *IRE Transactions on Aerospace and Navigational Electronics*, vol. ANE-8, no. 1, pp. 19–27, 1961.
- [12] I. Walterscheid, J. H. G. Ender, A. R. Brenner, and O. Loffeld, “Bistatic SAR Processing and Experiments,” *IEEE Transactions on Geoscience and Remote Sensing*, vol. 44, no. 10, pp. 2710–2717, 2006.
- [13] D. M. Mittleman, “Twenty Years of Terahertz Imaging [Invited],” *Opt. Express*, vol. 26, pp. 9417–9431, Apr 2018.
- [14] P. H. Siegel, “THz Instruments for Space,” *IEEE Transactions on Antennas and Propagation*, vol. 55, no. 11, pp. 2957–2965, 2007.
- [15] C. M. Snowden, “Prospects for Terahertz Technology,” in *IEE Workshop on Microwave and Millimetre-Wave Communications - the Wireless Revolution*, pp. 7/1–7/6, 1995.
- [16] T. S. Rappaport, Y. Xing, O. Kanhere, S. Ju, A. Madanayake, S. Mandal, A. Alkhatieb, and G. C. Trichopoulos, “Wireless Communications and Applications Above 100 GHz: Opportunities and Challenges for 6G and Beyond,” *IEEE Access*, vol. 7, pp. 78729–78757, 2019.
- [17] D. M. Slocum, E. J. Slingerland, R. H. Giles, and T. M. Goyette, “Atmospheric Absorption of Terahertz Radiation and Water Vapor Continuum Effects,” *Journal of Quantitative Spectroscopy and Radiative Transfer*, vol. 127, pp. 49–63, 2013.
- [18] A. Batra, J. Barowski, D. Damyanov, M. Wiemeler, I. Rolfes, T. Schultze, J. C. Balzer, D. Göhringer, and T. Kaiser, “Short-Range SAR Imaging From GHz to THz Waves,” *IEEE Journal of Microwaves*, pp. 1–12, 2021.
- [19] A. Batra, M. El-Absi, M. Wiemeler, D. Göhringer, and T. Kaiser, “Indoor THz SAR Trajectory Deviations Effects and Compensation With Passive Sub-mm Localization System,” *IEEE Access*, vol. 8, pp. 177519–177533, 2020.
- [20] S. Gui, J. Li, F. Zuo, and Y. Pi, “Analysis of Security Imaging Method for Walking Human Screening With Single Channel Synthetic Aperture Radar,” *IEEE Access*, vol. 7, pp. 111363–111374, 2019.
- [21] S. Gishkori, L. Daniel, M. Gashinova, and B. Mulgrew, “Imaging for a Forward Scanning Automotive Synthetic Aperture Radar,” *IEEE Transactions on Aerospace and Electronic Systems*, vol. 55, no. 3, pp. 1420–1434, 2019.
- [22] S. Stanko, S. Palm, R. Sommer, F. Klöppel, M. Caris, and N. Pohl, “Millimeter Resolution SAR Imaging of Infrastructure in the Lower THz Region using MIRANDA-300,” in *2016 European Radar Conference (EuRAD)*, pp. 358–361, 2016.

- [23] M. Nežadal, J. Schür, and L. Schmidt, “Non-Destructive Testing of Glass Fibre Reinforced Plastics with a Synthetic Aperture Radar in the Lower THz Region,” in *2012 37th International Conference on Infrared, Millimeter, and Terahertz Waves*, pp. 1–2, 2012.
- [24] S. Palm, R. Sommer, and U. Stilla, “Mobile Radar Mapping—Subcentimeter SAR Imaging of Roads,” *IEEE Transactions on Geoscience and Remote Sensing*, vol. 56, no. 11, pp. 6734–6746, 2018.
- [25] N. J. W. Morris, S. Avidan, W. Matusik, and H. Pfister, “Statistics of Infrared Images,” in *2007 IEEE Conference on Computer Vision and Pattern Recognition*, pp. 1–7, 2007.
- [26] H. D. Eom and J. W. Jeon, “Environment Map Building using Low-Cost IR Sensors and a Servo Motor for Mobile Robot,” in *The 18th IEEE International Symposium on Consumer Electronics (ISCE 2014)*, pp. 1–2, 2014.
- [27] C. Le, T. Dogaru, L. Nguyen, and M. A. Ressler, “Ultrawideband (UWB) Radar Imaging of Building Interior: Measurements and Predictions,” *IEEE Transactions on Geoscience and Remote Sensing*, vol. 47, no. 5, pp. 1409–1420, 2009.
- [28] C. J. Li and H. Ling, “Synthetic Aperture Radar Imaging Using a Small Consumer Drone,” in *2015 IEEE International Symposium on Antennas and Propagation USNC/URSI National Radio Science Meeting*, pp. 685–686, 2015.
- [29] R. Verschae and J. Ruiz-del Solar, “Object Detection: Current and Future Directions,” *Frontiers in Robotics and AI*, vol. 2, p. 29, 2015.
- [30] T. Bryllert, K. B. Cooper, R. J. Dengler, N. Llombart, G. Chattopadhyay, E. Schlecht, J. Gill, C. Lee, A. Skalare, I. Mehdi, and P. H. Siegel, “A 600 GHz Imaging Radar for Concealed Objects Detection,” in *2009 IEEE Radar Conference*, pp. 1–3, 2009.
- [31] J. T. Richard and H. O. Everitt, “Millimeter Wave and Terahertz Synthetic Aperture Radar for Locating Metallic Scatterers Embedded in Scattering Media,” *IEEE Transactions on Terahertz Science and Technology*, vol. 7, no. 6, pp. 732–740, 2017.
- [32] D. Damyanov, B. Friederich, M. Yahyapour, N. Vieweg, A. Deninger, K. Kolpatzeck, X. Liu, A. Czylwik, T. Schultze, I. Willms, and J. C. Balzer, “High Resolution Lensless Terahertz Imaging and Ranging,” *IEEE Access*, vol. 7, pp. 147704–147712, 2019.
- [33] D. Damyanov, A. Batra, B. Friederich, T. Kaiser, T. Schultze, and J. C. Balzer, “High-Resolution Long-Range THz Imaging for Tunable Continuous-Wave Systems,” *IEEE Access*, vol. 8, pp. 151997–152007, 2020.
- [34] “Mobile Material Characterization and Localization by Electromagnetic Sensing.” [Online]. Available: <https://trrmarie.de/sfbtrr196marie/>. Accessed: 14-11-2020.

- 
- [35] “Deutsches Zentrum für Luft- und Raumfahrt.” [Online]. Available: <https://www.dlr.de>. Accessed: 05-04-2021.
- [36] “Fraunhofer-Institut für Hochfrequenzphysik und Radartechnik.” [Online]. Available: <https://www.fhr.fraunhofer.de/en.html>. Accessed: 05-04-2021.
- [37] “CST Studio Suite Electromagnetic Field Simulation Software.” [Online]. Available: <https://www.3ds.com/products-services/simulia/products/cst-studio-suite/>. Accessed: 16-11-2020.
- [38] M. El-Absi, A. Alhaj Abbas, A. Abuelhaija, F. Zheng, K. Solbach, and T. Kaiser, “High-Accuracy Indoor Localization Based on Chipless RFID Systems at THz Band,” *IEEE Access*, vol. 6, pp. 54355–54368, 2018.
- [39] L. Pullagura, “Development of Software Accelerated THz SAR Imaging based on Python,” Master’s thesis, Institute of Digital Signal Processing, University of Duisburg-Essen, 04 2020.
- [40] L. Meng, “Development of GPU Based Acceleration of Indoor THz SAR Imaging,” Master’s thesis, Institute of Digital Signal Processing, University of Duisburg-Essen, 11 2020.
- [41] L. Y. Zhen, “Development of FPGA Based Acceleration of Indoor THz SAR Imaging.” Bachelor’s thesis, Institute of Digital Signal Processing, University of Duisburg-Essen, 02 2021.
- [42] M. Born and E. Wolf, *Principles of Optics: 60th Anniversary Edition*. Cambridge University Press, 7 ed., 2019.
- [43] W. L. Stutzman and G. A. Thiele, *Antenna Theory and Design*. Hoboken, NJ: Wiley, 3. ed ed., 2013.
- [44] A. Moreira, P. Prats-Iraola, M. Younis, G. Krieger, I. Hajnsek, and K. P. Papathanassiou, “A Tutorial on Synthetic Aperture Radar,” *IEEE Geoscience and Remote Sensing Magazine*, vol. 1, no. 1, pp. 6–43, 2013.
- [45] R. Piesiewicz, C. Jansen, S. Wietzke, D. Mittleman, M. Koch, and T. Kürner, “Properties of Building and Plastic Materials in the THz Range,” *International Journal of Infrared and Millimeter Waves*, vol. 28, pp. 363–371, 01 2007.
- [46] “Math. Graphics. Programming.” [Online]. Available: <https://www.mathworks.com/products/matlab.html>. Accessed: 04-04-2021.
- [47] A. Choudhury, *Principles of Colour and Appearance Measurement*. Woodhead Publishing, 1st edition ed., 2014.
- [48] M. I. Pettersson, “Detection of Moving Targets in Wideband SAR,” *IEEE Transactions on Aerospace and Electronic Systems*, vol. 40, no. 3, pp. 780–796, 2004.

- [49] C. Ben and M. Leeser, "Parallel Backprojection: A Case Study in High-Performance Reconfigurable Computing," *EURASIP Journal on Embedded Systems*, vol. 2009, 01 2009.
- [50] S. Nambari, K. Rao, G. Rao, N. Rani, and N. Sharma, "Radar RCS Estimation of a Perfectly Conducting Sphere Obtained from a Spherical Polar Scattering Geometry," pp. 1–7, 01 2015.
- [51] R. C. Rumpf, "Chapter Three - Engineering the Dispersion and Anisotropy of Periodic Electromagnetic Structures," vol. 66 of *Solid State Physics*, pp. 213–300, Academic Press, 2015.
- [52] N. Q. Vinh, "INS/GPS Integration System Using Street Return Algorithm and Compass Sensor," *Procedia Computer Science*, vol. 103, pp. 475–482, 2017. XII International Symposium Intelligent Systems 2016, INTELS 2016, 5-7 October 2016, Moscow, Russia.
- [53] F. Schultz, J. B. Mercer, and P. Button, "Digital Mosaicing Technology For Synthetic Aperture Radar Image Products," in *12th Canadian Symposium on Remote Sensing Geoscience and Remote Sensing Symposium*, vol. 1, pp. 120–123, 1989.
- [54] A. Batra, M. Wiemeler, T. Kreul, D. Goehringer, and T. Kaiser, "SAR Signal Processing Architecture and Effects of Motion Errors for mmWave and THz Frequencies," in *2019 Second International Workshop on Mobile Terahertz Systems (IWMTS)*, pp. 1–6, 2019.
- [55] V. T. Vu, T. K. Sjogren, and M. I. Pettersson, "Phase Error Calculation for Fast Time-Domain Bistatic SAR Algorithms," *IEEE Transactions on Aerospace and Electronic Systems*, vol. 49, no. 1, pp. 631–639, 2013.
- [56] Y. Zhang, J. Sun, P. Lei, and H. Wang, "High-Frequency Vibration Compensation of Helicopter-Borne THz-SAR [Correspondence]," *IEEE Transactions on Aerospace and Electronic Systems*, vol. 52, no. 3, pp. 1460–1466, 2016.
- [57] Y. Wang, Z. Wang, B. Zhao, and L. Xu, "Enhancement of Azimuth Focus Performance in High-Resolution SAR Imaging Based on the Compensation for Sensors Platform Vibration," *IEEE Sensors Journal*, vol. 16, no. 16, pp. 6333–6345, 2016.
- [58] D. Kaliyari, A. Shukla, Y. Rao, and H. B. Hablani, "Motion Compensation of Airborne Synthetic Aperture Radar," *IFAC Proceedings Volumes*, vol. 47, no. 1, pp. 627–634, 2014. 3rd International Conference on Advances in Control and Optimization of Dynamical Systems (2014).
- [59] M. Caris, S. Stanko, S. Palm, R. Sommer, A. Wahlen, and N. Pohl, "300 GHz Radar for High Resolution SAR and ISAR Applications," in *2015 16th International Radar Symposium (IRS)*, pp. 577–580, 2015.

- 
- [60] T. Jaeschke, C. Bredendiek, and N. Pohl, “3D FMCW SAR Imaging Based on a 240 GHz SiGe Transceiver Chip with Integrated Antennas,” in *GeMiC 2014; German Microwave Conference*, pp. 1–4, 2014.
- [61] H. Xia, Q. Chen, Y. Li, C. Fu, and H. Wang, “A High Frequency Vibration Compensation Approach in Terahertz SAR Based on Wavelet Multi-Resolution Analysis,” in *2018 China International SAR Symposium (CISS)*, pp. 1–5, 2018.
- [62] J.-T. González-Partida, P. Almorox-González, M. Burgos-Garcia, and B.-P. Dorta-Naranjo, “SAR System for UAV Operation with Motion Error Compensation beyond the Resolution Cell,” *Sensors*, vol. 8, no. 5, pp. 3384–3405, 2008.
- [63] M. Xing, X. Jiang, R. Wu, F. Zhou, and Z. Bao, “Motion Compensation for UAV SAR Based on Raw Radar Data,” *IEEE Transactions on Geoscience and Remote Sensing*, vol. 47, no. 8, pp. 2870–2883, 2009.
- [64] C. A. Balanis, *Antenna Theory : analysis and design ; [with multimedia CD]*. Hoboken, NJ: Wiley, 3. ed. ed., 2005.
- [65] F. T. Ulaby, R. K. Moore, and A. K. Fung, *Microwave Remote Sensing : active and passive. 2. Radar remote sensing and surface scattering and emission theory*. Reading, Mass. [u.a.]: Addison-Wesley, 1982.
- [66] “Rohde and Schwarz ZVA Vector Network Analyzers.” [Online]. Available: [https://www.rohde-schwarz.com/de/produkt/zva-produkt-startseite\\_63493-9660.html](https://www.rohde-schwarz.com/de/produkt/zva-produkt-startseite_63493-9660.html). Accessed: 11-04-2021.
- [67] “Rohde and Schwarz ZCxxx Millimeter-Wave Converters.” [Online]. Available: [https://www.rohde-schwarz.com/ph/product/zcxxx-products\\_63492-133190.html](https://www.rohde-schwarz.com/ph/product/zcxxx-products_63492-133190.html). Accessed: 11-04-2021.
- [68] Y. Zantah, F. Sheikh, A. A. Abbas, M. Alissa, and T. Kaiser, “Channel Measurements in Lecture Room Environment at 300 GHz,” in *2019 Second International Workshop on Mobile Terahertz Systems (IWMTS)*, pp. 1–5, 2019.
- [69] N. Smith, “21 - Lighting,” in *Electrical Engineer’s Reference Book (Sixteenth Edition)* (M. Laughton and D. Warne, eds.), pp. 21–1–21–31, Oxford: Newnes, sixteenth edition ed., 2003.
- [70] A. K. R. Choudhury, “2 - Object Appearance and Colour,” in *Principles of Colour and Appearance Measurement* (A. K. R. Choudhury, ed.), pp. 53–102, Woodhead Publishing, 2014.
- [71] F. Sheikh, Y. Gao, and T. Kaiser, “A Study of Diffuse Scattering in Massive MIMO Channels at Terahertz Frequencies,” *IEEE Transactions on Antennas and Propagation*, vol. 68, no. 2, pp. 997–1008, 2020.

- [72] M. Alissa, B. Friederich, F. Sheikh, A. Czylik, and T. Kaiser, “Experimental Investigation of Terahertz Scattering: A Study of Non-Gaussianity and Lateral Roughness Influence,” *IEEE Access*, vol. 8, pp. 170672–170680, 2020.
- [73] V. Korn, C. Surber, and G. Imanidis, “Skin Surface Topography and Texture Analysis of Sun-Exposed Body Sites in View of Sunscreen Application,” *Journal of Pharmaceutical and Biophysical Research*, vol. 29, pp. 291–299, 2016.
- [74] P. R. Bargo and N. Kollias, “Measurement of Skin Texture Through Polarization Imaging,” *British Journal of Dermatology*, vol. 162, no. 4, pp. 724–731, 2010.
- [75] L.-Y. Lin and S.-C. Chiou, “Influence of Facial Threading on Various Physiological Parameters of the Skin: non-randomized trial involving adult women in Taiwan\*,” *Anais Brasileiros de Dermatologia*, vol. 93, no. 5, pp. 659–664, 2018.
- [76] P. Hügler, M. Geiger, and C. Waldschmidt, “RCS Measurements of a Human Hand for Radar-Based Gesture Recognition at E-band,” in *2016 German Microwave Conference (GeMiC)*, pp. 259–262, 2016.
- [77] S. A. Nazmus Saqueeb, J. L. Garry, G. E. Smith, N. K. Nahar, and K. Sertel, “THz Imaging Using Rail-Based Synthetic Aperture Radar for the Detection of Concealed Objects,” in *2018 USNC-URSI Radio Science Meeting (Joint with AP-S Symposium)*, pp. 175–176, 2018.
- [78] A. Batra, M. Wiemeler, D. Göhringer, and T. Kaiser, “Sub-mm resolution 3d sar imaging at 1.5 thz,” in *2021 Fourth International Workshop on Mobile Terahertz Systems (IWMTS)*, pp. 1–5, 2021.
- [79] H. Bay, T. Tuytelaars, and L. Van Gool, “SURF: Speeded Up Robust Features,” in *Computer Vision – ECCV 2006*, vol. 3951 of *Lecture Notes in Computer Science*, (Berlin, Heidelberg), pp. 404–417, Springer Berlin Heidelberg, 2006.
- [80] P.-N. Tan, *Introduction to Data Mining, Global Edition*. Pearson, 2 ed., 2020.
- [81] “VDI Vector Network Analyzer Extenders.” [Online]. Available: <https://www.vadiodes.com/en/products/vector-network-analyzer-extension-modules>. Accessed: 11-04-2021.
- [82] “Rohde and Schwarz SMA100B RF and Microwave Signal Generator.” [Online]. Available: [https://www.rohde-schwarz.com/us/product/sma100b-productstartpage\\_63493-427776.html](https://www.rohde-schwarz.com/us/product/sma100b-productstartpage_63493-427776.html). Accessed: 12-04-2021.
- [83] “Mathworks SURF Extraction.” [Online]. Available: <https://www.mathworks.com/help/vision/ref/detectsurffeatures.html>. Accessed: 23-04-2021.
- [84] “Mathworks DBSCAN Clustering.” [Online]. Available: <https://www.mathworks.com/help/stats/dbscan.html>. Accessed: 23-04-2021.

- 
- [85] “Mathworks Bag of Features.” [Online]. Available: <https://www.mathworks.com/help/vision/ref/bagofeatures.html>. Accessed: 23-04-2021.
- [86] “Mathworks K-Means Clustering.” [Online]. Available: <https://www.mathworks.com/help/stats/kmeans.html>. Accessed: 23-04-2021.
- [87] “Mathworks Train Image Classifier.” [Online]. Available: <https://www.mathworks.com/help/vision/ref/trainimagecategoryclassifier.html>. Accessed: 23-04-2021.
- [88] “Mathworks Predict Label.” [Online]. Available: <https://www.mathworks.com/help/stats/compactclassificationtree.predict.html>. Accessed: 23-04-2021.
- [89] L. M. H. Ulander, H. Hellsten, and G. Stenstrom, “Synthetic-Aperture Radar Processing using Fast Factorized Back-Projection,” *IEEE Transactions on Aerospace and Electronic Systems*, vol. 39, no. 3, pp. 760–776, 2003.
- [90] V. T. Vu, T. K. Sjogren, and M. I. Pettersson, “A Comparison between Fast Factorized Backprojection and Frequency-Domain Algorithms in UWB Lowfrequency SAR,” in *IGARSS 2008 - 2008 IEEE International Geoscience and Remote Sensing Symposium*, vol. 4, pp. IV – 1284–IV – 1287, 2008.
- [91] G. Wang, F. Qi, Z. Liu, C. Liu, C. Xing, and W. Ning, “Comparison Between Back Projection Algorithm and Range Migration Algorithm in Terahertz Imaging,” *IEEE Access*, vol. 8, pp. 18772–18777, 2020.
- [92] H. El-Rewini, *Advanced Computer Architecture and Parallel Processing*. Hoboken, N.J.: John Wiley, 2005.
- [93] G. Barlas, *Multicore and GPU Programming : an integrated approach*. Amsterdam: Morgan Kaufmann, 2015.
- [94] R. Woods, *FPGA-Based Implementation of Signal Processing Systems*. Hoboken, NJ: John Wiley and Sons Inc., second editon. ed., 2017.
- [95] A. Batra, M. Wiemeler, T. Kreul, D. Goehringer, and T. Kaiser, “A Massive MIMO Signal Processing Architecture for GHz to THz Frequencies,” in *2018 First International Workshop on Mobile Terahertz Systems (IWMTS)*, pp. 1–6, 2018.
- [96] D. C. Marinescu, *Cloud Computing : theory and practice*. Amsterdam: Morgan Kaufmann, second edition. ed., 2017.
- [97] “Python.” [Online]. Available: <https://www.python.org/>. Accessed: 15-04-2021.
- [98] “Nvidia CUDA.” [Online]. Available: <https://developer.nvidia.com/cuda-zone>. Accessed: 15-04-2021.

- [99] “Mathworks Pricing and Licensing.” [Online]. Available: <https://www.mathworks.com/pricing-licensing.html?prodcode=DM>. Accessed: 15-04-2021.
- [100] “Mathworks Parallel Computing Toolbox.” [Online]. Available: <https://www.mathworks.com/products/parallel-computing.html>. Accessed: 15-04-2021.
- [101] “Mathworks Tic-Toc.” [Online]. Available: <https://www.mathworks.com/help/matlab/ref/tic.html>. Accessed: 15-04-2021.
- [102] “NumPy.” [Online]. Available: <https://numpy.org/>. Accessed: 16-04-2021.
- [103] “SciPy.” [Online]. Available: <https://www.scipy.org/>. Accessed: 16-04-2021.
- [104] “Python Cmath Module.” [Online]. Available: <https://docs.python.org/3/library/cmath.html>. Accessed: 16-04-2021.
- [105] “Python Time Module.” [Online]. Available: <https://docs.python.org/3/library/time.html>. Accessed: 16-04-2021.
- [106] “Matplotlib.” [Online]. Available: <https://matplotlib.org/>. Accessed: 16-04-2021.
- [107] “MPI for Python.” [Online]. Available: <https://mpi4py.readthedocs.io/en/stable/>. Accessed: 16-04-2021.
- [108] “OpenMP.” [Online]. Available: <https://www.openmp.org/>. Accessed: 16-04-2021.
- [109] D. Göhringer and J. Becker, “New Dimensions in Design Space and Runtime Adaptivity for Multiprocessor Systems Through Dynamic and Partial Reconfiguration: The RAMPSoC Approach,” in *VLSI 2010 Annual Symposium* (N. Voros, A. Mukherjee, N. Sklavos, K. Masselos, and M. Huebner, eds.), (Dordrecht), pp. 335–346, Springer Netherlands, 2011.
- [110] B. Falsafi, B. Dally, D. Singh, D. Chiou, J. J. Yi, and R. Sendag, “FPGAs Versus GPUs in Data Centers,” *IEEE Micro*, vol. 37, no. 1, pp. 60–72, 2017.
- [111] R. Mehler, *Digital Integrated Circuit Design using Verilog and Systemverilog*. Kidlington, England: Newnes, 2015.
- [112] “Vivado Design Suite - HLx Editions.” [Online]. Available: <https://www.xilinx.com/products/design-tools/vivado.html>. Accessed: 16-04-2021.
- [113] “Xilinx ZCU102 Evaluation Board.” [Online]. Available: <https://www.xilinx.com/products/boards-and-kits/ek-u1-zcu102-g.html>. Accessed: 16-04-2021.
- [114] A. Batra, A. Kamaleldin, L. Y. Zhen, M. Wiemeler, D. Göhringer, and T. Kaiser, “Fpga-based acceleration of thz sar imaging,” in *2021 Fourth International Workshop on Mobile Terahertz Systems (IWMTS)*, pp. 1–5, 2021.

- [115] “CUDA Programming Guide.” [Online]. Available: <https://docs.nvidia.com/cuda/cuda-c-programming-guide/index.html#abstract>. Accessed: 16-04-2021.
- [116] L. Ullman, *C++ Programming : Visual QuickStart Guide*. Peachpit Press, 1st edition ed., 2005.
- [117] “PyCuda Documentation.” [Online]. Available: <https://documen.tician.de/pycuda/>. Accessed: 16-04-2021.
- [118] “Using Shared Memory in CUDA C/C++.” [Online]. Available: <https://developer.nvidia.com/blog/using-shared-memory-cuda-cc/>. Accessed: 16-04-2021.
- [119] “Python Modules.” [Online]. Available: <https://docs.python.org/3/tutorial/modules.html>. Accessed: 16-04-2021.
- [120] A. Batra, J. Alam, M. Wiemeler, D. Goehringer, and T. Kaiser, “Long-range non-line of sight thz sensing,” in *2021 46th International Conference on Infrared, Millimeter and Terahertz Waves (IRMMW-THz)*, pp. 1–2, 2021.

# DuEPublico

Duisburg-Essen Publications online

UNIVERSITÄT  
DUISBURG  
ESSEN

*Offen im Denken*

ub | universitäts  
bibliothek

Diese Dissertation wird via DuEPublico, dem Dokumenten- und Publikationsserver der Universität Duisburg-Essen, zur Verfügung gestellt und liegt auch als Print-Version vor.

**DOI:** 10.17185/duepublico/75172

**URN:** urn:nbn:de:hbz:464-20211209-091205-7

Alle Rechte vorbehalten.